

# Towards the near-infrared detection of exoplanets

Jason James Neal

Tese de doutoramento apresentada à  
Faculdade de Ciências da Universidade do Porto  
Astronomia

2018

TOWARDS THE NIR DETECTION OF EXOPLANETS

by

Jason James Neal

A thesis submitted in conformity with the requirements  
for the degree of Doctor of Philosophy  
Graduate Department of Departamento de Física e Astronomia  
University of Porto

*To my wife Jessica,  
children Timothy and Amelia;  
For always supporting me.*

## Acknowledgements

First I would like to acknowledge my supportive wife Jessica, and children Timothy and Amelia for bearing with me and supporting me through this journey to a distant land. For all the late nights and trips away, and a mentally exhausted presence; it is now finally over.

I would also like to acknowledge my supervisors and group leader, Pedro, Claudio and Nuno for their patience, wisdom, support and guidance throughout these last four years.

I acknowledge support from Fundação para a Ciência e a Tecnologia (FCT) though the PhD::Space fellowship PD/BD/52700/2014. Without this fellowship we could not have moved halfway around the world to come to Portugal for me to undertake this research. I was also supported by the short term contract with reference CIAAUP-20/2018-BIM.

This work was undertaken within the Exoplanet team in the Instituto de Astrofísica e Ciências do Espaço and Centro de Astrofísica da Universidade do Porto. This team was supported by Fundação para a Ciência e a Tecnologia (FCT) (Portugal) research grants through Portuguese funds and from FEDER - Fundo Europeu de Desenvolvimento Regional, through COMPETE2020 - Programa Operacional Competitividade e Internacionalização (POCI) by the following grants:

UID/FIS/04434/2013  
PTDC/FIS-AST/1526/2014  
PTDC/FIS-AST/7073/2014  
POCI-01-0145-FEDER-007672  
POCI-01-0145-FEDER-016886  
POCI-01-0145-FEDER-016880  
POCI-01-0145-FEDER-028953  
POCI-01-0145-FEDER-032113 (**G.EANES**).

ARE there any GRANTS listed here that should not be here or any missing.(team ones that I [REDACTED] benefited from through flights etc.)

## Abstract

The contents of this work focus on detecting exoplanets in the nIR.

It starts of with reduction of nIR spectra from CRIRES.

In Chapter 6 we approach a differential subtraction technique to separate the spectra from the faint companion. Contrasting the result to other recent detections. In Chapter 7 a second technique is developed in which the BD companions are attempted to be recovered from the  $\lambda$ -infrared spectra by fitting to a complex model of two synthetic stellar spectra. Finding the technique unsuitable for the data on hand.

Focusing on BD as they should have a stronger flux ratio than planets.

In Chapter 8 we change focus towards RV precision of M-dwarf stars. Calculating the theoretical precision of stellar spectra  $t$ . Useful for the next-generation of near-infrared spectrographs to detect planets around M-dwarf stars.

Some thought on future are also provided.

## **Resumo**

Thesis abstract in Portuguese

# Todo list

████	.....	iii
████	.....	xiv
████	Pedro: I would only note that you can provide a more detailed description on the importance of determining RV information content measurement (at the very end of the chapter) .....	18
████	Fix title of plot Telluric correction by <b>different</b> models .....	37
████	Figure 4.7 needs improved style .....	44
███	Pedro it is my understanding that the ESO pipeline did not exist/was not publicly available when you created DRACS, correct? .....	51
████	.....	65
████	rotate table? .....	69
████	I am not sure if this is the best location for this section. ....	70
████	check it is in this chapter .....	72
████	put in advanced concepts chapter??? .....	72
████	this ignores $\gamma$ .....	72
Figure:	simulated example of combined binary spectra, and the subtraction, with a clear companion visible .....	72
████	check result .....	72
████	change RV scale for hd4747 orbit .....	77
████	Fix plot titles .....	77
████	Check M2sini labels - can we get M2 only for those that we know .....	77
████	Should RV of companion be scale by m2sini only or m2 if known? .....	77
████	Example with a large mass companion? and/or SNR. ....	88
████	find projected distance .....	92
████	Put error paragraph in a good location .....	93
████	finish this line .....	98
████	.....	99
████	remove duplication .....	100
███	rv method .....	100
████	put in introduction?? .....	100
████	derivation of rv? .....	100
Figure:	An example from Figueira et al. 2016 .....	101

■ add $\delta A$ to plots . . . . .	101
■ intensity change from connes is vertically in the slice d lambda . . . . .	101
■ Finish this equation (9 of bouchy 2001) . . . . .	103
■ Try the symbolic package from PC . . . . .	103
■ explain snr . . . . .	104
■ It is convenient to use this version when comparing observed spectra with different SNR.? . . . .	104
■ Does spectrograph pipelines such as HARPS use these equations to measure estimate/precision? . . . .	104
■ It is convenient to use this version when comparing observed spectra with different SNR.? . . . .	105
■ top view diagram of rotation? . . . . .	105
Figure: Example of CARMENES spectra before and after correction . . . . .	107
■ Add figure here . . . . .	108
■ Add figure here . . . . .	108
■ finish this . . . . .	108
■ works of software testing in research. . . . .	111
■ cite the equation when I refer to it . . . . .	116
■ Check this if it is previous . . . . .	116
■ Should I show the working of analytical working out of this in an appendix, or here? . . . . .	117
■ did I check this was equivalent . . . . .	117
■ put this some where . . . . .	117
■ put this line elsewhere. . . . .	117
■ add conclusions not affected . . . . .	118
■ is this needed . . . . .	119
■ SNR plot/diagram . . . . .	119
■ . . . . .	119
■ Check how to cite priv communication properly . . . . .	120
■ Fix up when accepted . . . . .	120
■ comparison of plots . . . . .	120
■ Change to $55 \text{ m s}^{-1}$ upper limit? . . . . .	120
■ NIR analysis work . . . . .	122
■ Precision table needs fixed up . . . . .	123
■ reread and fix up still . . . . .	155
■ Fix up at end . . . . .	158
■ add published Ulmer-moll version . . . . .	163

# Contents

<b>Todo list</b>	<b>vi</b>
<b>List of Tables</b>	<b>xi</b>
<b>List of Figures</b>	<b>xii</b>
<b>1 Introduction</b>	<b>1</b>
1.1 Towards the characterization of exoplanets . . . . .	1
1.2 Exoplanet detection methods . . . . .	2
1.2.1 Radial Velocimetry . . . . .	2
1.2.2 Transit methods . . . . .	4
1.2.3 Direct Imaging . . . . .	6
1.2.4 Astrometry . . . . .	7
1.2.5 Microlensing . . . . .	8
1.2.6 Pulsar timing . . . . .	9
1.3 Detecting atmospheres . . . . .	10
1.3.1 Occultation and phase variations . . . . .	10
1.3.2 Transmission spectroscopy . . . . .	12
1.3.3 High resolution spectroscopy . . . . .	14
1.4 The diversity of exoplanets . . . . .	15
1.5 Motivation for this thesis . . . . .	18
<b>2 Fundamental Radial Velocity</b>	<b>19</b>
2.1 Keplerian Orbits . . . . .	19
2.1.1 Mass function . . . . .	21
2.1.2 Binary mass ratio . . . . .	22
2.2 Measuring the RV . . . . .	23
2.3 RV precision . . . . .	23
<b>3 Near-infrared spectroscopy</b>	<b>26</b>
3.1 Spectrograph basics . . . . .	26
3.2 The detectors . . . . .	28

3.2.1	Spectrograph cooling . . . . .	30
3.3	CRIRES . . . . .	30
3.4	The new generation . . . . .	31
3.4.1	CRIRES+ . . . . .	32
3.4.2	CARMENES . . . . .	32
3.4.3	NIRPS . . . . .	33
3.4.4	SPIRou . . . . .	33
<b>4</b>	<b>Atmospheres and Models</b>	<b>34</b>
4.1	Earth’s atmosphere, in the nIR . . . . .	34
4.2	Telluric correction . . . . .	36
4.2.1	TAPAS web service . . . . .	37
4.2.2	Requests for this work . . . . .	38
4.2.3	Issues with TAPAS . . . . .	38
4.2.4	Telluric masking . . . . .	39
4.3	Synthetic Stellar models of cool stars . . . . .	40
4.3.1	PHOENIX-ACES models . . . . .	40
4.3.2	BT-Settl . . . . .	41
4.3.3	Model access . . . . .	42
4.3.4	Comparing models . . . . .	43
4.4	Evolutionary models . . . . .	44
4.4.1	Estimating Companion-host Flux ratio . . . . .	45
4.4.2	Baraffe tables . . . . .	46
<b>5</b>	<b>Spectroscopic reduction</b>	<b>47</b>
5.0.1	nIR reduction concepts . . . . .	47
5.0.1.1	Dark Current . . . . .	48
5.0.1.2	Flat-field . . . . .	48
5.0.1.3	Nodding and Jitter . . . . .	49
5.0.2	Th-Ar lamp calibration . . . . .	49
5.0.3	Extraction . . . . .	50
5.1	Pipeline Comparison . . . . .	51
5.1.1	ESO CRIRES pipeline . . . . .	51
5.1.2	DRACS . . . . .	52
5.1.3	Pipeline comparison and selection . . . . .	53
5.1.3.1	Reduction issues . . . . .	53
5.1.4	Reduction experience: . . . . .	57
5.2	Post reduction stages . . . . .	58
5.2.1	Wavelength calibration . . . . .	58
5.2.2	Telluric correction . . . . .	63
5.2.2.1	Separate H <sub>2</sub> O scaling . . . . .	63
5.2.3	Wavelength masking . . . . .	63
5.2.4	Barycentric RV correction . . . . .	64

<b>6 Separating the spectra of faint companions</b>	<b>65</b>
6.1 Spectral Disentangling techniques . . . . .	65
6.2 Motivation and target selection . . . . .	66
6.2.1 The Data . . . . .	68
6.2.2 CRIRES data . . . . .	68
6.2.3 Calculation of expected RV . . . . .	70
6.3 Direct Subtraction Method . . . . .	71
6.4 Results of spectral differential analysis . . . . .	73
6.4.1 Relative differential amplitude . . . . .	75
6.5 Orbital Solutions . . . . .	76
6.5.0.1 Differential scheduling challenges . . . . .	81
6.6 Contrast to other works . . . . .	81
6.7 Direct recovery in the mIR . . . . .	82
6.8 Summary . . . . .	83
<b>7 Synthetic companion recovery</b>	<b>84</b>
7.1 Binary $\chi^2$ spectral recovery . . . . .	84
7.1.1 The $\chi^2$ method . . . . .	84
7.1.2 Computed model spectra . . . . .	85
7.1.2.1 Single component model . . . . .	86
7.1.2.2 Binary model . . . . .	86
7.1.2.3 Effective radius . . . . .	87
7.1.3 Re-normalization . . . . .	87
7.1.4 Reducing parameters . . . . .	88
7.2 Results . . . . .	88
7.2.1 Simulated binaries . . . . .	91
7.2.2 HD211847 observation . . . . .	92
7.2.3 Companion injection-recovery . . . . .	94
7.2.4 Junk from paper about BT-settl . . . . .	98
7.2.5 Note about a target - discussion of results . . . . .	98
7.2.5.1 Wavelength range . . . . .	98
7.2.6 Comparison to other methods . . . . .	99
7.3 Summary . . . . .	99
<b>8 Information content of nIR Spectra</b>	<b>100</b>
8.1 Overview . . . . .	100
8.1.1 Fundamental photon noise limitation . . . . .	101
8.1.2 Prepare PHOENIX aces models . . . . .	105
8.1.3 Rotational convolution . . . . .	105
8.1.4 Instrumental Convolution . . . . .	106
8.1.5 Numerical Convolution . . . . .	106
8.2 . . . . .	107
8.2.1 Bands . . . . .	108
8.2.2 Comparing models to CARMENES . . . . .	108

8.3	Metallicity logg effects . . . . .	109
8.4	Updating RV precision software . . . . .	111
8.4.1	Automated testing . . . . .	111
8.4.2	Performance . . . . .	111
8.4.3	Model extension . . . . .	112
8.5	Numerical Gradient . . . . .	112
8.5.1	Masking Function . . . . .	116
8.5.1.1	Masking order . . . . .	117
8.5.2	Atmospheric masking bug . . . . .	117
8.5.3	SNR scaling . . . . .	118
8.6	SPIRou and NIRPS ETC . . . . .	119
8.7	Updated Figueira 2016 results . . . . .	120
8.8	metalicity / logg extension . . . . .	120
8.9	Application to CARMENES spectra . . . . .	120
<b>9</b>	<b>Conclusions</b>	<b>121</b>
9.1	Conclusions from Paper . . . . .	121
9.2	Future Work . . . . .	122
<b>A</b>	<b>RV Precision Tables</b>	<b>124</b>
<b>B</b>	<b>Artefacts in Optimal Extraction</b>	<b>147</b>
<b>C</b>	<b>Multi-detector wavelength calibration</b>	<b>153</b>
C.1	Comparing variable gaps . . . . .	155
<b>D</b>	<b>Vacuum wavelengths</b>	<b>157</b>
<b>E</b>	<b>PhD output</b>	<b>158</b>
E.1	Publications . . . . .	159
E.2	Talks and Seminars . . . . .	164
E.3	Posters . . . . .	165
E.4	Attended Conferences and Schools . . . . .	168
E.5	Outreach . . . . .	170
E.6	Other . . . . .	171
<b>Bibliography</b>		<b>172</b>

# List of Tables

2.1	Induced radial velocity semi-amplitudes. . . . .	22
3.1	Properties of popular optical/IR detector materials. . . . .	28
3.2	Summary of high-resolution nIR spectrographs. . . . .	32
4.1	Standard infrared pass-bands. . . . .	34
4.2	PHOENIX-ACES parameter space. . . . .	41
4.3	BT-Settl parameter space. . . . .	42
4.4	Companion/host flux ratios. . . . .	45
6.1	Stellar parameters of host stars. . . . .	67
6.2	Orbital parameters of companions. . . . .	67
6.3	List of CRIRES observations. . . . .	69
6.4	Semi-amplitude and RV separation of companions. . . . .	70
7.1	$\chi^2$ simulation results. . . . .	89
7.2	Upper mass limits from $\chi^2$ simulations. . . . .	95
8.1	Selection of targets from the CARMENES library. . . . .	108
8.2	CARMENES targets for RV precision analysis. . . . .	108
8.3	Effect of numerical gradient. . . . .	114
8.4	RV precision with different splitting. . . . .	118
A.1	RV precisions for the PHOENIX-ACES and BT-Settl spectral libraries. . . . .	125
A.2	RV precisions calculated for the SPIRou ETC. . . . .	131
A.3	RV precisions calculated for the NIRPS ETC. . . . .	134
B.1	Identification of nod spectra artefacts. . . . .	148
B.2	Nod position tally of artefacts. . . . .	148
C.1	Example of multi-detector fitting parameters and correlation. . . . .	155

# List of Figures

1.1	Number of exoplanet detections per year separated by method. . . . .	2
1.2	The RV method. . . . .	3
1.3	Exoplanet discovery year verses exoplanet mass. . . . .	3
1.4	Transit of Venus and successive transit corssings. . . . .	6
1.5	Direct detection of four exoplanets around HR 8799. . . . .	7
1.6	Modelled astrometric path on the sky. . . . .	9
1.7	Microlensing magnification of OGLE2005-BLG-390. . . . .	10
1.8	Flux contribution from a star and planet in a transiting exoplanet system. . . . .	11
1.9	Exoplanet phase variations and temperature map. . . . .	11
1.10	Transmission spectroscopy diagram. . . . .	13
1.11	Transmission spectra for several Hot-Jupiter exoplanets. . . . .	13
1.12	Cross-correlation signal from CRIRES observations of HD 209458 b. . . . .	14
1.13	Mass-Radius diagram for rocky planets with composition contours. . . . .	16
1.14	Mass-Radius relationship with probabilistic fit. . . . .	17
2.1	The basic elements of the Keplerian orbit. . . . .	20
2.2	Elements of an elliptical orbit. . . . .	21
3.1	Basic components of a spectrograph. . . . .	26
3.2	Dispersion mechanisms. . . . .	27
3.3	Schema differentiating CCD and CMOS detectors. . . . .	29
3.4	Side by side comparison of the NIRPS and SPIRou spectrographs. . . . .	30
3.5	CRIRES layout schematic. . . . .	31
3.6	CRIRES/CRIRES+ detector focal plane arrays. . . . .	32
4.1	Telluric absorption map from 0.3–30 $\mu\text{m}$ at $R \sim 10\,000$ . . . . .	35
4.2	Telluric correction applied using the Molecfit, TelFit and TAPAS. . . . .	37
4.3	Telluric spectra for the H <sub>2</sub> O and non-H <sub>2</sub> O species. . . . .	38
4.4	Difference in successive PHOENIX-ACES spectra around 5000 K. . . . .	42
4.5	Large scale comparison between the PHEONIX-ACES and BT-Settl spectra. . . . .	43
4.6	Comparision of the spectrum of Arcturus to synthetic spectra. . . . .	43
4.7	Comparision of the spectrum of 10 Leo to synthetic PHOENIX-ACES spectum. . . . .	44

5.1	Example dark frames for different exposure times. . . . .	47
5.2	Example of flat-field correction. . . . .	48
5.3	Illustration of the nodding technique. . . . .	49
5.4	Example Th-Ar calibration lamp frames for each detector. . . . .	50
5.5	Comparision between DRACS and ESOs reduction pipeline output. . . . .	54
5.6	Example of DRACS artefacts in the optimally extracted spectra HD 162020. . . . .	55
5.7	Artefacts comparision with and altered pipeline parameter. . . . .	56
5.8	Example of telluric corrected spectrum of HR 7329-B using TAPAS. . . . .	58
5.9	Example of the wavelength calibration using the synthetic telluric spectra. . . . .	61
5.10	Example reduced CRIRES spectra for each target. . . . .	62
6.1	Example of the spectral differential technique. . . . .	74
6.2	Simulated relative amplitude of differntial spectrum. . . . .	76
6.3–6.11	RV curves for the host and companion of each target. . . . .	78
7.1	$\chi^2$ contour for companion recovery of a simulated Sun - M-dwarf binary. . . . .	89
7.2	$\chi^2$ contour for companion recovery of a simulated observation of HD 211847. . . . .	90
7.3	$\chi^2$ contour for an observation HD 211847. . . . .	93
7.4	Comparison between observation of HD 211847 and the best fit synthetic binary model. .	94
7.5	Result of simulated injection-recovery of synthetic companions on HD 30501. . . . .	96
7.6	Shape of simulated $\chi^2$ with different injected companion temperatures. . . . .	97
8.1	Demonstration of a shifted arbitrary spectral line. . . . .	102
8.2	Quality factor verse [Fe/H] and logg for different spectral types and wavelength bands. .	110
8.3	Comparing of numerical gradient alogithms. . . . .	114
8.4	Comparision of RV precision results to Figueira et al. (2016). . . . .	120
B.1–B.7	Extra examples of reduced spectra with artefacts. One for each target. . . . .	149
C.1	Multi-detector fit and difference to individual fits. . . . .	154
C.2	Difference of multi-detector combined fit to the individual calibration mappings. . . . .	154
C.3	Multi-detector calibration parameter correlations. . . . .	156

---

# Chapter 1

## Introduction

### 1.1 Towards the characterization of exoplanets

The field of exoplanetary science is rapidly accelerating. Large scientific and instrumental investments have been undertaken, with the ultimate goal of detecting and characterizing an Earth-like planet that has the potential for life (as we know it). Since the very first exoplanet detection around a Sun-like star (Mayor et al., 1995) the number of confirmed exoplanets has grown to over 3869 with another 2898 candidates awaiting confirmation as of January 2019<sup>1</sup>. A planet transitions from a candidate to confirmed when the probability of false positives is very low, usually achieved using advanced analysis or a detection with a complementary method. However, simply detecting the presence of exoplanets is not nearly enough to satisfy our quest for knowledge. There is an exorbitant amount of insight to be gained through the full characterization of these known exoplanets, such as: density, composition, internal structure, atmosphere properties, and surface temperature.

When a new extra-solar planet is suspected, follow-up observation and analysis is required to confirm its existence, and its properties. In particular for the highly sought after Earth-twin, a full characterization is required to determine their habitability, for example (Shan et al., 2018) explore the axial tilts of Kepler-186f and Kepler-62f, two Earth-like planets found in their stars habitable zones. Notability, here have been several small planets, which have had early claims of Earth-twin status, later determined to be false (or fall below a 99% probability level) after follow up investigation (e.g. Mullally et al., 2018; Burke et al., 2019), and the presence of some have been heavily debated in literature such as Gliese 581g (Vogt et al., 2010; Gregory, 2011; Robertson et al., 2014). Detecting and analysing exoplanet atmospheres aid in the characterization of exoplanets by allowing their temperature, atmospheric structure, the presence any scattering aerosols, and the chemical composition. All providing clues towards a full exoplanet characterization.

In this chapter the common exoplanet and atmospheric detection methods will be introduced, followed by some exoplanet property distributions and the motivation for the work performed in this thesis.

---

<sup>1</sup> <https://exoplanets.nasa.gov>

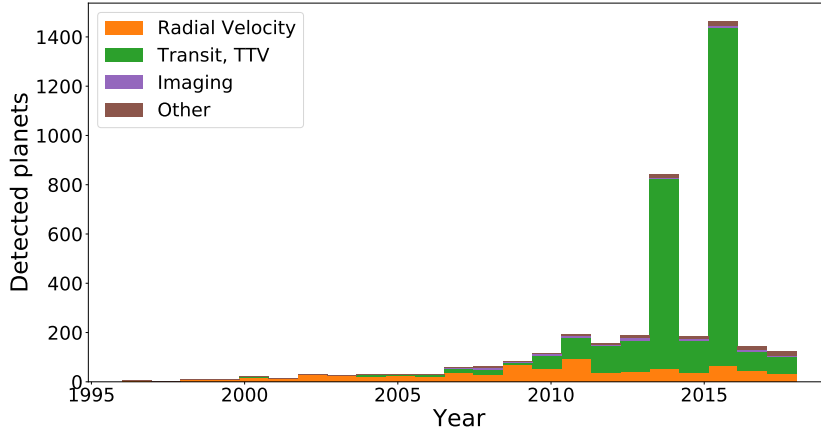


**Figure 1.1:** Number of exoplanet detections per year separated by method (data from exoplanet.eu October 2018).

## 1.2 Exoplanet detection methods

There are several detection methods used to build up the picture of the current understanding of exoplanet candidates. The different detection methods are often complementary, in that they are sensitive to different parameter spaces and are able to contribute different exoplanet properties, or detect different classes of exoplanet. The simplest example is that planetary mass and radius are obtained from the radial velocity and transit methods separately. Also the transit and radial velocity methods are both sensitive to large planets close to the star however, the direct imaging technique cannot see planets too close to the star, as the planets image is contaminated by the stellar image and speckles.

The exoplanet detection rates for different methods since 1995 are shown in Figure 1.1. The detection rates among different methods are not uniform, with the transit method having the majority of detections due to the use of the Kepler space telescope (Borucki et al., 2008). The radial velocity method has a fairly consistent detection rate, while direct imaging and other methods have only made a small contribution to the total number of detections so far. Details about the various main detection methods are provided in the following sections.

### 1.2.1 Radial Velocimetry

This technique measures the radial velocity<sup>2</sup> (RV) of the star by analysing the relative Doppler shift of its spectral lines due to the gravitational interaction with a companion. As the star and companion orbit around their common centre of mass (barycentre) the spectrum of the star periodically oscillates, with the orbital period of the planet, due to the change in relative motion to the observer as depicted in Figure 1.2 (left).

The radial velocity variation, directed along the line of sight, is given by:

$$RV = \gamma + K[\cos(\nu(t, P, T_0, e) + \omega) + e \cos(\omega)] \quad (1.1)$$

where  $\gamma$  is constant barycentre velocity of the system relative to the Sun<sup>3</sup>,  $K$  is the velocity semi-amplitude,

<sup>2</sup> Velocity projected along line of sight.

<sup>3</sup> Earth's barycentre motion is well known and removed.

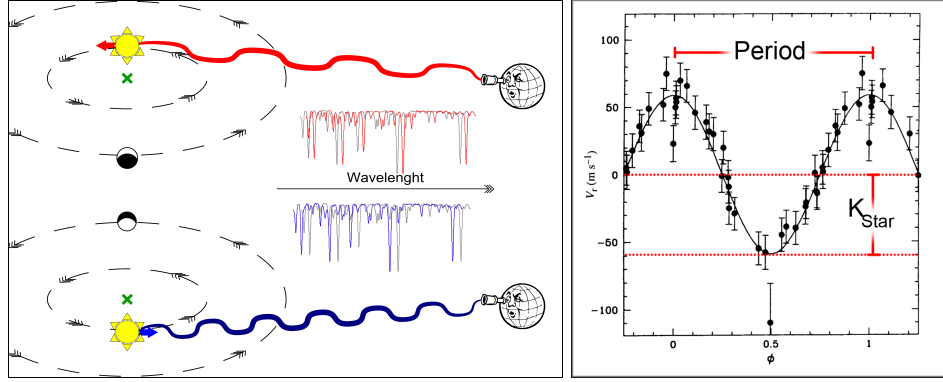


**Figure 1.2:** Left: Diagram of RV method. Right: RV variation for the detection of 51 Pegasi. Credit: Mayor et al. (1995)

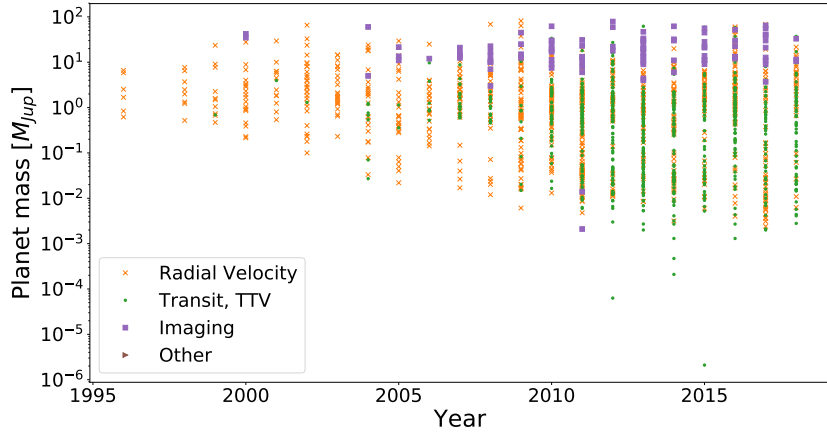


**Figure 1.3:** Exoplanet discovery year versus exoplanet mass showing a trend towards detecting lower mass planets. Exoplanets without a measured mass are not shown. The colours indicate the initial detection method.

$e$  the eccentricity, and  $\omega$  is the argument of periastron. The true anomaly  $\nu$ , is a function of time  $t$ , orbital period  $P$ , and the time of periastron passage  $T_0$ , and eccentricity.

The velocity amplitude  $K$  of a star of mass  $M_\star$  due to a companion with mass  $M_p$  with orbital period  $P$ , eccentricity  $e$ , and inclination<sup>4</sup>  $i$  is (e.g. Cumming et al., 1999):

$$K = \left( \frac{2\pi G}{P} \right)^{1/3} \frac{M_p \sin i}{(M_p + M_\star)^{2/3}} \frac{1}{\sqrt{1 - e^2}}, \quad (1.2)$$

where  $G$  is the gravitational constant.

The key exoplanet property determined by the amplitude RV technique is the companion mass, relative to the orbital inclination  $M_p \sin i$ . As the companion mass is in the numerator of Equation 1.2 the RV technique is more sensitive to larger mass planets. Also since  $K \propto P^{-1/3}$  the amplitude is greater for short period close in orbits<sup>5</sup>.

<sup>4</sup> Relative to a plane that is tangential to the celestial sphere,  $i = 90$  is edge on.  
<sup>5</sup> From Kepler's Law  $P^2 \propto a^3$

The RV method kick-started the exoplanet discipline by detecting the first exoplanet around a solar-type star 51 Pegasi (Mayor et al., 1995). The RV curve for 51 Pegasi is shown on the right side of Figure 1.2. The first discoveries were surprising as Jupiter mass planets in short period orbits<sup>6</sup> were unlike anything in our Solar System and not predicted by standard planet formation theories. Several exoplanet discoveries followed in quick succession (e.g. Butler et al., 1996; Marcy et al., 1996) with many confirming the existence of the type of planets now referred to as “hot-Jupiters” (Butler et al., 1997; Charbonneau et al., 2000).

The radial velocity amplitudes of the first exoplanets detected were around  $60 \text{ m s}^{-1}$  while the radial velocity signal of the Earth in a one year orbit around a solar-type star however is  $8.9 \text{ cm s}^{-1}$  (e.g. Figueira et al., 2010). Dedicated spectrographs, such as HARPS (Mayor et al., 2003) along with improved reduction techniques (Lovis et al., 2007) pushed this mass detection limit down to the  $\text{m s}^{-1}$  level. ESPRESSO (Pepe et al., 2014a; Mégevand et al., 2014) is the next generation high precision optical spectrograph aiming to push the detection limits to  $10 \text{ cm s}^{-1}$ , to detect an Earth twin. The gradual decrease in measured mass of exoplanets over time is shown in Figure 1.3. The different symbols indicate the detection method, not necessarily the method used to measure the exoplanet mass.

Most RV detection has been performed using optical spectrographs. However, as the amplitude of RV signal is inversely proportional to the mass of the star ( $\text{RV} \propto M_{\star}^{-2/3}$ ), there are dedicated surveys focusing on smaller mass M-dwarf stars (e.g. Reiners et al., 2018). M-dwarfs are inherently cooler and thus emit a majority of their stellar output in the near-infrared. New dedicated high-resolution nIR spectrographs have and are being designed and implemented to meet this demand e.g. CARMENES, NIRPS, SPIRou, CRIRES+.

### 1.2.2 Transit methods

The transit method detects the presence of an exoplanet by observing the periodic dimming of the star due to the passage of the exoplanet between the star and observer, partially blocking the star. Geometry requires the orbit of the exoplanet to be aligned edge-on to the line of sight (low inclinations) for a transit to occur. The geometric probability,  $P$ , that a exoplanet transits is estimated by

$$P \approx \frac{R_{\star}}{a(1 - e^2)}, \quad (1.3)$$

where  $e$  is the eccentricity of the orbit,  $R_{\star}$  is the star radii and  $a$  is the semi-major axis of the orbit (star-planet distance) (e.g. J. W. Barnes, 2007). The probability of transit increases with the size of the star but decreases with distance to the star.

The drop in stellar brightness during the transit allows the measurement of the planet/star radius ratio:

$$\frac{\Delta L}{L} \sim \left( \frac{R_p}{R_{\star}} \right)^2 \quad (1.4)$$

where  $L$  is the luminosity of the star,  $\Delta L$  is the maximum luminosity variation (transit depth), and  $R_{\star}$  and  $R_p$  are the radius of the star and planet respectively.

The transit method complements RV measurements as the inclination,  $i$ , of the orbit can be determined from the transit. This removes the  $\sin i$  ambiguity found in the  $M_p \sin i$  of RV detections so the true

---

<sup>6</sup>  $M_p \sin i = 0.47 M_{\text{Jup}}$  orbiting at 0.05 au for 51 Pegasi

mass,  $M_p$ , of the exoplanet can be revealed. The true mass along with the planet's radius provides a value for the exoplanet's average density<sup>7</sup>, hinting at the possible composition.

There are several other astrophysical phenomena which can mimic transiting exoplanet signals, created by configurations of two or more stars which may not involve an exoplanet. For example a transiting low-mass or white-dwarf star, grazing binary stars, or a transit in a multi-star system (see e.g. Cameron, 2012; Santerne et al., 2013). Follow-up RV observations (e.g. Santerne et al., 2011) are usually required to confirm the planet's existence. Statistical validation techniques are also possible, such as the PASTIS software (Díaz et al., 2014), when follow-up can not be performed. These techniques assess the likelihood of the planet being a true planet against the different false positive scenarios, validating or confirming the planet if the likelihood is high enough.

The transit method has the highest false positive rate among the detection methods presented here. With RV follow-up, Santerne et al. (2012) found a false positive rate as high as 35% for short period giant planets, while Santerne et al. (2016b) found a 54.6% false positive rate of 129 giant planets with periods less than 400 days. These sub-sample false positive rates are however higher than the global false positive rate of 9.4% (Fressin et al., 2013)/11.3% (Santerne et al., 2013) found for Kepler. Some of the currently known exoplanet systems with the smallest radii and lightest mass have been detected through transit and later confirmed with high-precision RV follow-up (e.g. Queloz et al., 2009; Pepe et al., 2013; López-Morales et al., 2016; Ment et al., 2018).

The identification of unresolved multiple stars, such as a binary or an unrelated background star, can be achieved through high-resolution spectroscopy in which the spectral lines of individual stars can be separated (Kolbl et al., 2015). This is important to measure the correct radii of exoplanets as the extra light contribution from an unresolved secondary star will reduce the transit depth, mimicking a smaller transiting planet.

The transit of a single planet can not directly determine the planetary mass. However, in multiple planet systems, the masses and sometimes the presence of other planets in the system can be determined from perturbations in the transit time and duration (e.g. Holman et al., 2005; Holman et al., 2010). A large number of systems have been detected that show transit timing variations (TTV) and transit duration variations (TDV) (e.g. Holczer et al., 2016) due to the gravitational interaction between planets. The statistical validity of multi-transiting planets is more straightforward than single planets as the probability of having multiple false positives, being the product of the individual probabilities, is lower than having multiple planets in the system (Lissauer et al., 2012), making multiple planet systems easier to validate.

The presence of star spots on the surface of a star can be observed during transit. A star spot is a dark region on the stellar surface due to magnetic fields, which decreases the luminosity slightly. Examples of spots can be seen in the middle of the Sun from an image of the 2012 transit of Venus in Figure 1.4 (left). It shows several dark sunspots alongside Venus, although Venus did not cross them. Unlike for other stars, sunspots are spatially resolved. If an exoplanet passes in front of a spot, the luminosity decrease from the spot is temporarily hidden and a small bump occurs in the transit shape. The presence of spots in successive transits (see Figure 1.4 (right)) can indicate the alignment of the stellar rotation to the planet orbital plane (Sanchis-Ojeda et al., 2013). In this simulation an orbit aligned with the stellar rotation and the transit crosses the spot in four successive orbits. In a misaligned case a spot would only be observed in one transit.

---

<sup>7</sup>  $\rho \equiv \frac{\text{Mass}}{\text{Volume}} = \frac{3}{4\pi} \frac{M_p}{R_p^3}$

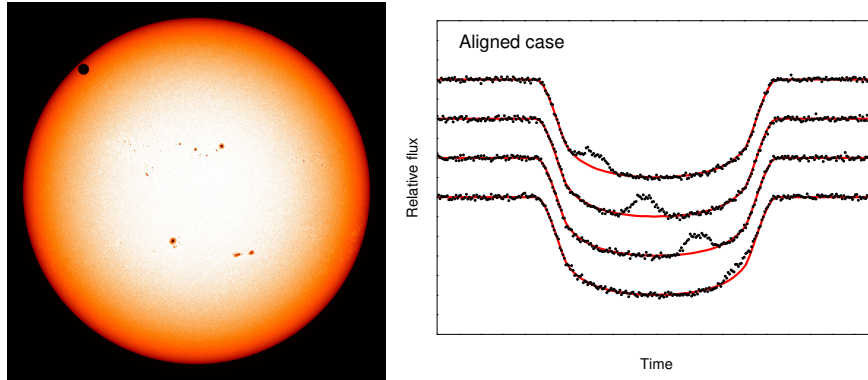


**Figure 1.4:** Left: Image from the 2012 transit of Venus obtained from the Solar Dynamics Observatory satellite. Venus is the dark circle in the top left of the Sun. Limb darkening is observed as the change in colour/brightness from white to red near the edge. Several sunspots are also observed on the surface of the Sun. Credit: NASA/SDO, HMI. Right: Simulation of 4 successive transits crossing a star spot with the orbit aligned with the stellar rotation. The stellar rotation is 1/10 the orbital period. Adapted from Sanchis-Ojeda et al. (2013, Figure 1).

The vast majority of transit detections have come from Kepler (Borucki et al., 2011), which focused on a small patch of sky (0.25%) for four years continuously. Kepler's impressive sensitivity compared to previous surveys, allowed it to detect planets down to around  $2 R_{\oplus}$ . However, CoRoT (Barge et al., 2008) and ground-based surveys, such as WASP (Pollacco et al., 2006), OGLE (Udalski et al., 2002), TreS (Alonso et al., 2004) have also had successful transit detections.

Following in Kepler's footsteps the next generation transit hunter TESS (Ricker et al., 2015) has already announced discoveries of new transiting planets only months after launch (Vanderspek et al., 2018; Gandolfi et al., 2018; Huang et al., 2018a). It will eventually cover more than 90% of the sky with an impressive planetary yield expected of  $\sim 10\,000$  exoplanets, with around 3500 the size of Neptune or smaller (Barclay et al., 2018; Huang et al., 2018b). However, the observation coverage is not uniform, with the majority of the ecliptic plane receiving only one month of observations, limiting the detection sensitivity to short period transiting planets. On the other hand, the ecliptic poles will receive almost one year continuous observation.

PLATO (Rauer et al., 2014) is another transit survey mission planned for launch in 2026. In contrast to Kepler it will focus on brighter nearby stars, with the goal to detect and accurately determine the planetary parameters of Earth-like planets in the habitable zone.

A smaller transiting mission, CHEOPS (Broeg et al., 2013), is also scheduled for launch at the end of 2019. Unlike the transiting surveys mentioned above, CHEOPS will perform dedicated transit follow-up of bright stars with known planets, such as those found with RV surveys. It will provide high precision transit photometry, if the geometry allows, to obtain precise planetary radii.

### 1.2.3 Direct Imaging

The direct imaging technique involves directly imaging an exoplanet in orbit around a star. The first planets directly imaged were 2MASSWJ 1207334–393254 b using adaptive optics with NACO on the VLT (Chauvin et al., 2004), three planets around HR 8799 using angular differential imaging on the Keck and Gemini telescopes (Marois et al., 2008), and Fomalhaut b using chronography on the HST (Kalas

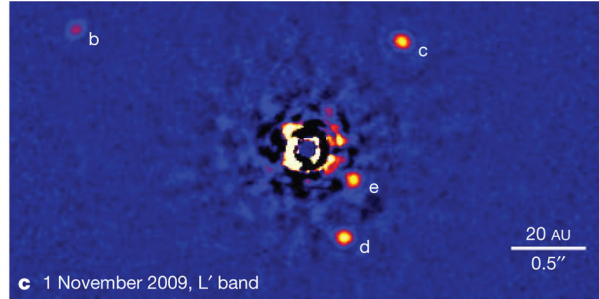


**Figure 1.5:** Direct detection of four exoplanets around HR 8799 (Marois et al., 2010).

et al., 2008). As an example, the direct image of HR 8799 is shown in Figure 1.5, where a fourth planet was revealed (Marois et al., 2010).

Direct imaging requires resolving the angular separation between the star and planet and is best suited to detect giant planets in wide orbits ( $>10$  au) around nearby stars. This is shown by the clustering of direct image detections shown in Figure 1.3. Extremely young giants observed in the infrared are favoured as they have higher thermal emissions (while they are still cooling) and larger surface area resulting in a higher contrast ratio to the host.

High-contrast adaptive optics instruments, such as SPHERE@VLT (Beuzit et al., 2008) and GPI (Macintosh et al., 2008), are being used with several different techniques to observe targets closer to the star and with smaller contrasts, usually involving blocking or cancelling out the light from the star while retaining the signal of the planet (e.g. Marois et al., 2005; Mawet et al., 2005; Schmid et al., 2005; Sirbu et al., 2017b; Sirbu et al., 2017a; Wang et al., 2017). Ground based direct imaging requires adaptive optics to reduce the turbulence induced by the atmosphere, increasing the angular resolution down to the telescope diffraction limit.

On top of hardware based solution to the stellar contamination, clever observing strategies and cancelling algorithms. Angular differential imaging (ADI) (eg. Marois et al., 2005) is one such technique. ADI, disables the field de-rotator component in the telescope so that the viewing field rotates relative to the plane of the detector during the night. Several images taken at different angles are rotated to a reference position and stacked. The stacking of images from different angles cancels out the pseudo-static speckle caused by the telescope and optics while increasing the contrast of any faint object in the stars vicinity, i.e. a planetary companion.

The direct imaging technique is also used to observe circumstellar and protoplanetary disks, and has even captured images of planets during formation (e.g. Sallum et al., 2015). Combining direct images from different photometric bands can allow for the creation of low-resolution exoplanet spectra (e.g. Kuzuhara et al., 2013; Zurlo et al., 2015).

#### 1.2.4 Astrometry

Astrometry measures the precise position of the stars on the plane of the sky. The motion of a star with an exoplanet about its centre of mass can be observed in the periodic oscillating of position from its proper motion in the sky.

For a circular orbit the angle of the semi-major axis of the apparent orbital ellipse, the amplitude of

the astrometric signature ( $\theta$ ), is given by

$$\theta = \frac{M_p}{M_{star} + M_p} \frac{a}{d} \quad (1.5)$$

where,  $M_p$  and  $M_\star$  are the planet and stellar mass,  $a$  is the semi-major axis (in au) and  $d$  is the distance from the observer to the system (in parsec) (M. Perryman, 2011).

This shows that the astrometric signal is proportional to the companion/star mass ratio and to the orbital radius,  $a$ . The amplitude also decreases inversely with distance, as the angles become smaller. This is unlike the RV and transit methods for which the amplitude is not affected by distance. Astrometry is complementary to the RV method as it measures the orbital motion perpendicularly to the line of sight, allowing the three-dimensional orbit to be determined.

A modelled astrometric signal is shown in Figure 1.6, for a star at a distance of 50 pc, with a proper motion of 50 mas yr<sup>-1</sup>, and orbited by a planet of  $M_p = 15 M_{Jup}$ ,  $e = 0.2$ , and  $a = 0.6$  au (M. A. C. Perryman, 2000). The straight dashed line shows the path of the system's barycentric motion viewed from the Solar System barycentre. The dotted line shows the effect of parallax (the Earth's orbital motion around the Sun, with a period of 1 year). The solid line shows the apparent motion of the star as a result of the planet, the additional perturbation being magnified by  $\times 30$  for visibility.

Although astrometry has detected many binary stars (e.g. Gontcharov et al., 2000) and found several brown-dwarf companions (e.g. Sahlmann et al., 2011), the exoplanet discovery's are few. A  $1.5 M_{Jup}$  mass planet in a roughly 1000 day orbit around HD 176051 was reported by Mutterspaugh et al. (2010), and recently the astrometric perturbation of a known planet, Beta Pictoris b, was performed utilizing measurements from GAIA (Collaboration et al., 2016) and HIPPARCOS (ESA, 1997) to determine a mass of  $11 M_{Jup}$  (Snellen et al., 2018).

The predicted astrometric variations for an exoplanet are at the level of sub-milliarcseconds and therefore are not achievable from the ground due to atmospheric turbulence. The most precise astrometric measurements come from spacecraft. These are currently being performed using GAIA with the recent release of astrometric parameters for 1332 million sources (Collaboration et al., 2018) and reaching a precision of 0.04 mas for the brightest stars (<14 magnitude). Simulations predict that more than 21 000 large mass planets ( $1\text{--}15 M_{Jup}$ ) in long-period orbits should be discovered during the 5 year nominal GAIA mission (M. Perryman et al., 2014).

### 1.2.5 Microlensing

Microlensing is an astronomical effect predicted by Einstein's General Theory of Relativity. The mass of an object bends space-time which causes light to be visibly deflected around large mass objects. As a star passes between Earth and a distant star it acts like a lens, bending and magnifying the light from the background star. The gravitation of a planet orbiting the lens star (if it exists) creates a distortion in the lens, leading to small caustics, deviations in the microlensing light curve for a single lens event (star without a planet).

An example is shown in Figure 1.7 where a lensing magnification of up to  $\times 3$  is observed for OGLE2005-BLG-390 (Beaulieu et al., 2006). On the falling edge of the lensing event (and inset top right) there is a bump due to the presence of a  $5.5 M_{Jup}$  companion.

The difficulties of microlensing is that they require the chance alignment between Earth, a nearby lens star, and a distance source star, which is unrepeatable. Some caustics are often difficult to fit and yield

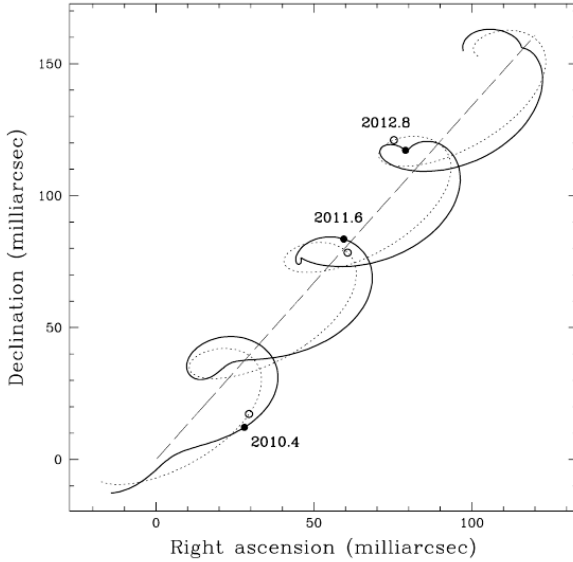


**Figure 1.6:** The modelled astrometric path on the sky from M. A. C. Perryman (2000). Showing a star at a distance of 50 pc, with a proper motion of  $50 \text{ mas yr}^{-1}$ , and orbited by a planet of  $M_p = 15 M_{\text{Jup}}$ ,  $e = 0.2$ , and  $a = 0.6 \text{ au}$ . The straight dashed line shows the path of the system's barycentric motion viewed from the Solar System barycentre. The dotted line shows the effect of parallax (the Earth's orbital motion around the Sun, with a period of 1 year). The solid line shows the apparent motion of the star as a result of the planet, the additional perturbation being magnified by  $\times 30$  for visibility.

degenerate results, making characterization of the planet difficult. Follow-up measurements of a handful of microlensing events have been performed (e.g. Kubas et al., 2012; Batista et al., 2015; Santerne et al., 2016a) to break degeneracies. However, follow-up can be difficult as microlensing is sensitive to distant host stars, which are outside the ability of current spectrographs. It is also sensitive to planets with a wider orbital separation compared to transits and RV. Currently there are 87 planets in 82 systems detected by microlensing, as listed in the exoplanet.eu database.

The microlensing technique has been efficient in detecting Neptune analogue planets, distant planets similar in size to Neptune. Showing that cold Neptune planets are likely most common type of planet outside of the snow line (Suzuki et al., 2016), the distance from a star at which point it is cold enough for volatile compounds (e.g.  $H_2O$ ,  $NH_3$ ,  $CO_2$ ) to condense into solid ice grains.

Microlensing events are detected and monitored using dedicated global telescope networks such as OGLE, MOA, microFUN and PLANET. They focus their viewing towards the galactic bulge where there are more stars and a higher chance for microlensing events to occur.

The precise stellar proper motions from the GAIA mission are being used to predict possible future alignments that could produce microlensing events (Klüter et al., 2018)

### 1.2.6 Pulsar timing

Pulsars are rapidly rotating neutron stars or white dwarfs formed after the death of a giant star, that radiate an intense electromagnetic beam. The timing variations of the millisecond pulsar<sup>8</sup> PSR1257+12

<sup>8</sup> Rotating at 9 650 revolutions per minute

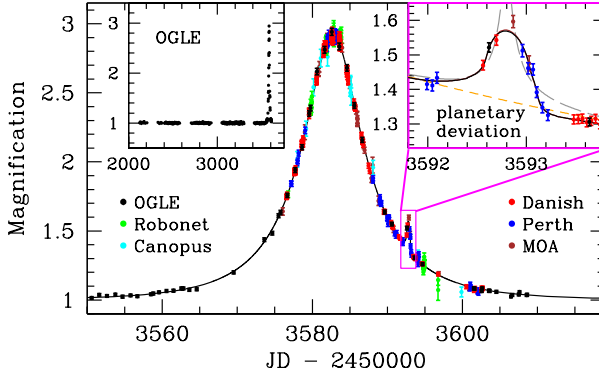


**Figure 1.7:** Microlensing magnification of OGLE2005-BLG-390 from (Beaulieu et al., 2006). The presence of the  $5.5 M_{Jup}$  planet causes the small bump shown in the upper right inset plot.

led to the first extrasolar planet detection (Wolszczan et al., 1992). There are two models of planet formation around pulsars: either they formed before the supernova explosion and survived, or they formed after, from the remnants of the supernova (Starovoit et al., 2017). There is still a rarity of less than 10 pulsars with known orbiting planets.

The rarity of these events is partially associated to the technique which requires very precise instrumentation on high cadence (< milliseconds) to precisely measure the electromagnetic radiation from the pulsar. For example the first pulsar was detected with the Arecibo radio telescope. With the primary dish fixed into the mountain, its pointing is limited and achieved by moving the receiver. It has a limited number of stars that can be observed with a sufficient time coverage to detect planets around pulsars.

## 1.3 Detecting atmospheres

To help characterize an exoplanet, a detection of its atmosphere can provide useful information. After the detection of exoplanets and the measurement of their bulk properties, detecting their atmospheres is the next step. The detection of planetary atmosphere is difficult due to the low planet-to-star flux ratio. This requires high precision instrumentation to detect. For example the planet-to-star flux ratio in the optical is  $\approx 10^{-4}$  for a hot Jupiter with a 3 day orbit, in which the main component is reflected star light. In the infrared the thermal emission of the planet dominates and the flux ratio rises to  $\approx 10^{-3}$ . These flux ratios requires observations with signal-to-noise ratios of  $10^4$  and  $10^3$  in the optical and infrared respectively to achieve a planetary signal at the same level as the noise level. These detections are only just at the capabilities of the current generation of technology, and with very long observation cost.

Several photometric and high-resolution spectroscopic techniques are showing promising results; these are detailed in the following sections.

### 1.3.1 Occultation and phase variations

Secondary transit and phase variations are an extension of the transit method, requiring higher precision to detect the reflection and thermal emission of the exoplanet. The observed light curve is analysed considering it has two components, not only light emitted from the star but also light from the planet, albeit at a much lower flux level. To help visualize and discuss the components of exoplanet atmospheres Figure 1.8 is provided showing a transiting planet in orbit around a star, in which the planet also passes

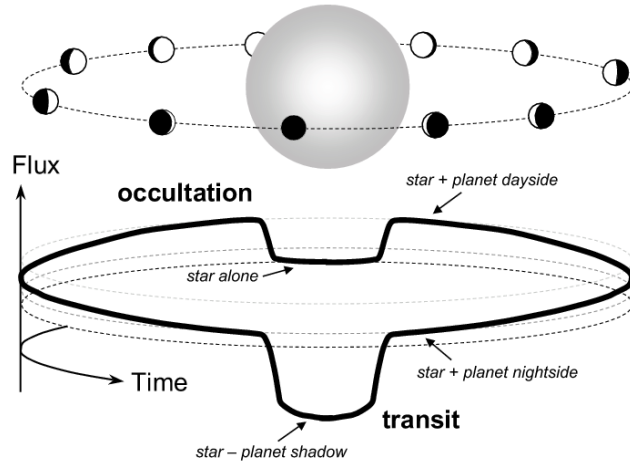


**Figure 1.8:** Illustration of the flux contribution from a star and planet in a transiting exoplanet system throughout its orbit. Credit Winn (2010).

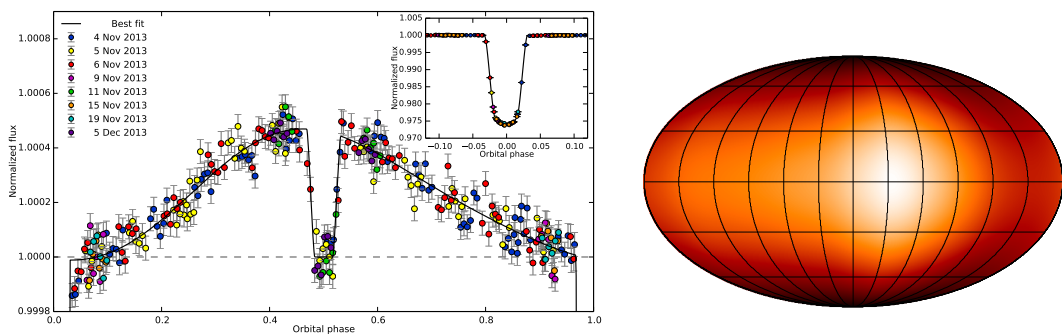


**Figure 1.9:** Left: Band integrated phase variation of WASP-43b from the HST (Stevenson et al., 2014). The primary transit is inset top right. The peak of brightness occurs before the secondary transit. Right: Global temperature map of the hot Jupiter HD 189733b obtained with Spitzer Space Telescope (Knutson et al., 2007a). The hottest point is offset from the sub-stellar point with the day side and night side temperatures around 930 K and 650 K respectively.

behind the star causing an occultation. The planet is shown at several positions of the orbit indicating the proportion of day side and night side observed. Below the star and planet is a diagram showing the changing flux variation (solid black line) over time, following the orbit. If the orbital alignment is such that the planet will pass behind the star it will cause an occultation of the planet. At this point the only light received is from the star alone, creating a baseline stellar measurement. While during the primary transit there is also a small thermal emission contribution from the night side of the planet, as well as it partially blocking the star.

Throughout the orbit of the planet there is a variation in the planetary flux due to the alternating day/night side of the planet observed. There are multiple components of the planetary flux, reflection and emission, that can be analysed with multi-band phase curves (e.g. Knutson, 2009; Esteves et al., 2013). Optical phase curves will mostly show the reflected light from the day side of the planet, allowing modelling of the atmospheric albedo (fraction of light reflected by the atmosphere), and can provide details on the atmospheric scattering (Madhusudhan et al., 2012) and aerosol composition (Oreshenko et al., 2016) through the optical phase function (day/night fraction). Thermal emission of the planet will provide stronger modulation of infrared phase curves and can provide insights into the atmospheres thermal structure and heat circulation (Goodman, 2009; Koll et al., 2016).

An example of phase variations in the infrared spectra of WASP-43b obtained with the Hubble Space telescope is given in Figure 1.9 (left). The large amplitude of phase variation between the day and night side indicates that the night side is much cooler and there is an inefficient heat circularity from the day to night side. A planet with an efficient day/night heat distribution mechanism would quickly equalize and have smaller phase variation. One key observable from Figure 1.9 is that the peak of the phase variation is offset from the location of the secondary transit. The hottest part of the atmosphere does not correspond to the sub-stellar point i.e. the point of the planet's surface closest to the star. This is also observed in surface temperature mapping of the hot Jupiter HD 189733b obtained with the Spitzer Space Telescope (Knutson et al., 2007a) shown in the right of Figure 1.9. Simulations of atmospheric circulation models find that this offset is caused by super-rotating equatorial jets which move the location of the hottest point of the planet (e.g. Heng et al., 2015, and references therein).

The point of occultation, at which the planet is completely blocked by the star, enables a baseline measurements for the star to be obtained without the planet. The depth of the occultation, gives a direct measurement of the relative brightness of the planetary disk if the star-planet radius ratio is known (Winn, 2010). It is a measure of the flux from the day side of the planet which can indicate the atmospheric reflection and thermal emission of the planet's atmosphere.

Spectra obtained during the occultation will have no planetary signal and can be used remove the stellar component from spectra obtained at other phases to obtain the planetary spectrum.

### 1.3.2 Transmission spectroscopy

When a transiting planet crosses in front of the host star it blocks out light from the star. However, a small portion of light passes through the atmosphere of the planet as shown in Figure 1.10. The light that passes through the exoplanet atmosphere is partially absorbed, and is faintly imprinted with absorption lines.

In planetary transits, usually defined by their duration and depth, there are degeneracies of the system properties from the transit shape in a single band, for example systems with differently sized planets and stars can have the same  $\frac{R_p}{R_*}$  ratio. Observing transits in multiple bandpasses (i.e. by splitting the

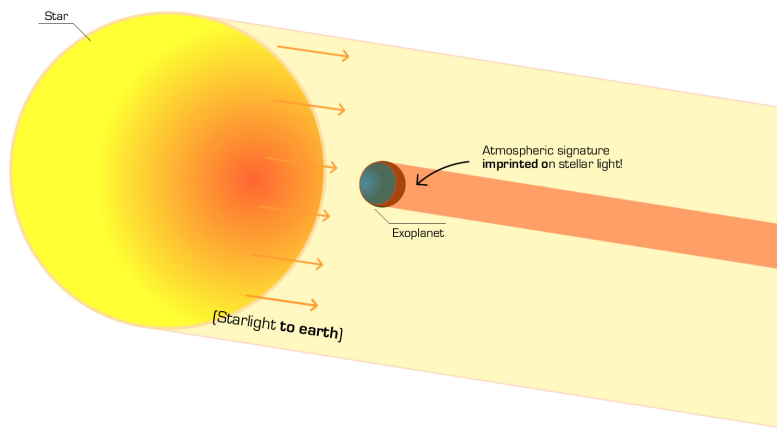


**Figure 1.10:** Diagram of transmission spectroscopy imprinting the atmosphere of the exoplanet. Sourced from <http://www.sc.eso.org/~esedagha/research.html>

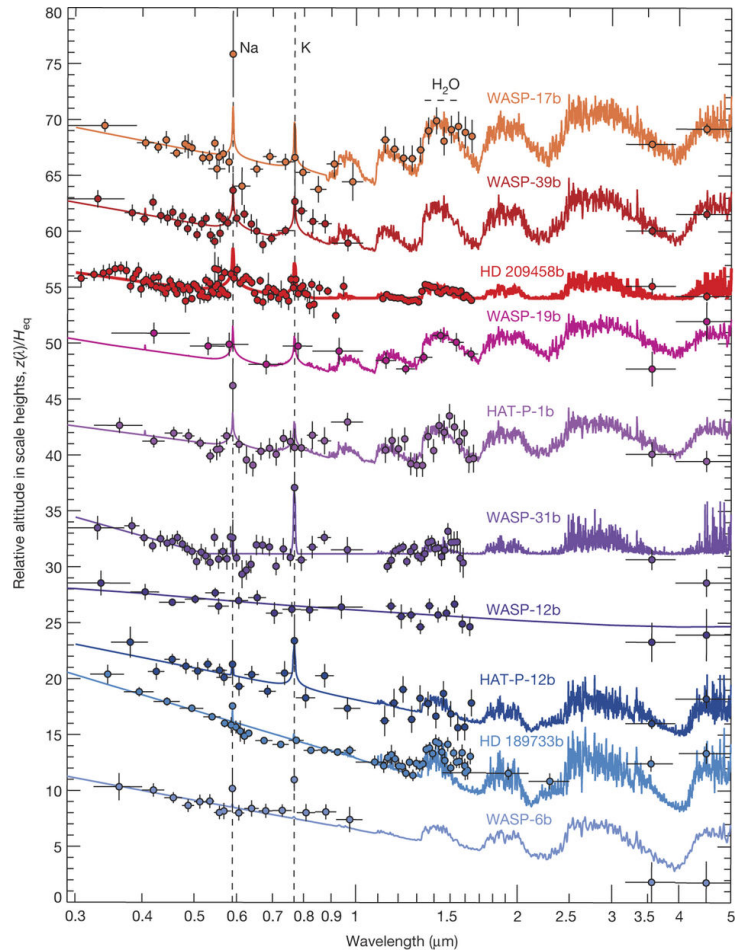


**Figure 1.11:** Transmission spectra (dots) for several Hot-Jupiter type exoplanets which increase in the amount of haze and clouds from top to bottom. The solid lines indicate the best fit atmospheric models. Credit Sing et al. (2016).

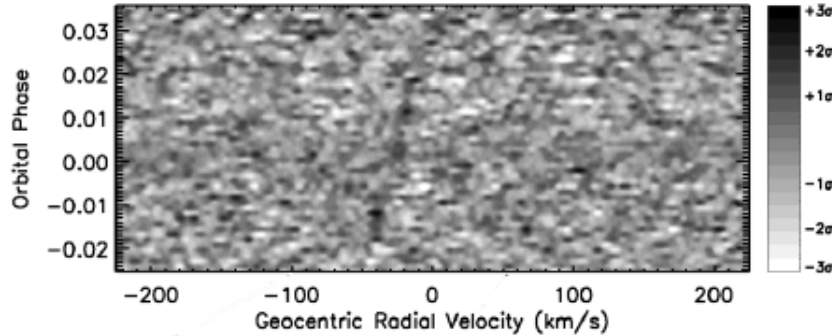


**Figure 1.12:** Cross-correlation signal of CRIRES observations during the transit of HD 209458 b with a CO template. Credit Snellen et al. (2010).

spectra observed during transits into several bands) has been shown to break the degeneracies between the stellar radius and the orbital inclination as well as determine the stellar limb darkening (Jha et al., 2000; Knutson et al., 2007b).

The radius of the transiting exoplanet can also appear to change size when observed at wavelengths where there is strong opacity in the atmosphere (e.g. Burrows et al., 2000; Seager et al., 2000). Transits in different wavelength bands will have varying depths, dependant on the opacity of the atmosphere to each band.

The transmission spectra observed with space observatories and ground based high resolution spectrographs has been used to detect several elements and molecules in the atmosphere. For example Na (Charbonneau et al., 2002; Redfield et al., 2008; Wyttenbach et al., 2015; Nikolov et al., 2016), H<sub>2</sub>O (Tinetti et al., 2007; Brogi et al., 2014), CO (Brogi et al., 2014; Snellen et al., 2018), CH<sub>4</sub> (Redfield, 2010), Fe and Ti (Hoeijmakers et al., 2018). The presence of clouds in the atmosphere have also been detected, as they mask the atmospheric constituents as they produce wavelength-independent fluxes (e.g. Barman et al., 2011; Kreidberg et al., 2014; Sing et al., 2016).

Transmission spectra for several transiting Hot-Jupiter exoplanets from Sing et al. (2016) is shown in Figure 1.11. The amount of haze and clouds present in the atmospheres increases in the spectra shown from the top to bottom. Hazes are particles produced from chemistry in the atmosphere that results in the formation of involatile solids, while clouds form through the process of condensation and comprise of liquid droplets or ice crystals suspended in the atmosphere. Sing et al. (2016) defines hazes as having a Rayleigh-scattering-like opacity, which could be due to sub-  $\mu\text{m}$  sized particles, while they define clouds as having a grey opacity, for simplicity. The spectra near the top have clearer atmospheres, with little or no haze and clouds, show large alkali (Na and K) and H<sub>2</sub>O absorption. Hazier and cloudier planets lower down the figure have strong optical scattering slopes with narrow alkali lines and have a partially or completely obscured H<sub>2</sub>O absorption. This shows how the transmission spectra can reveal properties of the planetary atmospheres.

### 1.3.3 High resolution spectroscopy

Precise high resolution spectrographs that are able to spectrally resolve individual absorption lines, are key to analysing the atmospheres of exoplanets. Unfortunately, these are too large and bulky to fly in space, and they would be near impossible to keep in precise alignment during a rocket launch. The large collecting area of current and future ground based telescopes make high resolution spectroscopy a great

contender for obtained high-resolution observations for detecting and exploring exoplanetary atmospheres. Transmission spectroscopy is one beneficiary of high-resolution spectroscopy, although it is not the only technique to utilize high-resolution.

Typically high-resolution and high SNR spectra are cross correlated with modelled stellar and/or planetary templates to recover the faint signal of the companion. This has been most successful in the nIR due to the larger planet-to-star flux ratio notably with CRIRES, with the detection of orbital motion, atmospheric constituents and exoplanetary winds (e.g. Snellen et al., 2010; de Kok et al., 2013; Brogi et al., 2014; Brogi et al., 2016; H. Schwarz et al., 2015). The rotation rate of exoplanets has been achieved by measuring the spectral line broadening (Snellen et al., 2014; Brogi et al., 2016). An example of a cross correlated result is given in Figure 1.12 showing the shift of the CO lines during a transit due to the orbital motion of the planet (Snellen et al., 2010).

The spectrum of the star and planet usually cannot be spatially resolved so methods to identify and remove the stellar component are required. This usually involves constructing a high SNR stellar mask from observations, possibly at different phases (e.g. Rodler et al., 2012), to subtract from the observed spectra leaving behind the planetary signal. If the planet is able to be spatially resolved, then a spectrum of the planet could be obtained without stellar contamination (e.g. Snellen et al., 2015).

High resolution spectroscopy of atmospheres is not limited to transit spectroscopy with detections also possible for non-transiting exoplanets (e.g. Brogi et al., 2012; Brogi et al., 2014; Lockwood et al., 2014; Piskorz et al., 2016).

An advantage of high-resolution spectra is that it allows the molecular absorption lines of Earth's atmosphere to be resolved. This way they can be identified and corrected/removed to avoid contamination with the atmosphere of the exoplanet. Lower resolution and photometric methods are unable to fully resolve and remove Earth's atmosphere from ground based observations.

## 1.4 The diversity of exoplanets

Exoplanetary detections have challenged the theoretical formation models with their variety and distribution of sizes and, locations. For instance, the discovery of the hot-Jupiter class (large mass planets on close in orbits) challenged the accepted planet formation theories at the time (e.g Pollack et al., 1996; Boss, 1997) in which our Solar System was thought to be typical with small rocky planets close to the Sun and large giant planets further away.

The precise characterization of more exoplanets with the detection of exoplanetary atmospheres will allow for the constraints of exoplanetary composition and formation mechanisms to be improved. For instance, the core accretion model has been able to reproduce the large number of Super-Earths, the correlation between star metallicity and planet frequency (e.g. Santos et al., 2004; Fischer et al., 2005), and the presence of many Hot-Jupiter and Neptune like planets in close-in orbits, with the help of migration mechanisms (e.g. Triaud, 2016). Recent models also combine both planetary formation and evolution to describe the observed exoplanets (e.g. Mordasini et al., 2012) and can reproduce general population properties in a statistically significant way (Mordasini et al., 2009).

A proxy for the composition and structure of an exoplanet is the average density, computed from the mass and radius. A mass-radius diagram is shown in Figure 1.13 for Earth-like rocky planets. The tracks show contours of mass-radius for different theoretical compositions (Brugger et al., 2017), while the circles indicate a number of detected small mass exoplanets, with K2-229 b being a Super-Earth with

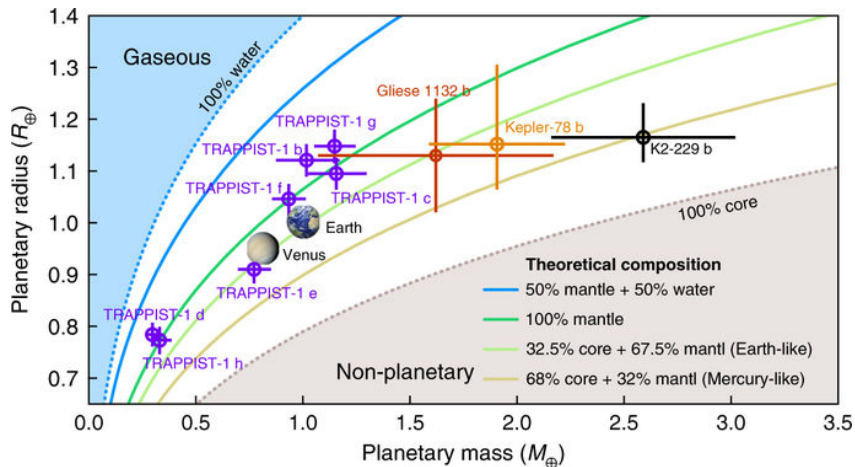


**Figure 1.13:** Mass-Radius diagram for rocky planets with composition contours. Adapted from Santerne et al. (2018)

a Mercury-like density (Santerne et al., 2018). The density can give an approximate composition but for a given mass there are an infinite number of combinations of metal/silicate/ice and gas that can produce the same radii (e.g. Seager et al., 2007). Low mass planets tend to be rocky and tend to have small or no atmosphere. With rock being in-compressible, to first order, it is relatively insensitive to the incident flux. The radii of solid exoplanets are sensitive to gas content of the atmosphere as a small increase in H and/or He can cause a large increase in radius (Adams et al., 2008).

When the gas component becomes dominate, planets begin to have radii independent of their mass (e.g. Lopez et al., 2014). The atmospheres of gas giants are also susceptible to stellar irradiation, with close in Hot-Jupiters having inflated atmospheres and larger radii (e.g Fortney et al., 2010).

Models of the mass-radius relation are important as they enable insight into the likely planetary properties when only either mass or radius can or has been measured. For example Chen et al. (2016) developed a probabilistic model over 9 orders-of-magnitude in mass and 3 orders-of-magnitude in radius, with the result shown in Figure 1.14. There are four separate power laws and three different transition regions fitted by the model. This breaks the mass radius relation into different regions classified after a representative example from our solar system. The lowest mass range is the rocky "Terran" worlds up to  $2.0 M_{\oplus}$  and inclusive of dwarf planets, "Neptunian" worlds between  $2.0 M_{\oplus}$  and  $0.41 M_{\text{Jup}}$  and, "Jovain" worlds between  $0.41 M_{\text{Jup}}$  and  $0.08 M_{\odot}$ . The transitions regions are indicative of a changing composition or physical processes (such as the hydrogen burning limit in stars) and consistent with other works (e.g. Weiss et al., 2013; Dieterich et al., 2014; Hatzes et al., 2015; Rogers, 2015).

Recently, there has been a renewed interest in Brown Dwarf (BD) candidates triggered by exoplanetary searches as they bridge the gap between giant planets and low-mass stars. It is difficult to distinguish between giant planets and BDs with a loosely suggested definition of mass between  $13-80 M_{\text{Jup}}$ <sup>9</sup> for Brown Dwarfs as this is between the Deuterium fusion mass of around  $13 M_{\text{Jup}}$  (e.g. Spiegel et al., 2011) and the Hydrogen fusion limit of  $80 M_{\text{Jup}}$  (Chabrier et al., 2000; Dieterich et al., 2014). Several works found similar properties on the two populations, like a similar density (Hatzes et al., 2015; Chen et al., 2016) seen in Figure 1.14 by the same power law spanning giant planets and BDs, while others have found intriguing differences. When classified using just mass and size Chen et al. (2016) find no difference

<sup>9</sup>  $0.01-0.08 M_{\odot}$

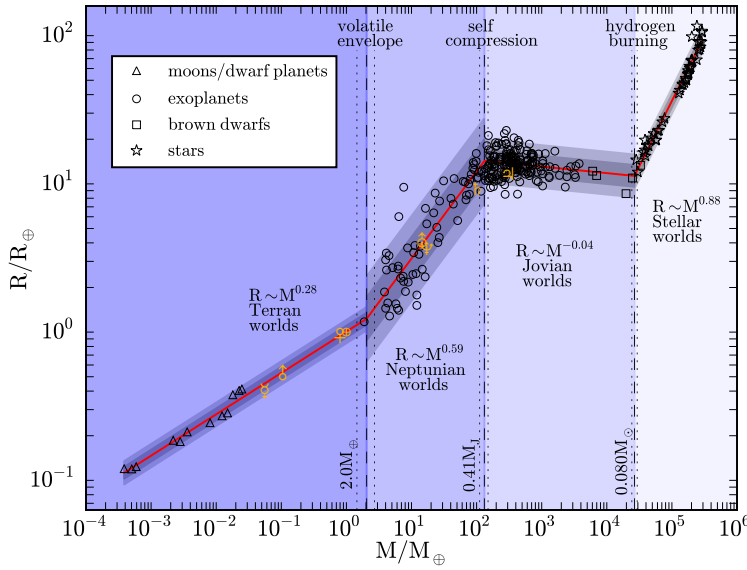


**Figure 1.14:** Mass-Radius relationship with probabilistic fit from dwarf planets to late-type stars from Chen et al. (2016). The black symbols represent the objects used to fit the model, with the key in the top-left, while the orange symbols represent the solar system planets. The red line indicates the average value, while the light and dark grey regions indicate the 65% and 95% confidence intervals.

between giant planets and Brown Dwarfs, with Brown Dwarfs just being large giant planets.

There is a paucity of BD companions in short period orbits around Sun-like stars ( $\lesssim 5$  au), compared to stellar or planetary companions, termed the *brown dwarf desert* (Halbwachs et al., 2000; Zucker et al., 2001; Sahlmann et al., 2011; Ranc et al., 2015) which can be seen as the gap in the "Jovian" worlds section of Figure 1.14. There are observed differences in the host star metallicity (Maldonado et al., 2017; Santos et al., 2017; Schlaufman, 2018) and orbital eccentricity distribution (Ma et al., 2014) either side of the period/mass gap with the lower mass BDs having properties similar to giant planets and high mass BDs having properties more like stars. There is a very strong hint of different formation mechanisms as BDs below the gap may primarily form via gravitational instability in protoplanetary disks, while above this gap BDs may form more like stellar binary from molecular cloud fragmentation (Ma et al., 2014).

As the number of known BDs orbiting solar type stars is low, the characterization of benchmark BDs in the brown dwarf desert (e.g. Crepp et al., 2016) is beneficial in understanding this sub-stellar population and to help constrain formation and evolution theories (Whitworth et al., 2007). There is an inherent degeneracy between the mass, age and luminosity of a given BD (Burrows et al., 1997) because without sustained fusion, BDs cool down over time with an age-dependent cooling rate.

BDs in binary systems, unlike free-floating BDs (e.g Gagné et al., 2017), allow for the determination of their masses, when complemented with radial velocity (RV) and astrometry measurements. The RV technique provides the mass lower-limit ( $M_2 \sin i$ ) of binary and planetary companions, while complementary astrometry measurements can often provide mass upper-limits (e.g. Sahlmann et al., 2011). Measuring or tightening the constraints of BD masses improves the understanding of mass dependence on BD formation processes. Photometry along with stellar evolution models (e.g. Baraffe

et al., 2003; Allard, 2013) can also be used to estimate the mass of BD companions (e.g. Moutou et al., 2017) if there is sufficient orbital separation, and a precise determination of the age (Soderblom, 2010).

## 1.5 Motivation for this thesis

As shown here there is a vast field of exoplanet research, with one of the current challenges being the detection of planetary atmospheres. The purpose of this thesis was to develop methodologies and tools to extract the minute signals of planetary spectra from nIR spectra. With access to nIR spectra of stars with suspected Brown Dwarf companions<sup>10</sup> the higher temperature and relatively larger size of BDs compared to giant-planets makes the development of spectral recovery techniques for BD companions a logical step towards the spectroscopic detection of planetary atmospheres. For one, the spectrum of the BD companion will have a higher flux ratio than an exoplanet, and hence should be easier to detect. Secondly, being able to recover the spectra of these BD companions would help to constrain their mass and differentiate them from low-mass stars, helping to complete the puzzle regarding BD companions and their formation.

The original plan was to use this as a stepping stone to request observational time and apply the techniques on giant exoplanets in the nIR with the state-of-the-art detectors that are *still* in development. In Chapters 2 and 3 the fundamental concepts of the radial velocity method and nIR spectroscopy are presented. In Chapter 4 models of the atmosphere are presented along with the stellar atmosphere and evolutionary models used in this work. The process of reducing nIR CRIRES spectra, with a comparison between two different reduction software is given in Chapter 5, followed by the post reduction calibration and atmosphere correction techniques required.

Chapter 6 presents spectral disentanglement techniques, focusing on the application of a differential subtraction technique to the nIR spectra of BD companions, as well as analysing the phase of the observations obtained. A second technique is developed in Chapter 7 which attempts to fit the observations with a model comprised of two synthetic spectral components.

Towards a slightly different goal, Chapter 8 contains work computing the fundamental RV precision of M-dwarf in the nIR. These are the best candidates for detecting small mass planets in their habitable zone, and are a focus for upcoming nIR RV spectrographs. A focus was shifted towards updating the tools to compute the RV precision to prepare for the release of the CARMENES nIR spectral library.

Pedro: I would only note that you can provide a more detailed description on the importance of determining RV information content measurement (at the very end of the chapter)

---

<sup>10</sup> Only the minimum mass  $M_2 \sin i$  known

# Chapter 2

## Fundamental Radial Velocity

The radial velocity method, has been a consistent power-horse for the measurement of the orbital motion of binary stars and stars hosting exoplanets. In this chapter some of the key properties of Keplerian orbits and the RV signal will be presented along with an introduction to the notion of RV precision.

### 2.1 Keplerian Orbits

When two bodies are in orbit (two stars or a star and a planet) they orbit about their common centre of mass. Their 3-dimensional motion can be derived with a combination of Newton's universal law of gravitation, and Kepler's laws. The full derivation is quite long and can be commonly found in several celestial mechanics texts (e.g. Moulton, 1914; M. Perryman, 2011; Fitzpatrick, 2012). The notes given here mainly follow Bozza et al. (2016).

Figure 2.1 shows the basic elements of the Keplerian orbit. There are several parameters required to situate the orbit in space. There is a *reference plane*, tangential to the celestial sphere, that cuts the orbital plane with a *line of nodes*. The *ascending node* is the point on the plane at which the body crosses the reference plane moving away from the observer, and is defined relative to the vernal reference point,  $\Upsilon$ , with the *longitude of the ascending node*,  $\Omega$ , setting the orientation.

To fully parametrize a Keplerian orbit requires seven parameters. These are:  $a$  the semi-major axis of the elliptical orbit,  $e$  the orbital eccentricity,  $P$  orbital period,  $T_0$  the *time of periastron passage*,  $i$  orbital inclination relative to the line of sight,  $\omega$  the *argument of periastron*, and  $\Omega$ . From RV measurements alone all of these parameters except for  $i$  and  $\Omega$  can be determined.  $\Omega$  is irrelevant for determining the orbital mass, but inclination  $i$  is very important as it affects the projection of the velocity towards the observer.

With a two body system with masses  $M_1$  and  $M_2$ , under the force of gravity, their orbits are elliptical orbits about their barycentre mass, as seen in Figure 2.2. In polar coordinates the ellipse of an orbit about the centre of mass (located at the focus  $F_1$ ) is described by:

$$r = \frac{a(1 - e^2)}{1 + e \cos \nu(t)}, \quad (2.1)$$

where  $a$  is the length of the semi-major axis for the body,  $e$  is the eccentricity,  $\nu$  is the *true anomaly* the

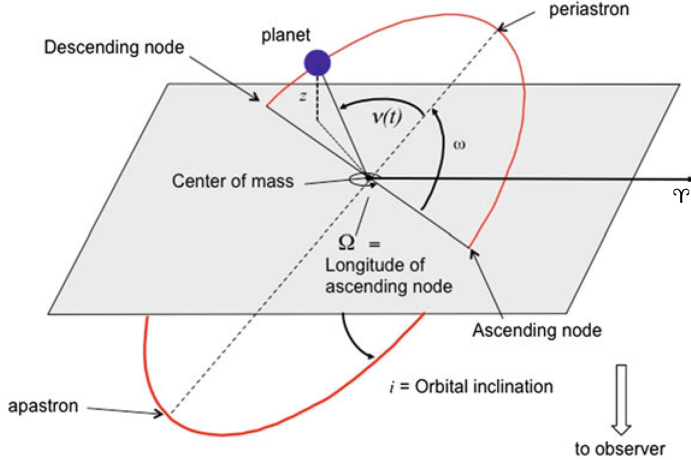


**Figure 2.1:** The basic elements of the Keplerian orbit. Adapted from Bozza et al. (2016).

angle between the current position of the orbiting body and periastron.

The true anomaly is not only a function time,  $t$ , but also the orbital period  $P$ , the *time of periastron passage*,  $T_0$ , and eccentricity. It is geometrically related to the eccentric anomaly:

$$\cos \nu(t) = \frac{\cos E(t)}{1 - e \cos E(t)} \quad (2.2)$$

which can be numerically determined from the mean anomaly  $M(t)$ :

$$M(t) = \frac{2\pi}{P}(t - T_0) = E(t) - e \sin E(t) \quad (2.3)$$

The mean anomaly is the angle for the average orbital motion of the body at a time after periastron passage  $t - T_0$ .

From Kepler's second law<sup>1</sup>  $\frac{1}{2}r^2 d\nu/dt = \text{constant}$ , while in one full period  $P$ , the total area of the ellipse  $\pi a^2(1 - e^2)^{1/2}$  will be covered, leading to:

$$r^2 \frac{d\nu}{dt} = \frac{2\pi a^2(1 - e^2)^{1/2}}{P} \quad (2.4)$$

The radial velocity is the change in  $r$  along the line of sight  $z$ . The component of  $r$  along the line of sight (from Figure 2.1) is:

$$r_z = r_1 \sin(\nu_1(t) + \omega) \sin i + \gamma \quad (2.5)$$

where  $\gamma$  is the mean velocity of the barycentre, and the subscripts '1' and '2' refer to the star and planet (or companion star), respectively. Differentiating Equation 2.5 and substituting in Equation 2.4 leaves

---

<sup>1</sup> Orbit sweeps out equal areas in equal times

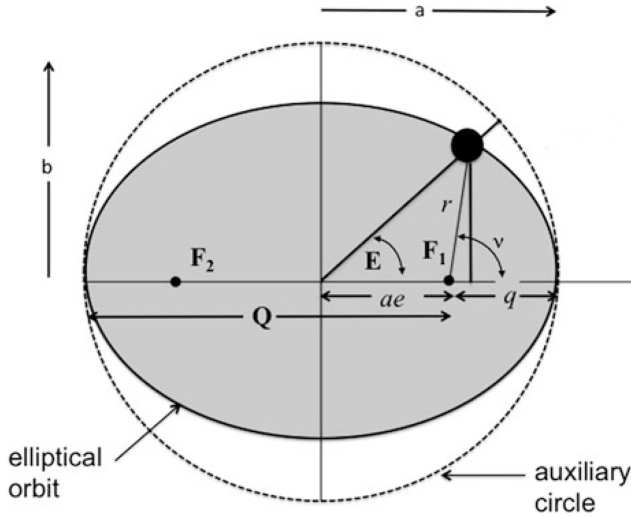


**Figure 2.2:** Elements of an elliptical orbit about the common centre of mass  $F_1$ .  $\nu$  is the angle to the position of the orbiting body from the perihelion (closest point to barycentre). The auxiliary circle has a radius equal to the semi-major axis of the ellipse. Adapted from Bozza et al. (2016).

the common RV equation:

$$RV = \dot{r}_z = \frac{2\pi a_1 \sin i}{P(1 - e^2)^{1/2}} [\cos(\nu(t) + \omega) + e \cos \omega] + \gamma \quad (2.6)$$

$$= K_1 [\cos(\nu(t) + \omega) + e \cos \omega] + \gamma, \quad (2.7)$$

where several parameters and constants have been condensed into  $K$ , referred to as the *semi amplitude*. In this case  $K_1$  is the semi amplitude for the star.

### 2.1.1 Mass function

Once the orbital parameters have been determined then it is possible to determine the mass function of the system. From the centre of mass the distance between the two bodies is  $a = a_1 + a_2$  where  $a_1$  and  $a_2$  are the respective distances to the barycentre, while the value  $M_1 a_1 = M_2 a_2$  can allow these re-arrangements:

$$a = a_1 \left(1 + \frac{a_2}{a_1}\right) = a_1 \left(1 + \frac{M_1}{M_2}\right) = \frac{a_1}{M_2} (M_1 + M_2) \quad (2.8)$$

Kepler's third law ( $G(M_1 + M_2)/4\pi^2 = a^3/P^2$ ) can be written as:

$$\frac{G(M_1 + M_2)}{4\pi^2} = \frac{a_1^3}{P^2} \left(\frac{M_1 + M_2}{M_2}\right)^3 \quad (2.9)$$

**Table 2.1:** The RV semi-amplitude induced by the planets with different masses and periods around a  $1 M_{\odot}$ -mass star.

$M_2$	$K_1(P = 3 \text{ d})$	$K_1(P = 1 \text{ yr})$	$K_1(P = 5 \text{ yr})$	
$M_{\text{Jup}}$	140.8	28.4	16.6	$\text{m s}^{-1}$
$M_{\text{Nep}}$	7.60	1.53	0.90	$\text{m s}^{-1}$
$M_{\odot}$	44.3	8.9	5.2	$\text{cm s}^{-1}$

replacing  $a_1$  with  $K_1$  from Equation 2.6 results in the *mass function*,  $f(M)$ :

$$f(M) = \frac{(M_2 \sin i)^3}{(M_1 + M_2)^2} = \frac{K_1^3 P (1 - e^2)^{3/2}}{2\pi G} \quad (2.10)$$

This function can be determined directly from the measurable parameters  $P$ ,  $e$  and  $K_1$ . It also depends on the stellar mass  $M_1$ , which needs to be measured by some other means to determine the planet mass. Also from this function it can be seen that the true mass of the planet  $M_2$  is not obtained but only the projected mass  $M_2 \sin i$ .

For a planetary companion the approximation  $M_2 \ll M_1$  can be made and for circular orbits ( $e = 0$ ) the radial velocity semi-amplitude can be re-written as:

$$K_1 = \frac{28.4}{\sqrt{1 - e^2}} \frac{M_2 \sin i}{M_{\text{Jup}}} \left( \frac{M_1}{M_{\odot}} \right)^{-2/3} \left( \frac{P}{1 \text{ yr}} \right)^{-1/3} [\text{m s}^{-1}] \quad (2.11)$$

This can be used to calculate the RV amplitude created by different mass planets in various circular orbits as given in Table 2.1. The recently commissioned ESPRESSO optical spectrograph is designed with the goal of achieving  $10 \text{ cm s}^{-1}$ , which is the level of precision required to detect an Earth mass planet in a one year orbit round a Sun-like star.

If there is more than one companion/planet then there will be a gravitational influence between each other and their orbits become non-Keplerian, i.e. an N-body problem (e.g. Chenciner, 2007). Assuming that the gravitational influence between companions is negligible, the RV signal observed in the host star can be treated as just a sum of tugs from each companion. For the two instances in this work where the target star has two companions, the companions will be treated separately, as if they were alone.

### 2.1.2 Binary mass ratio

In the above equation RV of the companion has not yet been addressed. Equation 2.6 above is the RV of the star in an elliptical orbit around the centre of mass between it and its companion. Similarly the elliptical orbit of the planet around the centre of mass is given by:

$$RV_2 = K_2 [\cos(\nu(t) + \omega_2) + e \cos(\omega_2)] + \gamma, \quad (2.12)$$

where  $\omega_2 = \omega + 180^\circ$  due to the phase difference between the two components, resulting in the relative velocity (ignoring  $\gamma$ ) of the companion being opposite the star and:

$$K_2 = \left( \frac{2\pi G}{P(1 - e^2)^{3/2}} \right)^{1/3} \frac{M_1 \sin i}{(M_1 + M_2)^{2/3}} = \frac{2\pi a_2 \sin i}{P(1 - e^2)^{1/2}} \quad (2.13)$$

The orbits of the host and companion are directly related through the mass ratio of the star and companion:

$$q = \frac{M_2}{M_1} = \frac{K_1}{K_2} = \frac{RV_1}{RV_2} = \frac{r_2}{r_1}. \quad (2.14)$$

Typically in exoplanet detections the companion (planet) is too faint to measure the planetary velocity. However in double lined spectroscopic binary the spectrum of both stars can be identified in the blended spectra and the RV of both star and companion can be measured and monitored over the orbit. With both velocities the mass ratio of the binary can be found. The individual masses however are still not determinable due to the inclination  $\sin i$  of the orbit.

In Chapter 6 the detection of the faint spectra of known companions is attempted, in order to determine the velocity change of the companion and hence the mass ratio. To help with the analysis and simulations the known orbital parameters (see Tables 6.1 and 6.2) are used along with the companion mass ( $M_2$  or  $M_2 \sin i$ ) to predict or estimate the RV of the companion using Equations 2.12 and 2.14. Note, that for the targets in which only the minimum mass ( $M_2 \sin i$ ) is known and used in the mass ratio, this will result in the maximum RV semi amplitude for the companion. The estimated  $K_2$  for each companion is provided in Table 6.4 while the RV for both components at the time of each observation is provided in Table 6.3.

## 2.2 Measuring the RV

The motion of the star towards and away from the Earth shifts the lines of its spectra through the Doppler Effect. In the non-relativistic limit this can be written as:

$$\frac{\Delta\lambda}{\lambda} = \frac{v}{c}, \quad (2.15)$$

where  $\Delta\lambda$  is the wavelength shift of wavelength  $\lambda$  with a velocity relative to the observer  $v$ . The speed of light is the constant  $c$ . To measure the RV the relative positions of the stellar lines need to be measured over time. Typically this is done via the cross-correlation (CCF) of the observed spectrum with a template mask (e.g. a binary mask (Baranne et al., 1996) or weighted mask (Pepe et al., 2002)) suitable for the spectral type of the observed star. The CCF stacks together the spectral lines creating an “average” line, reducing the random noise on the individual  $N$  spectral lines by a factor of  $\sqrt{N}$ . The CCF collapses the RV from all the lines into one number with higher precision than individual lines.

## 2.3 RV precision

To achieve a high-level RV precision, two sources of noise must be controlled: statistical error from the RV measurement and systematic errors induced by the spectrograph. This requires a stabilized spectrograph, precisely calibrated in wavelength, and the combination of thousands of lines (e.g. Pepe et al., 2014b). The fundamental source of noise is photon noise, which follows a Poisson distribution. That is, an observable with an average value of  $N$  has a standard deviation  $\sqrt{N}$ .

A very general formula for the RV precision achievable of a given spectrum, in terms of general

spectral parameters is given by Hatzes et al. (1992) as:

$$\sigma \propto \frac{1}{\sqrt{F} \sqrt{\delta\lambda} R^{1.5}}. \quad (2.16)$$

$\sqrt{F}$  represents the signal-to-noise ratio (SNR) of the spectrum in the Poisson-dominated noise regime, while  $\Delta\lambda$  is the bandwidth of the observed spectrum. This assumes that the spectrum contains a homogeneous distribution of uniform lines, per unit wavelength. The precision depends more steeply on the spectral resolution with  $R^{-1.5}$  occurring due to the bandwidth and the number of lines visible on a fixed detector size decreases with increased resolution. In high resolution RVs this tends to  $R^{-1}$  indicating the higher precision at the expense of wavelength coverage is desired Hatzes et al. (1992). As a star rotates its lines become broadened by an area preserving rotation kernel (see Section 8.1.3). In a similar way to the resolution the RV precision is dependant on rotational velocity of the star ( $vsini$ ) to the power 1.5.

Assuming a spectral line is comprised of Gaussian-shaped absorption lines it, the precision of a line can be shown to be:

$$\sigma \sim \frac{\sqrt{\text{FWHM}}}{C \cdot \text{SNR}} \quad (2.17)$$

where FWHM is the full width at half maximum of the line,  $C$  is the line contrast (depth relative to continuum) and SNR the signal-to-noise of the continuum. An alternate derivation comes from Bouchy et al. (2001) in which the optimal weight for each pixel is calculated for a spectrum  $A_0$  via:

$$W(i) = \frac{\lambda^2(i)(\partial A_0(i)/\partial\lambda)^2}{A_0(i) + \sigma_D} \quad (2.18)$$

with the RV precision calculated over all pixels as

$$\delta v_{RMS} = \frac{c}{\sqrt{\sum_i W(i)}}. \quad (2.19)$$

where  $\lambda$  is the wavelength and  $\sigma_D$  the detector noise.

In all these formulations there are some key properties to achieve high RV precision: a high stellar flux  $F$  to achieve a high SNR, observed at high resolution to have sharp spectral lines. The deeper (high C) and narrower (small FWHM) a spectral line<sup>2</sup>, the better defined the position of the line will be, allowing for a higher precision measurement of the RV. The flux  $F$  or SNR of an observation increases with the number of photons collected which depends on the stellar brightness as well as distance<sup>3</sup>, coupled with the telescope size and with the exposure time. This limits the highest precision RV measurements to relatively nearby stars. Cross-dispersed echelle spectrographs mounted on the largest telescopes are capable of delivering the high-resolution, high SNR and high bandwidth requirements necessary to achieve high precision RV measurements.

These formulae have recently been used to assess the theoretical RV precision of synthetic spectra for the development of instrument designs of new nIR spectrographs (e.g. Figueira et al., 2016) as well as compare precision of real and synthetic spectra (e.g. Artigau et al., 2018). The RV precision will be

---

<sup>2</sup> With steeper gradients  $\partial A_0(i)/\partial\lambda$ .

<sup>3</sup> Basically the stars apparent magnitude

analysed further in Chapter 8 with a detailed derivation of the Bouchy et al. (2001) method given and implemented to analyse the precision of nIR spectra.

# Chapter 3

## Near-infrared spectroscopy

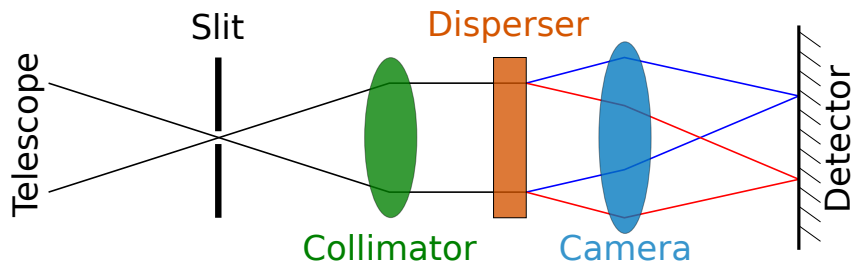
In this chapter the basics of spectroscopy will be laid out, with the difference between optical and infrared spectroscopy given. A summary of several high-resolution nIR spectrographs relevant to this thesis will end this chapter.

### 3.1 Spectrograph basics

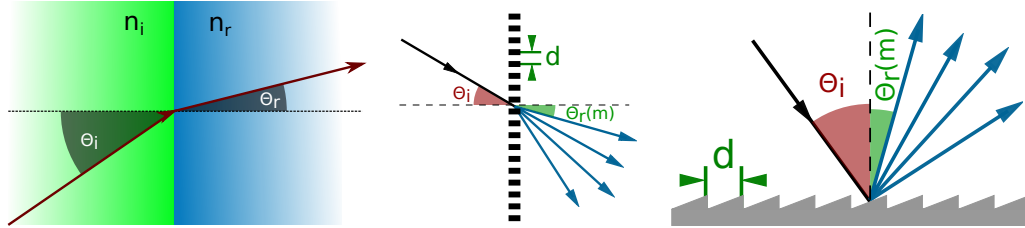
A spectrograph is a instrument of measuring the electromagnetic flux as a function of wavelength. All spectrographs have a few basic components common to all. A simple diagram with the basic components is shown in Figure 3.1. The first is the telescope which is used to collect light and focus the image of the sky onto its focal plane. A slit (or an optical fibre<sup>1</sup>) is placed on the telescopes focal plane to block all but the light from the desired target. The light passing through the slit is diverging so a collimator is used to turn the diverging light into a parallel beam. The dispersing element is next and is responsible for dispersing the light into its separate components. This can be either a prism, grating or even both. Following the dispersive elements are the optics for the camera, used to focus the dispersed (but still fairly collimated) light onto the detector, commonly a two-dimensional array of light sensitive pixels situated at the focal plane. Usually several optical elements, both lenses and mirrors, are used in combination to meet the constraints of the design specifications.

Figure Figure 3.2 shows the schematic for 3 different dispersion mechanisms: Snells law, a transmission grating and, a reflection grating.

<sup>1</sup> Fibres allow for the spectrograph to be situated far from the telescope.



**Figure 3.1:** Diagram of the basic components of a spectrograph.



**Figure 3.2:** Left: Dispersion at an optical boundary due to Snell's law. Middle: Dispersion from a transmission grating. Right: Dispersion from reflection grating.

The left hand picture is a depiction of the refraction of light when passing between two materials with a different refraction index,  $n_i$ , and  $n_r$ . The angle of incidence  $\theta_i$  and angle of refraction  $\theta_r$  relative to the normal (perpendicular) of the surface are related through Snell's law:

$$n_i \sin(\theta_i) = n_r \sin(\theta_r).$$

The index of refraction of a material is wavelength dependant as the angle of refraction will be different for each wavelength, causing dispersion, like a prism.

The two dispersion gratings in Figure 3.2 are comprised of parallel narrow slits (transmission) or grooves (reflection), very close together. Diffraction from these slits/grooves constructively and destructively interfere to create spectral orders that obey the grating equation:

$$m\lambda = d [\sin(\theta_i) \pm \sin(\theta_r)]. \quad (3.1)$$

Here  $m$  is the order number,  $\lambda$  the wavelength,  $d$  the spacing between the slits/grooves, and again  $\theta_i$  and  $\theta_r$  the incident and reflection angles respectively, relative to the normal.

This equation has degeneracy as different combinations of  $m\lambda$  will be dispersed at the same angles. For instance the value  $m\lambda$  for order  $m=54$  at  $\lambda=2100$  nm is that same as the order  $m = 55$  at  $\lambda = 2061.8$  nm. This degeneracy can be overcome in two ways, either by applying a wavelength filter to specifically select only one order or by adding a cross-disperser. A *cross-disperser* is a second dispersive element oriented to disperse the orders perpendicular to the grating. This allows for multiple orders to recorded simultaneously on a two-dimensional detector, dramatically increasing the wavelength coverage. Echelle spectrographs are a special type of spectrograph, with a groove shape and orientation specifically for high reflection angles, and able to observe at a high spectral order (high  $m$ ) to achieve a high dispersion and high resolution.

Some important concepts for discussing spectrographs are the spectral resolution, resolving power, spectral coverage and spectral sampling. The spectral resolution,  $\delta\lambda$ , is the smallest difference in wavelength able to be identified. It is related to resolving power which is defined as  $R = \frac{\lambda}{\delta\lambda}$ . The resolving power,  $R$  is colloquially also referred to as the resolution<sup>2</sup>. The higher the resolution (resolving power),  $R$ , the smaller the  $\delta\lambda$  that can be measured, leading to highly sampled spectral lines and more precise measurement. To be considered high-resolution, spectrographs typically have  $R > 20\,000$ , but the definition of "high" can differ between sub-fields of astronomy. The spectral coverage is the range of wavelengths able to be covered by the spectrograph, while the spectral sampling is the number of

<sup>2</sup> This document is no different.

**Table 3.1:** Properties of popular optical/IR detector materials.  $\varepsilon_g$  is the material band gap, the minimum excitation energy.  $\lambda_c$  is the cut-off wavelength corresponding to the maximum wavelength for each material. Common values for the detector operating temperature for the materials are given as  $T_{op}$ .

Material	Symbol	$\varepsilon_g$ [eV]	$\lambda_c$ [μm]	$T_{op}$ [K]
Silicon	Si	1.12	1.1	163–300
Mer-Cad-Tel	HgCdTe	0.09–1.00	1.24–14	20–80
Indium Antimonide	InSb	0.23	5.5	30
Arsenic doped Silicon	Si:As	0.05	25	4

pixels required to sample the FWHM of the spectral lines. This value should be higher than 2 pixels per resolution element to satisfy Nyquist sampling.

## 3.2 The detectors

The basic principles of spectroscopy are the same for optical and infrared are the same one difference is the design of the detector. Nowadays the most common type of detector are focal plane arrays, a two-dimensional array of pixels located at the focal plane of the spectrographs camera. The purpose of the detector is to count the number of photons hitting each pixel in the array. This is achieved via the photoelectric effect on a crystalline structure, in which incident photons are transformed into electrons which can be recorded electronically. The energy necessary to excite an electron from the *valence band* to the *conduction band*, the characteristic band gap, is different for every material. Silicon is the best material for the detection of optical light (0.3–1.1 μm), while in the near-infrared (1–5 μm) two materials are used: Mercury-Cadmium-Telluride (HgCdTe) and Indium Antimonide (InSb). In the mid-infrared (5–20 μm) arsenic doped Silicon is used (Si:As).

Since photon energy is inversely proportional to wavelength<sup>3</sup>, longer wavelengths must have smaller band gaps. However, smaller band gaps are also more susceptible to electrons excited by thermal energy, known as the dark current. The dark current is dependant on detector temperature, the pixel size, quality of material and the materials cut-off wavelength  $\lambda_c$ . A summary of values for different material properties is given in Table 3.1.

The technologies for optical and IR detectors are very different. Figure 3.3 shows the main architectural difference between CCD and CMOS with a very brief comparison between them given below. Charge-Coupled Devices (CCDs) are used in the visible. Their use of silicon allows for the photo-induced electrons to methodically transfer the charge from pixel to pixel along to one end. The electrons from each pixel pass into an amplifier to increase the signal, and are then measured as a voltage difference with an analogue-to-digital converter (ADC). As the charge is shifted between pixels, CCDs require high charge transfer efficiency (CTE) to not leave charge behind, which would be assigned to the incorrect pixels. CCDs have an almost 100% filling of photosensitive material. However the  $\lambda_c$  cut-off of silicon makes them unsuitable for the IR. More information on CCDs can be found in (Howell, 2000).

For IR the technology of choice is CMOS (Complementary Metal Oxide Semiconductor). Unlike CCDs, each individual pixel contains the electronic circuitry to read, amplify and, measure the collected charge. Since the charge is read and amplified at each pixel there is no charge transfer between pixels and

<sup>3</sup>  $E_{photon} = \frac{hc}{\lambda}$ , where  $c$  is the speed of light,  $h$  is Plank's constant and  $\lambda$  wavelength.

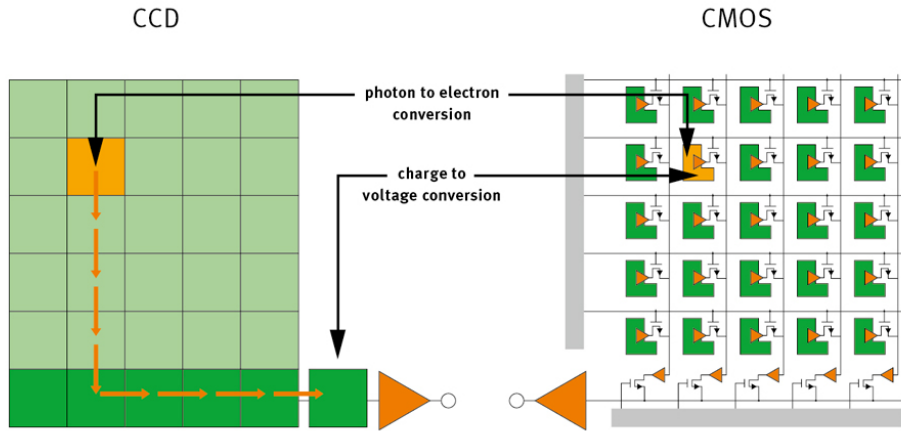


**Figure 3.3:** Schema differentiating CCD and CMOS detectors. In CCDs the charge is transferred to a specific pixel for measurement while in CMOS the charge is measured at the location of each pixel by individual amplifiers and ADCs. Credit <https://automatie-pma.com>.

the readout is non-destructive. As a consequence, the same pixel can be read several times, averaging and thus reducing the effective readout noise of each pixel. In theory, if one averages  $N$  measurements before an observation (of a freshly reset detector), and  $N$  measurements of the observed charge after the observation, the readout noise can be reduced by a factor of  $\sqrt{(N)}$ , referred to as *Fowler Sampling* (Fowler et al., 1990). Reading a CMOS detector is very versatile as it can be read in multiple ways, with the ability to randomly read any pixel at any time. The filling area of the photosensitive material is reduced in CMOS due to the presence of support architecture that is required for the circuitry on the top surface, partially blocking some of the incident light, reducing their efficiency.

As it is impossible to have every individual amplifier perfectly identical, there is a small sensitivity and gain difference between CMOS pixels, which are exposed by calibrating with a uniform light source. This contrasts with the one or few amplifiers used in CCDs, which lead to extremely homogenous amplification (as all pixels are amplified by the same amplifier). The CMOS circuitry is also intrinsically non-linear due to the changing capacitance as charge is collected. Irrespective if the charge is photo-induced or dark current, the circuitry measurement changes with the pixel charge level. This requires careful characterization of the non-linearities in the detector by calibrating its response to a uniform light source for a large range of integration times. For CRIRES there are a set of non-linearity coefficients that are applied while performing the flat-field corrections (see Section 5.0.1.2).

Other benefits of CMOS detectors are that they use lower power, and do not need a mechanical shutter (they can be reset electronically). While CCDs have been manufactured almost the same way for the last 40 years, CMOS technology is still advancing, partially driven by the consumer electronics market. Nowadays, most cellphone and laptop cameras use CMOS chips, helping to push investment in this technology. After the charge has been digitized into a number, the processes are once again similar for both technologies.

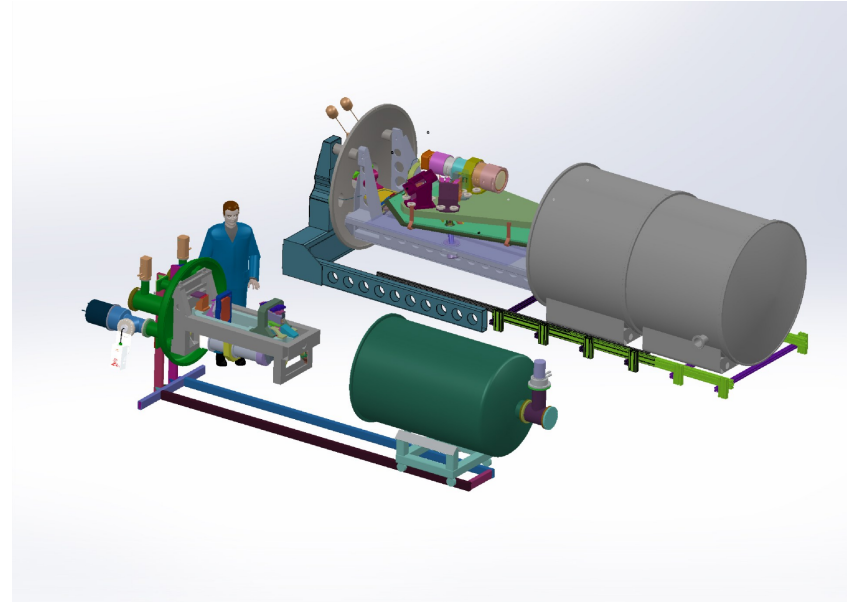


**Figure 3.4:** Side by side comparison of the NIRPS and SPIRou spectrographs. NIRPS is the smaller spectrograph. The cryostat's are shown in the open position and slide to enclose the instruments. Credit <http://www.astro.umontreal.ca/nirps/>.

### 3.2.1 Spectrograph cooling

Spectrographs must be cooled down for their detectors operate effectively as seen in Table 3.1. This is achieved by placing spectrographs and their supporting components inside a vacuum chamber, away from all warm (radiating) components and precisely cooled<sup>4</sup> to a low temperature. These are often referred to as cryostat's. Modern instruments use closed-cycle refrigerators, with for example, helium as the working fluid to achieve very stable low temperatures inside the cyrostat. Providing an isolated, and stable environment for the spectrograph allows spectra science to be performed with the highest precision possible, essential for detecting and characterizing exoplanets.

Cooling plays two important roles for IR astronomy. Firstly, the thermal infrared emission from the components of the spectrograph surrounding the detector is reduced, diminishing the local background. Secondly, the detectors own thermally-generated background (dark current) is greatly reduced at low temperatures, leading to a gain in sensitivity.

Examples of two cryostat housings surrounding the spectrograph (but shown open) can be seen in Figure 3.4.

## 3.3 CRIRES

CRIRES (Cryogenic InfraRed Echelle Spectrograph) is an ESO IR spectrograph that was mounted on the Unit Telescope (UT1, Autu) of the European Southern Observatory's Very Large Telescope (VLT) (Kaeufl et al., 2004) and available from April 2007 through July 2014<sup>5</sup>. The main optical elements consist of a prism pre-disperser and an echelle grating with 31.6 lines/mm. The instrument provides resolutions

<sup>4</sup> Temperature stability in the milli-Kelvin range.

<sup>5</sup> Note this PhD research began in October 2014.

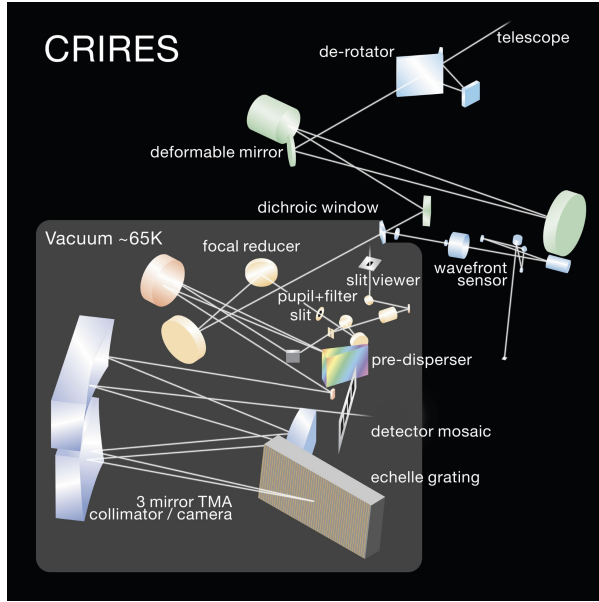


**Figure 3.5:** CRIRES layout schematic, taken from the CRIRES manual v93.

up to 100 000 when used with a  $0.2''$  slit<sup>6</sup>. The wavelength range is 960–5200 nm with an instantaneous wavelength coverage of  $\sim \lambda/50$ . The spectra are imaged on a detector mosaic, consisting of four Aladdin III detectors ( $4096 \times 512$  pixel) in a row, with a gap of  $\sim 250$  pixels between each chip. Adaptive optics (MACAO - Multi-Applications Curvature Adaptive Optics) can be used to optimize the signal-to-noise ratio and the spatial resolution. Figure 3.5 displays the schematic representation of the CRIRES optical layout.

CRIRES lead the way for high-resolution spectrograph in the IR with a resolution higher than any of its predecessors, and unique capabilities, like adaptive optics. As with any new instrument there were several problems that affected CRIRES during its science operations. For instance there were several mechanical issues with the slit: the slit edges were not parallel and there were issues with precise and reproducible positioning. Other issues that require post observation correction such as detector glow, the odd even effect, and the wavelength calibration are detailed in Sections 5.0.1.1, 5.0.1.2 and 5.2.1.

### 3.4 The new generation

Building off the success of CRIRES several other nIR spectrograph have and are being developed for different telescopes.

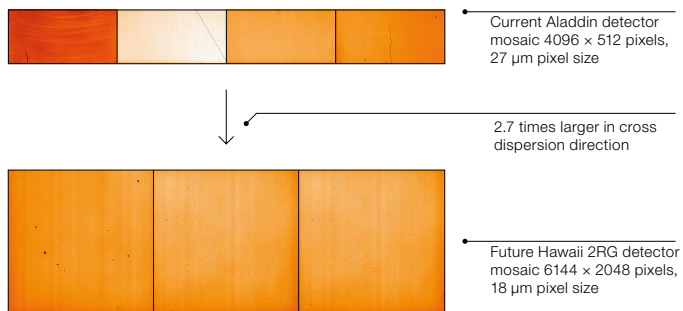
Their science goals for these instruments involve some or all of the following:

- Detecting low-mass planets in the habitable zone around late-type stars (M-dwarfs).
- Detecting and characterising the atmospheres of exoplanets.
- Observe and monitor clouds on brown dwarfs.
- Analysing the spectra and atmospheres of cool stars.
- The origin and evolution of stellar magnetic fields (through spectropolarimetry).

<sup>6</sup> The rule of thumb for the resolution of CRIRES is  $R = 100\,000 \times \frac{\text{slit width}}{0.2''}$ , with the slit width in arcseconds.

**Table 3.2:** A comparison between some high-resolution nIR spectrographs.

	CRIRES+	CARMENES (red)	NIRPS	SPIRou
Location	Paranal, Chile	Calar Alto, Spain	La Silla, Chile	Mauna Kea, Hawaii
Latitude	24°40' S	37°13' N	29°15' S	19°49' N
Available (* expected)	2019*	2016	2019*	2019*
Telescope diameter (m)	8.2	3.5	3.6	3.6
Wavelength Range ( nm)	920–5200	960–1710	970–1810	980–2350
Resolution	50 000/100 000	80 400	75 000/100 000	70 000
RV precision ( m s <sup>-1</sup> )	2–3	~ 1	1	1
Operating Temperature ( K)	70	140	80	77

**Figure 3.6:** CRIRES detector focal plane array comparison with the new detectors. Credit Dorn et al. (2014).

A few points about some of the nIR instruments used in this work are detailed below with a summary also provided in Table 3.2.

### 3.4.1 CRIRES+

CRIRES was removed from operation in 2014 to undergo significant upgrades (Dorn et al., 2014). These include adding a cross-disperser to increase the simultaneous wavelength coverage by up to a factor of 10, improving the wavelength calibration by replacing the Th-Ar calibration lamp with a U-Ne lamp which has a richer set lines in the IR, and developing new multi-species gas absorption cells for the IR. The new upgrade adds the capability for spectropolarimetry using a polarization selective beam-splitter, in which the polarization of light in the spectrum can be analysed. The current detector mosaic will be replaced by 3 Hawaii 2RG detectors ( $6144 \times 2048$  pixels) at a pixel size of  $18 \mu\text{m}$ . A comparison between the new and old detector size is shown in Figure 3.6. The new detector mosaic will not only provide a larger area but also have a lower noise, higher quantum efficiency, better cosmetic quality and, a lower dark current<sup>7</sup>. The current estimate for the first light of CRIRES+ is late 2019.

### 3.4.2 CARMENES

CARMENES (Calar Alto high-Resolution search for M dwarfs with Exoearths with Near-infrared an optical Échelle Spectrographs) has been operating since 2016, performing a dedicated RV survey of  $\sim 300$

<sup>7</sup> [https://www.eso.org/sci/facilities/develop/instruments/crires\\_up.html](https://www.eso.org/sci/facilities/develop/instruments/crires_up.html)

late-type main-sequence stars with the goal of detecting low-mass planets in the habitable zone. It is mounted on the 3.5 m telescope at the Calar Alto Observatory in Spain, the light from the telescope passes through a beam splitter and enters into two separate spectrographs, one in the optical (520–960 nm) and the other in the infrared (960–1710 nm). A library of single spectra of the M-dwarf targets CARMENES is monitoring was recently released in Reiners et al. (2018).

### 3.4.3 NIRPS

NIRPS (Near-InfraRed Planet Searcher), on the 3.6 m telescope at La Silla, Chile, is a nIR extension to the HARPS spectrograph, one of the most prominent spectrographs detecting exoplanets via the RV method. A replacement for the HARPS telescope adapter will be used to split the light and send the optical wavelengths to HARPS and IR to NIRPS via fibres. The adaptor also includes adaptive optics and a new calibration unit.

This will allow for the RV monitoring of cooler stars which emit more of their photons in the infrared but also have less stable optical spectra due to convection; infrared spectra are less affected by the stellar activity.

### 3.4.4 SPIRou

SPIRou (SPectroplorimètre InfraROUge) is another high-resolution nIR spectrograph that will be installed at the CFHT (Canada-France-Hawaii Telescope) in Hawaii. It will provide a spectrum covering from 950–2340 nm in a single exposure at a resolution of around  $\sim 75\,000$ . Like the other spectrographs detailed here it is built to obtain very high radial velocity accuracy, of the order meters/second over several years. It also includes spectropolarimetry, being able to derive the linear and circularly polarized state of the observed target.

A physical side-by-side comparison of the NIRPS and SPRIou spectrographs is shown in Figure 3.4, with NIRPS being the smaller of the two spectrographs.



# Chapter 4

## Atmospheres and Models

### 4.1 Earth's atmosphere, in the nIR

While the Earth's atmosphere is important for life on Earth, it can be a nuisance for ground-based astronomical observations. While the atmosphere is mostly transparent in the visible, with only minor transmission and emission features, it is not uniformly transparent in the infrared.

As light from astronomical sources passes through Earth's atmosphere, the molecular species absorb specific wavelengths (corresponding to molecular rotational and vibrational energy levels) densely populating the nIR with absorption lines, commonly referred to as telluric absorption. Figure 4.1 contains the model telluric absorption spectrum for the atmosphere from 0.3–30  $\mu\text{m}$  at  $R \sim 10\,000$  from Smette et al. (2015). It clearly shows that there are regions where the atmosphere is mostly transparent (transmission of 1), with other wavelength regions (e.g. at 4.5  $\mu\text{m}$ ) that are completely opaque. Molecules which are the main contributors to the absorption are labelled.

The windows of transmission defined the location of photometric bands in the infrared, with the common ones listed in Table 4.1 (see e.g. Sterken et al., 1992; Binney et al., 1998). There are also variations on these bands for specific to different sites. These photometric bands are chosen for high average photometric<sup>1</sup> throughput, and do not consider the variable spectroscopic content inside the individual bands that becomes evident when observing at high resolution.

<sup>1</sup> Considering all photons in the band equally, regardless of wavelength (Very low resolution)

**Table 4.1:** Standard infrared pass-bands.

Band	Central wavelength [ $\mu\text{m}$ ]	Bandwidth [ $\mu\text{m}$ ]
Z	0.9	0.06
Y	1.05	0.12
J	1.25	0.38
H	1.65	0.48
K	2.2	0.4
L	3.5	1.2
M	4.8	0.6
N	10.6	2.5
Q	21	5.8

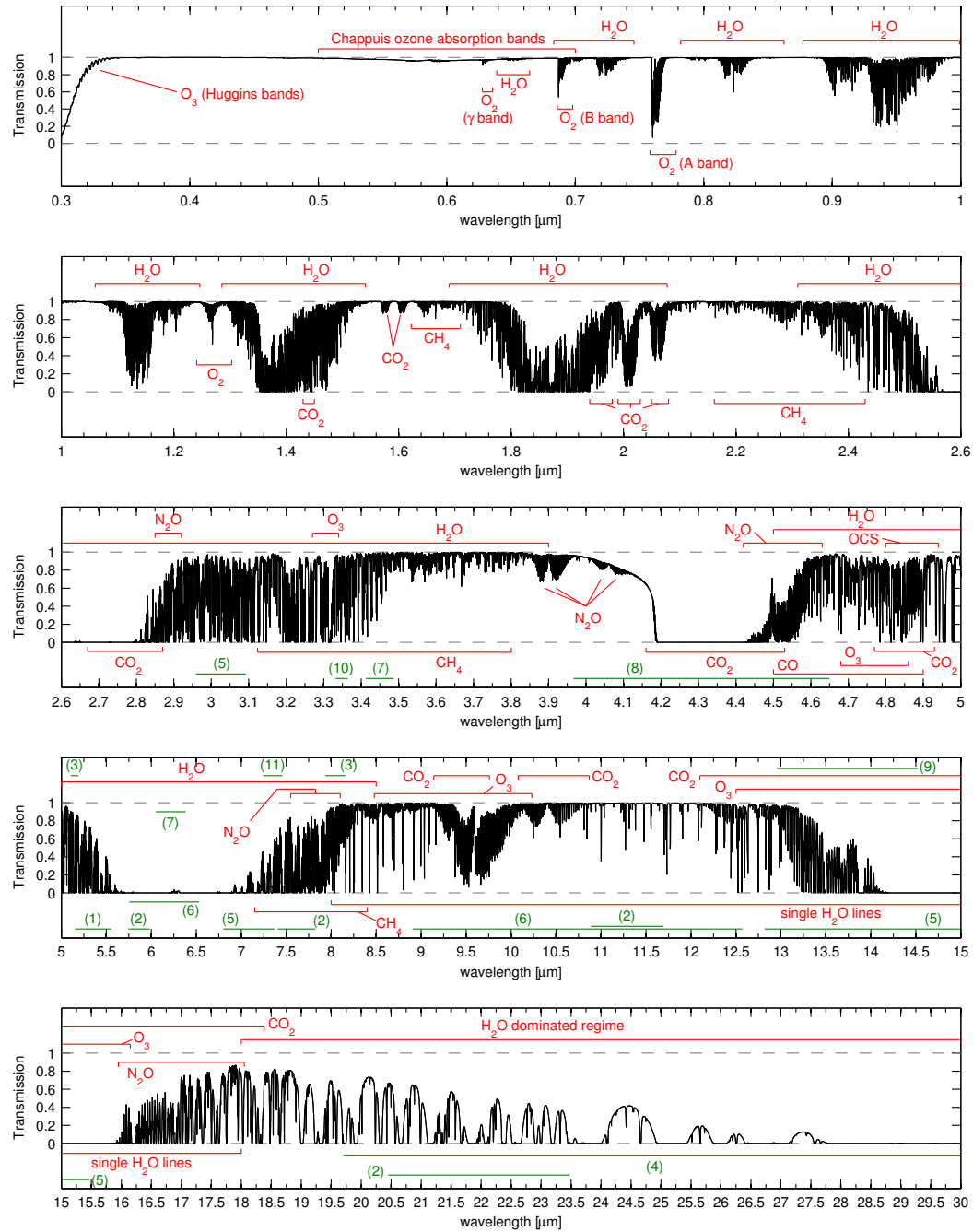


**Figure 4.1:** Telluric absorption map from 0.3–30  $\mu\text{m}$  at  $R \sim 10\,000$ . The eight main molecules  $\text{O}_2$ ,  $\text{O}_3$ ,  $\text{H}_2\text{O}$ ,  $\text{CO}$ ,  $\text{CO}_2$ ,  $\text{CH}_4$ ,  $\text{OCS}$ , and  $\text{N}_2\text{O}$  contribute more than 5% to the absorption in some wavelength regimes. The red regions mark the ranges where they mainly affect the transmission, minor contributions of these molecules are not shown. The green regions denote minor contributions from the following molecules: (1)  $\text{NO}$ ; (2)  $\text{HNO}_3$ ; (3)  $\text{COF}_2$ ; (4)  $\text{H}_2\text{O}_2$ ; (5)  $\text{HCN}$ ; (6)  $\text{NH}_3$ ; (7)  $\text{NO}_2$ ; (8)  $\text{N}_2$ ; (9)  $\text{C}_2\text{H}_2$ ; (10)  $\text{C}_2\text{H}_6$ ; and (11)  $\text{SO}_2$ . Credit Smette et al. (2015, Figure 1).

The most prominent absorber in the infrared is water vapour ( $H_2O$ ) which is a strong absorber and defines the photometric bands as seen in Table 4.1. Water vapour is mostly concentrated in the lower 5 km, so infrared observatories are situated in dry places at high altitude. Even under ideal conditions the absorption of water vapour defines the IR bands. Other molecular species in the atmosphere such as: CO, CO<sub>2</sub>, CH<sub>4</sub>, are also important at various wavelengths.

When performing spectroscopy from the ground, the absorption spectrum of Earth's atmosphere contaminates the spectrum of the intended target. In high-resolution spectroscopy the stellar and atmospheric lines can be resolved allowing for the identification and separation of the spectra. The removal or correction for the telluric lines is very important for accurate science, especially for detecting exoplanet atmospheres in which the species trying to be detected also reside in our atmosphere (Snellen et al., 2010; Brogi et al., 2014; de Kok et al., 2013).

The absorption of atmosphere is highly variable on many different time scales. The change in water vapour can occur rapidly over the course of the night while the concentrations of atmospheric constituents vary seasonally and even longer<sup>2</sup>.

On top of this is the observational dependence on the airmass of the target. The airmass<sup>3</sup> is the relative path length through the atmosphere compared to zenith. The light of a target at a higher airmass passes through more of the atmosphere and is contaminated with deeper telluric lines.

Works such as Snellen et al. (2010), fit and remove the telluric variation during a series of continuous observations<sup>4</sup>, to accurately remove the varying telluric lines and detect the absorption lines of exoplanet atmospheres.



## 4.2 Telluric correction

Typically the absorption of the Earth's atmosphere (telluric lines) is corrected with the standard star method (e.g. Vacca et al., 2003). This method observed a “standard star”, a very hot (O or A-type), fast rotating star. These stars have minimal spectral features themselves so reveal the spectrum of the telluric lines. The telluric lines present in a spectrum of the science target can be corrected/removed by dividing it by the spectrum of the standard star.



The observation of the standard star needs to be observed close in the sky and time to the science observation to have a similar atmospheric absorption to the science target. For high-resolution spectroscopy this technique is not sufficient to correct telluric with residuals greater than 2% remaining.

Recently synthetic modelling of telluric absorption has gained popularity with several works focusing on correcting telluric absorption with synthetic models (e.g. Bailey et al., 2007; Cotton et al., 2014; Seifahrt et al., 2010) and achieving better correction than the standard star method. There are several different software packages available which usually build upon the standard line-by-line radiative transfer model code LBLRTM (Clough et al., 1995). Some examples are TelFit (Gullikson et al., 2014), and ESO's Molecfit (Smette et al., 2015) which both model and fit a synthetic absorption spectra to observations, whereas TAPAS (Bertaux et al., 2014) just creates synthetic models based on atmospheric data for an observation (without fitting). The synthetic models at high resolution are very sensitive to atmospheric constituents, especially water vapour, and observing conditions such as the airmass.

<sup>2</sup> For instance the increase in atmospheric CO<sub>2</sub> caused by anthropomorphic climate change has caused a 6% change to CO<sub>2</sub> line depths since 2000 (Smette et al., 2015).

<sup>3</sup> Airmass  $m = \sec \theta$  where  $\theta$  is the zenith angle.

<sup>4</sup> 51 spectrum of the same target in 180 minutes for Snellen et al. (2010)

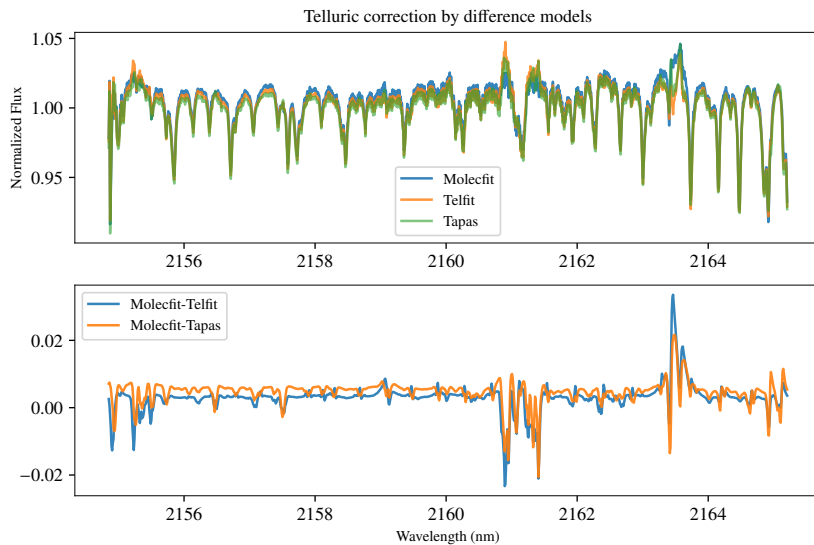


**Figure 4.2:** CRIRES spectra with telluric correction applied using the Molecfit, TelFit and TAPAS. Top: The telluric corrected spectra. Bottom: Difference between the corrected spectra from the different methods.

Recently Ulmer-Moll et al. (2018) compared the telluric correction efficiency between TelFit, Molecfit, TAPAS, and the standard star method. They found that Molecfit and Telfit synthetic corrections lead to smaller residuals for lines arising from H<sub>2</sub>O, while the standard star method corrects for O<sub>2</sub> lines best. All methods (synthetic and standard star) result in a scatter inside the telluric lines of 3–7%. They also find that an observatory tailored atmospheric profile leads to reduced scatter inside telluric lines and that the correction performed better with lower precipitable water vapour.

As an example Figure 4.2 shows the telluric correction using the three different methods, Molecfit, TelFit and TAPAS<sup>5</sup>, of a spectrum extracted for this work, detector #4 of observation HD 4747-1 (see Table 6.3). There are differences between the models of around 2% level, with the largest difference near the deep telluric line around 2163 nm.

Since sufficient telluric correction can be achieved through synthetic modelling, the observational requirement is halved as the standard star is not required, allowing more observing time for science. This is the case with the CRIRES observations analysed in this work. This work utilizes the synthetic telluric spectra produced from TAPAS to used correct the telluric lines in CRIRES spectra. This is detailed further below.



Fix title of  
plot Telluric  
correction by  
different mod-  
els

#### 4.2.1 TAPAS web service

Telluric absorption spectra can be obtained with the TAPAS (Transmissions of the Atmosphere for ASTRonomical data) web service<sup>6</sup> (Bertaux et al., 2014). TAPAS uses the standard line-by-line radiative transfer model code LBLRTM (Clough et al., 1995) along with the 2008 HITRAN spectroscopic database (Rothman et al., 2009) and ARLETTY atmospheric profiles derived using meteorological measurements from the ESPRI data centre<sup>7</sup> to create telluric line models.

<sup>5</sup> Performed here by Solène Ulmer-moll.

<sup>6</sup> <http://cds-espri.ipsl.fr/tapas>

<sup>7</sup> <https://cds-espri.ipsl.upmc.fr>

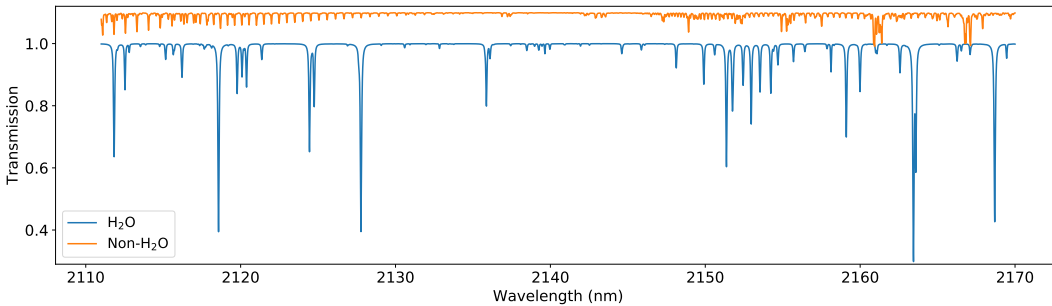


**Figure 4.3:** Telluric absorption spectrum for  $\text{H}_2\text{O}$  and the non- $\text{H}_2\text{O}$  species available from TAPAS. In the wavelength range 2110–2170 nm and both at a resolution of 50 000. A vertical offset of 0.1 has been added to the non- $\text{H}_2\text{O}$  spectrum.

The ARLETTY atmospheric profiles have a 6 hour resolution, so there may be a slight difference between the actual profile at the time of observation.

There are several parameters that can be submitted to the web service to define the requested telluric spectra, such as: target coordinates, date and time, location, spectral resolution, wavelength range and units choice observations, as well as the atmospheric profile and the choice of several atmospheric constituents to be included in the model spectra. TAPAS produces the telluric spectrum and sends a link to the results via email.

#### 4.2.2 Requests for this work

Synthetic telluric absorption were requested from the TAPAS web service for this work. These were to match the CRIRES observations which are presented in Table 6.3.

The mid-observation time for each observation was used to request a synthetic spectra individually for each observation, with the ARLETTY atmospheric profiles and vacuum wavelengths selected. The telluric models were retrieved without barycentric correction to keep the telluric lines at a radial velocity of zero with respect to the instrument. For each observation one model was requested with all available atmospheric species present, convolved to a resolution of  $R = 50\,000$ , and a further two models without the instrumental profile convolution applied. For these two extra models, one contained only the transmission spectra of  $\text{H}_2\text{O}$  while the other contained contributions from the all other constituents except  $\text{H}_2\text{O}$ . This was to explore a known issue with the depth of  $\text{H}_2\text{O}$  absorption lines in the TAPAS models (Bertaux et al., 2014) (see Section 5.2.2). An example of the telluric spectrum for the  $\text{H}_2\text{O}$  and the non- $\text{H}_2\text{O}$  species is given in Figure 4.3. To obtain a combined model of all species these two can be multiplied together.

#### 4.2.3 Issues with TAPAS

There are a number of issues encountered when using the TAPAS web service, mainly due to interaction with the website. Often their service was down for weeks at a time without any warning or notification. With this, time was wasted filling out and submitting a requests via the the web form without a response, or a returned spectra. There was also a variable level of success between different web browsers. A number of bug reports were submitted to the owners of the webpage without any acknowledgement.

The webpage is useful for quickly obtaining a small number of spectra but can be tedious for many spectra. For this work this was around upwards of 50 telluric spectra, (3 for each of the 17 observations). TAPAS offers the ability to request multiple spectra at a time but this was found to be unreliable when attempting to request more than four spectra in a single request.

A script<sup>8</sup> was created to automatically generate the data necessary to fill out a TAPAS request for each CRIRES observations. The script scanned the CRIRES header for information such as the mid-time of observations, target coordinates, slit width etc. and populated the XML request form provided by TAPAS. The script output is copied and pasted into the web browser for submission.

Trial and error was needed to understand all the XML form entries, such as the molecules requested and the atmospheric model to use (ARLETTY) to achieve a valid TAPAS request. The main issue was with the TAPAS ID number. Each TAPAS request has an ID number (which is provided with the email response). This ID number needs to be correctly set in the XML form before submission. This number is incremented by 1 with each submission **but its initial value is unknown unless you made the very last request.** If a submission is made via the XML request with the incorrect ID number a response will be returned with the correct ID number, but the failed request will be returned. This can then be used to increment the ID number by 1 and hopefully make a valid request. Unfortunately, if another user makes a TAPAS request between submissions the ID number will again be invalid. It is unknown if multiple transmission spectra could have been requested at the same time with the XML form.

There is another issue with a one hour time offset between the requested and the time returned by TAPAS. For instance if the requested time was for an observation at 0200h UTC then the transmission spectrum returned by TAPAS is for 0100h UTC. This changes the position of the target, the airmass and potentially the ARLETTY model used (6 hour time steps), affecting the strength of the telluric lines. It is tedious to remember to offset your input time by one hour to obtain the correct time, and slightly more work when you also have to adjust the date when going backwards past 0000h. When submitting the XML script the time that is returned is the time requested. Attempts were made to bring this issue to the attention of the TAPAS team in 2016 but as of August 2018 this issue is still present.

These issues need to be considered when requesting TAPAS spectra, adding unnecessary difficulty to the relatively simple process.

#### 4.2.4 Telluric masking

The telluric spectra from TAPAS can not only be used for correcting individual spectra but are also easily used to create a wavelength mask telluric lines. For instance Figueira et al. (2016) and Artigau et al. (2018) use TAPAS spectra to mask out atmospheric lines deeper than 2% for computing the photon noise limited radial velocity precision. A telluric wavelength mask is similarly used in Chapter 8 when extending the analysis of Figueira et al. (2016). The telluric model used for this is an average of 52 TAPAS spectra (one per week in 2014), simulated at La Silla Observatory at an airmass of 1.2 ( $z = 33.5^\circ$ ). This is to incorporate long-term variations of absorption over the year. Masking is applied by defining a cut-off line depth, typically 2%, at which to mask out any deeper lines.

---

<sup>8</sup> Available at <https://github.com/jason-neal/equanimous-octo-tribble/blob/master/octotribble/Tapas/>

## 4.3 Synthetic Stellar models of cool stars

Modelling of stellar structure, atmospheres and evolution is used to try and understand the observations, pieced together with several physical, chemical and hydrodynamical models. One output from these models is synthetic stellar spectra. These spectra can be compared to observed spectra to attempt to classify and understand the stellar populations. There is an ever evolving effort to improve these stellar models and synthetic spectra to better match the observations; incorporating more physics, chemical reactions and line lists, and using the latest element abundances. In this work extensive use of the PHOENIX-ACES models is made with some experimentation with the BT-Settl models. A collection of several theoretical stellar spectral libraries can be found at the Spanish Virtual Observatory Theoretical Spectra Web Server.

The Kurucz (1979) models are popular synthetic models for stars ranging between G-O type with effective temperatures between 5500–50 000 K. For cooler stars, M-dwarfs and even Brown Dwarfs the stellar models are based on the PHOENIX code (e.g. Hauschildt et al., 1997). Initially created for studying the ejecta of Novae it was *Extended* to low mass stars and Brown Dwarfs (Allard et al., 1995). The PHOENIX modelling code has evolved over time incorporating new physical models to better explain the atmospheres. The *NextGen* models (Hauschildt et al., 1999) treated the stellar atmosphere as a gas in chemical equilibrium, but the resulting spectra for very low mass stars was poor due to no treatment of dust in the stellar atmospheres.

The Allard et al. (2001) *COND* and *DUSTY* models both investigate the extreme limits of clouds in the atmospheres of cool stars. They include condensation physics (Gibbs free energy, gas partial pressures etc.) into the chemical equilibrium model, as well as the optical interaction of light with the dust/condensates (dust opacities and scattering). The *DUSTY* models simulate ‘inefficient/no settling’ where condensation/dust forms and stays in the atmosphere and it affects the spectrum through the dust opacities. At the other extreme the *COND* models ignore the dust opacities and simulate ‘efficient settling’, in which all the condensates and dust clouds fall below the spectrum forming region.

The treatment of clouds and dust is important for the modelling of low mass stars and Brown Dwarfs. The *DUSTY/COND* models are similar above 2600 K but below this temperature they diverge due to the crystallization of silicates in the atmosphere (Allard et al., 2001). These are only a few of the physical considerations implemented in the synthetic models. The other notable changes in the name convention for the synthetic spectra are due to use of specific line lists. The models beginning with AMES use the NASA-AMES H<sub>2</sub>O and TiO line lists, while the BT models use the Barber et al. (2006) H<sub>2</sub>O line list. Between models the use of improved solar abundance measurements is also included (Asplund et al., 2009).

In this work synthetic spectral from the PHOENIX-ACES and to a lesser extent the BT-Settl stellar models are used. These are further evolutions of the *DUSTY/COND* models and are detailed below.

Both sets of synthetic models do not handle the affects of radiation from a neighbouring star, which may have an affect on the BD companions studied here.

### 4.3.1 PHOENIX-ACES models

The PHOENIX-ACES models (Husser et al., 2013) are a descendant of the *COND* models. They include condensation in equilibrium with the gas phase while ignoring dust opacity and any mixing or settling which is important for cooler atmospheres. As such the PHOENIX-ACES models are restricted to

**Table 4.2:** Full parameter space of the PHOENIX-ACES spectral grid. Reproduced from Husser et al. (2013).

	Range	Step size
$T_{\text{eff}}$ [K]	2 300 – 7 000	100
	7 000 – 12 000	200
logg	0.0 – 6.0	0.5
[Fe/H]	-4.0 – -2.0	1.0
	-2.0 – +1.0	0.5
[ $\alpha$ /Fe]	-0.2 – +1.2	0.2

$T_{\text{eff}} > 2300 \text{ K}$  as the treatment of dust/clouds is not handled. It uses the most recent version (16) of the PHOENIX code and is suitable for the spectra of cool stars. THE PHOENIX-ACES models uses the Astrophysical Chemical Equilibrium Solver (ACES, Barman 2012) new in version 16 of PHOENIX to perform state-of-the-art treatment of the chemical equilibrium. It also adds parametrisations for the mass and mixing-length, and uses the solar abundances of Asplund et al. (2009).

As noted in (Husser et al., 2013) there are significant differences between the spectra from PHOENIX-ACES and previous PHOENIX model spectra. For instance the equation of state solver ACES strongly affects the stellar structure and different line and molecular band strengths. Unfortunately there are several changes introduced with PHOENIX-ACES making it difficult to distinguish and quantify the different effects.

The full parameter grid space of the pre-computed PHOENIX-ACES spectra is given in Table 4.2 although this full range is not utilized in this work. This work uses models below  $> 7000 \text{ K}$  with no  $\alpha$  variation<sup>9</sup>. The spectral sampling of the grid are  $R \approx 50 000$  for 300–2500 nm, covering the wavelengths used here.

The lower temperature limits of this library limits the stellar mass to the high mass BDs. For example a  $T_{\text{eff}} = 2300 \text{ K}$  corresponds to a BD with  $M \sim 84 M_{\text{Jup}}$  at 5 Gyr from the Baraffe et al. (2003) evolutionary models, (see Section 4.4).

While using the PHOENIX-ACES models a discontinuity in the stellar flux is observed between 5000 K and 5100 K. In Figure 4.4 several PHOENIX-ACES spectra in incremental steps are shown in a small wavelength range of 2113–2115 nm. The line profile seems to change suddenly between the model with 5000 K and 5100 K, causing a slight discontinuity in the models. This slightly impacts the use of these models while attempting  $\chi^2$  fitting in Chapter 7. The bottom panel shows the flux difference between models separated in temperatures of 100 K (one grid step). The difference between 5000 and 5100 K (green) is offset from the other model differences. This is potentially caused by the change in treatment of the model atmospheres at 5000 K. For instance Husser et al. (2013) mention that the reference wavelength defining the mean optical depth grid, is fixed to  $\lambda_{\tau} = 1200 \text{ nm}$  for  $T_{\text{eff}} > 5000 \text{ K}$  and  $\lambda_{\tau} = 500 \text{ nm}$  for hotter stars in the PHOENIX-ACES modelling.

### 4.3.2 BT-Settl

The BT-Settl models (Allard et al., 2012a; Allard et al., 2012b; Rajpurohit et al., 2013; Baraffe et al., 2015), are an evolution of both the *DUSTY* and *COND* models. They are better suited for the entire

<sup>9</sup>  $\alpha$  elements are created during nuclear fusion by the successive addition of helium nuclei (alpha particles), thus have atomic numbers with an integer multiple of 4.

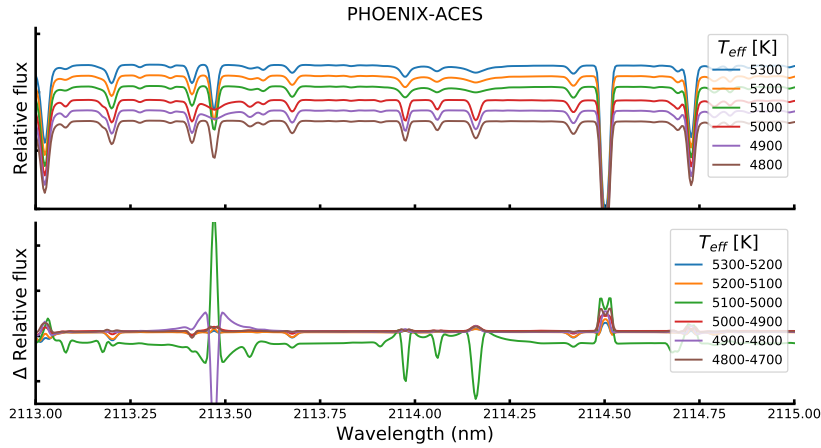


**Figure 4.4:** Top: Incremental PHOENIX-ACES model spectra between 4800–5300 K with  $\log g=4.5$  and  $[\text{Fe}/\text{H}]=0.0$  fixed. Bottom: Difference in flux between successive models separated by 100 K. Apart from near absorption lines there is a discontinuity in the flux of the PHOENIX-ACES models between 5000 and 5100 K.

**Table 4.3:** Full parameter space of the BT-Settl (CIFIST2011\_2015) spectral grid (Baraffe et al., 2015).

	Range	Step size
$T_{\text{eff}}$ [K]	1 200 – 7 000	100
$\log g$	2.5 – 5.5	0.5
$[\text{Fe}/\text{H}]$	0 – 0	-
$[\alpha/\text{Fe}]$	0 – 0	-

range of BD temperatures down to 400 K, through hydrodynamical modelling of the mixing and settling of dust/clouds in the atmosphere of cool dwarfs (Freytag et al., 2010). The BT-Settl models now also include 3-D radiation transfer (Seelmann et al., 2010).

The BT-Settl are generally more difficult to work with due to their file format (in comparison to PHOENIX-ACES). The most recent BT-Settl spectral library, using version 15.5 of the PHOENIX code, is designated CIFIST2011\_2015<sup>10</sup> (Baraffe et al., 2015) and includes newer Caffau et al. (2011) solar abundances and is combined with evolutionary modelling. It is available in a fits format which is easier to use. The parameter range available from the pre-computed library is given in Table 4.3.

In this work the BT-Settl models used did not go below the PHOENIX-ACES limit of 2300 K, used as a comparisons. Above this temperature there are some difference observed in the line strengths between the two models but their spectra are similar in the nIR (see Section 4.3.4).

### 4.3.3 Model access

The pre-computed synthetic spectral libraries for the PHOENIX-ACES models (Table 4.2) are easily obtainable from <http://phoenix.astro.physik.uni-goettingen.de/> while pre-computed models for the BT-Settl (Table 4.3) and other PHOENIX spectra can be found at <https://phoenix.ens-lyon.fr/Grids/>. A simulator is also available to generate BT-Settl spectra or other PHOENIX spectra from Allard France at [phoenix.ens-lyon.fr](https://phoenix.ens-lyon.fr), for specific parameters or abundances.

<sup>10</sup> [https://phoenix.ens-lyon.fr/Grids/{BT-Settl}/CIFIST2011\\_2015/](https://phoenix.ens-lyon.fr/Grids/{BT-Settl}/CIFIST2011_2015/)

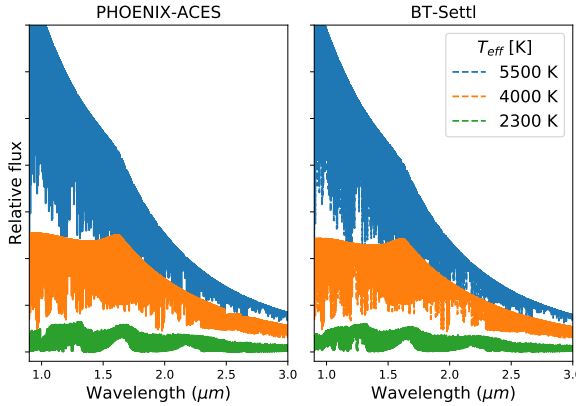


**Figure 4.5:** PHOENIX-ACES (left) and BT-Settl (right) spectra in the nIR wavelength region for three different temperature stars,  $\log g=4.5$ ,  $[Fe/H]=0$ .

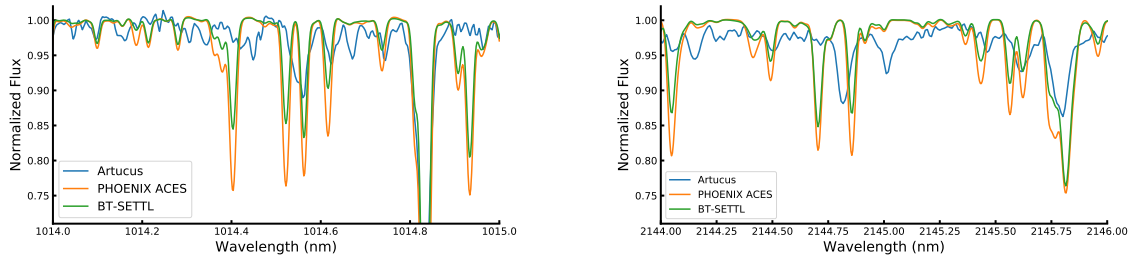


**Figure 4.6:** Spectrum of Arcturus compared to synthetic spectra with the closest spectral parameters at wavelengths around 1014 nm (left) and 2145 nm (right).

The spectral model libraries were downloaded using the above links and accessed using the “grid tools” interface provided in the *Starfish*<sup>11</sup> Python package (Czekala et al., 2015). The “grid tools” enables the fast, efficient, and simple loading of stellar spectra for use in the simulation performed in this work. For instance a spectra from a given model can be loaded simply using the four values of identifying parameter values [ $T_{\text{eff}}$ ,  $\log g$ ,  $[Fe/H]$ ,  $[\alpha/Fe]$ ]<sup>12</sup>.

#### 4.3.4 Comparing models

Here a comparison between the PHOENIX-ACES and BT-Settl spectra is briefly given. Figure 4.5 shows the model spectral flux in the nIR range of  $0.9\text{--}3\,\mu\text{m}$  for three different stellar temperatures: 5500, 4000, and 2300 K. At this large scale the spectra look fairly similar.

On closer inspection though, the spectra are slightly different with the PHOENIX-ACES spectra having deeper absorption lines compared to the BT-Settl models; however they do appear to have most of the same absorption lines. This can be seen in Figure 4.6 which contains the PHOENIX-ACES and BT-Settl at two different regions in the nIR, 1013 nm and 2110 nm. Temperature of both models is 4300 K while the  $\log g$  is 1.5 for PHOENIX-ACES and 2.5 for BT-Settl (closest available) and the models are

<sup>11</sup> <https://github.com/iancze/Starfish>

<sup>12</sup>  $[Fe/H]$  and  $[\alpha/Fe]$  are abundances of Fe and  $\alpha$  elements relative to those in the Sun. The definition of the scale is  $[X/H] = \log_{10} \left( \frac{n_X}{n_H} \right)_* - \log_{10} \left( \frac{n_X}{n_H} \right)_\odot$ , where  $n_X$  is the number of atoms of element X and  $n_H$  is the number of atoms of Hydrogen.

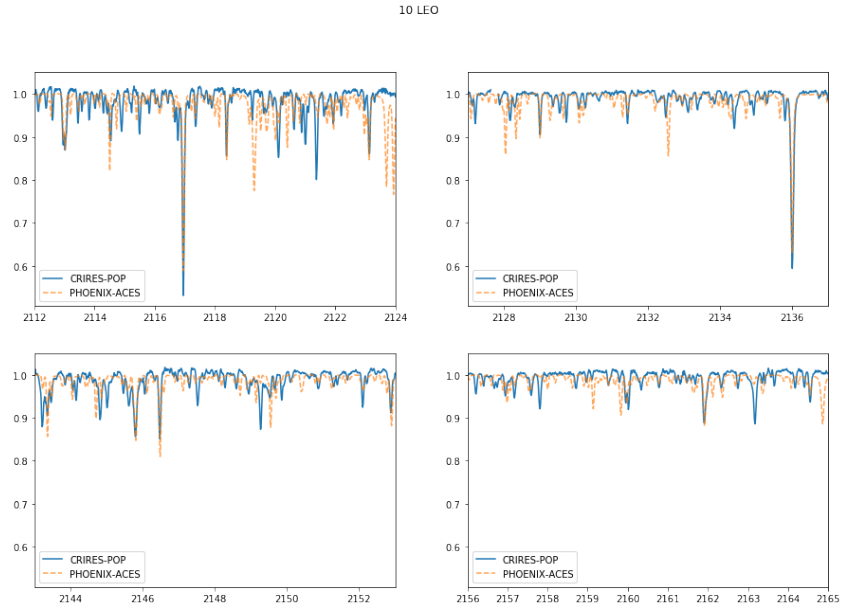


**Figure 4.7:** CRIRES-POP spectra of 10 Leo compared for PHOENIX-ACES model for the wavelength range setting used in Chapters 6 and 7.

convolved to  $R=100,000$ . This is in an attempt to match the parameters to the observations of Arcturus at  $R=100\,000$  shown blue. Cross-correlation and a Doppler shift has been used to align the model spectra to the observations. There is a striking difference between the models and observations with several lines present in the models that are not seen in the real observation, while a few lines observed that are not seen in the models. When the observed absorption lines do align with the models there is a difference in the depth of the lines. These differences are shown at two different wavelengths and reveal that there is still room for improvement in the synthetic models to match observed spectra in the nIR and at high resolution. Spectral dependencies in the BT-Settl models are noted by Rajpurohit et al. (2013).

A further example of this is shown in Figure 7.4 in which the fitted model, dominated by a single PHOENIX-ACES model, is compared to the observed CRIRES spectra. This caused issues with the fitting procedure in Chapter 7. Figure 4.7 is a further example of the spectral differences at the nIR wavelengths specifically used in this work, in a spectra from (in reduced form) the CRIRES-POP library (Lebzelter et al., 2012; Nicholls et al., 2017). It shows differences between the CRIRES-POP  $K$ -band spectra of 10 Leo and the PHOENIX-ACES spectrum with corresponding parameters ( $T_{\text{eff}}=4800$ ,  $\log g=3.00$ ,  $[\text{Fe}/\text{H}]=0.0$ ).



Figure 4.7  
needs improved  
style

## 4.4 Evolutionary models

Modelling of the evolution of a star, from birth thorough its journey on the main sequence until its death as it slowly cools as a dwarf or explodes as a super-novae, is important for understanding how the observable properties (temperature/photometric colours) change over time. The main factor for the fate and evolution rate is a stars mass, with large stars evolving quickly and dying explosive deaths while low mass stars sustain fusion for several orders of magnitudes longer. Brown Dwarfs do not have enough

**Table 4.4:** Estimated companion/host flux ratios given the companion mass ( $M_2$  or  $M_2 \sin i$ ) from Table 6.2.

Companion	Host $m_K$	Host $\pi$ mas	Companion $M_K$	Estimated $F_2/F_1$ $K$ -band	Estimated $N_2/N_1$ (noise ratio)
HD 4747	5.305	53.184	3.82	$7 \times 10^{-5}$	76
HD 162020	6.539	32.410	4.10	$2 \times 10^{-8}$	1 615
HD 167665	5.038	32.014	2.60	$6 \times 10^{-5}$	105
HD 168443b	5.211	25.208	2.35	$1 \times 10^{-16}$	$1 \times 10^8$
HD 168443c	5.211	25.208	2.35	$1 \times 10^{-11}$	$4 \times 10^5$
HD 202206B	6.485 <sup>a</sup>	21.726	3.04	$21.63$	$4 \times 10^{-8}$
HD 202206c	6.485 <sup>a</sup>	21.726	3.04	$45.63$	$9 \times 10^{-18}$
HD 211847B	7.018	20.489	3.50	8.40	0.011
HD 30501	5.525	49.081	3.96	10.38	0.003
					27

<sup>a</sup> Magnitude from 2MASS catalogue instead of SIMBAD.

mass to achieve stable hydrogen fusion and slowly cool down over their lifetime.

This work uses stellar evolutionary models of Baraffe et al. (2003) and Baraffe et al. (2015) to estimate the properties of the giant planets, brown dwarfs and low-mass stars given the mass and age. The models range in mass between  $0.0005\text{--}1.4 M_\odot$  and ages  $0.001\text{--}10.0$  Gyr of which span temperatures  $sim100\text{--}6000$  K. Stellar or BD properties such as  $T_{\text{eff}}$ ,  $\log g$ , radius, and absolute magnitudes in different photometric bands can be determined from the tables given by the evolution models.

#### 4.4.1 Estimating Companion-host Flux ratio

In order to visually or spectroscopically detect binary or planetary companions it is helpful to calculate the flux/contrast ratio between the host and companion.

The companion-host flux or contrast ratio of the system can be estimated using:

$$\frac{F_2}{F_1} \approx 2.512^{m_1 - m_2}, \quad (4.1)$$

where  $m_1$  and  $m_2$  are the magnitude of the host and companion respectively.

The photometric apparent magnitudes for the host stars,  $m_1$ , in several wavelength bands are easily obtained through online catalogues such as SIMBAD (Wenger et al., 2000) or 2MASS (Skrutskie et al., 2006). However, the magnitudes of the companions,  $m_2$ , are not readily available as they have not been directly measured. The stellar evolution models of Baraffe et al. (2003) and Baraffe et al. (2015) are used to estimate the magnitude of the companion. A given companion mass, and a stellar age will uniquely identify a point in the Baraffe models which corresponds to a specific magnitude for the companion. The evolution tables are also interpolated to reach companion masses and stellar ages between the models provided.

In Table 4.4 the host-companion flux ratio estimates for the targets analysed in this work are presented. The K-band flux ratios are calculated to match the observed CRIRES spectra at  $2.1\mu\text{m}$ . The stellar ages used for the each system are given in Table 6.1 while the companion masses are given from Table 6.2. The age and companion mass are both used to obtain the absolute magnitude for the companions. For the companions in which only the minimum mass ( $M_2 \sin i$ ) is known then the flux-ratio given will be the lower limit, or worst case scenario.

The magnitudes provided by SIMBAD are given in apparent magnitude,  $m$ , while the magnitudes in the evolutionary models are absolute magnitudes  $M$ . That is, the apparent magnitude that the star would have if it was observed at a distance of 10 parsecs (32.6 light-years). The apparent magnitudes of the hosts are converted to absolute magnitudes using  $M = m - \mu$  where  $\mu$  is the distance modulus:

$$\mu = 5 \log_{10}(d_{pc}) - 5. \quad (4.2)$$

Here  $d_{pc}$  is the distance to the object in parsec. The distance is obtained from the trigonometric parallax  $\pi$  using the formula  $d(pc) = 1/\pi(arcsec)$ , with the parallax in arcseconds<sup>13</sup>. In this work the recent high-precision parallax measurements from GAIA (Collaboration et al., 2018) are used.

From the flux ratio the noise ratio between the host and companion can also be calculated in a similar way using the equation  $N_2/N_1 = \sqrt{2} \times \sqrt{F_1/F_2}$ .



#### 4.4.2 Baraffe tables

A simple tool<sup>14</sup> was created to calculate/estimate the host-companion flux ratio using the Baraffe et al. (2003) and Baraffe et al. (2015) evolution tables. Given the name of the target star, the mass of a companion and the stellar/system age the tool determines the flux ratios in the available spectral bands. The tool uses the targets name and the *astroquery* package to obtain the stellar properties from SIMBAD, specifically the flux magnitudes and parallax. It then interpolates the Baraffe tables to the desired companion mass and age, calculating and returning values for all parameters of the companion given in the tables (e.g.  $T_{\text{eff}}$ ,  $\log g$ ,  $R/R_{\odot}$ ). The stellar magnitudes are converted to absolute values using Equation 4.2 and the flux ratios computed using Equation 4.1.

An extension of this tool is that can be used to perform the reverse calculation also. That is, given the target name, age and flux ratio in a given band it can estimate the mass of the companion mass using the evolution tables.

<sup>13</sup> Most parallax values e.g. GAIA are tabulated in milliarcseconds (mas). Therefore it is important to remember to convert the parallax to arcseconds first, to avoid embarrassing calculation errors!

<sup>14</sup> Available at [https://github.com/jason-neal/baraffe\\_tables](https://github.com/jason-neal/baraffe_tables)

# Chapter 5

## Spectroscopic reduction

The work of this thesis relies on the use of nIR spectra obtained by the CRIRES instrument. Specifically 17 observations around 2110–2160 nm which are detailed in Table 6.3. This chapter contains an overview of the steps undertaken to extract astronomical spectra, focusing on the CRIRES instrument specifically. A comparison between two different reduction pipelines for CRIRES is performed with the chosen pipeline used. Details of the issues encountered with the reduction output are presented. This chapter also includes the post reduction steps performed, specifically wavelength calibration and telluric correction. The reduced spectra produced in this chapter will be analysed in Chapter 6 and Chapter 7.

### 5.0.1 nIR reduction concepts

In reducing nIR spectra, or any spectra in general a number of calibration steps that are performed to achieve the best possible output such as removing signals arising from the detector. The main calibration steps required for nIR spectra are given below with examples from CRIRES. More information about the different effects with regards to CRIRES can be found in the CRIRES user manual and reduction cookbook.



**Figure 5.1:** Master dark frames for exposure times of 3 and 180 seconds. Each master is created by averaging 3 images in which the detector received no incident light. Both frames are on the same scale and show dark current grows with exposure time. The colour has been inverted so that black is the recorded measurement.

### 5.0.1.1 Dark Current

The dark current is a form of instrumental noise, in which the detector measures photons while not being illuminated. It is the detection of thermal electrons moving inside the detector, creating spurious photon counts. Calibration and removal of the dark current is performed by taking exposures in which the detector is not illuminated. The detectors in the CRIRES instrument are cryogenically cooled to a temperature of  $\sim 27\text{ K}$  (within  $0.1\text{ K}$ ) to significantly reduce the dark current, and to maintain consistency. The electrical components of the CRIRES detectors create thermal energy while operational which impacts the dark current. A strong “glow” is observed in the bottom corners of the CRIRES detector in Figure 5.1 due to nearby amplifiers. As per the CRIRES calibration plan, “dark frames” need to be taken for each exposure time used. Figure 5.1 shows the master dark frame created from averaging three dark frames for exposure times of 3 seconds (for the flats) and 180 seconds (for the science), both on the same amplitude scale. For the CRIRES detectors the dark current per pixel is around  $0.2\text{--}0.4\text{ }(\text{e}^{-}\text{s}^{-1})$ , while the glow at the two corners of the 180 second exposure shown here is  $\sim 9000/180 \approx 50\text{ }e^{-\text{s}^{-1}}$ .

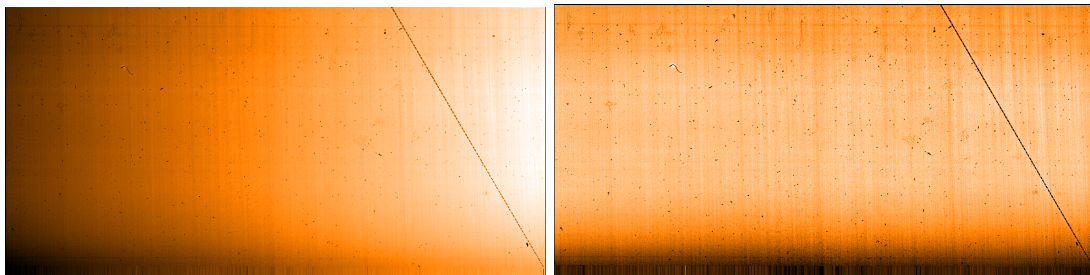


**Figure 5.2:** A flat-field image for detector #2 before (left) and after (right) the non-linearity corrections are performed.

### 5.0.1.2 Flat-field



No detector is truly perfect, with all pixels performing equally well. To correct for pixel-to-pixel variations in photon sensitivity across the detector and for any distortions in the optical path, a flat-field correction is needed. Exposures of a uniform<sup>1</sup> light source are taken, allowing the individual pixel-to-pixel sensitivity to be measured and corrected. The flat-field frames are corrected for dark current by subtraction of the master dark frame with the appropriate exposure time.

The CRIRES detector suffers from non-linearities in sensitivity across the detector. This can be seen in the flat-field image on the left of Figure 5.2 where there is an intensity gradient from dark to light across the detector. A set of coefficients for each pixel is provided by ESO<sup>2</sup> to apply the correction for the non-linearity of the detectors. This also corrects for a slight difference in sensitivity between the pixels from the odd and even columns in the CRIRES detectors, commonly called the “odd-even effect”. The frame on the right of Figure 5.2 has been corrected for the non-linearities.



The flat-field can also reveal defects in the detector e.g. dead pixels, dust and scratches: a large scratch is clearly visible in Figure 5.2.

<sup>1</sup> Ideally uniform intensity and spectral distribution

<sup>2</sup> Available at <https://www.eso.org/sci/facilities/paranal/instruments/cires/tools.html>

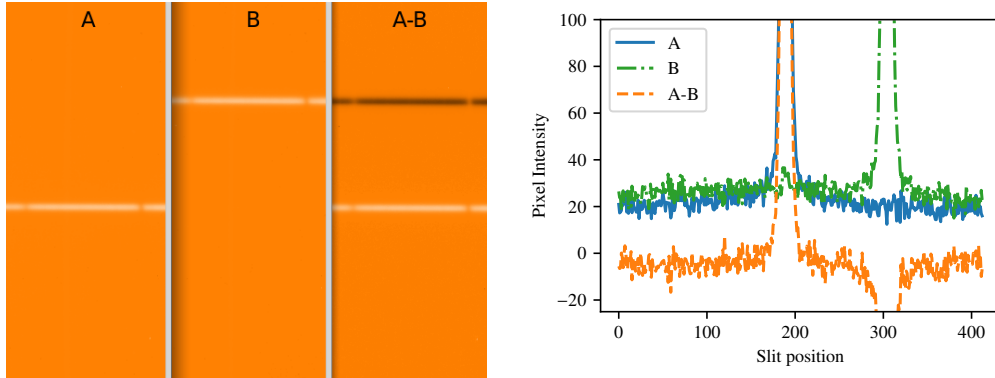


**Figure 5.3:** Illustration of the nodding technique. Left: Sample slice of successive images at nod positions A and B, and their difference A minus B for detector #1. Right: A vertical slice along the slit at column 512 (middle of detector). The background level observed in A and B is effectively removed by the subtraction.

#### 5.0.1.3 Nodding and Jitter



The technique of *nodding* is used to remove sky emission, detector dark current, and glow. First, an observation is divided into multiple separate exposures. Between each exposure the telescope is moved to change the vertical position of the target in the slit. The light from the star travels through a slightly different optical path and is recorded on a different part of the detector. The frames from the two nod positions (A, B) are then subtracted ( $A - B$ ) to remove the background measurement from each spectra.

A visual example of the nodding is shown in Figure 5.3. On the left are slices of 150 pixel columns from successive nod positions A and B as well as the difference A minus B. On the right is a single pixel column from each image on the left. The background signal at the level of 20–30 counts in the image is almost cancelled out by the opposite nod. This efficiently removes the background signal/noise from the observed spectra target.

Observations of faint targets, that need long exposure times to achieve a sufficient SNR, are also broken up into multiple images so that the instrument glow from Figure 5.1 does not saturate the detector. A small random vertical offset is applied to each observation which ensures that all spectra at the same nod position do not consistently land on the same pixels each time. This is known as the *jitter* and allows for the correction of bad pixels and decreases the effect from any systematics of the detector. As an example, the CRIRES observations analysed for the work performed in Chapters 6 and 7 were performed with an ABBAABBA nod cycle pattern (including jitter) with an exposure time of 180 s each, totalling 24 minutes when combined.

#### 5.0.2 Th-Ar lamp calibration

As part of the CRIRES calibration procedure, spectra are taken of Th-Ar lamps. The Th-Ar spectra are placed into the instrument using 6 optical fibres, creating six uniformly spaced spectra across the detector. Figure 5.4 contains the Th-Ar spectra for all four detectors. There are  $\sim 50$  Th-Ar lines that fall across the four detectors for the wavelength setting here, although most of them are faint.

The purpose of the Th-Ar fibres is to perform cross-correlation against a Th-Ar template to obtain a wavelength solution for each detector. Optical defects (e.g. scratches on the detector) interfere with the

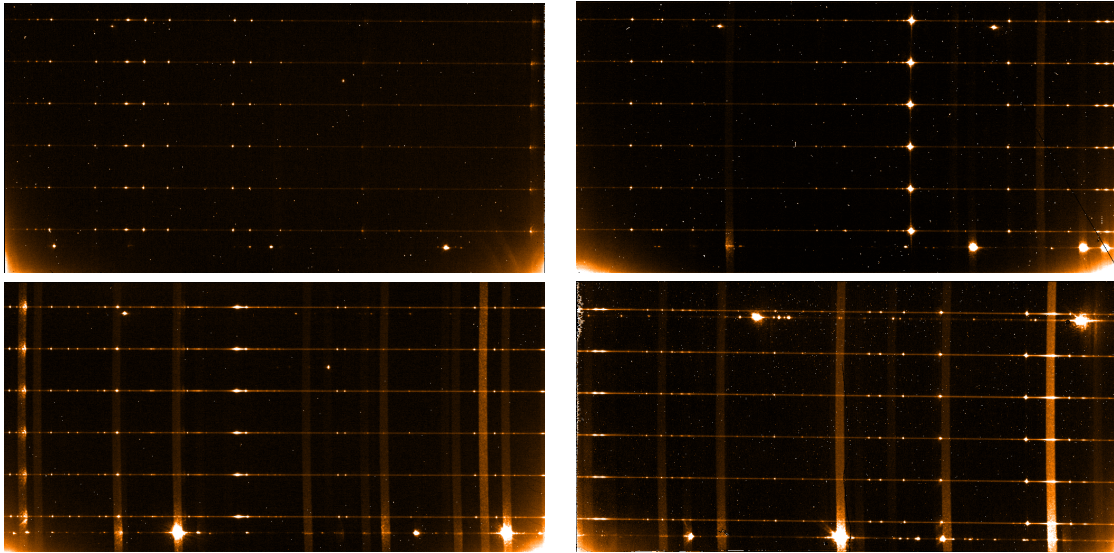


**Figure 5.4:** Example Th-Ar calibration lamp frames for each detector. These are the raw frames in which dark current correction has not been performed (i.e the dark current is still visible on the bottom corners).

performance of the correlation between Th-Ar lines and the spectral template in ESO pipeline. This can be resolved by first applying a pixel mask (although we did not attempt it). At the top and bottom there are also two meteorological fibres that can not be used for wavelength calibration as they pass through a different optical pathway. The brightest one at the bottom has strong features that seem to overwhelm or washout many columns in detector #2–4 (vertical stripes). This information is included here for completeness, as the Th-Ar were not used in the chosen data reduction method, see Section 5.2.1.



### 5.0.3 Extraction

The process of extraction is, in brief, turning the two-dimensional image of the spectrum into a one-dimensional representation. This is done by summing the photon counts along the spatial direction, for each column in the dispersion direction in a small window around the spectrum. To do this one needs to identify the position of the spectrum across the detector, referred to as order tracing. In our case there is only one spectral order present but **in a cross-dispersed configuration there can and will be many orders.** A rectangular box, with a specified aperture width, is centred along the traced spectrum.

There are two types of extraction commonly used. The *rectangular* extraction performs a simple aperture sum in the spatial direction, counting all photon counts that fall within the aperture. An *optimal* extraction (Horne, 1986) also includes variance weighting to reduce the impact of the noise and deviant pixels on the spectral extraction. A spatial profile is fitted to the spectra and the pixels weighted such that those furthest away from the centre have less impact on the sum. Optimal extraction can increase the effective exposure time by up to 1.69 times at  $3\sigma$  (Horne, 1986). Both rectangular and optimal extraction methods are available from both the ESO CRIRES and DRACS pipeline, compared below.



## 5.1 Pipeline Comparison

To transform the observed 2-D image from the telescope into an extracted 1-D spectrum of the target a number of steps (some outlined above in Section 5.0.1) have to be performed in sequence. The series of steps, performed by various software tools, is referred to as a *pipeline*. Each stage in the pipeline performs a specific task, for example creating the master dark frame, or performing the nod subtraction. The result of one stage is passed to the next (either automatically or manually). Two different pipelines were available to reduce the CRIRES observations used in this work. The first is the standard CRIRES pipeline<sup>3</sup>, available from ESO. The second is an in-house pipeline previously used in Figueira et al. (2010) called DRACS (Data Reduction Algorithm for CRIRES Spectra). In these next sections the experience gained using both pipelines, comparing the extracted spectra and user experience is documented.

Pedro it is my understanding that the ESO pipeline did not exist/was not publicly available when you created DRACS, correct?



### 5.1.1 ESO CRIRES pipeline

The ESO CRIRES pipeline was used to reduce CRIRES nodding spectra following direction from the CRIRES pipeline user manual<sup>4</sup> and the CRIRES reduction cookbook<sup>5</sup>.

The GASGANO<sup>6</sup> graphical user interface (GUI) was used to interact with the pipeline with guidance from the GASGANO manual<sup>7</sup>. This pipeline provides a number of *recipes* which perform the required extraction steps. From the GUI each recipe is manually selected, then the correct calibration and observation files need to be selected to use with each recipe. The final output from the ESO pipeline is a table in a fits format with the combined extracted spectra (both *rectangular* and *optimal* extractions), pixel errors and a wavelength solution.

For a novice of spectral extraction this pipeline and the available documentation was very helpful to get started and perform the extraction. However, to reduce many spectra it soon became a long tedious process.

Constant revision of the documentation was necessary to ensure all the correct image and calibration files were added to each recipe. The ESO pipeline makes all the recipe parameters easily accessible to modify via a window of the recipe interface, but the recipe parameter defaults get restored for each observation, making it difficult to reduce all of the observations in a consistent manner. Having the parameters adjustment on the recipe interface is great for adjusting the parameters and for identifying which parameters are relevant to each recipe. Unfortunately, when trying to experiment with the recipe parameters to achieve a high quality spectral extraction it was repetitive to change the same parameters for each observation, and it was also difficult to keep track of all the changes while assessing their effect on the final output.

The parameters for the wavelength calibration were the most tedious. To try and improve the wavelength calibration, the y-positions of the 6 Th-Ar fibres were manually found from the images for each detector and every observation and then entered as input parameters for the calibration recipe. This helped the wavelength calibration recipe to correctly identify/fit more of the Th-Ar spectra in most cases, but this took time. Because of this, it was chosen to use the other pipeline and these calibration were not used.

<sup>3</sup> <https://www.eso.org/sci/software/pipelines/>

<sup>4</sup> <ftp://ftp.eso.org/pub/dfs/pipelines/cires/crire-pipeline-manual-1.13.pdf>

<sup>5</sup> [https://www.eso.org/sci/facilities/paranal/instruments/cires/doc/VLT-MAN-ESO-14200-4032\\_v91.pdf](https://www.eso.org/sci/facilities/paranal/instruments/cires/doc/VLT-MAN-ESO-14200-4032_v91.pdf)

<sup>6</sup> <https://www.eso.org/sci/software/gasgano.html>

<sup>7</sup> <https://www.eso.org/sci/software/gasgano/VLT-PRO-ESO-19000-1932-V4.pdf>

ESO has a new reduction “workflow” called ESO Reflex (Freudling et al., 2013)<sup>8</sup>. This enables automated reduction with the ability to chain together the extraction recipes in the specific order desired, repeat steps to optimize the reduction, and automatically handle the data organization (no need to manually select the files for each recipe). This would likely have enabled a quicker and more consistent reduction of the spectra. Unfortunately, it is not available for the CRIRES pipeline.



### 5.1.2 DRACS

DRACS (Data Reduction Algorithm for CRIRES Spectra) is a custom reduction pipeline (Figueira et al., 2010) written in IRAF’s CL<sup>9</sup> (Tody, 1993). It provides for automated dark and nonlinearity corrections (using the nonlinearity coefficients provided by ESO), as well as the flagging and replacement of bad pixels. Sensitivity variations are corrected by dividing by a flat-field which was corrected from the blaze function effect. The nodding pairs are mutually subtracted and the order tracing is accomplished by fitting cubic splines. Order tracing allows the extraction algorithm to follow the shape for the dispersion across the detector<sup>10</sup>. By default the pipeline returns the *optimal* extraction (Horne, 1986), but the *rectangular* extraction can also be obtained. The extracted spectra from each nod is continuum normalized by dividing by a polynomial fitted to the continuum, with the polynomial degree selected individually for each spectrum and detector. Finally, the normalized nod-cycle spectra are averaged together to give a single reduced spectrum, normalized to 1.



The DRACS pipeline was originally developed to work with *H*-band spectra. Because of this, some of the parameters were adjusted in an attempt to achieve a better reduction on the *K*-band spectra analysed here. The parameters adjusted were the tracing and normalization polynomial functions and their specific order on the detector. Also, there was initially no reduction parameters present for detector #3 as detector #3 was not reduced in previous works using this pipeline. Therefore, the pipeline was extended to be able to reduce detector #3 of CRIRES, by adjusting the pipeline code and finding suitable parameters for detector #3.

When using the DRACS pipeline on a new target, the tedious part is initially creating the lists of files identifying which files are the dark, flat, and the science frames<sup>11</sup>. After these lists are created, the reduction pipeline can be run and re-run easily, making the effort worth it.

The first time through is interactive with a number of manual checks and decisions to be made (e.g. confirming the order tracing position, and fit is good). DRACS remembers choices in a database, allowing for a reduced level of user interaction a second or third time through the pipeline. This was useful to experiment with and iterate the reduction parameters of the pipeline. When changing the parameters which affect the order tracing, the database with the order tracing results needed to be deleted so that it would not influence the new fits. These parameters were therefore slower to iterate on.

This semi-autonomous nature of the DRACS pipeline means that all the spectra can be reduced in a consistent way, relatively quickly, and does not require manual spectra selection for each individual recipe as was done with the ESO pipeline.

There are a couple of drawbacks with using the DRACS pipeline. The first is the lack of documentation

<sup>8</sup> <https://www.eso.org/sci/software/esoreflex/>

<sup>9</sup> IRAF is distributed by the National Optical Astronomy Observatories, which are operated by the Association of Universities for Research in Astronomy, Inc., under cooperative agreement with the National Science Foundation.

<sup>10</sup> The spectra do not fall perfectly horizontally on the detector and usually contain some curvature due to the optics of the instruments.

<sup>11</sup> The GASGANO GUI was helpful to identify the distinction of each fits file for a beginner.

on how to use it. This required looking through the source code to find which functions and scripts do which part of the extraction. DRACS makes use of many IRAF packages which have documentation available online<sup>12</sup>. Searching through this documentation was difficult, but required, to understand how to use and modify DRACS.

The second drawback is that DRACS does not perform wavelength calibration, which is included with the ESO pipeline. This means an external wavelength calibration was the only option (see Section 5.2.1). The last drawback is the discovery of artefacts present in the nod spectra, which are discussed in detail in Section 5.1.3.1.

### 5.1.3 Pipeline comparison and selection

Both reduction methods were applied to the same CRIRES spectra to check the quality and consistency of both methods. Two examples of the extraction for HD 30501-1 (left) and HD 202206-1 (right) from both pipelines are provided in Figure 5.5. The blue lines are the extracted spectra from the ESO pipeline, the orange dashed lines are the optimal extraction from the DRACS pipeline, while the green dash-dotted line is the DRACS extraction after dealing with artefacts in the optimal extraction addressed in Section 5.1.3.1.

One of the important things checked was the line depths of each spectra to ensure that the pipelines were consistent. The ESO pipeline has noticeable issues, with many large spikes still present in the spectra, likely caused by bad pixels or cosmic rays that are not correctly removed. There also appears to be problems with the edges of the ESO reduced spectra, with very large spikes at either end.

At this stage the DRACS pipeline was chosen, as it was considered that the DRACS pipeline produced better extracted spectra than the ESO pipeline. This decision was based on the quality of the reduced spectra, as well as the relative ease of use of the pipeline (being semi-automated once set up). Another deciding factor was the need to create software to remove the bad pixels observed in the ESO reduced spectra. However, this was unavoidable as it was eventually required for the DRACS reduced spectra (see Section 5.1.3.1). Though the ESO pipeline provided a wavelength solution for the spectra, this did not factor into the decision as it was considered too unreliable due to known issues with CRIRES wavelength calibration, necessitating a new wavelength calibration anyway.

The spectra for the pipeline comparison in Figure 5.5 are the combination of the 8 nod spectra. Later, it was discovered that individual nod spectra from the DRACS pipeline had issues (see Section 5.1.3.1). These are difficult to notice on this scale as they each constitute one eighth of the information in the combined spectrum. An example of this is seen in detector #2 of HD202206-1 in Figure 5.5. In Section 5.1.3.1 an artefact from a single nod spectra, is barely visible in the pipeline comparison of Figure 5.5, shown as a slight depression of the orange dashed line between 2132 and 2134 nm. The identification of these artefacts and how they are removed (green lines) are explained in the following section.

#### 5.1.3.1 Reduction issues

After the decision to use the DRACS pipeline large artefacts in the DRACS-extracted spectra were observed. An investigation into the cause of these artefacts was undertaken to identify their source and attempt to remove them from the spectra. The eight individual nod spectra were displayed side-by-side

---

<sup>12</sup> Such as at the [http://stsdas.stsci.edu/gethelp/pkgindex\\_noao.html](http://stsdas.stsci.edu/gethelp/pkgindex_noao.html).

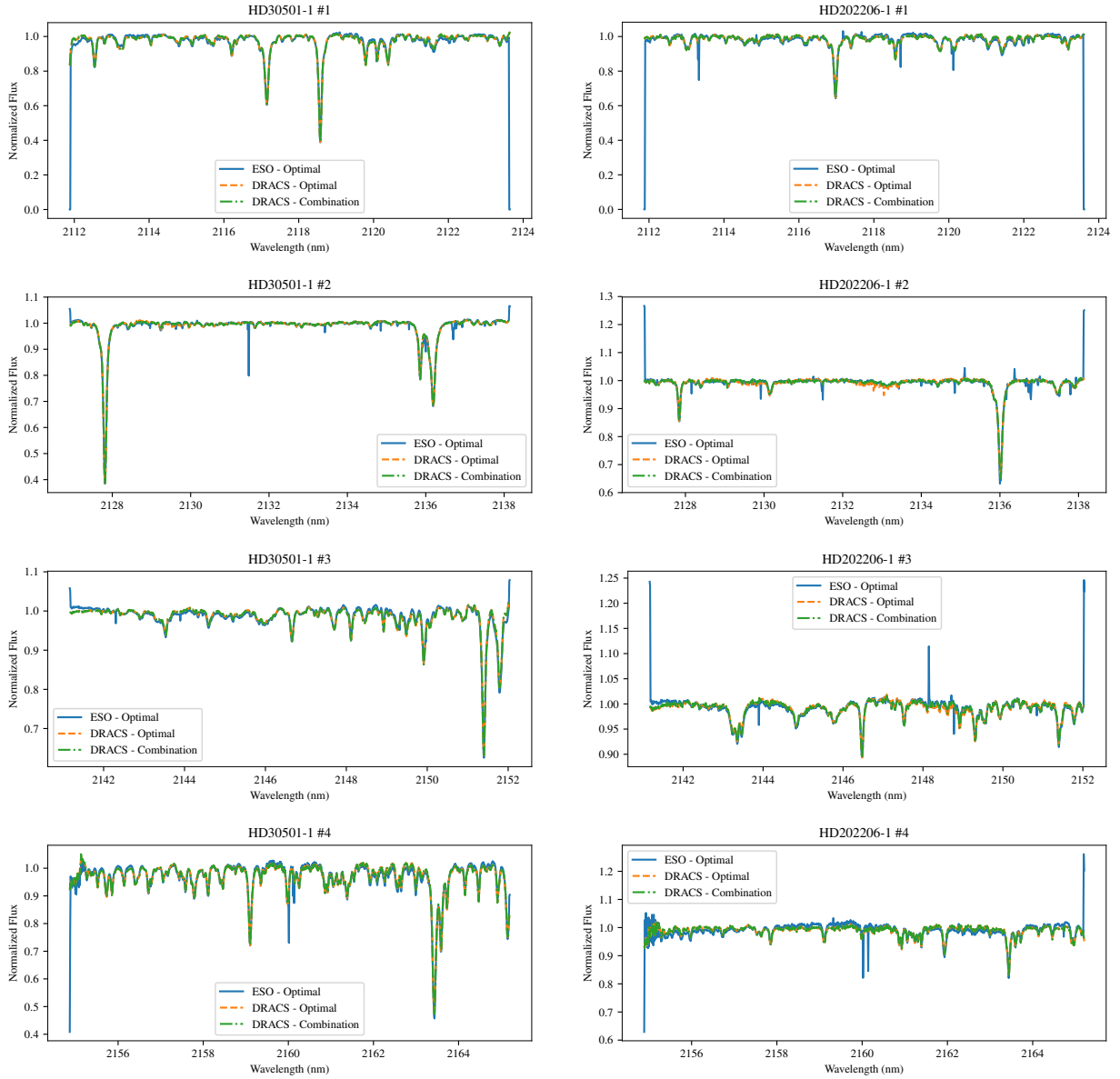


**Figure 5.5:** Comparison between the ESO pipeline and DRACS pipeline for two observations, HD30501-1 and HD202206-1. The blue lines are the extracted spectra from the ESO pipeline, the orange dashed lines are the combined optimal extraction from the DRACS pipeline, and the green dash-dotted line is the modified DRACS extraction (after removing artefacts addressed in Section 5.1.3.1). The wavelength information applied to both spectra is from the ESO pipeline.

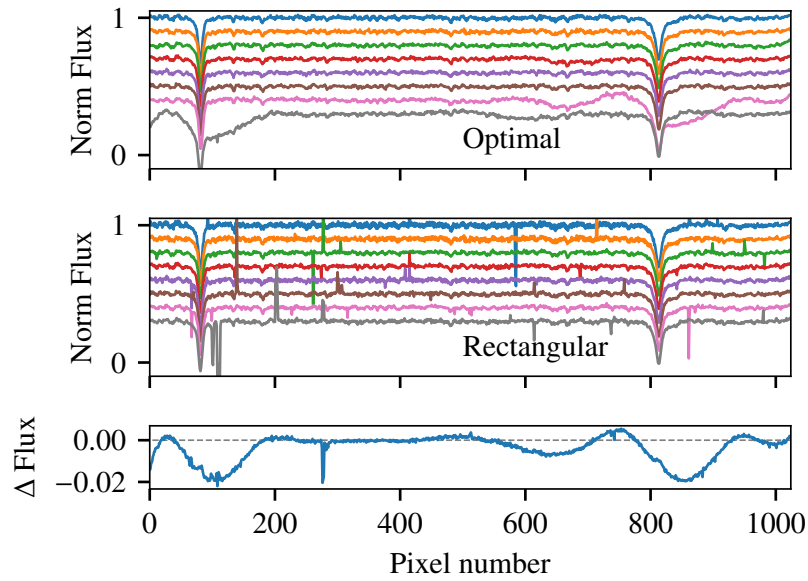


**Figure 5.6:** Example of DRACS artefacts in the optimally extracted spectra second detector of the first observation of HD 162020. top: The 8 normalized nod spectra obtained using *optimal* extraction, vertically offset from each other. middle: The 8 normalized nod spectra obtained using *rectangular* extraction, vertically offset from each other. bottom: Difference between the combined average spectra from the top and improved result from the mixed method developed here. The middle panel creates the small spikes, while the large deviations are due to the artefacts in the optimal reduction. There are three bad pixel spikes that cause artefacts in this optimal extraction. These are located in the seventh nod (pink) around pixel 850, and two in the eighth nod (grey) around pixel 100 and 620. Several other spikes do not cause any artefacts in the optimal reduction.

which revealed that occasionally the spectra from one of the nods deviated significantly from the others. Eventually it was identified that the artefacts were only in the *optimally* reduced spectra, and that they were not present in the *rectangular* extracted nods. An example is shown in Figure 5.6 in which sharp spikes in the middle panel (rectangular extraction) correspond to deviations observed in the top panel (optimal extraction). The bottom panel shows the difference in the combined average spectra from the optimal extraction and the corrected mixed spectrum resulting from the method given in this section to remove the artefacts. In this case the deviation in the combined spectra are at 2%. Further visual examples of artefacts, selected to show a variation in appearance, are given in Appendix B along with a table identifying the observations and nod spectra the artefacts were observed in.

It is clear that the artefacts in the optimal extraction occur when there is a corresponding “bad-pixel” spike<sup>13</sup> in the rectangular extraction. However this is not always the case with many spikes observed (e.g. first nod around pixel 580 in Figure 5.6) that are automatically removed in the optimal extraction. The occurrence of artefacts in the observations did not appear to have a pattern with nod position or detector with 14% (79/544 spectra) of the nod spectra having an optimal extraction that seemed to misbehave. The artefacts in the optimal extraction are also largely extended, significantly affecting more of the spectrum than the individual spikes (up to 100s of pixels). Artefacts were observed arising from both large and

<sup>13</sup> Their exact origin is unknown but are likely uncorrected bad-pixels or a cosmic ray. Here they will be referred to as bad-pixels.

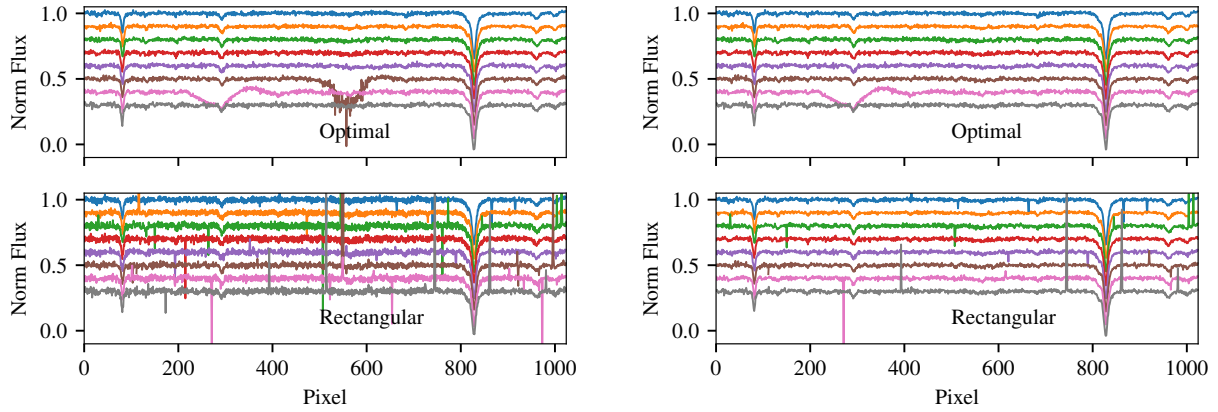


**Figure 5.7:** Two DRACS reductions for detector #2 of HD 202206-1 with one pipeline parameter changed. Left: The reduction with the DRACS pipeline with the “doslit.resize” set to “no”. Right: The reduction from the same pipeline but with “doslit.resize” set to “yes”, all else equal. During the order tracing the aperture size is automatically adjusted while the rest of the parameters remain identical. One large artefact is removed in the sixth nod (brown) while the artefact in the seventh nod (pink) is not removed.

small spikes alike while other large and small spikes are removed correctly. This possibly suggests that their size is of less important than some other unknown factor (possibly location).

As mentioned in Section 5.0.3 the *optimal* extraction includes variance weighting across the spatial direction. It appears that the presence of the bad pixel spikes heavily affects the variance weighting procedure during the *optimal* extraction.

Numerous parameters in the DRACS pipeline were experimented with in the attempt to remove the observed artefacts with limited success. For instance, no complete removal of the artefacts was found by adjusting the  $\sigma$  rejection limits (between  $1 - 5\sigma$ ) or increasing the tracing width parameter in IRAFs DOSLIT<sup>14</sup> recipe, although they did slightly affect the shape of the artefacts. Section 5.1.3.1 shows the extraction of HD 202206 with one parameter changed in the reduction pipeline. The only difference between the left and right panels the automated aperture resizing<sup>15</sup> was enabled by setting the “resize” parameter to *yes* in the right hand panel. This manages to remove an ugly artefact in the sixth nod (brown), but not the artefact in the seventh nod (pink). This was only discovered in the writing of this thesis so could not be utilized earlier. However, it does indicate that some improvements may be obtained with extensive time and patience tweaking the parameters of the DRACS pipeline.

The purpose of these observations was to detect faint companion spectra with expected flux ratios  $F_2/F_1 < 1\%$ . As the artefacts created large and extended deviations in the combined spectra (up to 2%) measures were needed to remove these artefacts from the combined spectra. To avoid contaminating the spectra of the faint companions.

After the unsuccessful tweaking of parameters the solution that was chosen was to replace the optimally extracted nods that contained artefacts with their rectangular counterparts. This would create a combined spectra that had a mix of optimally reduced and rectangularly reduced nod spectra, without any artefacts. To replace the spikes in the rectangular extraction that created the artefacts and others an

<sup>14</sup> Documentation for DOSLIT can be found here <http://stsdas.stsci.edu/cgi-bin/gethelp.cgi?doslit>

<sup>15</sup> Using <http://stsdas.stsci.edu/cgi-bin/gethelp.cgi?apresize.hlp>

iterative  $4\sigma^{16}$  rejection algorithm<sup>17</sup> was applied to the rectangular extractions. The  $\sigma$  for each pixel was calculated as the standard deviation of the nearest 2 pixels on either side of it, across all 8 nod spectra (a  $5 \times 8$  grid). Any rejected pixels were replaced using linear interpolation along the spectra. The spectra that contained artefacts and that were replaced using this method are given in Table B.1.

Combined spectra were finally constructed by averaging the eight nod-cycle spectra together, where some of the optimally extracted spectra were replaced using the above method. The actual spectra from the two different methods can be seen in Figure 5.5 where orange is the combination of optimally reduced spectra only and green uses the replacement method outlined here. The easiest to notice a difference is HD 202206-1 #2 in which the artefacts from Section 5.1.3.1 are removed.

The continuum normalization of the spectra is performed in IRAF while the swapping of nods creating a mixed combination is carried out in *Python* along with the post reduction procedures detailed below.

The DRACS pipeline was originally chosen over the ESO CRIRES pipeline because it seemed relatively simpler to use, being semi-automated, and appeared to have less bad pixel/cosmic ray artefacts in the resulting spectra. In hindsight the DRACS pipeline had several unexpected challenges due to these artefacts which took time to investigate and find a solution for.

One hypothesis for these artefacts is detector glow, the heating of the detector by the nearby amplifiers in the chip (see Section 5.0.1.1). The artefacts in the  $K$ -band spectra were not observed in previous works in the  $H$ -band using this pipeline (e.g. Figueira et al., 2010), and as such may have a wavelength dependent effect, like detector glow. However, it seems plausible that a glow related effect would be spatially distributed like the glow shown in Figure 5.1, but the location of the artefacts do not seem to have a discernible pattern. It could also be that there were artefacts in intermediate steps of the previous works that were missed due to the semi-automated pipeline, with the resultant combined spectrum being only slightly affected at the level of  $>1\%$  it could easily be missed (e.g. Figure 5.5). Another possibility is that the artefacts are bad pixels not removed correctly. Regardless, in the end they do not have a significant impact on the results found in this work, though it is expected that mixing the optimal and rectangular extracted spectra will have a slight negative impact on the noise or SNR of the combined spectrum. Much time and effort was invested attempting to extract the spectra, without artefacts, to have the best chance at obtaining high quality scientific results of the faint features sought after in this work.

#### 5.1.4 Reduction experience:

The experience gained in reducing CRIRES spectra enabled participation in collaboration with other science cases. The DRACS pipeline was used to extract the spectra of two other targets. A target and a very brief aim of each science case is given below.

- Barnard’s Star<sup>18</sup>: The carefully reduced nIR spectra of Barnard’s Star was meant to extend the work of Andreasen et al. (2016) in deriving the spectroscopic parameters of cool M-stars in the nIR. Unfortunately the work did not advance enough to analyse M-star’s and a spectrum of Arcturus (K0) and a fully reduced spectrum of 10Leo (K1) from the CRIRES-POP library Nicholls et al., 2017 were analysed instead in Andreasen et al. (in prep.).

<sup>16</sup> There is no scientific justification why  $4\sigma$  was chosen over the commonly used  $3\sigma$ .

<sup>17</sup> Found at [https://github.com/jason-neal/nod\\_combination](https://github.com/jason-neal/nod_combination)

<sup>18</sup> Programme ID: 085.D-0161(A)

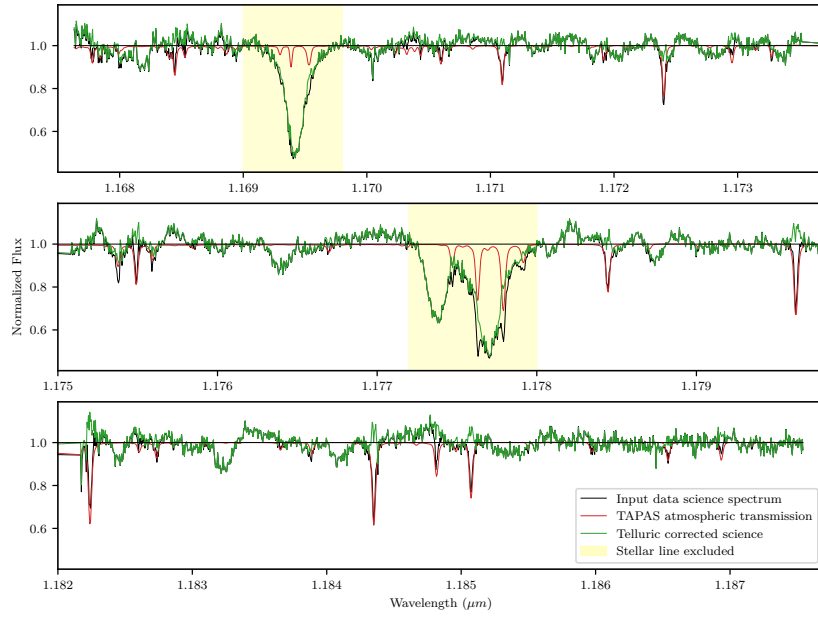


**Figure 5.8:** Example of telluric corrected spectrum of HR 7329-B using TAPAS. Credit Ulmer-Moll et al. (2018). The yellow shaded region is the region of stellar lines that was avoided while applying the correction methods.

- $\eta$  Tel<sup>19</sup>: The spectra of a telluric standard star (HIP100090) and HR 7329-B ( $\eta$  Tel-B) a rapidly rotating Brown Dwarf, were reduced to accurately determine the BD rotation rate by measuring the line broadening. The results from this data will be published in an upcoming paper Hagelberg et al. (in prep.).
- The same spectra of HR 7329-B were also used in Ulmer-Moll et al. (2018) to compare different telluric correction methods in the nIR. An example from Ulmer-Moll et al. (2018, (B.3)) of the reduced target spectrum (black), the telluric model (red) and the telluric corrected spectrum (green) is provided in Figure 5.8.

For these works only the spectral extraction outlined above was performed. The post extraction and reduction steps detailed in the following sections were not.

## 5.2 Post reduction stages

From the DRACS pipeline the 1-D spectra of each target has been extracted. However, the spectra still need to undergo some post-extraction steps. In particular, wavelength calibration and telluric correction. A detailed look of how these steps were developed and performed are addressed in the following section.

### 5.2.1 Wavelength calibration

Wavelength calibration is the process of assigning accurate wavelength values to each pixel in the spectra. For CRIRES in the nIR this is challenging. CRIRES uses a Thorium-Argon (Th-Ar) lamp to place 6 emission spectra on the detector using fibres. The spectra of the Th-Ar emission lines are used to

<sup>19</sup> Programme ID: 083.C-0759(A)



determine the spatial distribution of the wavelength solution across each detector using correlation with a spectral template. Th-Ar lamps are excellent at optical wavelengths where the numerous (several thousand) spectral lines enable precision of sub- $\text{m s}^{-1}$  radial velocity measurements HARPS spectrograph.

However, in the nIR there is a relatively low density of Th-Ar lines (Kerber et al., 2009), which, in combination with the alignment of the narrow wavelength range of the detector, causes a poor wavelength calibration to be obtained (e.g. CRIRES-POP (Nicholls et al., 2017)). Above 2.2  $\mu\text{m}$  there are O-H sky lines that can be used for wavelength calibration but according to the CRIRES manual for observations below 2.2  $\mu\text{m}$  they are too dim. These wavelength calibration issues were experienced when using the ESO CRIRES pipeline, with non-Th-Ar features sometimes affecting the correlation.

Between the wavelength range 2.1–2.17  $\mu\text{m}$  there are roughly 80 Th-Ar lines across all four detectors, as seen in Figure 5.4. The DRACS pipeline does not use the Th-Ar lamp files for wavelength calibration and leaves this as a post reduction step.

A common method for wavelength calibration that does not rely on Th-Ar lamps of CRIRES involves using the telluric lines present to provide the wavelength solution (e.g. Brogi et al., 2012; Brogi et al., 2014; de Kok et al., 2013; Piskorz et al., 2016). This is made possible by the use of high resolution spectra, in which the telluric lines are well resolved, as well as accurate spectral information of the atmosphere.

Likewise, in this work the wavelength calibration is performed using the telluric absorption lines present in each observation as the wavelength reference. Instead of directly using the HITRAN database (Rothman et al., 2013) for the telluric line positions, such as Brogi et al. (2012), Brogi et al. (2014), and de Kok et al. (2013), use the TAPAS atmospheric transmission models (see Section 4.2). The TAPAS models use the HITRAN database but also includes atmospheric profiles and physical meteorological measurements to model the telluric absorption strength.

To calibrate the wavelength the telluric lines in the model need to be associated to the corresponding telluric lines in the observed spectrum. The centroid<sup>20</sup> of each telluric line in the model is obtained by fitting the telluric transmission spectrum,  $T(\lambda)$ , as a simple sum of Gaussian functions (subtracted from the continuum):

$$T(\lambda) = 1 - \sum_i G(\lambda, A_i, \mu_i, \sigma_i), \quad (5.1)$$

where  $G$  is a Gaussian function of the form

$$G(\lambda, A, \mu, \sigma) = Ae^{-(\lambda-\mu)^2/2\sigma^2}, \quad (5.2)$$

and  $A$ ,  $\mu$ ,  $\sigma$  are the amplitude, central wavelength, and standard deviation for each line respectively. Telluric lines actually have a Voigt profile<sup>21</sup> although they are not fully resolved in the nIR and their shape is dominated by the instrumental profile. Seifahrt et al. (2010) measured the instrumental profile of CRIRES using singular-value decomposition and showed that it is extremely well represented by a single Gaussian below a SNR  $\sim 300$ . Therefore, wavelength calibration using single Gaussian fits to each line is sufficient.

The observed spectra contain two different spectral components: stellar and telluric lines, which are multiplied together: The observed spectra are therefore fitted with a multiplication of two Gaussian-sum

<sup>20</sup> Centre of the line

<sup>21</sup> A Voigt profile is a convolution of two broadening profiles, a Gaussian and a Lorentzian. Gaussian broadening results from thermal Doppler broadening, and instrumental broadening while the Lorentzian broadening comes from molecular vibrational bands(Meier, 2005).

models.

$$\begin{aligned} I_{obs}(x) &= I_{tell}(x) \times I_{star}(x) \\ I_{obs}(x) &= \left(1 - \sum_j G(x, A_j, \mu_j, \sigma_j)\right)_{tell} \times \left(1 - \sum_k G(x, A_k, \mu_k, \sigma_k)\right)_{star}, \end{aligned} \quad (5.3)$$

where  $x$  is the pixel coordinates of the extracted spectra.

The identification between telluric and stellar lines is performed by hand for each spectra, using the telluric model as the reference. Care was taken to fit the correct components to blended spectra where possible to improve the number telluric lines use for calibration. The fits were inspected to ensure that they reasonably matched the line positions. There was difficulty in identifying the shallow lines with depths below 1–2%, but these were needed in some spectra to obtain a suitable fit. If there were blended lines that did not appear to fit correctly they were not considered in the calibration step.

After fitting  $I_{obs}(x)$  to the observed spectrum and  $T(\lambda)$  to the telluric model, the wavelength solution was obtained by fitting a second order polynomial to the centroid values  $\{\mu_j(x), \mu_i(\lambda)\}$  from the telluric components of the observed spectra and telluric model respectively. A second order polynomial has been shown to be sufficient for higher precision RV studies (e.g. Bean et al., 2010; Figueira et al., 2010). This polynomial is then used to map the whole spectrum from pixels into wavelength. Higher 3<sup>rd</sup> and 4<sup>th</sup> order polynomials that are also used in the literature (e.g. Seifahrt et al., 2010; Ulmer-Moll et al., 2018) were attempted but had limited success here due to the limited number and uneven spacing of telluric lines in the narrow wavelength range analysed, especially on the second detector. There were often large deviations due to the uneven spread of telluric lines, especially at the extremities. Higher order terms for wavelength calibration are usually used in regions with a higher density of telluric lines and/or a longer wavelength span (Piskorz et al., 2016; Seifahrt et al., 2010; Ulmer-Moll et al., 2018).

An example of the wavelength fitting is given in Figure 5.9. The top panel shows the (slightly) quadratic fit (blue dashed) to the centroid values  $\{\mu_j(x), \mu_i(\lambda)\}$  (black) while the bottom panel shows the newly calibrated observation alongside the telluric spectrum. The black crosses indicate the lines used for calibration. To two decimal places the equation of the fit  $\lambda = -1.85e^{-7}x^2 + 1.16e^{-2}x + 2111.86$ .

Much like with the Th-Ar calibrations, this technique performs better when there is sufficient coverage of telluric lines on the detectors. For the wavelength setting of these observations, the spectra from the second detector (top right panel of Figure 5.10) only has two large telluric lines present with several small lines, with relative depths smaller than 1%, which are often difficult to accurately identify. This deteriorated the calibration stability for the second detector. The second detector may have been ideal for the detection of a faint secondary spectra, with the lack of telluric contamination and stellar lines. Unfortunately the wavelength calibration quality varies in an inverse way, being more difficult with few lines.

It is noted that there are many variations on this wavelength calibration technique including those integrated within programs such as *TelFit* Gullikson et al. (2014), and ESO’s *Molecfit* Smette et al. (2015), that perform telluric correction and re-calibrate the wavelength axis themselves at the same time. It is recommended to attempt using those first before independently creating wavelength calibration software.

One improvement could have been to include a concurrent fitting of a stellar spectral model, adjusted for RV, along with the telluric model, which could help to improve the wavelength calibration performed here. Piskorz et al. (2016) performed wavelength calibration using only a telluric line model at other nIR

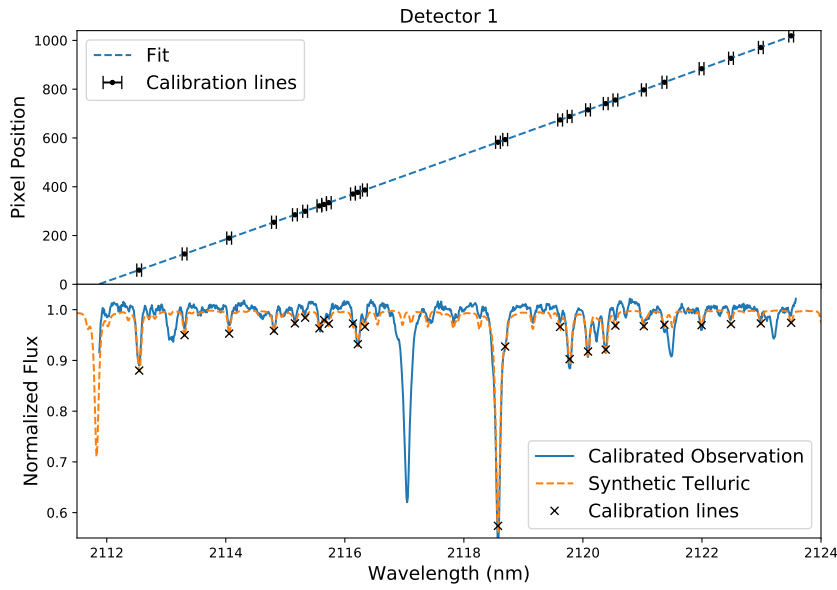


**Figure 5.9:** Example of the wavelength calibration using the synthetic telluric spectra. Top: The pixel/wavelength mapping and associated wavelength fit. The horizontal error bars shown are the Gaussian line width, around 0.04 nm. Bottom: The wavelength calibrated observation and the telluric model used for calibration. The black crosses indicate the peaks of the telluric lines used in the fitting process.

wavelengths (*L*-band between 3.0–3.4 μm) successfully. However, around 2 μm they needed to include a fitted stellar model to obtain good wavelength calibration due to the weaker telluric lines in this region. This is the same wavelength region of the data analysed here. Having experience of performing wavelength calibration at other wavelengths may have revealed the difficulties of calibration from the telluric lines at 2 μm sooner.

A brief attempt of wavelength calibration using the iterative calibration method outlined in Brogi et al., 2016 was made. This involved generating a set of quadratic wavelength solutions for the observed spectrum and cross-correlating each one against the telluric model. The solutions for the next iteration are obtained by refining the parameters from the wavelength solution with the highest correlation. The method worked well for Brogi et al. (2016) as they included templates for both the star and telluric lines and they were observing in a wavelength domain in which there is a large number of strong and uniform stellar CO lines across the detector. The brief experiments with this method were not successful as they did not include a stellar model or mask, which lead to incorrect fitting solutions. Without adding any stellar masking the telluric lines would strongly correlate to the stellar lines present, especially where there were blended lines. This lead to visibly incorrect wavelength solutions and this method was abandoned. If a stellar mask was used it may have been possible to achieve more sensible results, although still challenging to the low density of telluric lines at this wavelength range.

At one point it was considered to attempt a global fit of the wavelength calibration, using all four CRIRES detectors together. This would create a consistent fit to the dispersion across all 4 detectors at once. This would require extra fitting parameters to define the size of the 3 gaps between the detectors

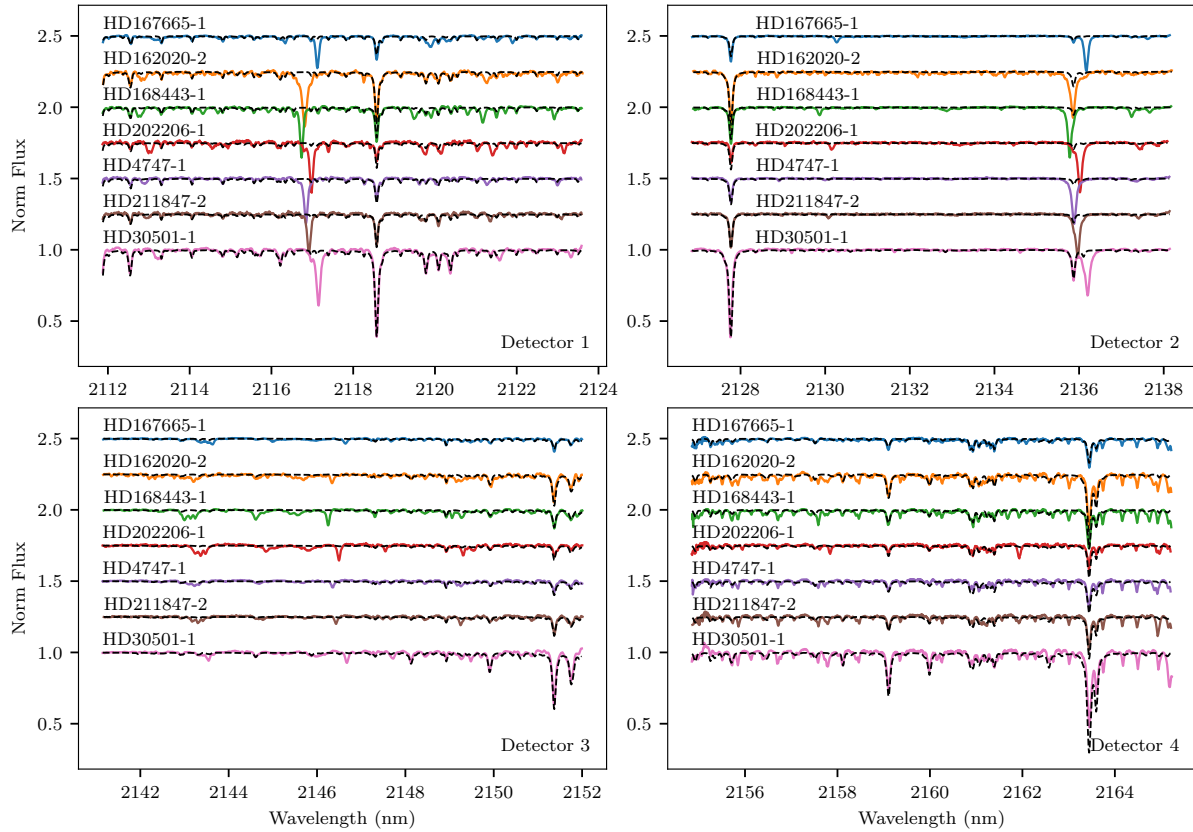


**Figure 5.10:** An example spectra for each target and each detector #1–4 in order of increasing wavelength. The solid lines are the spectra while the black dashed lines are the telluric models used for wavelength correction, showing good alignment with the spectra.

and any vertical offsets. This fit may even need to be performed on the two-dimensional images, before the 1-D extraction. This may have allowed for the telluric lines from neighbouring detectors to help fit the calibration on detectors where there are very few telluric lines (e.g. detector #2). The fitted instrument parameters such as the detector gaps may even be constrained so that they are physically consistent across all observations. However, this idea was not explored further or implemented due to time constraints. An example of the wavelength calibration using all four detectors is provided in Appendix C. In the future it may be possible or necessary to combine all of the methods above, including the Th-Ar calibration lines, telluric models, stellar templates, and multiple detectors fitted at once to achieve precise wavelength calibration.

In hindsight using the wavelength solution from the ESO pipeline may have been a good starting point, rather than the pixel positions, for calibration of the DRACS reduced spectra. This may have made the line identification simpler.

In simulations of a differential technique similar to what is presented in Chapter 6, Kostogryz et al. (2013) simulate the affect of wavelength calibration errors on differential result. They found that calibration error  $>0.1$  pixels will produce signals greater than the photon noise level in spectra with a SNR of around 500. They show that this upper limit only just the level achieved by (Brogi et al., 2012) calibrated using the telluric lines from the observation. This shows how important the wavelength calibration is to detect the spectra of the companion.



### 5.2.2 Telluric correction

After wavelength calibration telluric correction is performed using the same TAPAS atmospheric transmission models. When inspecting the models and observations there was slight difference in the airmass,  $m$ , between the synthetic spectra and the airmass in the fits header. The depth of the telluric lines were re-scaled to match the airmass of the observations using the relation  $T = T^\beta$ , where  $T$  is the transmission of the telluric spectrum and  $\beta$  is the airmass ratio between the observation and model  $\beta = m_{\text{observed}}/m_{\text{model}}$ . This scaling adjusted the depth of most absorption lines to better match the observations, but does not correctly scale the deeper H<sub>2</sub>O lines, for which there were still differences.

The scaled telluric model is interpolated to the wavelengths of the observed spectrum and then used to correct the observed spectra through division, leaving behind a telluric corrected spectra. Telluric spectra used for correction can be observed alongside the non-corrected spectra in Figure 5.10 as the black dashed lines.

#### 5.2.2.1 Separate H<sub>2</sub>O scaling.

A technique suggested by Bertaux et al. (2014) was attempted to address the poor H<sub>2</sub>O airmass scaling. This involved fitting a scaling factor to the H<sub>2</sub>O absorption lines before convolution to the instrument resolution. This was achieved by first dividing the spectrum by a telluric model containing the non-H<sub>2</sub>O constituents, convolved to the observed resolution, and scaled by the airmass to remove the non-H<sub>2</sub>O lines. Then the telluric model with only H<sub>2</sub>O lines at full resolution was scaled by a factor  $T^x$  and convolved to the instrumental resolution<sup>22</sup> and compared to the remaining telluric lines in the observed spectra. This scaled and convolved model was fitted to the observations to find the best was fitted to find the best scaling factor  $x$ , for the H<sub>2</sub>O lines.

It was found that for a few spectra in the sample this method corrected the deeper telluric lines well, but in many cases the fitted scaling factor was affected by the presence of blended stellar lines (attempting to fit those also). It was also strongly influenced by the deepest H<sub>2</sub>O telluric lines present. The telluric correction of the deep H<sub>2</sub>O lines could be improved with this technique, but at the cost of worsening the correction of the many smaller H<sub>2</sub>O lines. Since the smaller H<sub>2</sub>O lines covered more of the spectrum in this region than the larger lines, the separate H<sub>2</sub>O scaling was not continued. One possible solution for this would be to perform a piece-wise telluric correction, performing this step only for the deeper H<sub>2</sub>O lines. This technique could also benefit from a larger wavelength span that would enable blended lines to be ignored while having sufficient deep H<sub>2</sub>O lines to fit the scaling factor correctly. This small experiment shows that a simple scaling is not enough to correct for the absorption of H<sub>2</sub>O in an effective way, for this case. Another better solution would be using proper atmospheric fitting tools that fits the telluric model to the observations, such as Molecfit, in which the atmospheric composition can be changed to match the observed telluric line strengths.

### 5.2.3 Wavelength masking

Throughout the course of this work several wavelength regions were found where the extraction could not be performed reliably due to the wavelength calibration and telluric line corrections. Different wavelength masks are applied to these areas to remove them from the spectra. The main reasons that wavelength masking is used are collated below.

---

<sup>22</sup>  $R = 50\,000$  for this work

Firstly, regions near the edges of each detector where the wavelength solution is extrapolated outside of the calibrating telluric lines are removed, reducing the effective size of each detector by about 10% or  $\sim 100$  pixels.

Secondly, any remaining artefacts present in the spectra and the centres of deep telluric lines where telluric correction was not corrected properly are masked out. The telluric correction sometimes results in “emission-like” peaks in the corrected spectrum, which are removed. These factors combined result in masking out around a further 10% of the observed spectra.

In Section 7.2 a further wavelength restriction is applied to mask out regions where there is a large mismatch between the observed spectrum and the closest synthetic spectra to the host. This significantly restricts the wavelength span utilized for that purpose to around only 43%. The masked regions created by this last mask are shown in Figure 7.4.

#### 5.2.4 Barycentric RV correction

After the telluric correction is performed, the spectra are corrected for Earth’s barycentric motion. The orbital and rotational motion of the Earth imparts a daily and seasonal radial velocity measurement offset onto observations. To accurately compare the radial velocity (or spectral shift) between two measurements, they need to be translated into a common rest frame. The rest frame of choice is the barycentre of the Solar System. Equations to relate the observed spectral shift to the RV shift at the *Barycentric Celestial Reference Reference System* (Rickman, 2001) rest frame are provided in Lindegren et al. (2003).

In this work the barycentric velocity correction is calculated using PyAstronomy’s<sup>23</sup> *helcor* function ported from the REDUCE IDL package (see Piskunov et al. (2002)). This calculates radial velocity of the observer towards the astronomical target, accounting for Earth’s barycentric motion as well as Earth’s rotation. This computation requires the date and time of the observation, the location of the observatory and the celestial coordinates of the target. The observed spectra are Doppler shifted by the negative value of the barycentric velocity calculated, placing all spectra as if they were observed from the barycentre of the Solar System.

The maximum barycentric velocity of the Earth is around  $30 \text{ km s}^{-1}$ . It is common to see spectral regions  $\pm 30 \text{ km s}^{-1}$  either side of telluric lines with an absorption depth  $>2\%$  avoided in analysis (such as RV determination), as these will be affected by the telluric lines at some point in the year.




---

<sup>23</sup> <https://pyastronomy.readthedocs.io>

# Chapter 6

## Separating the spectra of faint companions

Spectral observations of binary systems contain the spectra of both bodies, in proportion to their flux ratio, and Doppler shifted relative to each other due to their orbital motion. There many different techniques to disentangle the spectra of binary objects. This chapter focuses on applying a direct subtraction method to near-infrared (nIR) spectra of FGK stars which have Brown Dwarf (BD) companions, with the goal to isolate the spectrum of the companions. The data used was obtained with the CRIRES instrument in 2012<sup>1</sup> observed with the purpose to apply the differential technique specifically. A level of trust was placed in the quality of the observations, which was unfortunately misplaced. This chapter begins with the motivation for these specific targets and details the observations obtained. The direct subtraction technique will be presented and its application to the observations will explored. The limits of the differential technique at low RV separations is given by simulation with synthetic spectra.

### 6.1 Spectral Disentangling techniques

Spectral observations of binary systems contain the spectra of both bodies, in proportion to their flux ratio, and Doppler shifted relative to each other due to their orbital motion. One technique to recover the spectra of the companion is secondary reconstruction through a differential spectrum (Ferluga et al., 1997). Spectra from different phases are shifted to the rest frame of the host star and subtracted to mutually cancel out the spectrum of the host star allowing the faint companion spectra to become visible. Advances in high-resolution and near-infrared (nIR) capabilities should enable this technique to be applied to BDs and planet companions, in which smaller RV shifts can be resolved and the contrast ratio of the smaller companion is improved.

Binary stars through brown dwarfs... to planets.

Mention the other technique here first. Then move to the one we tried...

Spectral Disentangling techniques - PSOAP - Differencing Fruluga - Templates?

TODCOR - 2-d from binary analysis (Zucker et al., 1994) (Mazeh et al., 1997)

cite LOCKWOOD 2014 2-D-cross-correlation? Piskorz et al. (2016) seems to have promising technique

<sup>1</sup> Before this thesis began

See Kostogryz et al. (2013) for lots of useful references regarding differential works Simon et al. (1994)

Rodler et al. (2012) uses differential of a series of phases to construct a stellar mask for the host to subtract from all measurements.

Kolbl et al. (2015) Use HIRES spectra at 364–799 nm ( $R=60\,000$ ) to determine statistically determine the presence of a faint secondary companion spectra (if any). They use  $\chi^2$  fitting of the observed spectra against the SPecMatch library of observed spectra to find a spectra to best remove the primary star lines, accounting for dilution and rotational broadening. They also find that a secondary spectrum with a  $\Delta RV$  relative to the host would blend and remain undetectable. When searching for the secondary they median normalize the spectra into 100 K spectra since the difference between stars  $<100$  K different is almost indiscernible in the secondary. The residuals are renormalized and then a  $\chi^2$  fit is again performed to identify any secondary spectra. For a low temperature companion (3500 K) at a 1% flux ratio to a 5000–6000 K primary star their recovery technique achieves 80% injection-recovery, in the optical.

## 6.2 Motivation and target selection

The work of Sahlmann et al. (2011) used the astrometry technique to identify several candidate brown dwarf companions of FGK stars with  $M_2 \sin i$  values  $> 10 M_{Jup}$ . Seven candidates from Sahlmann et al. (2011), which were visible in Period 89 (2012), were selected for further observation in order to identify their stellar nature. That is, to refine the mass of the companions to distinguish if their companion is: a large giant planet ( $M \lesssim 13 M_{Jup}$ ), a Brown dwarf ( $13 \lesssim M \lesssim 80 M_{Jup}$ ), or a low-mass star ( $M \gtrsim 80 M_{Jup}$ ).

The list target host stars that were observed are presented in Table 6.1 along with their stellar parameters, while Table 6.2 details the orbital parameters of each system from the literature.

It is noted that the orbital parameters of some targets have been refined in the literature since the observations took place. For example three candidates have had their masses refined in recent works. The companion to HD 211847 was determined to be a low mass star with  $M_2 = 155 M_{Jup}$  (Moutou et al., 2017), while the companion to HD 4747 was found to have a mass of  $M_2 = 60 M_{Jup}$  (Crepp et al., 2016). The two companions of HD 202206 (B and c) were found to have masses of  $M_B = 93.6 M_{Jup}$  and  $M_c = 17.9 M_{Jup}$ , respectively, classifying HD 202206c as a “circumbinary brown dwarf” (Benedict et al., 2017). These three companions with recently refined masses, along with HD 30501, create a good set of benchmarks to compare any results from the techniques used here, and show that the masses of these targets do span the BD to low-mass star range. All target companions except HD 162020 ( $P=8.4$  days) are in (very) long period orbits ( $P=0.7$ –38 years) with masses (or  $M_2 \sin i$ ) greater than  $10 M_{Jup}$ .

**Table 6.1:** Stellar parameters of the host stars. V is the apparent visual magnitude taken from SIMBAD (Wenger et al., 2000). Distances were calculated using the GAIA DR2 parallax measurements.

Star	SpT	V	$T_{\text{eff}}$ (K)	$\log g$ ( $\text{cm s}^{-2}$ )	[Fe/H]	$M_1$ ( $M_{\odot}$ )	Age (Gyr)	d (pc)	Reference
HD 4747	K0V	7.15	$5316 \pm 50$	$4.48 \pm 0.10$	$-0.21 \pm 0.05$	$0.81 \pm 0.02$	$3.3 \pm 2.3$	$18.80 \pm 0.04$	1, 2, 3, 8
HD 162020	K3V	9.12	$4723 \pm 71$	$4.31 \pm 0.18$	$-0.10 \pm 0.03$	$0.74 \pm 0.07$	$3.1 \pm 2.7$	$30.85 \pm 0.06$	4, 5, 6, 8
HD 167665	F9V	6.40	$6224 \pm 50$	$4.44 \pm 0.10$	$0.05 \pm 0.06$	$1.14 \pm 0.03$	$0.7 - 3.6$	$31.24 \pm 0.06$	1, 8
HD 168443	G6V	6.92	$5617 \pm 35$	$4.22 \pm 0.05$	$0.06 \pm 0.05$	$1.01 \pm 0.07$	$10.0 \pm 0.3$	$39.67 \pm 0.12$	5, 6, 8
HD 202206	G6V	8.07	$5757 \pm 25$	$4.47 \pm 0.03$	$0.29 \pm 0.02$	$1.04 \pm 0.07$	$2.9 \pm 1.0$	$46.03 \pm 0.14$	5, 7, 8
HD 211847	G5V	8.62	$5715 \pm 24$	$4.49 \pm 0.05$	$-0.08 \pm 0.02$	$0.92 \pm 0.07$	$0.1 - 6.0$	$48.81 \pm 0.13$	1, 2, 4, 8
HD 30501	K2V	7.59	$5223 \pm 50$	$4.56 \pm 0.10$	$0.06 \pm 0.06$	$0.81 \pm 0.02$	$0.8 - 7.0$	$20.37 \pm 0.01$	1, 4, 8

References: (1) Sahlmann et al. (2011); (2) Santos et al. (2005); (3) Crepp et al. (2016); (4) Tsantaki et al. (2013); (5) Bonfanti et al., 2016; (6) Santos et al. (2004); (7) Sousa et al. (2008); (8) Collaboration et al. (2018);

**Table 6.2:** Orbital parameters for the BD companions obtained from the literature.

Object	$\gamma$ ( $\text{km s}^{-1}$ )	Period (day)	$e$	$K_1$ ( $\text{m s}^{-1}$ )	$T_0$ (JD-2,450,000)	$\omega$ (deg)	$M_2 \sin i$ ( $M_{\text{Jup}}$ )	$M_2$ ( $M_{\text{Jup}}$ )	Ref.
HD 4747	$0.215 \pm 11$	$13\,826.2 \pm 314.1$	$0.740 \pm 0.002$	$755.3 \pm 12$	$463.1 \pm 7.3$	$269.1 \pm 0.6$	39.6	60.2	1
HD 162020	$-27.328 \pm 0.002$	$8.42819 \pm 6e^{-5}$	$0.277 \pm 0.002$	$1\,813 \pm 4$	$1\,990.68 \pm 0.01$	$28.4 \pm 0.2$	14.4	-	2
HD 167665	$8.003 \pm 0.008$	$4\,451.8 \pm 27.6$	$0.340 \pm 0.005$	$609.5 \pm 3.3$	$6\,987.6 \pm 29$	$-134.3 \pm 0.9$	50.3	-	3
HD 168443b	$-0.047 \pm 0.552$	$58.1124 \pm 4e^{-4}$	$0.529 \pm 0.001$	$475.13 \pm 0.9$	$5\,626.20 \pm 0.02$	$172.9 \pm 0.1$	7.7	-	4
HD 168443c	$-0.047 \pm 0.552$	$1\,749.83 \pm 0.57$	$0.211 \pm 0.002$	$297.7 \pm 0.6$	$5\,521.3 \pm 2.2$	$64.9 \pm 0.5$	17.1	-	4
HD 202206B	14.721	$256.33 \pm 0.02$	$0.432 \pm 0.001$	$567 \pm 1$	$2\,176.14 \pm 0.12$	$161.9 \pm 0.2$	17.4	$93.2 \pm 7.3$	5, 6
HD 202206c	14.721	$1\,260 \pm 11$	$0.22 \pm 0.03$	$41 \pm 1$	$3\,103 \pm 452$	$280 \pm 4$	2.3	$17.9 \pm 2.9$	5, 6
HD 211847	$6.689^a$	$7\,929.4 \pm 2\,500$	$0.685 \pm 0.068$	$291.4 \pm 12.2$	$12\,030.1 \pm 2\,500$	$159.2 \pm 2.0$	19.2	155	3, 7
HD 30501	$23.710 \pm 0.028$	$2\,073.6 \pm 3.0$	$0.741 \pm 0.004$	$1\,703.1 \pm 26.0$	$3\,851.5 \pm 3.0$	$70.4 \pm 0.7$	62.3	89.6	3

**References.** (1) Crepp et al. (2016); (2) Udry et al. (2002); (3) Sahlmann et al. (2011); (4) Pilyavsky et al. (2011); (5) Correia et al. (2005); (6) Benedict et al. (2017); (7) Moutou et al. (2017)

**Notes.** <sup>(a)</sup> fixed

The spectral differential approach was chosen with the goal to constrain the companion masses while minimizing the observational time required to observe. It was determined that it should be possible to obtain a detection of a companion with a 1% contrast ratio with an exposure time of around 20 minutes. Two observations at “clearly separate RVs” were requested to constrain each target. Observations were performed without telluric standard star observations to avoid the extra observing time overhead, choosing to instead rely on synthetic model correction (see Section 4.2). The *K*-band was chosen to achieve a high contrast relative to the host star, detected in the extreme V-K colour indexes ( $>7.8$ ), while the specific atmospheric window (2110–2070 nm) was chosen in order to reduce the absorption introduced by the atmosphere (J. R. Barnes et al., 2008).

### 6.2.1 The Data

#### 6.2.2 CRIRES data

Observations were performed with the CRIRES instrument (Kaeufl et al., 2004) configured to observe a narrow wavelength domain of the *K*-band between 2120–2165 nm. The slit width of  $0.4''$  resulted in an instrumental resolving power of  $R = 50\,000^2$ . No adaptive optics were used to ensure that the entrance slit was entirely covered by each target. This is to prevent strong slit illumination variations that could change the shape of spectral lines.

The observations were performed in service mode during Period 89 with run ID. 089.C-0977(A) between April and August 2012. A single observation is composed of eight individual spectra with an integration time of 180s each, observed in the ABBAABBA nod cycle pattern to obtain a high signal-to-noise ( $>100$ ) when combined. The list of observations obtained with CRIRES are provided in Table 6.3.

There is a slight inconsistency with the some of the observations, taken in service mode. For instance HD 202206 has two observations taken with the Ks filter, while one is taken with the J filter. There is also the last observation of HD 30501 taken with a different filter compared to the others. The documents for the phase two observing proposal were unable to be obtained to determine if these ‘odd’ filters were requested or if this was an observational mistake.

There is also an inconsistency with the naming or ordering of the observations again with the target HD 202206. The observation that was performed first in time is labelled with the observation name of HD 202206-3 in the fits header file, while the second and third observations are labelled -1 and -2 respectively.

There could be two possible reasons for the single observation of HD 4747. The first reason could be that only one observation was requested due to the very long orbital period of the target, although this would not have fulfilled the science goal. The second and more likely reason is that these observations were performed in service mode, as a filler program, and there was no time to observe a second observation of HD 4747.

---

<sup>2</sup> The rule of thumb resolution for CRIRES is  $100\,000 \times \frac{0.2''}{\text{slit width}}$  with the slit width in arcseconds

**Table 6.3:** Details regarding each of the CRIRES observations. The number of artefacts removed in Section 5.1.3.1 as well as the SNR of the combined spectra is provided. The last three columns are the RV calculated from the orbital solution for both the host and largest companion, and the RV difference between them.

Object	Obs. #	Start date (yyyy-mm-dd hh:mm:ss)	Filter	Airmass (at start)	Artefacts / 32	SNR	$RV_1$ $\text{km s}^{-1}$	$RV_2$ $\text{km s}^{-1}$	$rv_2$ $\text{km s}^{-1}$
HD 4747	1	2012-07-06 07:36:06	Ks	1.25	7	340	-0.219	-0.154	0.065
HD 162020	1	2012-07-04 06:23:22	Ks	1.30	2	127	-28.760	50.785 <sup>a</sup>	79.545 <sup>a</sup>
HD 162020	2	2012-07-04 06:57:48	Ks	1.44	2	128	-28.717	48.440 <sup>a</sup>	77.157 <sup>a</sup>
HD 167665	1	2012-07-28 05:00:53	Hx5e-2	1.24	7	371	7.581	18.024 <sup>a</sup>	10.443 <sup>a</sup>
HD 167665	2	2012-07-28 05:37:27	Hx5e-2	1.39	4	374	7.581	18.025 <sup>a</sup>	10.444 <sup>a</sup>
HD 167665	3	2012-08-05 02:54:03	Hx5e-2	1.04	4	358	7.575	18.163 <sup>a</sup>	10.588 <sup>a</sup>
HD 168443	1	2012-08-05 04:29:32	Ks	1.31	2	192	-0.121	50.932 <sup>a,b</sup>	51.053 <sup>a,b</sup>
HD 168443	2	2012-08-05 04:58:50	Ks	1.47	4	190	-0.121	51.189 <sup>a,b</sup>	51.310 <sup>a,b</sup>
HD 202206	1	2012-07-12 06:54:44	Ks	1.01	3	189	14.843	12.992 <sup>b</sup>	-1.851
HD 202206	2	2012-07-13 05:41:40	J	1.01	3	209	14.837	13.065 <sup>b</sup>	-1.772
HD 202206	3	2012-07-11 08:29:55	Ks	1.15	4	180	14.849	12.920 <sup>b</sup>	-1.929
HD 211847	1	2012-07-06 07:02:57	Ks	1.07	4	272	6.613	7.171	0.558
HD 211847	2	2012-07-13 06:54:37	Ks	1.05	5	283	6.614	7.167	0.553
HD 30501	1	2012-04-07 00:08:29	Hx5e-2	1.60	3	217	22.372	36.377	14.005
HD 30501	2	2012-08-01 09:17:30	Hx5e-2	1.42	10	212	22.505	35.120	12.615
HD 30501	3	2012-08-02 08:47:30	Hx5e-2	1.53	8	237	22.507	35.102	12.595
HD 30501	4	2012-08-06 09:42:07	Ks	1.28	7	235	22.514	35.031	12.517

<sup>a</sup> Maximum RV given  $M_2 \sin i$  only.

<sup>b</sup> Largest mass companion only.

**Table 6.4:** Estimated orbital semi-amplitude and RV separation of the companions, given the companion mass ( $M_2$  or  $M_2 \sin i$ ) from Table 6.2 and observation times from Table 6.3.

Companion	Estimated $K_2$ ( $\text{km s}^{-1}$ )	Estimated $ \Delta RV $ ( $\text{m s}^{-1}$ )	Phase coverage (%)
HD 4747	-10.65	—	—
HD 162020	-98.92 <sup>a</sup>	2388	0.28
HD 167665	-14.47 <sup>a</sup>	145	0.18
HD 168443b	-64.65 <sup>a</sup>	258	0.035
HD 168443c	-18.05 <sup>a</sup>	<1	0.001
HD 202206B	-6.79	78	0.74
HD 202206c	-2.50	<1	0.15
HD 211847B	-1.85	5	0.09
HD 30501	-16.12	1410	5.8

<sup>a</sup> Maximum  $K_2$  only given  $M_2 \sin i$ .

All observations were reduced using the DRACS pipeline with the artefact corrections method applied (see Section 5.1.3). Each observation was then: wavelength calibrated using a synthetic telluric spectrum, corrected for telluric absorption, and then corrected for the barycentric RV following Sections 5.2.1, 5.2.2 and 5.2.4.

### 6.2.3 Calculation of expected RV

Before the differential subtraction method is presented, calculations are performed to estimate the RV of both components in each observations and the likely separation between the companions between observations. The time of each observation is used as input into Equation 2.6 along combined with the orbital parameters from Table 6.2 to calculate the expected RV of the host star. These values calculated are provided in Table 6.3 as  $RV_1$ . For the companion, the mass ( $M_2$  or  $M_2 \sin i$ ) is used alongside the stellar mass from Table 6.1 to calculate the RV of the companion (see Section 2.1.2). This is given as  $RV_2$  in Table 6.3. The RV difference in between the host and companion for each observation is also computed and provided as  $rv_2 = RV_2 - RV_1$  although this will not be used until Chapter 7.

I am not sure if this is the best location for this section.

For these observations the maximum estimated RV separation between the two companion spectra in  $\Delta RV$  is calculated following Equation 6.5 below and provided in Table 6.4. This table also contains the estimated semi-major RV amplitude for the companion  $K_2$  (from Equation 2.14) and the phase coverage of the observations. The phase coverage is the maximum fraction of the orbit covered between the observations for each target. For HD 4747 the  $\Delta RV$  and phase coverage values are missing due to the single observation.

The full orbital solution for the components along with the times of observations are displayed later in Section 6.5.

### 6.3 Direct Subtraction Method

Here the direct subtraction method used is presented. The basic premise is to take two high resolution spectra of a binary system at separate phases, transform them to the rest frame of the star and take the difference to remove the spectrum of the host star, leaving behind a residual comprised of difference of two companion spectra with different Doppler shifts. Similar techniques originally developed to separating binary stars (Ferluga et al., 1997) and has been used for a M-dwarf with a low-mass companion (e.g. Kostogryz et al., 2013).

Assuming that the instrumental profile and atmospheric absorption are dealt with appropriately the spectra of the observed targets are assumed to be composed of two spectral components: a bright host star blended with the spectrum of a faint companion. The spectrum received from the host-companion pair is given by the superposition of two spectral components ( $J_1, J_2$ ):

$$I(\lambda) = J_1(\lambda - v_1) + J_2(\lambda - v_2), \quad (6.1)$$

where the subscripts 1 and 2 indicate the spectrum of the host and companion respectively,  $\lambda$  represents the wavelength of the spectra and  $\lambda - v$  represents the Doppler shift  $\lambda(1 - v/c)$  by a velocity  $v$ .

This can be shifted into the rest frame of the host star by applying the shift  $v_1$ :

$$I(\lambda + v_1) = J_1(\lambda) + J_2(\lambda - v_2 + v_1). \quad (6.2)$$

To analyse  $J_2$ , the spectral component of interest, the component from the host needs to be carefully removed. If two observations of the same target are observed, denoted with subscripts  $a$  and  $b$ , there will be relative motion between the components due to the orbit. Assuming that the stellar spectra do not change over time<sup>3</sup> ( $J_{1a} = J_{2a}$ ) and each spectrum can be individually Doppler shifted to the rest frame of the host star  $J_1(\lambda)$ , then the spectrum of the host star can be removed through subtraction of the two observations. Mutually cancelling the host component leaves two components of the companion subtracted from each other, with a relative Doppler shift between them.

$$\begin{aligned} S(\lambda) &= I_a(\lambda + v_{1a}) - I_b(\lambda + v_{1b}) \\ &= (J_{1a} + J_{2a}(\lambda - v_{2a} + v_{1a})) - (J_{2b} + J_{2b}(\lambda - v_{2b} + v_{1b})) \\ &= J_{2a}(\lambda - v_{2a} + v_{1a}) - J_{2b}(\lambda - v_{2b} + v_{1b}) \end{aligned} \quad (6.3)$$

$$S(\lambda + v_{2a} - v_{1a}) = J_{2a}(\lambda) - J_{2b}(\lambda - v_{2b} - v_{1a} + v_{1b} + v_{2a}) \quad (6.3)$$

$$S(\lambda') = J_{2a}(\lambda) - J_{2b}(\lambda - \Delta RV_2) \quad (6.4)$$

where,

$$\Delta RV_2 = v_{1a} - v_{1b} - v_{2a} + v_{2b} \quad (6.5)$$

is the RV difference between the two companion spectral components when the host components are mutually subtracted, and  $\lambda' = \lambda + v_{2a} - v_{1a}$ .

The resulting differential spectra  $S(\lambda')$ , dubbed *s-profile* by Ferluga et al. (1997), is composed of just the companion spectra, shifted and subtracted from itself.

---

<sup>3</sup> (Kostogryz et al., 2013) find the stellar activity residual is smaller than the companion differential flux.

Ferluga et al. (1997) provide an analytical form for the *s-profile* given a single Gaussian line of the form  $J(\lambda) = 1 - D \cdot \exp^{-\pi(\lambda-\lambda_0)^2/W^2}$ :

$$S(\lambda) = 2D \cdot \exp^{-\pi D^2[(\lambda-\lambda_0)^2+(k/2)^2]/W^2} \cdot \sinh \frac{\pi D^2(\lambda-\lambda_0)k}{W^2}, \quad (6.6)$$

where  $\lambda_0$ ,  $D$ , and  $W$  are the central wavelength, depth and equivalent width of the Gaussian line, and  $k = \Delta RV_2$  is the shift between the two companion spectra.

From binary dynamics (e.g. Murray et al., 2010) the RV amplitudes of the host and companion (ignoring the system velocity *gamma*) are related through the mass ratio,  $q$ , while having an opposite sign<sup>4</sup> (see Section 2.1.2):

$$v_2 = -q * v_1 \quad (6.7)$$

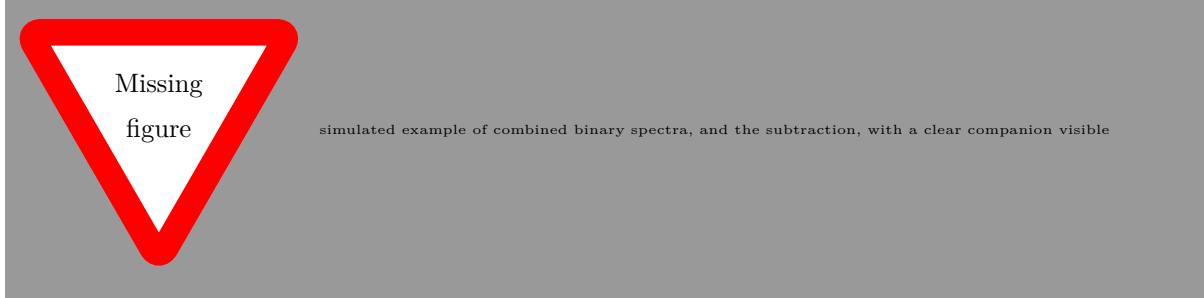
We can simplify Equation 6.5 by expressing it in terms of the mass ratio and host RV only:

$$\begin{aligned} \Delta RV_2 &= qv_{1a} - qv_{1b} + v_{1a} - v_{1b} \\ &= (1+q)(v_{1a} - v_{1b}). \end{aligned} \quad (6.8)$$

If the  $\Delta RV_2$  between the companion spectra is able to be constrained or derived from the s-profile (see Ferluga et al., 1997) then the mass ratio of the system,  $q$ , can be determined, thereby constraining the mass of the companion.

The values  $v_{1a}$  and  $v_{1b}$  are radial velocity of the host components. The host's RV are calculated using the Equation 2.6 with the orbital parameters from the literature and provided in Table 6.2. These are used to shift each spectrum into the rest frame of the host star to mutually cancel the host's spectrum. These components can also be determined directly from the spectrum by cross-correlating the observed spectrum with a stellar template of the host and gave results in reasonable agreement. There should be checks for consistency between  $v_{1a}$ ,  $v_{1b}$  and how well the host component is removed in the s-profile.

Example simulations?



This method is very similar to Kostogryz et al. (2013), which obtain two observations from the extrema of the RV curve of a M-dwarf with a low-mass companion. They also perform a number of simulations regarding observing CRIRES spectra with different brown dwarfs. Figure out the flux ratio limit they get too???

It is necessary to have a consistent instrumental setup (Ferluga et al., 1997), to avoid introducing extra instrumental effects (e.g. slit-width and/or filters) into the spectral differentials and to always observe the same wavelength range and maximize the information to be extracted. For these observations,

<sup>4</sup> The opposite sign arises from a 180° difference in the angle of periapsis,  $\omega$ , for the companion.

check it is in this chapter

put in advanced concepts chapter???

this ignores  $\gamma$

check result

the second observation of HD 202206 and fourth of HD 30501 were taken with different filters compared to the other observations. Therefore, these two observations could not be used for this differential analysis. As noted in Hadrava (2009), any spectral differences in the filters would add extra unknown signal/noise making it harder to disentangle the faint spectral differences.

## 6.4 Results of spectral differential analysis

The spectral differential procedure outlined above was applied to the wavelength-calibrated, telluric- and barycenter- corrected CRIRES observations. The spectra were first Doppler shifted to the rest frame velocity of the system by applying a shift of  $-\gamma$ . Each spectra is then shifted by its  $-RV_1$  so that the host lines are at rest. Finally one spectrum is subtracted from the other as described above.

Although this is attempted on all targets only the most favourable case, HD 30501, is shown in Figure 6.1. It is favourable because it is the second largest companion in the sample at  $90 M_{\text{Jup}}$  but also has the second largest RV separation between observations. The top panel shows the reduced CRIRES spectrum of HD 30501 from detector 1 without telluric correction. The telluric model is also shown in the top panel. The middle panel shows the CRIRES spectra corrected with the telluric model. The differential spectra recovered for HD 30501 is shown at the bottom panel of Figure 6.1. The shaded regions indicate where the telluric green and host star blue spectra are  $> 4\%$  deep. This indicates that the features of the differential spectrum near these shaded regions are likely due to imperfect telluric correction and host cancellation.

The mutual cancellation of the stellar host seems to work well for the  $\sim 40\%$  deep line near 2117 nm, with the line being completely removed, but it does not do so well for the smaller  $\sim 10\%$  deep line around 2121.5 nm. The residual for the large  $\sim 40\%$  deep telluric line near 2118.5 nm is still quite prominent. Around 2120 nm there is wide negative residual around three neighbouring telluric lines,  $\sim 10\%$  deep. One possible explanation for this is that the continuum normalization near 2120 nm was influenced by this grouping of lines.

To understand the observed differential signal simulations were performed of a differential spectrum of HD 30501 using a synthetic PHOENIX-ACES spectra with parameters  $T_{\text{eff}}=2500 \text{ K}$ ,  $\log g=5.0$ , and  $[\text{Fe}/\text{H}]=0.0$ , with the RV offset estimated from the observation times. These parameters represent an estimated companion  $T_{\text{eff}}$  with the metallicity and  $\log g$  similar to the host (closest grid model). The model spectra were convolved to  $R = 50\,000$ , continuum normalized and scaled by the estimated flux ratio of the companion. In this simulation a synthetic host or telluric spectra is not included and as such simulates the differential result of a “perfect” host cancellation with no telluric contamination present. This is the ideal-case scenario, and it is stressed that it is impossible to simulate the effect of improper telluric correction in a meaningful way. When comparing the simulated and observed differential in the bottom panel of Figure 6.1, there is a striking amplitude difference. The orange-dashed line of the simulated differential spectrum amplitude is of a much smaller scale than the observed differential. This simulation demonstrates that the amplitude of the differential signal of HD 30501 expected is much smaller than the residuals created by the differential technique applied to these observations.

The amplitude of the differential signal is lower than expected due to the very low  $\Delta RV$  between the observation pairs. The maximum  $\Delta RV$  between observational pairs, for the targets investigated in this work, are provided in Table 6.4. In the best target in this sample, HD 30501, the  $\Delta RV_2$  of the companion between observations is  $1.41 \text{ km s}^{-1}$ . For comparison, a single Gaussian absorption line, to be

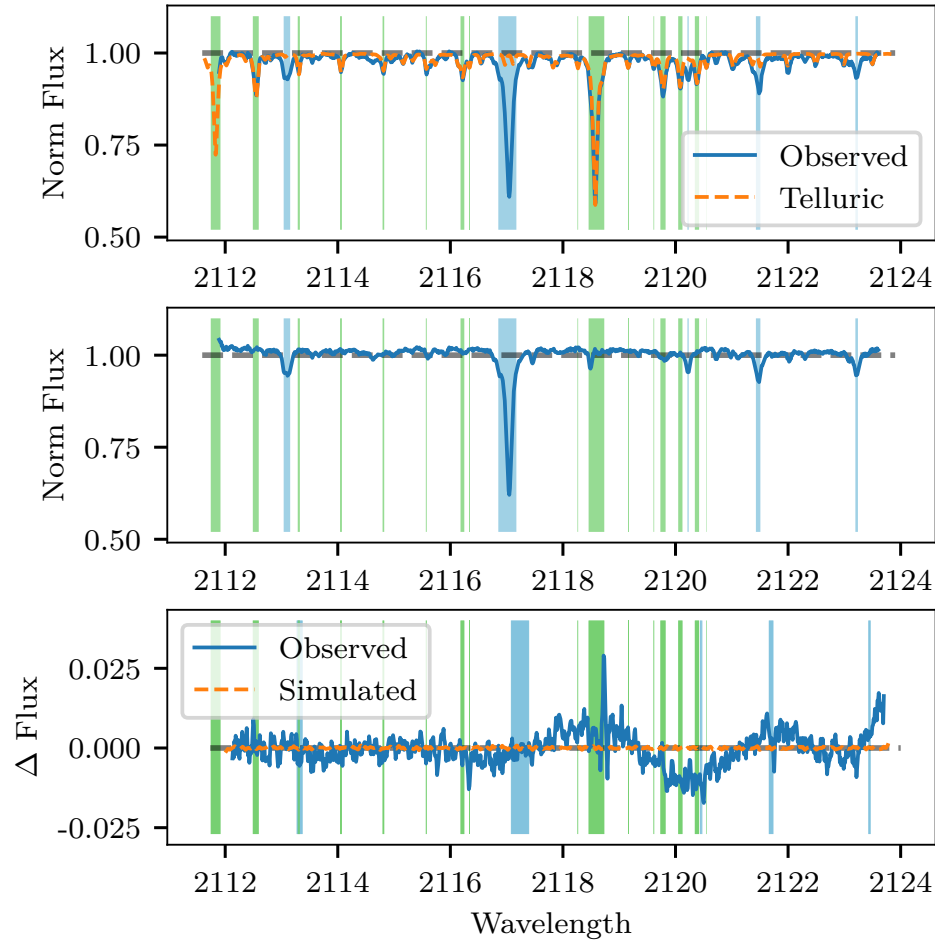


**Figure 6.1:** Top: A reduced CRIRES observation of HD 30501 (blue) for detector 1 between 2112–2124 nm along with the TAPAS telluric absorption model (orange dashed) used for the wavelength calibration and telluric correction. Middle: The telluric corrected spectra. Bottom: (blue) Differential spectra for HD 30501 between observations 1 and 3. (orange dashed) Simulated “perfect” differential using PHOENIX-ACES spectra with parameters  $T_{\text{eff}}=2500$  K,  $\log g=5.0$ , and  $[\text{Fe}/\text{H}]=0.0$ , with the same  $\Delta RV$  as the observations. The shaded regions indicate where the telluric green and host star blue spectra are > 4% deep.

shifted by  $\Delta\lambda = \text{FWHM}$  would need a  $\Delta RV$  of  $v_{\text{FWHM}} = c/R \approx \sim 6 \text{ km s}^{-1}$ . Since the  $\Delta RV_2$  are shifted by a significant smaller value than the line FWHM, the spectral lines of the companion also mutually cancel themselves, diminishing the amplitude of the differential signal significantly. As the companion spectra are already faint (with a flux ratio at the percent level) the differential signal is not detectable in these observations at the achieved noise level.

When the  $\Delta RV$  of the companion is smaller than the FWHM of a line there is a mutual subtraction of the companion spectra, diminishing the detected amplitude of the differential signal, and removing the ability to detect the companions using this method. The observations need to be spaced further apart in time/phase to achieve a larger  $\Delta RV_2$  separation and increase the amplitude of the differential. Once there is a separation there will be complex interactions between neighbouring lines that need to be accounted for.

#### 6.4.1 Relative differential amplitude

Further investigation was performed into the differential subtraction under small  $\Delta RV$ . This is done by exploring the amplitude of the differential against a variation in RV. Simulations were performed creating a differential spectra for a range of  $\Delta RV$ s between  $\pm 10 \text{ km s}^{-1}$  using the same PHOENIX-ACES spectra for the companion of HD 30501 ( $T_{\text{eff}}=2500 \text{ K}$ ,  $\log g=5.0$ ,  $[\text{Fe}/\text{H}]=0.0$ ) convolved to  $R = 50\,000$ . These simulations were focus on the wavelength range 2110–2123 nm, corresponding to detector #1 of the CRIRES observations. The differential spectra was created for each by taking the synthetic spectrum for the companion, Doppler shifting a copy of the spectrum and subtracting it from the original. At each RV step the maximum absolute differential amplitude (peak to peak) of the simulated differential spectrum observed was recorded. Again these simulations are performed assuming perfect telluric correction and removal of the host star by only considering the spectrum of the companion alone.

The result of this simulation is shown in Figure 6.2. As this absolute amplitude is specific to the lines present in the analysed wavelength range, the values were normalized by the median amplitude value outside of the line FWHM (dashed vertical lines), between  $\pm(7 - 10) \text{ km s}^{-1}$ , to give a relative differential amplitude, independent from the depth of a specific line. Differential subtraction simulations we also performed using a spectrum made up of a single Gaussian or Lorentzian line; these are shown in Figure 6.2 as the orange dashed and green dash-dotted lines respectively. The spectral profile shape of the differential for the Gaussian line was also checked for consistency with the analytical form of the differential spectra from Ferluga et al. (1997, Equation A.1) (included above as Equation 6.6).

Figure 6.2 shows that with a  $\Delta RV$  of zero between companion spectra the spectral lines of the companion completely cancel each other out, resulting in zero amplitude. As the RV separation increases in either direction, the individual lines stop completely cancelling begin as they begin to separate. A maximum differential amplitude is achieved when the individual lines are fully separated. The shape/width of the differential spectral lobes Ferluga et al. (e.g. 1997, eqn. A.1) was not considered, but this could also have been measured.

At simulated separations beyond  $10 \text{ km s}^{-1}$  the neighbouring spectral lines begin to strongly interfere, leading to a variable (quasi-sinusoidal) relative amplitude, although this is not shown here. The shape of the relative amplitude becomes complicated due to the line interaction and because the  $\Delta RV$  for all observations fall well short of this region it was not investigated further. It is suspected that the interaction of neighbouring lines is one possible cause for the difference in the relative differential amplitude between the single theoretical line profiles and synthetic spectrum between 2 and  $6 \text{ km s}^{-1}$ .

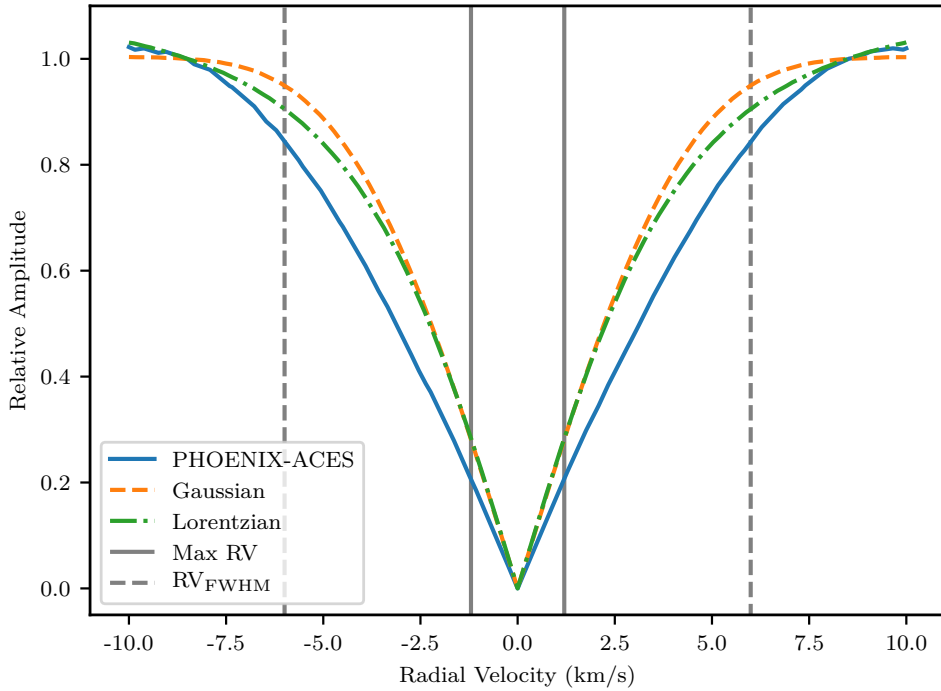


**Figure 6.2:** Simulated relative amplitude of differential spectra at different companion  $\Delta RV$  separations revealing the diminished amplitude at very small orbital separations. The solid blue line shows the maximum relative amplitude of the differential signal (from a shifted copy of itself) of a PHOENIX-ACES spectrum with  $T_{\text{eff}}=2500$  K,  $\log g=5.0$ ,  $[\text{Fe}/\text{H}]=0.0$  in the wavelength region 2110–2123 nm. The maximum difference is normalized by the median amplitude between  $\pm 7$ – $10 \text{ km s}^{-1}$ , representing a complete line separation. The orange (dashed) and green (dot-dashed) lines represent the relative amplitude of a spectrum differential for a spectrum containing a single Gaussian or Lorentzian absorption line respectively, each with a unitary amplitude and a  $\text{FWHM} = \lambda/R$ . The solid vertical lines indicate the estimated companion  $\Delta RV$  in these observations while the dashed vertical lines indicate the RV corresponding to the FWHM at this wavelength and resolution.

The vertical dotted lines indicate the line  $\text{FWHM} = \lambda/R = v/c$  with a velocity of  $6 \text{ km s}^{-1}$  at  $2 \mu\text{m}$  with  $R=50\,000$ , showing that the amplitude is almost maximum when the lines are separated beyond their line width. The two solid vertical lines in Figure 6.2 indicate the  $\Delta RV=1.41 \text{ km s}^{-1}$  separation calculated for our best target, HD 30501 from Table 6.4, given known orbital parameters and the observation times. This shows that our differentials have severely reduced amplitude,  $< 20\%$  relative to well separated individual lines. As the companion spectra are already faint and in combination with a host star at  $>1\%$  flux ratio the  $>80\%$  extra reduction in signal amplitude makes this detection impossible with these observations.

## 6.5 Orbital Solutions

The insufficient observational spacing becomes clear when the orbits are visualized by plotting the RV variation. Figures 6.3 to 6.11 show the RV curves for each target observed for this project. The target stars that have two companions are shown twice, with each companion treated as a single Keplerian (ignoring the presence of the other companion). For each figure the left hand plot shows the RV variation

across a full orbit of the companion, while the plot on the right shows the RV variation for the 6 month observation window of Period 89 only. The solid black line indicates the RV of the host star (with scale on the left hand axis), while the blue dashed line shows the RV of the companion (with the scale on the right hand axis). The orange crosses and red stars indicate on the RV curves the times at which observations were obtained for each target, for the host and companion respectively.

The first thing that is apparent is the variation of shape of the RV curves. This is normal with the variations in shape arise from the different orbital parameters of each target (provided in Table 6.2). In the left hand plots, in which a full orbit is shown, the different shapes are created from the eccentricity,  $e$ , and argument of periapsis,  $\omega$ . In the right hand panels, for which a fixed time period is shown, the orbital period of the companion also plays a role. Specifically the ratio of orbital period to the 6 month observing period determines what fraction (or multiples) of the orbit is displayed.

The RV curves of the star and the planet mirror each other about the systems mean velocity,  $\gamma$ , with the amplitude scaled by their mass ratio,  $q$  (see Equation 2.14), and  $\omega$  offset by  $180^\circ$ .

All the plots, apart from HD 4747, have more than one observations shown, although it can be difficult to see as there observational spacing is small.

For the companions HD 162020b (Figure 6.4) and HD 168443b (Figure 6.6) their orbital periods are shorter than 6 months, allowing for multiple orbits to occur during Period 89. As such the full amplitude range was available to measure in the observing Period if observations were taken at correct times, at the locations of the extrema. It should have been possible to obtain observations in which the companion spectra were sufficiently separated for the differential separation technique. However in reality, the two observations for these two targets were taken immediately after each other, making any differential extremely small. This is ignoring the fact that the flux ratios (from Table 4.4) for these short period companions are estimated to be very low, meaning they would have been very difficult to detect even if observed at the extrema.

The larger companion HD 168443c in Figure 6.7 has a longer orbital period, so it appears as straight line in the right hand panel, although the amplitude variation of the companion during Period 89 is about  $8\text{--}9 \text{ km s}^{-1}$ . Therefore observations taken at the extreme ends of Period 89 may have provided just enough separation to be suitable for the differential.

For HD 202206 about 3/4 of the orbit is covered in Period 89 with a RV amplitude of the companion possible of over  $40 \text{ km s}^{-1}$ . Therefore, in this case well separated RVs could have been obtained.

For the remaining targets with long periods, it is clear that sufficiently separated RVs were not obtained, but also that they were not possible within a single observing period with a RV variation less than  $6 \text{ km s}^{-1}$  during Period 89. For HD 30501 the largest time separation between observations obtained is clearly visible in Figure 6.11. Unfortunately, this did not result in a large enough companion separation. Looking at the full period, if the observations had been obtained in the previous period then sufficient separation could have possibly been obtained.

The code used to create orbital plots similar to those shown here is available under the iastro-pt/Observationtools *Github* repository with documentation available on Read the Docs.

The sampling of points in the orbit reveal that the choice of points was not favourable for the application of the direct subtraction technique. This was unfortunately discovered after attempting to apply the technique.



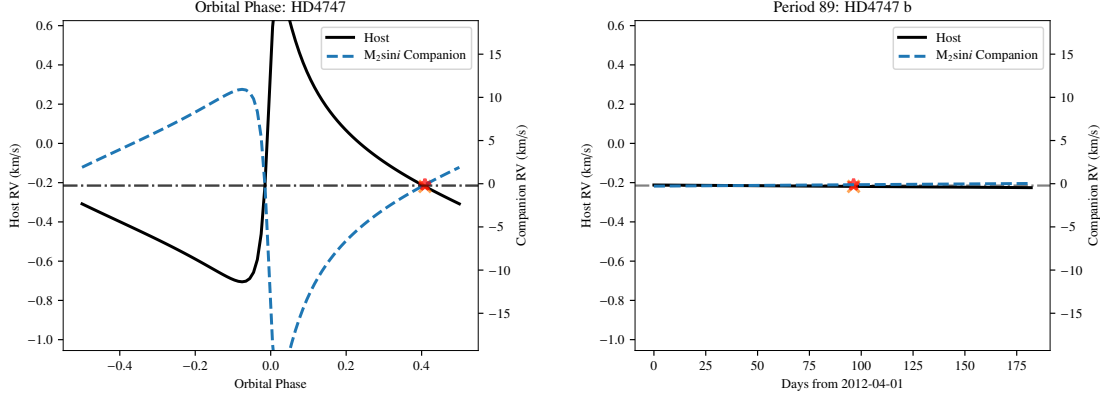


**Figure 6.3:** RV single companion Keplerian orbit for HD 4747. The left hand plot shows the RV curve for one full orbit while the right hand panel shows the RV curve over 6 months (Period 89). The solid black line indicates the RV of the host star (with scale on the left), while the blue dashed line indicates the RV of the companion (with scale on the right axis). The orange crosses and red stars indicate the times at which observations were obtained for the target, for the host and companion respectively.

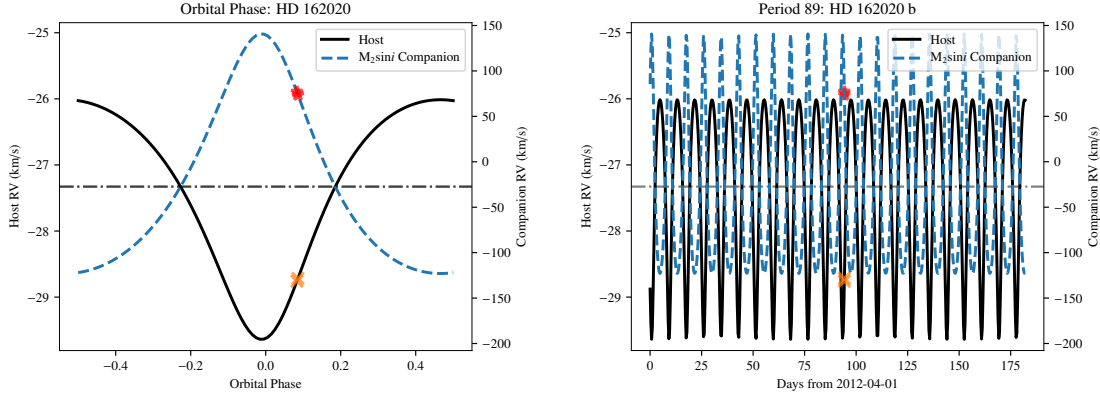


**Figure 6.4:** Same as Figure 6.3 but for HD 162020.

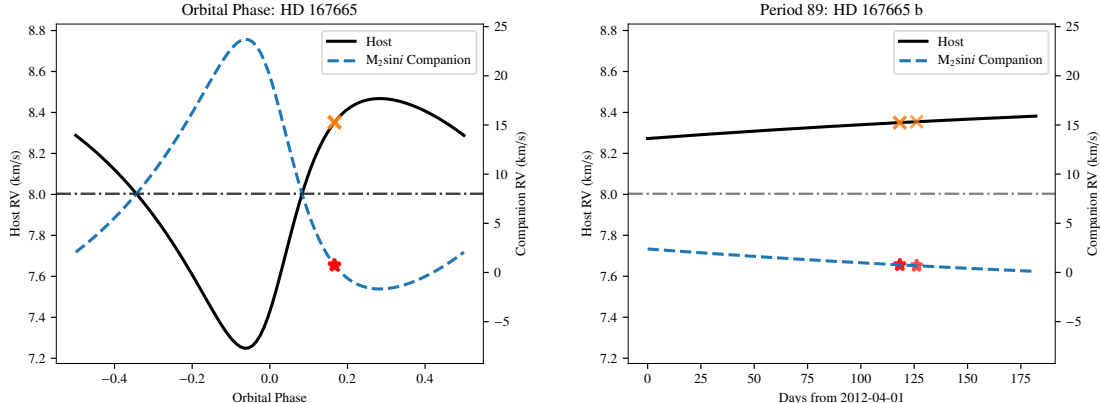


**Figure 6.5:** Same as Figure 6.3 but for HD 167665.

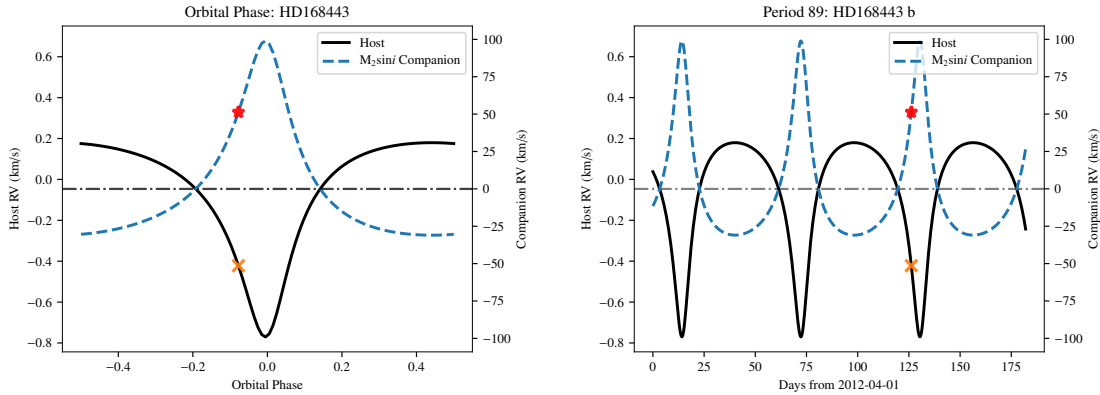


**Figure 6.6:** Same as Figure 6.3 but for HD 168443b. Analysed as if this was a single companion.

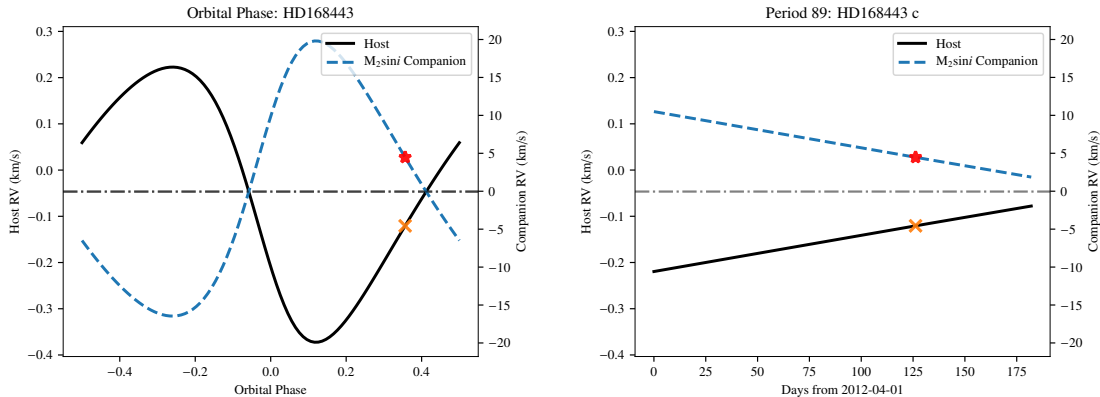


**Figure 6.7:** Same as Figure 6.3 but for HD 168443c. Analysed as if this was a single companion.

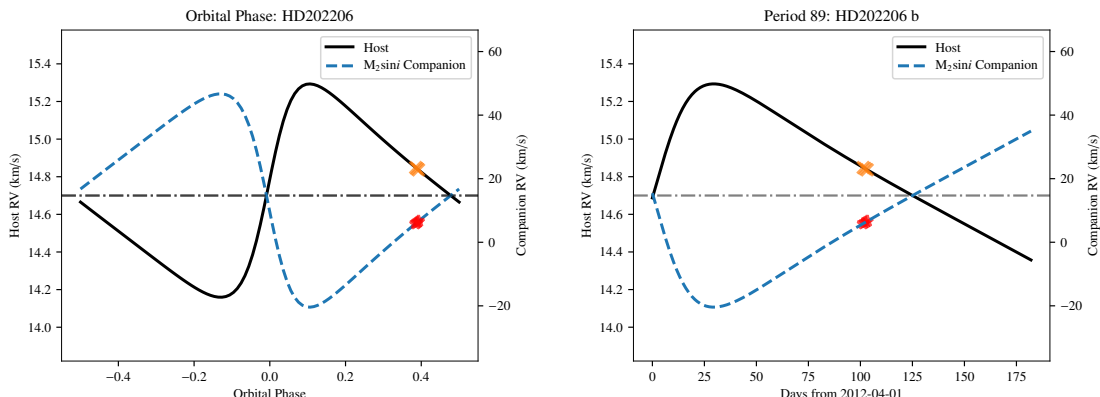


**Figure 6.8:** Same as Figure 6.3 but for HD 202206B. Analysed as if this was a single companion.

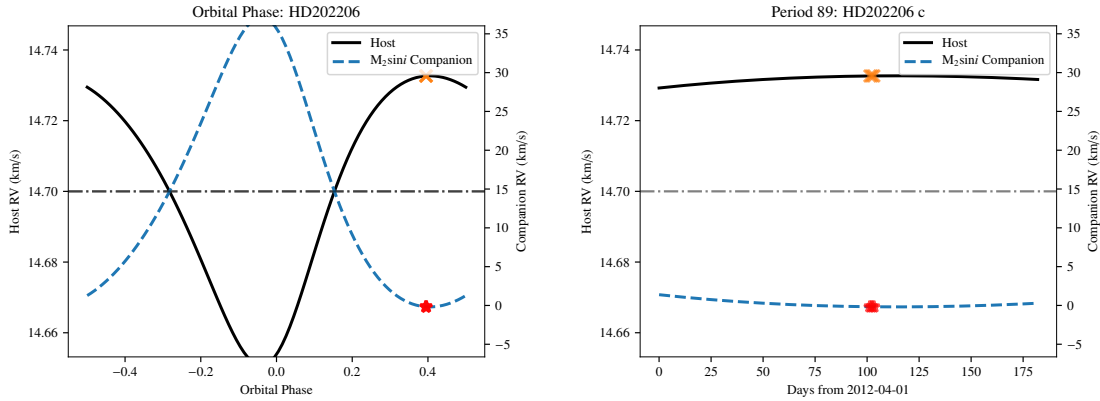


**Figure 6.9:** Same as Figure 6.3 but for HD 202206c. Analysed as if this was a single companion.

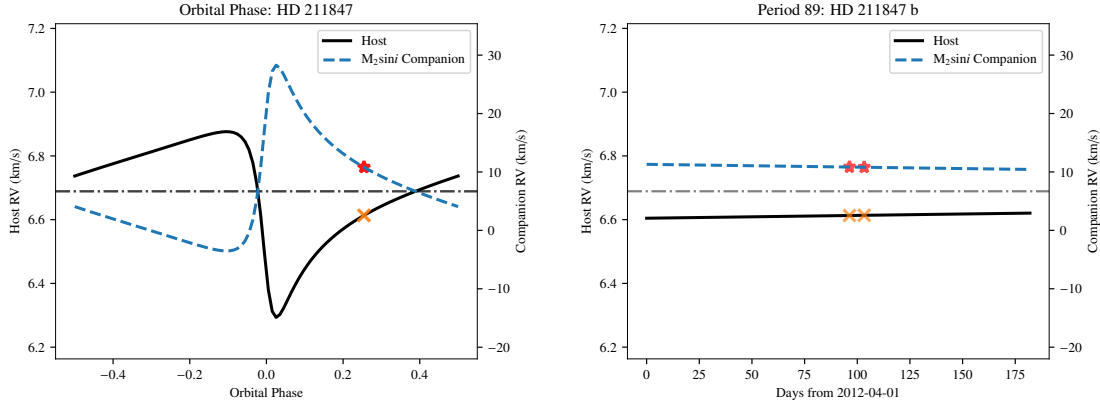


**Figure 6.10:** Same as Figure 6.3 but for HD 211847.

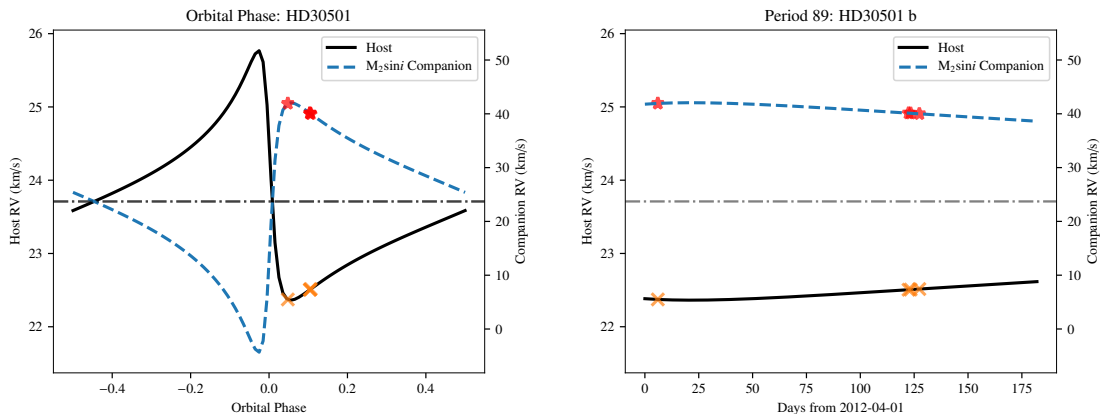


**Figure 6.11:** Same as Figure 6.3 but for HD 30501.

### 6.5.0.1 Differential scheduling challenges

This work has revealed that care needs to be taken in planning the observations for the application of the spectral differential technique of faint companions in the future. Future attempts need to pay attention in particular to: the FWHM of the lines in the region (governed by resolution and wavelength), the estimated companion separation  $\Delta RV_2$ ; and the previous observations from different observing periods, all while keeping the detector settings consistent.

The original goal for the observations was to obtain two different and “clearly separated radial-velocities” for the secondary companion. However, the program was assigned a low-priority (C, in ESO grading) and, possibly due to operational reasons, the original time requirements necessary to secure well separated RVs for the companion spectra could not be met. This meant that all observations were insufficiently separated to extract a differential spectra for the companion.

The long orbital periods of these targets is also a strong contributing factor to the insufficient separations. Most of the targets observed here have orbital periods much longer than an observing semester (183 days). An optimal pair of observations (achieved at the extrema) would need to have been obtained from separate observing periods (between 2 months and 19 years apart). In some cases, even observations taken at the beginning and end of a single observing semester would not be sufficient to achieve a companion separation (depending on the phase and orbital parameters), requiring separate observing periods to even achieve the minimum  $\Delta RV$  larger than the line FWHM. At the time (2012) it was impossible to ask for observation time over several semesters in a regular proposal.

This study demonstrates the importance of proposals for projects that need to be extended over several semesters or years. In the ESO context, this corresponds to “Monitoring proposals” (e.g. ESO, 2017, pg. 18). Observations of the targets explored here, with long orbital periods in particular, would benefit from the new abilities for multi-period proposals and scheduling systems which allow for tighter scheduling constraints, such as a companion RV separation.

For future observations in the context of the differential subtraction technique it is suggested that the best possible orbital solution of the host and companion be used to estimate the companions’ RV curve during the observing period, with the companion  $M_2 \sin i$  providing an RV upper-limit. Radial velocity constraints are also valid for other studies such as the detection of reflected light from exoplanets Martins et al., 2015, e.g. Knowing the instrumental wavelength and resolution, an observing constraint can be set to avoid taking observations when the companion spectra are insufficiently separated, or the  $\Delta RV_2 < \text{FWHM}$ . This constraint can be set using the absolute and relative *time-link* constraints available in ESO’s Phase 2 Proposal Preparation (P2PP) tool. Additionally, analysing the known orbital solution beforehand to determine RV constraints will also help identify the best time to observe, if observations from separate periods will be required or, if an optimally separated companion differential is even feasible. Again the P2PP documentation for this observational proposal could not be obtained to check if these observations had used any of these features, which were available at the time, and set any constraints.

## 6.6 Contrast to other works

In this section brief contrast to other works is given. As stated previously the differential technique is not new being first formulated for binary star separation in Ferluga et al. (1997). This work tried to

Should RV of companion be scale by  $m2\sin i$  only or  $m2$  if known?

extend this to lower contrast ratios, to a hosts with smaller companions.

For lack of high-resolution CRIRES data Kostogryz et al. (2013) explore simulations of the differential approach to a BD companion of a M-dwarf star, in which the contrast ratio is around 1/50 between 1/200 and were observed at the RV extrema. Their favourable wavelength choice to achieve a good contrast ratio is K-band, as done in work, however they chose the CO line region ( $\sim 2310\text{ nm}$ ) where there is several narrow spectral lines. One thing explored in Kostogryz et al. (2013) that is not considered here is the effect of rotational broadening on the mass determination, finding that it should be possible to determine the mass of a slowly rotating companion, but a fast rotating companion is more difficult.

The limitations with regards to the RV separation between spectral components has also been observed in other works. Similarly to the companion-companion RV separation focused on here, Kolbl et al. (2015) find a limitation of  $\sim 10\text{ km s}^{-1}$  RV separation required between the host and the companion. This is because if lines of the host and companion are blended, it is likely the companion spectra will be fitted, or incorporated into the hosts spectra, making it difficult to accurately detect the companions lines a similar RV. The RV difference between the host an companion is given in the last column of Table 6.3 as  $rv_2$ . It can be seen HD 4747, HD 202206, and HD 218447 do not exceed this  $10\text{ km s}^{-1}$  separation with the obtained observations.

## 6.7 Direct recovery in the mIR

It was investigated if this differential technique could be extended into the mid-infrared mIR domain. There were two reasons for this: to develop experience with the mIR domain where the contrast ratios are higher, and due to the lack of high-resolution nIR spectrographs available at the time (see Section 3.4).

VISIR is a mIR spectrograph on the VLT, offering diffraction-limited imaging at high sensitivity in three mid-infrared (mIR) atmospheric windows: the *M*-band at  $5\text{ }\mu\text{m}$ , the *N*-band between  $8\text{--}13\text{ }\mu\text{m}$  and the *Q*-band between  $17\text{--}20\text{ }\mu\text{m}$ , respectively. The use of VISIR to detect the spectra of Brown Dwarf companions in the mIR was briefly explored. The candidate selected as the best target to investigate was HD 219828 which has a hot-Neptune ( $M_2 \sin i = 21\text{ M}_\oplus$ ) (Melo et al., 2007) and a recently discovered super Jupiter ( $M_2 \sin i = 15.1\text{ M}_{\text{Jup}}$ ) on a long period (13 yr) eccentric orbit ( $e=0.81$ ) (Santos et al., 2016).

Based on the spectra of a cool brown dwarfs in the mIR, and the detector configuration available at the time, the best option for the observations was the low resolution mode covering the wavelength region  $8\text{--}13\text{ }\mu\text{m}$ . This wavelength region would have encompassed the  $\text{NH}_4$  signature at  $10.5\text{ }\mu\text{m}$  and the edge of a  $\text{CH}_4$  band at  $7.7\text{ }\mu\text{m}$ , both large features in the BD mIR spectrum.

After performing flux ratio calculations between the host and companion using the Baraffe et al. (2003) models (see Section 4.4.1) and considering the performance of the VISIR instrument and the exposure time calculator it was determined that observations with VISIR to achieve a SNR of 100 were infeasible, requiring 1000's of hours of observing time to achieve the necessary signal-to-noise level to separate the companion from a blended spectra. For a different target, HD 189733 it was calculated that with an exposure time 2 hours the SNR of the host and companion would be 85 and 4 respectively, using the low resolution spectroscopy mode. As such the direct separation approach was not explored further in the mIR.

## 6.8 Summary

This chapter presented the observations that were gathered having in mind the application of a differential subtraction method to recover the spectra of the faint BD companions. Due to the poorly separated observation times relative to the long orbital periods, the differential subtraction method presented in Section 6.3 was revealed to be inappropriate for these observations as the RV separation of the companion spectra between observations is significantly smaller than the width of individual spectral lines. The small separation of the companion causes the lines of the companion to also mutually cancel, severely reducing the residual signal to well below the available noise level. The requirement of well separated RVs for the companion spectra was clearly stated in the original proposal but was not satisfied by the observations, however the very large orbital periods of some of the targets would not produce a sufficient RV signal during one semester was possibly an oversight during the proposal stage. In the following chapter a different technique will be explored in the attempt to extract details of the companion from these observations which were insufficient to apply the differential.

# Chapter 7

## Synthetic companion recovery

Following on from Chapter 6, in which the differential subtraction technique was unsuccessful due to the insufficient separation observations, a second method was attempted to detect the presence of the faint companions. This chapter  $\chi^2$  fitting is used to fit the observed spectra with a two component binary model comprised of synthetic spectra. The preparation of the models is presented as well as an overview of the method. A simulation with an M-dwarf companion is presented first then the observations are attempted. Injection-recovery simulations are performed to understand the results obtained. A discussion of the results and a comparison to other similar techniques is presented at the end.

### 7.1 Binary $\chi^2$ spectral recovery

The approach developed here is to fit the observed CRIRES spectra with a model comprised of a combination of two synthetic spectra, one for the host star and one for the companion. This will be done using  $\chi^2$  methods which have been extensively used in the literature (e.g. Astudillo-Defru et al., 2015; Passegger et al., 2016; Zechmeister et al., 2018; Nemravová et al., 2016; Kolbl et al., 2015). The recoverable from the models will be the temperature of synthetic spectra fitted to the companion which will provide some indication of the companion's spectral type, but will not produce a direct mass constraint that was the original aim of this work.

#### 7.1.1 The $\chi^2$ method

The well known  $\chi^2$  technique measures the weighted sum of the squared deviation between the observation ( $O_i$ ) and the computed models ( $C_i$ ), with the minimum  $\chi^2$  value representing the best-fit parameters:

$$\chi^2 = \sum_i \frac{(O_i - C_i)^2}{\sigma_i^2},$$

where  $\sigma_i$  is the error on each measurement.

The inverse survival function of the  $\chi^2$  distribution is used to determine the confidence levels on the minimum  $\chi^2$  parameters. The inverse survival function returns a  $\Delta\chi^2$  value from the minimum  $\chi^2$  value for a given  $\sigma$  level and degree of freedom<sup>1</sup>. For example, the  $\Delta\chi^2$  for a single degree of freedom required

<sup>1</sup> In Python with the `scipy` package this is a single line `scipy.stats.chi2(dof).isf(1-p)`, where  $p = 0.68$  for  $1-\sigma$ , and

for the 1-, 2-, and 3- $\sigma$  levels is 1, 4, and 9 respectively (Bevington et al., 2003). This method assumes that the measured flux is observed with a SNR sufficiently high so that the noise on the spectrum is approximately Gaussian, and the  $\chi^2$  method appropriate.

For a given observation, the  $\chi^2_{red}$  is computed by  $\chi^2_{red} = \chi^2/\nu$  where  $\nu = n - m$ , the number of observed pixels,  $n$ , minus the number of parameters of interest,  $m^2$ , and is performed after the summation over the detectors. For each observation  $O$ , the  $\sigma$  is estimated using the  $\beta\sigma$  method (Czesla et al., 2018), using the MAD (median absolute deviation about the median) robust estimator. This method estimates the spectral noise using numerical derivatives of the spectra. We followed the procedure outlined in Czesla et al. (2018) to analyse the results from successive parameter combinations to settle on an order of approximation (derivative level) of 5, and a jump parameter (pixels skipped to avoid correlations) of 2. The same  $\sigma$  is applied to all points in the spectrum so that  $\sigma_i = \sigma$ . The  $\beta\sigma$  method provided  $\sigma$  estimates for the target spectra which correspond inversely to signal-to-noise ratios between 100–400, which are similar to the values given in Table 6.3 calculated only from the continuum of detector 2.

The computed models  $C(i)$  are described in Section 7.1.2 and result in a multidimensional grid of  $\chi^2$  values for each combination of model parameters, namely the spectral temperature, host RV, and companion RV for each: detector, observation, and target.

The global minimum of the multidimensional  $\chi^2$ -space is used to represent the best fitting model combination to the observed spectra. The multidimensional  $\chi^2$  grid is summed across multiple detectors to also determine a global minimum  $\chi^2$  for the whole observation  $\chi^2_{obs} = \sum_{n=1}^N \chi_n^2$ , where  $N$  is the number of detectors used. However, the separate observations are not combined as the RV parameters of the host and companion will vary between each observation<sup>3</sup>. For that a model that incorporates the phase information will be needed but is beyond the scope here due to the limited number of observations (1–4). A promising method to incorporate the phase information and detection planetary spectra is given by (Lockwood et al., 2014; Piskorz et al., 2016).

### 7.1.2 Computed model spectra

In this section the transformation of the synthetic PHOENIX-ACES spectra into the computed models ( $C_i$ ) is explained. These computed models are then used to fit to the observed spectra.

Firstly, this assumes that the synthetic spectra are loaded and converted to consistent units. The loading is easily performed using Starfish’s GridTools, which can load the library spectra with a list of stellar parameters [ $T_{eff}$ ,  $\log g$ , [Fe/H],  $[\alpha/Fe]$ ]. The PHOENIX-ACES spectra are then converted from spectral energy distribution **add unit** to photon flux **add unit** by multiplying by the wavelength (multipliable constants ignored). The spectra are also convolved to the matching resolution of the observations, in this case  $R=50\,000$ . Due to the properties of convolution this is performed first and not required to be performed after the model spectra are created. It would be computationally expensive, to perform convolution on every model combination  $C_i$ .

These synthetic spectra are used individually for the single component model and combined together into a binary model. The results of these models are interpolated to the wavelength grid of the observed spectra and the  $\chi^2$  calculated by comparing the model and observation at each point.

---

<sup>2</sup> dof is the degree of freedom.

<sup>2</sup>  $m = 2$  or  $4$  in the examples explored below

<sup>3</sup> Since the current observations are insufficiently separated, it may be possible to combine the separate observations; but in general this would not be the case

The synthetic spectra are multiplied by the wavelength to convert it into photon counts, ignoring multiplicative constants, as done in Figueira et al. (2016)<sup>4</sup>. The spectra were convolved with a Gaussian kernel to match the resolution of the observations ( $R = 50\,000$ ). Due to the distributive property of convolution it is efficient to apply it once to each spectra first, before the spectral pairs are combined.

### 7.1.2.1 Single component model

The single model  $C_i^1$  comprises of a single synthetic spectrum,  $J$ , (with model parameters  $T_{\text{eff}}$ ,  $\log g$ ,  $[\text{Fe}/\text{H}]$ ,  $[\alpha/\text{Fe}]$ )  $[\alpha/\text{Fe}]$  and is Doppler shifted by a RV value  $rv_1$ .

$$C_i^1(\lambda) = J(\lambda_0(1 - \frac{rv_1}{c})) \quad (7.1)$$

where  $\lambda$  is the shifted wavelength,  $\lambda_0$ , the model rest wavelength and,  $c$ , the speed of light in a vacuum. The model's flux is then continuum normalized to unity to match the observed spectra, and interpolated to the wavelength grid of the observation.

This single component model analysis is similar to the Passegger et al. (2016)  $\chi^2$  fitting. A similar re-normalization (see Section 7.1.3) as Passegger et al. (2016) is used to account for slight differences in the continuum level and possible linear trends between the normalized observation and model. However, no dynamical masking was applied to sensitive lines to make the  $\chi^2$  minima more distinct or linearly interpolate the stellar parameters between the grid models to obtain high precision stellar parameters. This is because we are not trying to derive precise stellar parameters but to detect the spectra of the companions. Instead radial velocity components are included in the  $\chi^2$  fitting, which is not included in Passegger et al. (2016).

### 7.1.2.2 Binary model

The model spectrum in the binary situation is considered to be the superposition of two synthetic spectral components, one each for the host and companion respectively. Both spectra are Doppler shifted by  $rv_1$  which represents the RV motion of the host star, while the companion spectra is also Doppler shifted by a second RV,  $rv_2$ , representing the RV offset between the host and companion. This choice is arbitrary, but in this way the mean motion of the system relative to Earth is captured only in  $rv_1$ . The two spectra are scaled by their squared radius (see Section 7.1.2.3) then added together, thus fixing the relative amplitude of the two components. Given two spectral components  $J_1$  and  $J_2$  with radii  $R_1, R_2$  this equates to

$$\begin{aligned} C_i^2(\lambda) = & J_1(\lambda_0(1 - \frac{rv_1}{c})) \times R_1^2 + \\ & J_2(\lambda_0(1 - \frac{rv_1}{c})(1 - \frac{rv_2}{c})) \times R_2^2 \end{aligned} \quad (7.2)$$

The combined spectra is continuum normalized by dividing by an exponential fitted to the continuum of the combined spectrum, as the Rayleigh-Jeans regime is assumed. This assumption here is wavelength dependent and other appropriate continuum normalization techniques are also valid. In the case of a BD companion around an FGK star investigated here, the continuum is dominated by the contribution from the host star as it contributes the majority of the spectrum with flux ratios around 2110–2165 nm below  $\sim 1\%$ .

---

<sup>4</sup> Synthetic models provide the spectral energy distribution ( $\text{erg s}^{-1} \text{cm}^2 \text{cm}^{-1}$ ).

We combine the models in this way to represent the correct absolute flux ratio of the components. The median flux ratio between the two components is calculated for the wavelength range used here as an indication of the flux ratio level.

The binary model should provide meaningful information about the companion parameters (e.g.  $T_{\text{eff}}$ ) and an estimate of the flux ratio of the system. These can be combined with the Baraffe et al. (2003) models to constrain the mass of the companion. However, we need to be careful with this model as the inclusion of extra spectral components and associated parameters could also provide a better fit to observations which do not have a companion, by fitting components of the noise.

The full list of grid parameters for the binary model are  $T_{\text{eff}}_1$ ,  $\log g_1$ ,  $[\text{Fe}/\text{H}]_1$ ,  $[\alpha/\text{Fe}]_1$ ,  $rv_1$ ,  $T_{\text{eff}}_2$ ,  $\log g_2$ ,  $[\text{Fe}/\text{H}]_2$ ,  $[\alpha/\text{Fe}]_2$ ,  $rv_2$  where the subscripts 1 and 2 indicate the host and companion models respectively.

### 7.1.2.3 Effective radius

To combine the two synthetic spectra with the correct observed flux ratio we need to integrate the emitted flux over the effective surface area of each emitting body respectively. Ignoring the common multiplicative constants that will disappear with normalization, we scale the two synthetic spectra individually by the square of their respective radii,  $R_1$  and  $R_2$ .

In this work we use the effective radius (PHXREFF keyword) of each component from the PHOENIX model headers. This is the radius used in modelling the stellar atmospheres. We use this radii as it is directly tied to each model spectrum, and already available. The ratio of the radii from the two synthetic spectra in the binary models are provided in Table 7.1.

We are aware that using these radii has its limitations since as stated previously: there is a degeneracy in BD mass, age, and luminosity of the companion, and in particular a combination of radius-mass and radius-age relationships (Sorahana et al., 2013). Using the PHOENIX-ACES model effective radius does not allow for any independent age constraints to be incorporated, or allow for any variability in the radii to account for uncertainties.

The targets analysed here do not have transits, but if the radius ratio can be independently determined from the photometric transit method (Deeg, 1998) then this could be used to constrain the radius ratio used when combining the binary model spectra instead.

### 7.1.3 Re-normalization

Slight trends in the continuum level between the observed spectra and computed models were removed using the re-normalization following Passegger et al. (2016):

$$F_{re-norm}^{obs} = F^{obs} \cdot \frac{\text{continuum fit}_{model}}{\text{continuum fit}_{observations}}. \quad (7.3)$$

The polynomial continuum fits to the normalized observations and models are used to re-normalize the observed spectrum to the continuum of the models. For detectors 1–3 a polynomial of first degree was used, while for detector 4 a quadratic is needed to fit the edge of a strong Hydrogen line (Brackett- $\gamma$ ) at 2166 nm, which lies just off of detector 4. This broad line is only observed in the synthetic spectra and not in the reduced observations. It is assumed that this was normalized out during the reduction process.

For each model we further allow the continuum level to be varied by  $\pm 0.05$  as a free parameter taking the model with the smallest  $\chi^2$  value.

### 7.1.4 Reducing parameters

The high dimensionality of the binary model makes it computationally challenging and difficult to analyse the  $\chi^2$  space. For reference, the multiplicative parameter space is squared when increasing from one spectral component in the single model to a binary model, and therefore becomes computationally expensive. In general the number of possible parameter combinations for  $c$  spectral components each with a grid of  $m$  models increases to  $c^m$ . If the full set of PHOENIX-ACES library spectra (66456) is explored with a binary fit then this naively balloons to over 4.4 billion possible combinations. Half of these are not unique as the host and companion components are swapped. This is the worst case scenario and we implement a number of assumptions to vastly reduce the parameter-space enabling faster computation.

Our first assumption is to restrict ourselves to models with an Alpha element abundance ( $[\alpha/\text{Fe}]$ ) of zero. This is likely a very good approximation as all our targets have solar metallicity and are thus very likely to belong to the thin disk of the Galaxy, where  $[\alpha/\text{Fe}]$  values are close to zero (i.e., solar) Adibekyan et al. (2012, e.g.). Our second is to assume that we can significantly reduce the search space with literature values for the host star. We fix the metallicity of both components to the closest grid to the literature value (usually  $[\text{Fe}/\text{H}]=0.00$ ). We also fix the  $\log g$  of the host star to its literature values given in Table 6.1. The uncertainties on the literature measurements for  $\log g$  ( $\sim 0.1$ ) and metallicity ( $\sim 0.05$ ) are both smaller than the grid steps of 0.5 for these parameters. The  $\log g$  of the companion is obtained from the Baraffe et al. (2003) and Baraffe et al. (2015) evolutionary models for the given companions  $M_2/M_2 \sin i$  and hosts age.

We use the estimated companion temperatures from the Baraffe evolutionary models given the companion (minimum) mass and stellar age as a starting point for the companion spectra grid computation and extend the grid in each direction, within the model limits. For example we show the companion temperature grid spanning  $-600$  to  $+400$  K in Figure 7.1 and  $\pm 400$  K in Figures 7.2 and 7.3.

The large numbers stated above also do not include the RV grid for each component. The RV grid is user defined and the number of spectra /models to consider increases when the RV grid step size is decreased (finer RV resolution). We can reduce the RV grid space significantly by tailoring it to the target being examined. For each target, we use the estimated RV values from the observation time and orbital parameters, given in Table 6.3 as a centre starting point for the  $rv_1$  and  $rv_2$  values and increment the RV within a few FWHM around those values, or out to the targets  $K_1$  and estimated  $K_2$  values.

An iterative process could be implemented to refine the RV grids, starting at a larger grid with lower RV resolution then performing a higher resolution grid about the minimum  $\chi^2$  RV values. This was only done manually but could have been automated. One could expect that a good starting RV grid step be governed by the spectral resolution, e.g. comparable to the FWHM velocity.

For the companions targets with fully resolved orbits the known RV of the host star,  $rv_1$  could also have been fixed. We however left this free to see if the known value would be recovered by the fitting.

Example with  
a large mass  
companion?  
and/or SNR.

## 7.2 Results

Here we show the results from applying the companion recovery model to simulated observations and to an observation.

**Table 7.1:** Input and recovered parameters on simulations and an observation when applying a single ( $C^1$ ) and binary ( $C^2$ ) models. The logg and metallicity were fixed at  $\log g_1 = 4.50$ ,  $\log g_2 = 5.0$  and  $[Fe/H]=0.0$  equally for both components. Gaussian noise was added to both simulations with a SNR of 150. Here  $m$  and  $n$  are the number of data points and parameters used in each model.

	Simulation 1			Simulation 2			Observed HD 211847		
	Input	Recovered		Input	Recovered		Expected	Recovered	
		$C^1$	$C^2$		$C^1$	$C^2$		$C^1$	$C^2$
$T_{\text{eff}1}$	5800	5800	5800	5700	5800	5700	$5715 \pm 24$	5900	5800
$T_{\text{eff}2}$	4000	—	3800	3200	—	3100	$\sim 3200$	—	$>3800^{\text{a}}$
$rv_1$	0	0.1	0	6.6	6.6	6.6	$6.6 \pm 0.3$	7	7.6
$rv_2$	10	—	9.8	0.5	—	-1	$0.5 \pm 2$	—	-12.6
$R_1/R_2$	2.57	—	2.71	3.16	—	3.27	3.16	—	$<2.71^{\text{a}}$
$F_2/F_1$	0.084	—	0.066	0.030	—	0.026	0.030	—	$>0.066^{\text{a}}$
$m$	-	3072	3072	—	3072	3072	—	2612	2612
$n$	-	2	4	—	2	4	—	2	4
$\chi^2$	—	4978	3792	—	3746	3630	—	37 688	33 860
$\chi^2_{\text{red}}$	—	1.62	1.24	—	1.22	1.18	—	21.3	19.2
BIC	—	-20 145	-22 315	—	-21 477	-21 377	—	18 281	14 468

<sup>a</sup> At the arbitrary upper limit for companion temperature grid (3800 K).

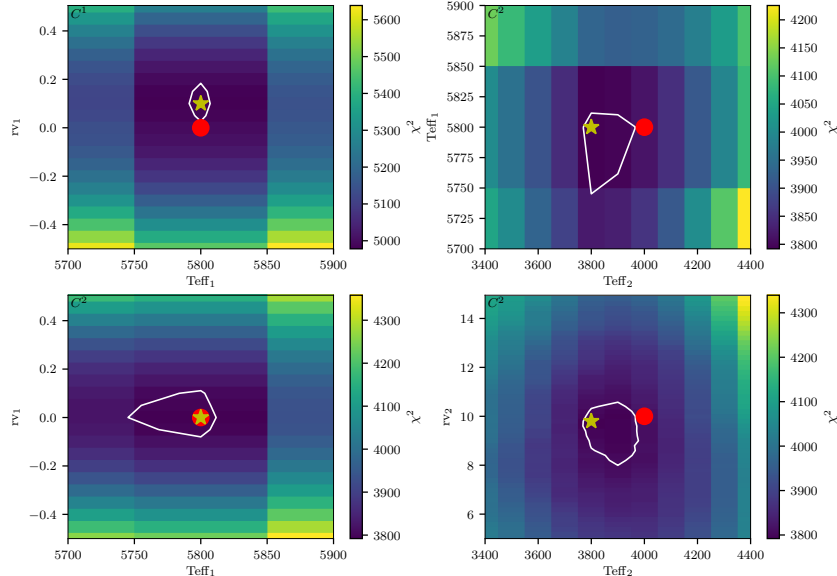


**Figure 7.1:**  $\chi^2$  results for companion recovery of a simulated binary observation of a Sun-like star ( $T_{\text{eff}1} = 5800$  K) with an M-dwarf companion ( $T_{\text{eff}2} = 4000$  K). The top right plot shows the application of a single component model ( $C^1$ ) while the other three are using a binary model ( $C^2$ ). Both left hand panels show the distribution of host temperature and host RV. The top right panel shows the distribution for host and companion temperature, and the bottom right the companion temperature and radial velocity. The red circle and yellow star indicate the location of the simulation input and recovered parameters respectively. The white box is centred on the parameter values and shows the grid resolution.

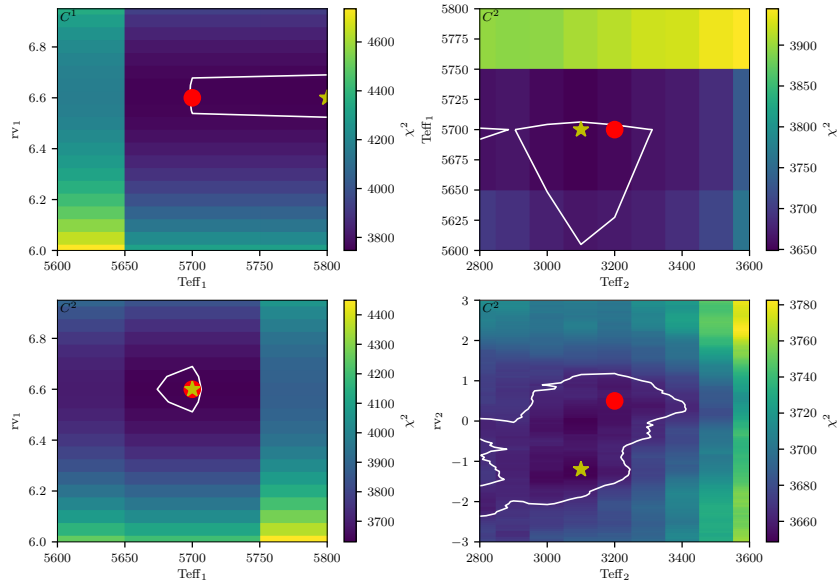


**Figure 7.2:** Similar to Figure 7.1,  $\chi^2$  results for companion recovery of a simulated binary observation similar to HD 211847, ( $T_{\text{eff}1} = 5800\text{K}$ ,  $T_{\text{eff}2} = 3200\text{K}$ ). The top right plot shows the application of a single component model ( $C^1$ ) while the other three are using a binary model ( $C^2$ ). Both left hand panels show the distribution of host temperature and host RV. The top right panel shows the distribution for host and companion temperature, and the bottom right the companion temperature and radial velocity. The red circle and yellow star indicate the location of the simulation input and recovered parameters respectively. The white line shows a  $3-\sigma$  confidence level about the minimum  $\chi^2$  solution grid point. Each box is centred on the parameter values and shows the grid resolution.

### 7.2.1 Simulated binaries

To test the companion recovery method we create simulated binary observations using PHOENIX-ACES spectra. White noise was added with a standard deviation  $\sigma = 1/\text{SNR}$ , for a given signal-to-noise (SNR) level. We then applied the grid-matching recovery technique detailed above and compared the resulting parameters to the inputs.

The results of two example binary simulations are displayed in Figures 7.1 and 7.2, both simulated with a SNR of 150. The input and recovered parameters for the binary components are indicated by the red circles and yellow stars respectively, and are given in Table 7.1. The  $3\sigma$  contour is shown in white on the plots to indicate the shape of the confidence level only. The  $1\sigma$  contours are not shown here as they are much smaller than the temperature grid step and are not easy to visualize at this scale as they are often smaller than the marker shown at the minimum location. Each coloured rectangle is centred on the grid point, with its shape indicating the resolution of the grid space searched.

The first simulation shown in Figure 7.1 is for a Sun-like star with a M-dwarf companion, with a  $T_{\text{eff}2} = 4000$  K. The top-left panel shows the recovered host parameters when the single model is applied to the simulated binary. The top-right and both bottom panels are the parameters recovered when using the binary model. Both left-hand panels display the parameters for the host component to easily compare between models. With both models the host temperature  $T_{\text{eff}1}$  is correctly recovered. The host RV,  $rv_1$ , is  $0.1 \text{ km s}^{-1}$  (two grid spaces) different from the simulated value for the single component model and is correctly recovered with the binary model.

The minimum  $\chi^2$  location for the companion temperature is 200 K below the simulated value, and the RV of the companion recovered is  $0.2 \text{ km s}^{-1}$  below the input value. The input values for the companion are just outside of the  $3\sigma$  contours shown. The flux ratio for the input is 0.08 while the flux ratio recovered is 0.066.

The second simulation shown in Figure 7.2 is performed with parameters to mimic the observation of our target with highest flux ratio, HD 211847. In this simulation the single component model recovers a host with the correct RV but a temperature 100 K higher than the input value. Again, adding the companion with the binary model recovers the correct host temperature. The companion temperature recovered is 100 K lower than the input temperature and the RV is different by  $2 \text{ km s}^{-1}$  which is around one third the FWHM.

In this case with a companion RV offset,  $rv_2$ , near  $0 \text{ km s}^{-1}$  the host and companion lines are blended. The same spectral lines from both components are trying to match to the same features of the spectra, making it more difficult to recover the companion parameters. In the bottom right panel there appears to be multiple minima for different  $rv_2$  and  $T_{\text{eff}2}$  combinations, which we assume is partially due to the small  $rv_2$ .

In both simulations the reduced  $\chi^2_{\text{red}}$  for the binary model is closer to 1. This is not surprising as the binary model contains extra parameters. As mentioned above, we need to be careful, as the extra components from the binary may just happen to fit components of the noise when a binary is not present, or in our case has a low flux ratio. the significance between the two models is analysed using the “Bayesian Information Criterion” (BIC) (G. Schwarz, 1978);

$$BIC = n \ln(m) - 2 \ln(\hat{L}). \quad (7.4)$$

Here  $n$  and  $m$  are the number of parameters and data points respectively and  $\hat{L}$  is the maximum of the

### Gaussian likely-hood function

$$\hat{L} = \left( \frac{1}{\sigma\sqrt{2\pi}} \right)^m \exp \left( -\frac{\chi^2}{2} \right), \quad (7.5)$$

written in terms of  $\chi^2$  and a fixed  $\sigma$  for all data points. The maximum likely-hood of a Gaussian distribution is equivalent to minimizing the  $\chi^2$ . In both simulations  $\Delta BIC > 10$  so the preference of the binary model, with the lower BIC value, over the single component model is considered *significant*.

#### 7.2.2 HD211847 observation

HD 211847 is the best candidate for detection as it has a  $155 M_J$  low-mass star companion Moutou et al. (2017). The angular separation of the two bodies is 222 mas (or 11.3 au). Even though it is not a BD it has the highest estimated flux ratio in our sample, of 0.03 based on the Baraffe et al. (2015) evolution models and the known companion mass (see Table 4.4). The angular separation of HD 211847B is 222 mas with a projected distance of XXX. The result of applying  $\chi^2$  fitting to the second observation of HD 211847 is shown in Figure 7.3.

[find projected distance](#)

For this target the metallicity of both components was fixed to 0.0 and the logg for the host was fixed at 4.5. The logg for the companion is fixed to 5.0, based on the Baraffe et al. (2015) evolutionary models for the given companion mass and system age. The orbital solution was used to refine the RV search space of both components. The span RV for the companion was extended until a value inside the RV bounds was found.

Again the top left panel of Figure 7.3 shows the recovery with a single component model with the other three for the binary model. The single component model finds a temperature of 5900 K for the host with a  $rv_1$  of  $7 \text{ km s}^{-1}$ . This is 200 K and  $0.4 \text{ km s}^{-1}$  different above the expected parameters. The binary model finds a host temperature of 5800 K, which is the second closest model to the literature value,  $>100$  K different. The host RV value recovered with the binary model is  $7.6 \text{ km s}^{-1}$ , which is  $1 \text{ km s}^{-1}$  higher than expected. For the single component model there is a barely noticeable secondary minima near this  $7.6 \text{ km s}^{-1}$  RV value recovered by the binary model. Again these RV differences are smaller than the FWHM of the lines. The  $3-\sigma$  contour is small, just visible on the right hand side of the star in the bottom left panel, and hidden behind the markers in the other panels.

For the companion in the binary model, on the right side of Figure 7.3, the minimum  $\chi^2$  for the companion temperature is at the upper temperature limit of the grid shown. If we extend the grid of companion temperature towards higher temperatures the best fit location continues to increase in temperature, continually hitting the upper limit until it is close to the host temperature,  $>2000$  K above the expected companion temperature. When the companion temperature becomes this high it also affects the recovered parameters for the host star to offset the features of the brighter companion.

The  $\chi^2_{red}$  values for the single and binary models are 21 and 19 respectively, far from 1, indicating that both models are a poor fit to the observations. The  $\Delta BIC = 3812 > 10$  indicating that binary model is still preferred. We plot the binary model for the best fit solution alongside the observed spectra in Figure 7.4. We see that there is a large spectral mismatch between the synthetic models and the observation. Extra wavelength masking was applied to many of the largest mismatched synthetic lines to remove their influence. The grey areas mark regions which have been masked out, either from the centres of deep telluric lines (the thin masks matching spectral gaps), or the more prominent mismatched lines in the synthetic spectrum excluded from the  $\chi^2$  analysis. One clear example of a mismatched line is a

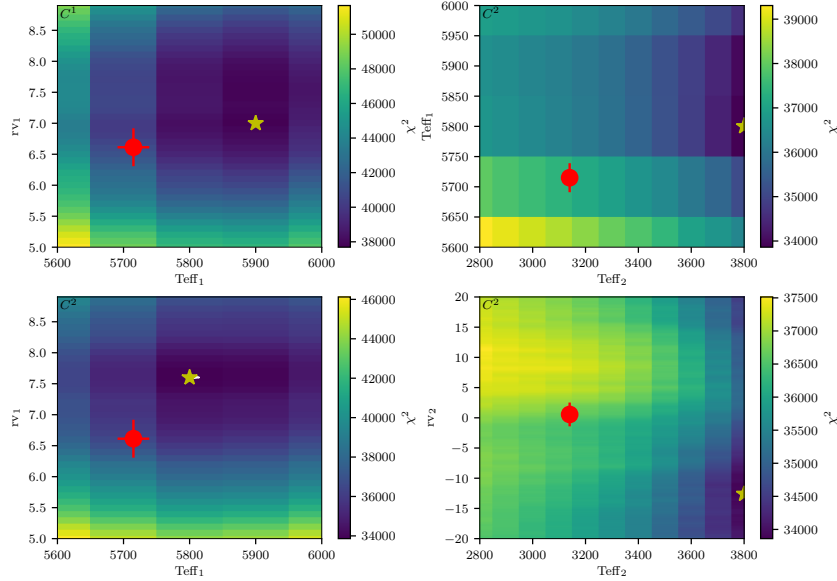


**Figure 7.3:**  $\chi^2$  result grid for observation 2 of HD 211847, similar to Figures 7.1 and 7.2. The top right plot shows the application of a single component model ( $C^1$ ) while the other three are using a binary model ( $C^2$ ). Both left hand panels show the distribution of host temperature and host RV. The top right panel shows the distribution for host and companion temperature, and the bottom right the companion temperature and radial velocity. The red circles indicate the literature values or calculated parameters for the target while the yellow star indicates the minimum  $\chi^2$  solution. The error bar on the  $T_{\text{eff},1}$  is from the literature while the error bars on  $rv_1$  and  $rv_2$  are calculated by propagating the orbital parameter uncertainties through the radial velocity equation. The white line shows a 3- $\sigma$  confidence level about the minimum  $\chi^2$  solution grid point, not always visible here due to the large  $\chi^2$  values.

synthetic line at 2132.5 nm that is clearly not observed in detector 2 (top right). Even with the majority of the mismatched lines removed the detection of the companion was still unsuccessful.

For detectors 1 and 2 it appears that the synthetic spectra contain many more deeper lines than observed. For detector 3 the red half of the detector was masked out as there appears to be an offset between the observed lines. With 3–4 lines that appear to be consistently offset from the observation it could be a wavelength calibration issue, although the telluric lines appear to be sufficiently corrected in this region, attesting for the quality of the wavelength calibration, and making it incompatible with the offset. For detector 4 the observed lines do not agree at all with the models. With many observed lines not in the model and only one line with some agreement in wavelength, detector 4 is masked out completely and not used in the  $\chi^2$  fit. Individual inspection of the  $\chi^2$  results for each detector also revealed that there was a large discrepancy between the 4th detector and the other three, with a different RV value for the host star and a  $\chi^2$  values an order of magnitude higher. The edge of a deep Hydrogen line (Brackett- $\gamma$ ) off the edge of the detector 4 is also clearly seen in the continuum of the model >2162 nm.

We applied this same method to the remaining targets, with similar results. In brief, we conclude that the companion spectra cannot be correctly detected in our data using this method.

The error on estimated RV values, shown in Figure 7.3, is calculated by applying the general error propagation formula (Ku, 1966) to the RV equation (Equation 2.12) and using the errors on the published

Put error paragraph in a good location

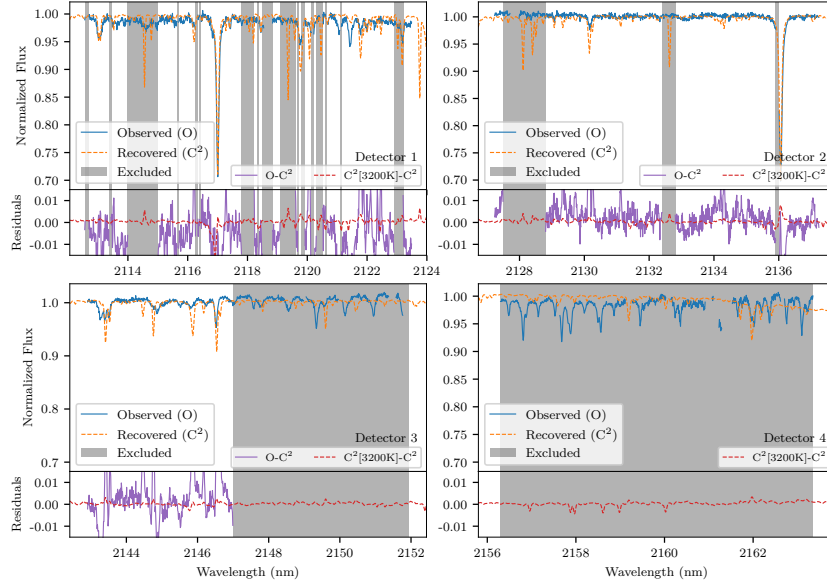


**Figure 7.4:** Comparison between the observed HD 211847 spectrum (blue) and the best fit synthetic binary model (orange dashed) for each detector. The bottom section of each panel shows the residuals between the parts of the observation used in the  $\chi^2$  fit and recovered binary model ( $O - C^2$ ) in purple. The red dashed line shows the difference between the recovered binary model and the binary model with the exact same parameters except for the estimated companion temperature of 3200 K ( $C^2[3200\text{K}]-C^2$ ). The grey shading indicated the wavelength regions where masking has been applied. The thinner masked regions that match with cuts in the observed spectra are where the centres of deep (>5%) telluric lines that have been masked out are.

orbital parameters. For a function,  $f$ , with errors on the inputs  $\delta x, \delta y$  etc., it follows:

$$f = f(x, y, z, \dots) \quad (7.6)$$

$$\delta f = \sqrt{\left(\frac{\partial f}{\partial x}\delta x\right)^2 + \left(\frac{\partial f}{\partial y}\delta y\right)^2 + \left(\frac{\partial f}{\partial z}\delta z\right)^2 + \dots} \quad (7.7)$$

### 7.2.3 Companion injection-recovery

To determine the detection limits for this method we employ an injection-recovery approach. We take the observed spectra and inject onto them a synthetic companion, at the absolute flux ratio to which it would have been added to a synthetic host with the same parameters. The injected companion RV is set to  $100\text{ km s}^{-1}$  so that the companion lines are well separated from the lines of the host. This separation chosen is slightly larger than what we have with our observations,  $rv_2$  given in Table 6.3.

We restrict the search space by fixing the host parameters  $T_{\text{eff},1}$  and  $\log g_1$  to those recovered fitting the non-injected spectra by a single component model. The wavelength masking is used to reduce the level of mismatch between synthetic and observed spectra.

We apply the recovery method developed above on the injected spectrum, leaving only the companion  $T_{\text{eff},2}$  and  $rv_2$  parameters free, to recover the injected companion. We repeated this for injected companions with temperatures below 5000 K.

**Table 7.2:** Upper mass limits of target companions assuming a companion  $\log g=5.0$ . Masses are derived from Baraffe et al. (2015) evolutionary models using  $T_{\text{eff}}$  and  $\log g$ . The flux ratio  $F_2/F_1$  is the absolute flux ratio between the cut-off temperature and the target host star.

Target	$T_{\text{eff}}$ cut-off (K)	$F_2/F_1$	Mass limit ( $M_{\text{Jup}}$ )
HD 4747	3 900	0.084	598
HD 162020	3 900	0.147	598
HD 167665	3 800	0.054	560
HD 168443	4 000	0.094	618
HD 202206	3 900	0.075	598
HD 211847	3 900	0.079	598
HD 30501	3 800 <sup>a</sup>	0.106	560

<sup>a</sup> From observed spectra

We also perform the injection-recovery with synthetic host spectra, representing each target. The wavelength range of the synthetic spectra used for this is three sections interpolated to 1024 values in the wavelength span of detectors 1, 2, and 3. For each section, Gaussian noise is added at the level measured in the corresponding detector in the observation of the target being represented.

In Figure 7.5 we show the results of the injection-recovery on HD 30501. The blue dots represent the recovered companion temperature when injected into real observations, while the orange triangles represent injection into a synthetic host. Error bars of  $\pm 100$  K are included to indicate the grid size, and do not come from the recovery itself. The black dashed diagonal is the temperature 1:1 relation, where a correctly recovered companion should lie.

The grey shaded region indicates the  $\pm 1000$  K temperature range explored for the injection-recovery of the companion. This shows how the bounds of the grid are recovered at low temperatures.

For HD 30501 the injection onto synthetic and observed spectra produce similar results. At temperatures above 3800 K, in both the real and synthetic spectra, the injected companion is recovered within 100 K. For injected companion temperatures below 3800 K the temperature recovered is systematically higher than the injected value. This indicates that the companion is not correctly recovered and is affected by the added noise. We determine this temperature to be the upper temperature limit for the recovery. For the other stars we could not conclude on the upper limit due to spectral mismatch issues. In these cases we use the results from the synthetic injection to derive a temperature recovery cut-off for each target, each simulated with the closest host star spectrum.

In Figure 7.6 we show the minimum  $\chi^2$  for each companion temperature in the recovery grid. We do this for 7 different injected companion temperatures between 2500 and 4500 K. For the higher temperature companions, the  $\chi^2$  is parabolic in shape, recovering the correct temperature, as expected. At lower temperatures there is a strong asymmetry in the  $\chi^2$  with it flattening out on the lower temperature side. The 1-, 2-, 3- $\sigma$  values (with 2 degrees of freedom) of 2, 6 and 11 above the minimum  $\chi^2$  are not shown in the bottom panel of Figure 7.6 which is a close-up around the minimum  $\chi^2$  as are indistinguishable in the top panel due to the  $\chi^2$  y-scale. The black vertical line indicates the 2300 K temperature limit of the PHOENIX-ACES models.

Using the temperature cut-off values, we derive an upper mass limit for the companions around

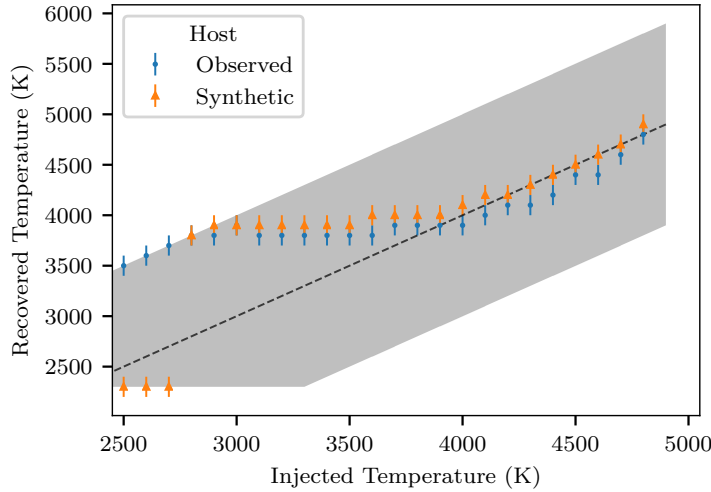


**Figure 7.5:** Result of simulated injection-recovery of synthetic companions on HD 30501. The blue dots and orange triangles indicate the recovered companion temperature for the observed and synthetic spectra respectively. The  $\pm 100$  K error bars are the grid step of the synthetic models. The black dashed diagonal shows the 1:1 temperature relation. The grey shaded region indicates the  $\pm 1000$  K temperature range explored. Gaussian noise added to the synthetic spectra was derived from the observed spectra.

our stars using the Baraffe et al. (2015) evolutionary models, finding the closest point matching the spectral temperature cut-off and  $\log g = 5.0$ . These values are given in Table 7.2 and are between 560 and  $618 \text{ M}_{\text{Jup}}$ . The flux ratio between the cut-off and the host star are also provided for, being between 5 and 15% in this wavelength span.

Hoeijmakers et al. (2015) Context. The spectral signature of an exoplanet can be separated from the spectrum of its host star using high-resolution spectroscopy. During these observations, the radial component of the planet's orbital velocity changes, resulting in a significant Doppler shift that allows its spectral features to be extracted.

Aims: In this work, we aim to detect TiO in the optical transmission spectrum of HD 209458b. Gaseous TiO has been suggested as the cause of the thermal inversion layer invoked to explain the dayside spectrum of this planet.

Methods: We used archival data from the 8.2 m Subaru telescope taken with the High Dispersion Spectrograph of a transit of HD 209458b in 2002. We created model transmission spectra that include absorption by TiO, and cross-correlated them with the residual spectral data after removal of the dominating stellar absorption features. We subsequently co-added the correlation signal in time, taking the change in Doppler shift due to the orbit of the planet into account.

Results: We detect no significant cross-correlation signal due to TiO, though artificial injection of our template spectra into the data indicates a sensitivity down to a volume-mixing ratio of  $\sim 10^{-10}$ . However, cross-correlating the template spectra with a HARPS spectrum of Barnard's star yields only a weak wavelength-dependent correlation, even though Barnard's star is an M4V dwarf that exhibits clear TiO absorption. We infer that the TiO line list poorly matches the real positions of TiO lines at spectral resolutions of  $\sim 100\,000$ . Similar line lists are also used in the PHOENIX and Kurucz stellar atmosphere suites and we show that their synthetic M-dwarf spectra also correlate poorly with the HARPS spectra of Barnard's star and five other M dwarfs. We conclude that the lack of an accurate TiO line list is currently

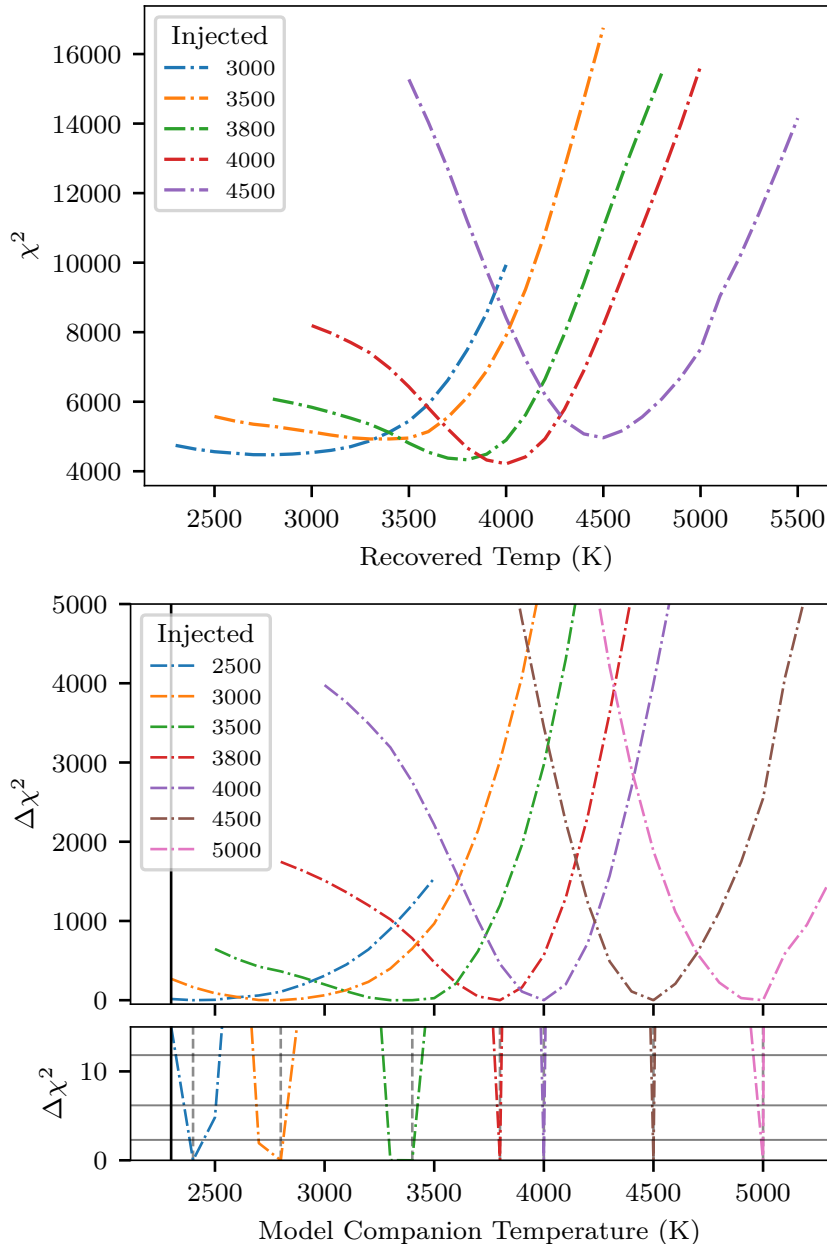


**Figure 7.6:** Top: Companion temperature versus  $\chi^2$  for simulations with different injected companion temperatures. Other fixed parameters for these fully synthetic simulations was  $T_{\text{eff}1} = 5200$  K,  $\log g_1 = 4.5$ ,  $\log g_2 = 5.0$ , and both  $[\text{Fe}/\text{H}] = 0.0$ . A fixed Gaussian noise corresponding to a SNR of 300 was used. Bottom: A close up view of  $\chi^2 < 15$ . The three horizontal grey lines indicate the 1-, 2-, 3- $\sigma$  with 2 degrees of freedom. The vertical dotted lines indicate the location of the minimum  $\chi^2$  recovered for each companion. The black solid vertical in both panels shows the 2300 K cut-off of the PHOENIX-ACES models

critically hampering this high-resolution retrieval technique.,

#### 7.2.4 Junk from paper about BT-settl

The PHOENIX-ACES models also provide dimensions of effective radius of the star, in the header. This is required for the method presented here as we need to scale the spectra by their respective surface area when combining together.

The effective radius of the modelled star are provided in the fits header and required for the calculation of the flux ratio.

As we do not recover suitable results for HD 211847 which is supposed to have a temperature around 3400 K we suspect that it is not possible for lower temperature either so don't try to extend to the BT-Settl models.

**PHOENIX-ACES defines grid as  $T_{\text{eff}}$ ,  $\log g$  and Mass which can then be used to determine Radii. See (Husser et al., 2013) section 2.3.1 Mass.**

#### 7.2.5 Note about a target - discussion of results

Another example is HD 162020, which has the lowest orbital period (8.4 days) of our targets. It should have been possible to obtain an optimal pair of observations in one semester, but the second observation was taken immediately following the first. This means that the  $\delta RV = 0.363 \text{ km s}^{-1}$  between the two observations, is comparable to the  $\Delta RV$  that occurs during each individual observation. With tighter scheduling restrictions this target could have been observed with the optimal RV separation at the extrema of  $\Delta RV = 2K_2$ . Whether the flux ratio of  $7e^{-6}$  for this target and the interaction of different spectral lines would have made it possible to recover companion mass is a separate issue.

##### 7.2.5.1 Wavelength range

The wavelength choice for the spectra analysed here, observed with the intention to apply the spectral differential technique, was selected due to the location of the  $K$ -band telluric absorption window. This wavelength range, with a narrow wavelength range  $\sim 50 \text{ nm}$  set by the CRIRES instrument. This wavelength range is likely not the best choice for the proposed study. may contribute to the poor results Finish this line

For instance Passegger et al. (2016) used four different spectral regions for the precise parameter determination of M-dwarfs. Specific lines from the different wavelength regions are affected differently by the model parameters:  $T_{\text{eff}}$ ,  $\log g$ , and  $[\text{Fe}/\text{H}]$ ; and are used to break degeneracies in the PHOENIX-ACES parameter space.

Changing the wavelength coverage to regions with lines sensitive to stellar parameters for both stars and BDs, as well as using a larger wavelength range that will be achieved by CRIRES+, may help to improve the recovery results of the companion recovery technique presented here. We note that if the wavelength range is increased by taking separate observations at different wavelengths, not covered by a single exposure, then changes in the RV of both components between the different wavelength observations may need to be accounted for.

### 7.2.6 Comparison to other methods

kolbl 2014, passenger 2016, 2018

Contrast our result to other works. More phases, longer integration time, higher SNR.

kolbl 2015 also have difficult separating spectra with a RV separation below 10 km/s, or when the spectra of the spectra and comandion have small separation.

**CHECK out LOCKWOOD 2014 - maximum likelihood with todcor 1e-4 flux ratio  
double lined spectra**

## 7.3 Summary

# Chapter 8

## Information content of nIR Spectra

The work presented in this chapter focuses on calculating and analysing the information content of stellar spectra, specifically the radial velocity precision in the nIR. This work is not directly related to detecting exoplanet atmospheres themselves but investigates the theoretical and observed RV precision of M-dwarf spectra in the nIR. Aiding future detections of the detection of future This can help in detecting the presence of “habitable Earth-like” planets around M-dwarfs which could become prime targets for future exoplanet atmosphere studies.

The field of exoplanet detection in the nIR is expanding with several new high-resolution nIR spectrographs becoming available in the near future (see Section 3.4). One science objective common to all four instruments is the detection of small mass planets around M-dwarf stars utilizing the radial velocity technique. The fundamental radial velocity precision of M-dwarf spectra attainable at different wavelength regions calculated in Figueira et al. (2016) was used to influence some design choices of SPIRou, NIRPS. For instance NIRPS opted not to cover the  $K$ -band, favouring a higher spectral resolution and simplicity, but preserved the possibility for adding a  $K$ -band spectrograph in a separate cryostat in the future.

The purpose of the work presented in this chapter is to extend the work of Figueira et al. (2016), computing the theoretical RV precision of stellar spectra over a wider range of situations. An investigation into the effect of  $\log g$  and  $[Fe/H]$  on precision is performed and a comparison of RV precision of the recently observed nIR M-dwarf spectra from CARMENES library and their synthetic counterparts will be performed. This is to test how the RV precision of synthetic models compares to reality. The aim is to compare the fundamental precision of observed nIR spectra to the synthetic models.

### 8.1 Overview

The pursuit of detecting exoplanets, especially “habitable” and “Earth-like” planets, requires state-of-the-art instrumentation with high precision. One of the key detection methods, the Radial Velocity (RV) method, measures the wobble induced on the Star by the planet as they orbit their common barycentre .  
add Some stuff about mass and period from Pedros paper

The number of nIR spectrographs focusing on cooler M-dwarfs stars is increasing, which have a

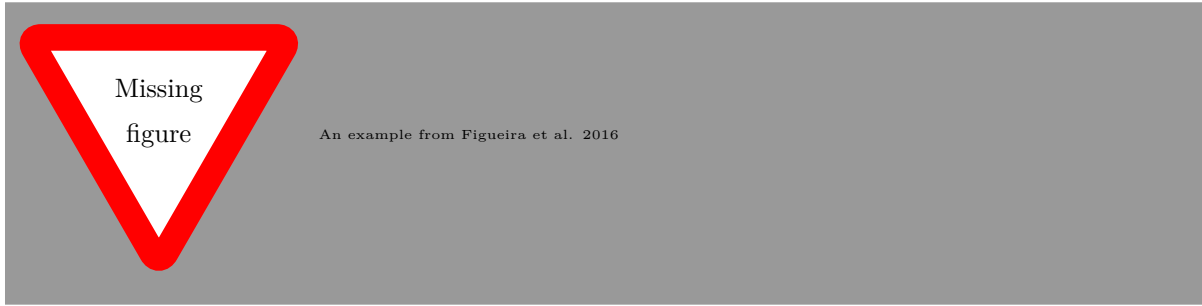
remove duplication

rv method

put in introduction??

derivation of rv?

relatively better chance of detecting Earth-like planets in the habitable zone. This work continues the assessment of RV precision levels possible in the nIR domain, an extension of (Figueira et al., 2016).



Artigau et al. (2018) recently compared archival spectra of Barnard’s Star, an M-dwarf, and found that state-of-the-art atmosphere models over-predict the *Y*- and *J*-band RV content by more than a factor of  $\sim 2$ , while under-predicting the *H* and *K*-band content by half. **in this work we find similar?**

This has previously helped to aid the direction of instrument design by identifying the wavelength regions with the best RV precision (Figueira et al., 2016) but can also help in the planning of observations, by understanding how the precision changes with spectral type and observed SNR.

**THIS is from spie 2018 conference.** red (Quirrenbach et al., 2018) With this strategy it has been possible to achieve  $1\text{--}2 \text{ m s}^{-1}$  precision in the visible and  $5\text{--}10 \text{ m s}^{-1}$  precision in the near-IR; further improvements are expected from ongoing work on temperature control, calibration procedures and data reduction. Comparing the RV precision achieved in different wavelength bands, we find a “sweet spot” between  $0.7$  and  $0.8 \mu\text{m}$ , where deep TiO bands provide rich RV information in mid-M dwarfs. This is in contrast to our pre-survey models, which predicted comparatively better performance in the near-IR around  $1 \mu\text{m}$ , and explains in part why our nIR RVs do not reach the same precision level as those taken with the visible spectrograph.

### 8.1.1 Fundamental photon noise limitation

A technique to calculate the theoretical radial velocity precision of a spectrum using the full spectral information in an optimal way was presented by Connes (1985). Here we provide the radial velocity precision derivation following Connes (1985), Bouchy et al. (2001), and Figueira et al. (2016). A majority of this derivation follows Bouchy et al. (2001) with extra explanations and notes added.

For demonstration purposes Figure 8.1 show a portion of an arbitrary spectrum  $A(\lambda)$ , for demonstration purposes over a wavelength range  $\Lambda$ . Here  $A_0(\lambda)$  is the reference spectrum while  $A(\lambda)$  is observed some later time with an apparent wavelength shift observed. It shows most of a single Gaussian line as spectral lines contain the most information but the requirement of spectral lines is not a requirement.

The Doppler shift of a spectrum is given by:

$$\frac{\delta V}{c} = \frac{\delta \lambda}{\lambda}, \quad (8.1)$$

where  $c$  is the speed of light in a vacuum, and  $\delta\lambda$  is the shift in wavelength  $\lambda$  due to the velocity  $\delta V$ .

Using basic calculus  $\delta y = \frac{\partial y}{\partial x} \delta x$ , and for a Doppler shift that is small compared to the line-width<sup>1</sup>,

add  $\delta A$  to plots

intensity  
change from  
connes is ver-  
tically in the  
slice d lambda

<sup>1</sup> Although Connes (1985) show that the approximation in Equation 8.2 is adequate under all circumstances

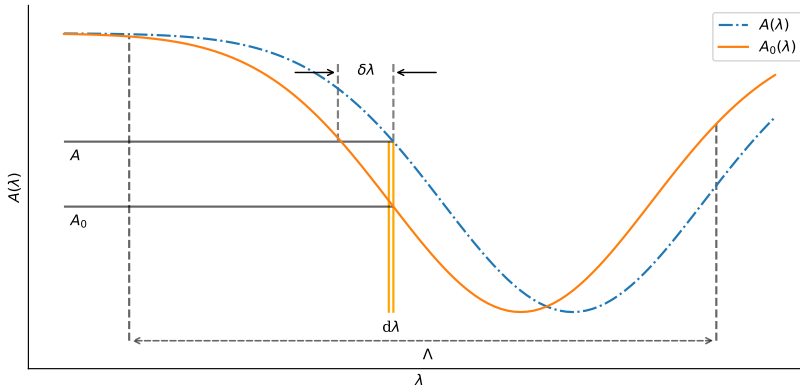


**Figure 8.1:** Arbitrary spectral line with a shift  $\delta\lambda$ , inspired by Connes (1985).  $\Lambda$  is the wavelength range considered.

the observable intensity change in a wavelength slice  $d\lambda$  (or at a given pixel) can be expressed by:

$$\delta A(i) = A(i) - A_0(i) \simeq \frac{\partial A_0(i)}{\partial \lambda(i)} \delta\lambda. \quad (8.2)$$

Rearranging Equation 8.2 for  $\delta\lambda$  and combining it with Equation 8.1, the Doppler shift of then becomes:

$$\frac{\delta V(i)}{c} = \frac{A(i) - A_0(i)}{\lambda(i)(\partial A_0(i)/\partial \lambda(i))} \quad (8.3)$$

This equation shows that the radial velocity measured at pixel,  $i$ , through a change in the intensity in the recorded spectrum,  $A(i) - A_0(i)$ , and inversely proportional to the slope of the spectrum,  $\partial A_0(i)/\partial \lambda(i)$ . Equation 8.3 provides a separate measurement of the radial velocity shift for every pixel,  $i$ , in the spectrum. The sensitivity of the velocity measurement can be improved, and the noise decreased by using the information from the whole spectral range,  $\Lambda$ . This is achieved by taking the weighted average<sup>2</sup> over all pixels in the spectral range using an optimal pixel weight  $W(i)$ .

$$\frac{\delta \bar{V}}{c} = \frac{\sum \frac{\delta V(i)}{c} W(i)}{\sum W(i)}. \quad (8.4)$$

Statistically, the optimal weights are proportional to the inverse square of the individual dispersion (variance),

$$W(i) = \frac{1}{\left(\frac{\delta V_{\text{RMS}}(i)}{c}\right)^2}, \quad (8.5)$$

where  $X_{\text{RMS}}$  is the dispersion on the quantity  $X$ .

The individual dispersion of the velocity measurement  $\delta V_{\text{RMS}}(i)$  is the dispersion that would result from several measurements of the reference spectrum all with the same Doppler shift (e.g. zero). Equation 8.3

<sup>2</sup> Weighted average on  $x$  is  $\bar{x} = \frac{\sum x(i)W(i)}{\sum W(i)}$

thus becomes:

$$\frac{\delta V_{\text{RMS}}(i)}{c} = \frac{[A(i) - A_0(i)]_{\text{RMS}}}{\lambda(i)(\partial A_0(i)/\partial \lambda(i))}. \quad (8.6)$$

The noise of the spectrum  $A$  is the quadratic sum of the photon noise  $\sqrt{A}$  and the detector noise  $\sigma_D$ . The spectrum  $A_0$  is considered noise free.

$$[A(i) - A_0(i)]_{\text{RMS}} = [A(i) - 0]_{\text{RMS}} = \sqrt{\sqrt{A(i)^2} + \sigma_D^2} \quad (8.7)$$

Considering that the Doppler shift is small and that  $A$  and  $A_0$  have the same intensity level, then  $A = A_0$  can be set. Using Equations 8.3, 8.5 and 8.7 the optimum weights then become solely dependent on the reference spectrum.

$$W(i) = \frac{\lambda^2(i)(\partial A_0(i)/\partial \lambda(i))^2}{A(i) + \sigma_D^2} \quad (8.8)$$

This weighting function can be modified to mask out and eliminate unwanted lines in the spectrum. For instance in the removal of telluric absorption lines in observed spectra. This is achieved to setting the particular pixel weights to zero.

With the optimal weights set, the weighed average velocity change measured from the full spectral range  $\Lambda$ , is given by:

$$\frac{\delta \bar{V}}{c} = \frac{\sum_{i=1}^{A(i)-A_0(i)} W(i)}{\sum W(i)} \quad (8.9)$$

$$= \frac{\sum_{i=1}^{(\lambda(i)-A_0(i))} \frac{\lambda^2(i)(\partial A_0(i)/\partial \lambda(i))^2}{A_0(i)+\sigma_D^2}}{\sum_{i=1}^{(\lambda(i)-A_0(i))} \frac{\lambda^2(i)(\partial A_0(i)/\partial \lambda(i))^2}{A_0(i)+\sigma_D^2}} \quad (8.10)$$

$$= \quad (8.11)$$

$$= \frac{\sum_{i=1}^{(A(i)-A_0(i))} \left( \frac{W(i)}{A_0(i)+\sigma_D^2} \right)^{1/2}}{\sum W(i)} \quad (8.12)$$

---

The important quantity for RV measurements is not just the velocity values themselves but also the dispersion on the measured velocity, the RV precision,  $\delta V_{\text{RMS}}$ , from the spectrum. This allows one to assess the planetary detectability limitations attainable in the spectra. From rearranging Equation 8.5 the dispersion is given by:

$$\frac{\delta V_{\text{RMS}}}{c} = \frac{1}{\sqrt{\sum W(i)}} = \frac{1}{Q \sqrt{\sum A_0(i)}}. \quad (8.13)$$

With this the velocity precision is inversely proportional to the sum of the optimal pixel weights.

A spectral quality factor,  $Q$ , is defined as for the pure photon noise case in Connes, 1985; Connes

Finish this equation (9 of bouchy 2001)

Try the symbolic package from PC

et al., 1996, as:

$$Q = \frac{\sqrt{\sum W(i)}}{\sqrt{\sum A_0(i)}}. \quad (8.14)$$

The radial velocity precision or uncertainty can be rearranged in terms of the spectral quality;

$$\delta V_{\text{RMS}} = \frac{c}{Q\sqrt{\sum A_0(i)}} = \frac{c}{Q\sqrt{N_{e^-}}} \approx \frac{c}{Q \cdot \text{SNR}}, \quad (8.15)$$

where  $\sum A_0(i) = N_{e^-}$  is considered to be the total number of photo-electrons  $N_{e^-}$  counted in the spectral range considered. where the  $\text{SNR} = \sqrt{N_{e^-}}$  for large N where the  $\text{SNR} = \sqrt{N_{e^-}}$  for large N.

explain snr

This quality factor, Q, is flux independent and is purely a function of the spectral profile within the spectral range considered. It is a measure of the line richness i.e., quantity and depth. For example a spectrum with many sharp lines will have a high Q. This quality factor is valid for the pure photon noise case only in which  $\sigma_D = 0$  and  $[A(i)]_{\text{RMS}} = A_0$ . The instrumental resolution of the spectrograph also effects the spectral quality as it induces line broadening.

It is convenient to use this version when comparing observed spectra with different SNR.?

The number of photo-electrons counted  $N_{e^-}$  depends on the stellar magnitude, detector efficiency and integration time. It can be estimated using

$$N_{e^-} = P_{avg} * S_{tel} * T_{exp} * \alpha * \Lambda, \quad (8.16)$$

where  $P_{avg}$  is the average monochromatic stellar brightness across the wavelength range  $\Lambda$  in photons  $\text{s}^{-1} \text{cm}^{-2} \text{cm}^{-1}$ ,  $S_{tel}$  is the telescope collecting area in  $\text{cm}^2$ ,  $T_{exp}$  is the integration time in s,

and  $\alpha$  the overall efficiency (including atmosphere, telescope, spectrograph and detector).

This can be used to determine the RV precision for a given instrument, and be useful in exposure time calculators for planning observations for RV surveys and exoplanet detection.

In the case of several  $\delta V$  measurements computed for  $k$  spectral slices (or spectral orders) then the error on the average  $\overline{\delta V}$  is given by the error on a weighted average:

$$\overline{\delta V_{\text{RMS}}} = \frac{1}{\sqrt{\sum_k \left( \frac{1}{\delta V_{\text{RMS}(k)}} \right)^2}} \quad (8.17)$$

This work follows Figueira et al., 2016 by exclusively considering a high signal-to-noise regime in which  $A(i) + \sigma_D^2 \sim A(i)$  can be approximated.

<sup>3</sup>

This technique has been tested and demonstrated on observations by Connes et al. (1996) and been used to determine predict the accuracy or performance limits of spectrograph instrumentation (e.g. Connes, 1985; Bouchy et al., 2001) and can influence the design (and/or use) of spectrographs (e.g. SPIROU (Artigau et al., 2014; Figueira et al., 2016))

Considering that  $\sum A_0(i) = N_{e^-}$  is the total number of photoelectrons counted over the whole spectral

<sup>3</sup> pure detector noise the fluctuation are independent of the spectrum  $A$  and the quality factor for pure detector noise is  $Q_D = \frac{\sum \lambda^2 (\partial A_0(i)/\partial \lambda(i))^2}{\sum A_0(i)}$  as derived by Connes, 1985.

Does spectrograph pipelines such as HARPS use these equations to measure estimate/precision?

range then the uncertainty in the velocity change is finally given by:

$$\delta V_{\text{RMS}} = \frac{c}{Q\sqrt{N_{e^-}}} \approx \frac{c}{Q(\text{SNR})}, \quad (8.18)$$

where the  $\text{SNR} = \sqrt{N_{e^-}}$  for large N.

In the unrealistic case where all the pixel weights are identical  $W(i) = w$ , then we can also see that the precision with decreases as  $1/\sqrt{N}$  due to an increase in the number of pixels, or a increase in spectral range.

$$\delta V_{\text{RMS}} = \frac{c}{\sum W(i)} \approx \frac{c}{\sqrt{Nw}} = \frac{c}{\sqrt{N}\sqrt{w}}, \quad (8.19)$$

A separate general formula for RV precision is given by Hatzes et al. (1992) in terms of general spectral parameters.

$$\sigma = \frac{1}{\sqrt{F}\sqrt{\Lambda}R^{1.5}} \quad (8.20)$$

Here the  $\sqrt{F}$  represents the SNR of the spectrum in the Poisson-noise dominated regime. The  $\Lambda$  comes from assuming a homogeneous distribution of line, with the same line properties, per unit length.

### 8.1.2 Prepare PHOENIX aces models

: # see Figueira et al. (2016)

Convert SED to counts.

Scale to 100 SNR per resolution element in *J*-band.

Convolutions

### 8.1.3 Rotational convolution

Stellar rotation has the affect of broadening spectral lines as the different portions of the stellar surface have a variation of radial velocity between  $\pm v \sin i$ . Rotation is applied to a non-rotating spectrum by convolution with a rotation kernel. The stellar rotational kernel used is given by Gray (2005);

top view dia-  
gram of rota-  
tion?

$$G(\Delta\lambda) = \frac{2(1-\varepsilon)[1 - (\Delta\lambda/\Delta\lambda_L)^2]^{1/2} + \frac{1}{2}\pi\varepsilon[1 - (\Delta\lambda/\Delta\lambda_L)^2]}{\pi(1-\varepsilon/3)v \sin i} \quad (8.21)$$

$$= c_1[1 - (\Delta\lambda/\Delta\lambda_L)^2]^{1/2} + c_2[1 - (\Delta\lambda/\Delta\lambda_L)^2] \quad (8.22)$$

where

$$c_1 = \frac{2(1-\varepsilon)}{\pi(1-\varepsilon/3)v \sin i}, \quad c_2 = \frac{\frac{1}{2}\pi\varepsilon}{\pi(1-\varepsilon/3)v \sin i}, \quad (8.23)$$

are constants which depend on the equatorial rotational velocity *v*sin*i*.

Here  $\Delta\lambda$  is the wavelength position from the non-rotating line centre,  $\Delta\lambda_L$  is the maximum line shift of the line centre at the edge of the stellar disk at which point the Doppler shift is *v*sin*i*;  $\Delta\lambda_L = \lambda \frac{v \sin i}{c}$ .

This kernel arises from integrating the rotational velocity profile across the surface of the stellar disk and as such the rotation kernel is bounded in the range  $[-\Delta\lambda_L, \Delta\lambda_L]$  from the line centre. This kernel also accounts for limb-darkening on the stellar disk with the linear limb darkening coefficient used in this work fixed at  $\varepsilon = 0.6$  as done in Figueira et al. (2016).

Since the synthetic models do not have a consistent wavelength grid, the discretization of applying the convolution kernel onto the changing wavelength grid causes the result of each pixel to be multiplied by a slightly different kernel area. Therefore, the result is divided by a convolution of a spectrum of ones with the same wavelength resolution to normalize the convolution.

As the Doppler shift  $vsini$  is transformed into wavelength by multiplication of  $\lambda/c$  there is a wavelength dependence on the rotation kernel shape. That is, the rotation kernel at each pixel is unique and requires separate calculation. For small wavelength ranges this can be held fixed to improve performance. This simplification is not performed in this work as large wavelength ranges are considered.

### 8.1.4 Instrumental Convolution

Following the rotational convolution the spectra are convolved with Gaussian instrumental profile (IP) with the FWHM constrained by the spectral resolution  $R$ ,  $\text{FWHM} = \lambda/R$ .

The Gaussian convolution kernel is of the form

$$IP(\Delta\lambda) = \frac{1}{\sigma\sqrt{2\pi}} \exp^{-\frac{\Delta\lambda^2}{2\sigma^2}} \quad (8.24)$$

with  $\sigma = \frac{\text{FWHM}}{2\sqrt{2\ln(2)}}$ , and  $\Delta\lambda$  again the difference from the line centre (normally this would be written as  $(x - \mu)$  where  $\mu$  is the Gaussian centre).

This assumes that the instrument profile of a particular instrument is in-fact Gaussian. This assumption of a Gaussian instrumental profile is a good starting point for high-resolution spectrographs, and shown to be valid for CRIRES (Seifahrt et al., 2010). If the instrument profile of a particular instrument is well characterized, then it could replace the Gaussian profile used here.

For instance Artigau et al. (2018) state that the instrumental profile of a (circular) fibre-fed spectrograph such as HARPS is mathematically equivalent to a cosine between  $-\frac{\pi}{2}$  and  $\frac{\pi}{2}$  with a width equivalent to the Gaussian FWHM.

The integration of a circular fibre is given by

$$IP_{\text{fibre}}(\Delta\lambda) = \cos(B \cdot \Delta\lambda), \quad [-\frac{\pi}{2B}, \frac{\pi}{2B}] \quad (8.25)$$

where  $B = \frac{\text{FWHM}_0}{\text{FWHM}}$  is scaled to give the same area, following the description from Artigau et al. (2018). They also mention that the result using this  $IP_{\text{fibre}}$  are all consistent with just using a Gaussian kernel.

### 8.1.5 Numerical Convolution

In this work the stellar models undergo broadening by convolution with rotation and instrumental profile kernels (Equations 8.22 and 8.24). The convolutions are performed by analysing a single pixel at a time, and selecting the neighbouring pixels that fall within the convolution window<sup>4</sup> for that pixel. The value of the convolution kernel is calculated at the position of each pixel selected, multiplied by the flux of

---

<sup>4</sup> Region in which the convolution kernel will affect this particular pixel

each pixel and then summed to provide the new value at the selected single pixel\*. The shape of the convolution kernels and the size of convolution window are wavelength dependant ( $\text{FWHM} = \lambda/R$  and  $\Delta\lambda_L = \lambda \frac{v \sin i}{c}$ ) and must be calculated separately for each pixel, making the convolution computationally expensive.

However, the computation of the convolution of individual pixels is an “embarrassingly parallel”<sup>5</sup> problem. What this means is that convolution result for pixel  $i + 1$  does not depend on the convolution result obtained for pixel  $i$ . Therefore, parallel processing was implemented to improve the performance of the convolution, roughly dividing the convolution time by the number of processors used.

The python package *PyAstronomy* also contains functions that perform rotational and instrumental broadening. Those functions however require that the spectrum have uniformly spaced  $x$ -coordinate spacing which is not a requirement for the implementation of *eniric* used here. *PyAstronomy*, while implemented a “slow” full version of the rotational convolution, with a wavelength dependent kernel, they also provide “fast” convolution kernels that are fixed, taking the central wavelength value. These are significantly faster but are only valid for very short wavelength regions, in which the kernels do not significantly change. They are not suitable for use in this work due to the large wavelength span of spectroscopic bands and the wavelength dependant spacing of the spectra. A comparison of the performance between *PyAstronomy* convolution and the convolutions implemented in *eniric* and used here are given in a *Jupyter* notebook in the repository of “eniric”, basically they fall in between the “fast” and “slow” implementation of *PyAstronomy*.

One factor the needs consideration when convolving with a non-uniformly spaced spectrum is effect of the sampling on the convolution. For instance the number of point inside the convolution, as well as their location will effect the area of the convolution kernel. To normalize the convolution result it is divided by the convolution of a unitary spectrum of ones, with the same spacing. Figueira et al. (2016) performed this unitary convolution separately and applied the normalization afterwards. In the improved implementation the convolution normalization is performed directly after the convolution kernel multiplication at \*.

For example for the rotational convolution result of the value for pixel  $i$  becomes

$$A'(\lambda_i) = \frac{\sum A(\Delta\lambda_i) \cdot G(\Delta\lambda_i)}{\sum G(\Delta\lambda_i)},$$

where  $\Delta\lambda_i$  are the values between in the range  $\lambda_i(1 - \frac{v \sin i}{c}) \leq \lambda_i \leq \lambda_i(1 + \frac{v \sin i}{c})$ , instead of only

$$A'(\lambda_i) = \sum A(\Delta\lambda_i) \cdot G(\Delta\lambda_i).$$

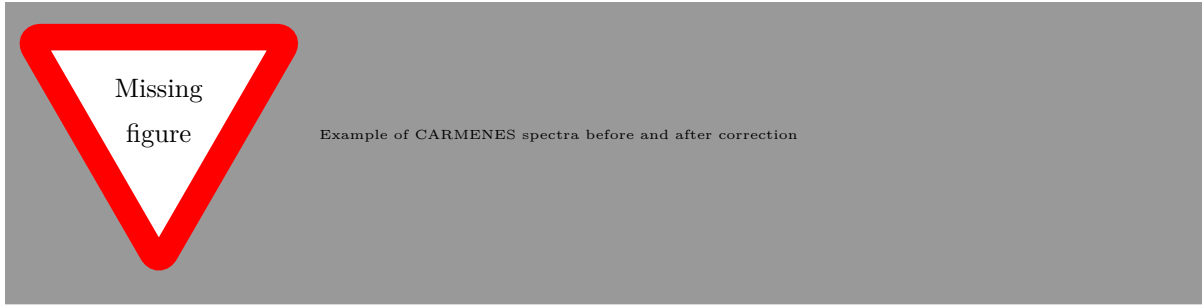
By default edge effects are avoided by providing an input spectra sufficiently wider than the desired output spectrum to prevent edge effects on the portion of the spectrum desired. Since two convolutions are performed one after the other the original input spectrum is selected wider than needed so that no edge effects will be present after both addition of rotation and instrumental broadening by  $v \sin i$  and  $R$ .

## 8.2

Preparation of CARMENES spectra.

---

<sup>5</sup> [https://en.wikipedia.org/wiki/Embarrassingly\\_parallel](https://en.wikipedia.org/wiki/Embarrassingly_parallel)



### 8.2.1 Bands

The bands analysed avoid the strong water absorption in the nIR that can be seen in the CARMENES spectra in Figure . These are the Z, Y, J, H, K- bands found in Table 4.1.

Add figure here

Add figure here

### 8.2.2 Comparing models to CARMENES.

Already somewhat done in Reiners. (use all spectra). They measured the precision obtained in the spectra.

Band by band like Figueira et al. (2016)? Certain% steps like Bouchy or Artigau

Can do Barnard's star in CARMENES. compared to models in Artigau.

finish this

**Table 8.1:** Selection of targets from the CARMENES library spanning the M-dwarf spectral range.

Karmn	Name	SpT	SNR <sub>NIR</sub>	Temp (K)	logg	[Fe/H]	vsin <i>i</i> (km s <sup>-1</sup> )
J20533+621	BD+61 2068	M0.5	257	3772	NaN	-0.01	2.66
J04290+219	BD+21 652	M0.5	212	4037	3.99	-0.21	1.11
J07274+052	Luyten's Star	M3.5	254	3467	NaN	-0.11	NaN
J17578+046	Barnard's Star	M3.5	236	3247	NaN	-0.32	NaN
J11055+435	WX UMa	M5.5	140	3304	NaN	NaN	NaN
J10564+070	CN Leo	M6.0	133	2960	NaN	NaN	NaN
J18356+329	LSR J1835+3259	M8.5	50	2578	NaN	-0.4	37.6
J04198+425	LSR J0419+4233	M8.5	42	NaN	NaN	0.22	NaN

**Table 8.2:** csv2tex table

Karmn	Name	SpT	nIR-SNR	T <sub>eff</sub>	logg	[Fe/H]	ROT- <i>vsini</i>
J20533+621	BD+61 2068	M0.5	257	3772.0	-	-0.01	2.66
J04290+219	BD+21 652	M0.5	212	4037.0	3.99	-0.21	1.11
J07274+052	Luyten's Star	M3.5	254	3467.0	-	-0.11	-
J17578+046	Barnard's Star	M3.5	236	3247.0	-	-0.32	-
J11055+435	WX UMa	M5.5	140	3304.0	-	-	-
J10564+070	CN Leo	M6.0	133	2960.0	-	-	-
J18356+329	LSR J1835+3259	M8.5	50	2578.0	-	-0.40	37.60
J04198+425	LSR J0419+4233	M8.5	42	-	-	0.22	-

### 8.3 Metallicity logg effects

We explore the effect of metallicity and logg on the spectral quality of spectra in the PHOENIX-ACES library by extending the quality factor and precisions computation to [Fe/H] between -1–1 and logg of 4.0–5.5. In Figure 8.2 the variation of quality factor with broadening of  $R=100\,000$  and  $v \sin i = 1.0 \text{ km s}^{-1}$  across the M-dwarf spectral types and the nIR bands is shown. We observed multiple different effects present.

The  $Z$ -band has a large separation in spectral quality due to spectral type, this is because the continuum the  $Z$ -band is severely eroded in the spectra of late M's as they cool. Each spectral type also behaves very differently to a change in [Fe/H] and logg. For M0 and M3 there is an increase with [Fe/H] below solar metallicity, above solar metallicity the slopes of the lines dramatically increase, especially for M3. For M6 and M9 there is a step slope with [Fe/H] below solar metallicity, which flattens off at solar metallicity, and even decreases for the M9 spectra above solar metallicity. As logg increases in the  $Z$ -band there is a decrease in quality. There is a consistently large separation between early and late M's that. The quality for M6 is very shallow, while for M9 the quality is nearly flat for logg=4.0 and 4.5 but then decreases sharply at higher logg.

$Y$ -band -

$J$ -band -

For the  $H$  and  $K$ -band there is fairly consistent linear trend for all spectral types, with the quality factor increasing with an increase in [Fe/H] and decreasing with an increase in logg. There is also only a relatively small variation in quality factor due to the spectral type.

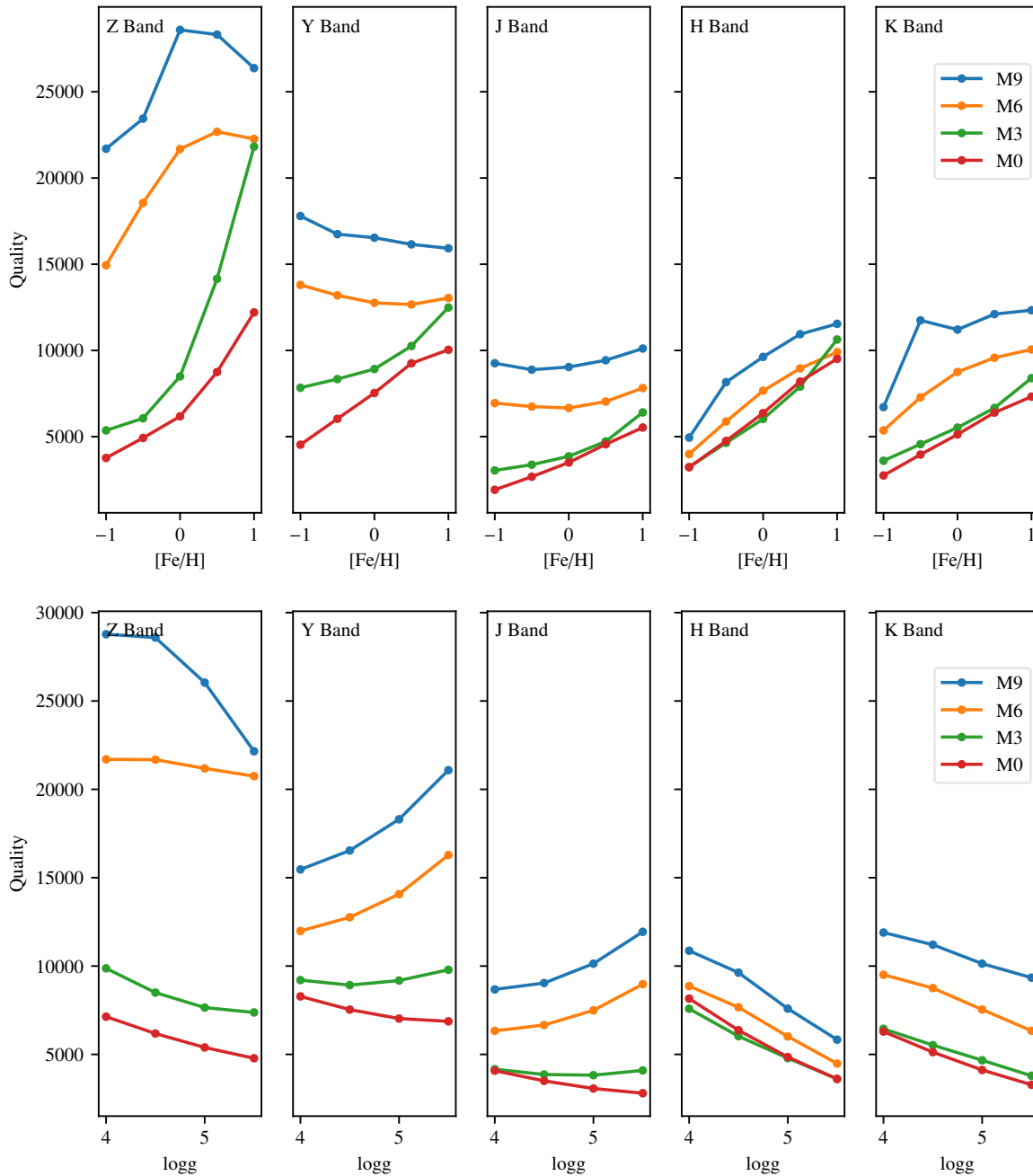


**Figure 8.2:** Quality factor changes across spectral type and bands for variations in  $[Fe/H]$  and  $\log g$ . Broadening values are  $R=100\,000$  and  $vsini = 1.0 \text{ km s}^{-1}$ . Top: Quality factor variation of  $[Fe/H]$  between -1.0 to 1.0 at a fixed  $\log g=4.5$ . Bottom: Quality factor variation of  $\log g$  between 4 and 5.5 with fixed  $[Fe/H]=0.0$ . Note a higher quality factor corresponds to an increased RV precision.

## 8.4 Updating RV precision software

To undertake the calculation of RV precisions A large section of this work involved optimizing the original code used in Figueira et al. (2016). Care needs to be taken to optimize the code. The original code used in Figueira et al. (2016) was slow, taking around 2 hours per simulation, this led to multiple weeks of processing time to compute the precision's for the original paper.

In this section we document the changes made to the code in the course of attempting to improving it. Features that change the derived RV precision are specifically documented in detail, with relative precision changes provided.

This work resulted in a submission of a publication<sup>6</sup> to *The Journal of Open Source Software*<sup>7</sup> (JOSS) Neal and Figueria 2018 (in prep.) with the source code openly available on <https://github.com/jason-neal/enric>.

### 8.4.1 Automated testing

To insure that any changes made to the code did not change the underling results. This involved writing automatic tests for the software. This practice is crucial in computer science ins commercial software development but seldom done in research but is becoming more popular. Some work focused on testing ideology from computer science. Although not perfect implementation I began by adding automated tests to the code to check individual parts of it. Before making changes I created automated tests that would confirm the functionality of pieces of the code. I could then make changes to the code, to improve the performance without worrying that the results were different. Namely that the same precision were calculated in the end.

Functional test and unit tests.

works of software testing in research.

### 8.4.2 Performance

There was a major performance bottleneck in the convolution stage, which increased the performance around 250 X itself. The algorithm looped though the pixels in the spectrum, selecting out the necessary section around a given pixel with a comprehension list (for loop if inside range). Turning the result into a *numpy* array, performing the sum for that pixel and appending it to a list. The performance issue was a python implementation detail to do with applying a comprehension list to a *numpy* array, then slicing the *numpy* array with the ends of the list, then converting it back into a *numpy* array, all of which is performed on a very large spectrum array. Creating a *numpy* boolean mask instead of the comprehension list, and applying the boolean mask to the array is much faster. Remaining entirely in the compiled *numpy* code and not converting between lists and *numpy* arrays (with involve type checking overhead). This slow operation was done for every pixel/wavelength in the spectrum twice, once for each convolution.

caching convolution result to prevent recomputing the same values with *Joblib*. Also embarrassingly parallel so added multiprocessing support.

The convolution is still the slowest part. There are other methods that work on uniform spectra, which have not been tried to see how they affect the performance or RV precision results. **Insert code samples.**

<sup>6</sup> Available at <http://joss.theoj.org/papers/384bfc031df47ecef2d88328f63e5479>

<sup>7</sup> [joss.theoj.org/](http://joss.theoj.org/)

### 8.4.3 Model extension

The solution is to iterate over each pixel but create a mask array and use *numpy* indexing to select the required pixel span. (this remains in *numpy*) These operations all remain in *numpy* so do not waste time converting between lists and *numpy* arrays, in which Python need to constantly check and convert the type of each item.

This shows a lesson in the usefulness of test driven development, or testing of code in science.

An normalization step was originally done after the convolution, to normalize out the effect of the convolution on a spectrum of 1s, due to the changing wavelength grids sampling. This was brought inside the main convolution by dividing the pixel by the convolution of a spectrum of ones at the same time. (again in *numpy* so it is quick)

Parallelization as embarrassingly parallel, the result of each pixel is independent of result of neighbours.

This is not a criticism of the work done by the original author (my supervisor). It is easier to modify a working system then to create one from scratch.

Computer code is not the important part in scientific exploration., although becoming more important in open source and reproducibility efforts. Often forgotten in

```
# Handle any PHOENIX aces models.
```

## 8.5 Numerical Gradient

One of the key insights from Equations 8.8 and 8.13 is that the radial velocity error is inversely proportional gradient of the spectra, In numerically computing the RV precision, the result is dependent on the numerical method used to compute the gradient. In original code used in Figueira et al. (2016) the gradient or slope is approximated using the forward finite difference method. The *numpy* package provides a function to calculate the gradient using a more advanced methods that compute a more precise gradient. In this section we explore the affect of improving the precision of the numerical gradient on the final RV precision.

The simplest way to calculate the derivative using finite difference methods (Quarteroni et al., 2000). These arising from the Newton's definition of the derivative for a continuous function  $f(x)$  which should be familiar from introductory calculus:

$$f'(x) = \lim_{h \rightarrow 0} \frac{f(x + h) - f(x)}{h} .$$

There are three common varieties of the finite difference,

$$FFD = \frac{f(x + h) - f(x)}{h}, CFD = \frac{f(x + \frac{1}{2}h) - f(x - \frac{1}{2}h)}{h}, BFD = \frac{f(x) - f(x - h)}{h}, \quad (8.26)$$

called the forwards (FFD), central (CFD), and backwards (BFD) finite differences respectively. The order of uncertainty on the FFD/BFD is  $\mathcal{O}(h)$  while for the CFD it is  $\mathcal{O}(h^2)$  (Quarteroni et al., 2000). As the wavelength spacing between samples/pixels ( $h$ ) is small the CFD will a more precise value for the gradient at each pixel.

In our case  $h$  is the difference in wavelength between the two pixels considered. In the FFD case the

gradient at pixel  $i$  becomes:

$$\frac{\partial A_0(i)}{\partial \lambda(i)} = \frac{A_0(i+1) - A_0(i)}{\lambda(i+1) - \lambda(i)}, \quad 1 \leq i \leq n-1. \quad (8.27)$$

At each pixel the numerical derivative is evaluated to the average slope between itself and the following pixel and is an approximation to the derivative. This only extends to  $i = n-1$ , where  $n$  is the number of points in the spectrum, and the last pixel is dropped from the RV calculation.<sup>8</sup>

The *gradient*<sup>9</sup> method provided in *numpy* contains a more advanced numerical methods to calculate the derivative. It uses a *compact difference* method (Quarteroni et al., 2000) which expand the finite differences using a Taylor expansion and then selecting coefficients to minimize the *consistency error*. From the *numpy* documentation the consistency error here is

$$\eta_i = \partial f(x_i)/\partial x - [\alpha f(x_i) + \beta f(x_i + h_d) + \gamma f(x_i - h_s)],$$

where  $h_s$  and  $h_d$  are the spacing to the left and right of  $i$  respectively. With Taylor expansion this turns into solving a linear system of equations:

$$\begin{cases} \alpha + \beta + \gamma = 0 \\ -\beta h_d + \gamma h_s = 1 \\ \beta h_d^2 + \gamma h_s^2 = 0 \end{cases}$$

which result in the approximation of the gradient of the central values to be

$$\frac{\partial f(x_i)}{\partial x} = \frac{h_s^2 f(x_i + h_d) + (h_d^2 - h_s^2) f(x_i) - h_d^2 f(x_i - h_s)}{h_s h_d (h_d + h_s)} + \mathcal{O}\left(\frac{h_d h_s^2 + h_s h_d^2}{h_d + h_s}\right).$$

If the spectrum is evenly spaced  $h_s = h_d$  reduces to the standard second order CFD approximation:

$$\frac{\partial f(x_i)}{\partial x} = \frac{f(x_{i+1}) - f(x_{i-1})}{2h} + \mathcal{O}(h^2)$$

Applying this to our situation, similar to Equation 8.27, we get:

$$\frac{\partial A_0(i)}{\partial \lambda(i)} = \frac{\lambda(i-1)^2 A_0(i+1) + (\lambda(i+1)^2 - \lambda(i-1)^2) A_0(i) - \lambda(i+1)^2 A_0(i-1)}{\lambda(i-1)\lambda(i+1)(\lambda(i+1) + \lambda(i-1))}, \quad 2 \leq i \leq n-1$$

with an uncertainty of  $\mathcal{O}\left(\frac{\lambda(i+1)\lambda(i-1)^2 + \lambda(i-1)\lambda(i+1)^2}{\lambda(i+1) + \lambda(i-1)}\right)$ .

Wavelength spacing  $\delta\lambda$  between pixels is a function of  $\lambda$ , Resolution and sampling choices. Can I do something with this??

The *gradient* function from *numpy* implements central differences for the interior points, accurate to second order, and first order accurate one-sided (forward or backward) differences at the boundaries, computed using the same compact difference procedure.

In Figure 8.3 we visualize the gradients of two small spectral regions computed with the original

<sup>8</sup> This is important in the case of Condition #2.

<sup>9</sup> Documentation available at <https://docs.scipy.org/doc/numpy/reference/generated/numpy.gradient.html#id1>

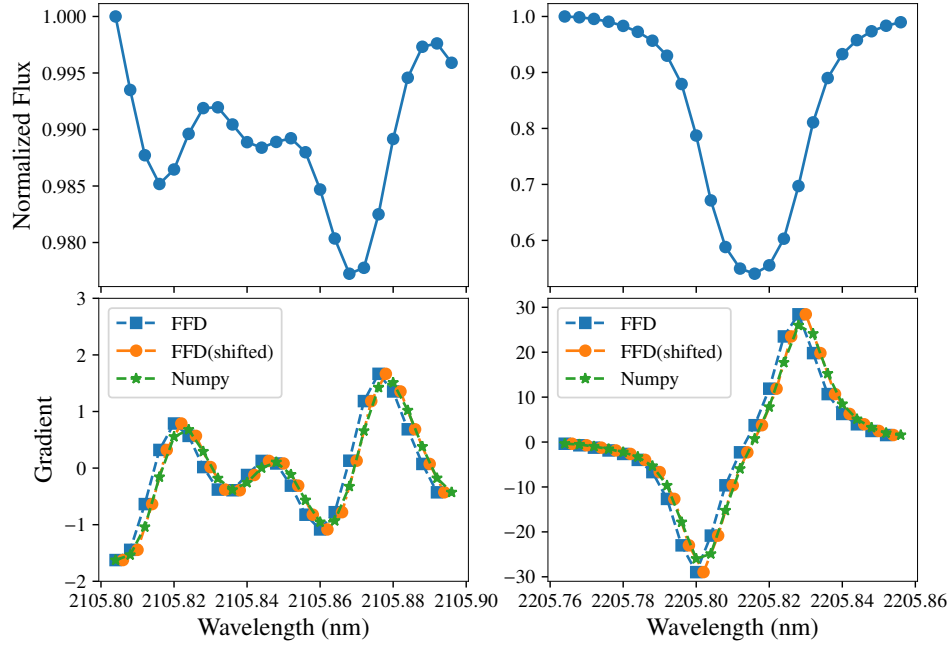


**Figure 8.3:** Visualization of the numerical gradient of some spectral lines. Top: The two spectral regions of a stellar spectrum the left hand slide contains short lines near the normalized continuum while on the right a single deep absorption line is shown. Bottom: The numerical gradients for the spectra shown in the top panels; the original FFD method is displayed with *blue squares* while *numpy* gradient is shown with *green stars*. The *orange circles* are the FFD version shifted to the mid-points between pixels for illustrative purposes.

**Table 8.3:** The effect of the numerical gradient function on RV precision. The band label VIS and NIR indicate the full visible and nIR bands while CARM<sub>VIS</sub> and CARM<sub>NIR</sub> indicate the two wavelength bands of the CARMENES spectrograph.  $\Delta\lambda$  is a wavelength shift applied to move the FFD values between pixels for this comparison only. The M0 spectra used here had no rotation, or instrument broadening performed and was normalized to a maximum of 1 in each band. The precision values given here are for accessing the relative precision change due to the different gradient methods.

Gradient method		A	B	C	(B-A)/A	(C-A)/A
Band	$\lambda$ range ( $\mu\text{m}$ )	FFD	FFD+ $\Delta\lambda$ $\delta V_{rms}$ ( $\text{m s}^{-1}$ )	NumPy	$\Delta\delta V$ ratio (%)	$\Delta\delta V$ ratio (%)
VIS	0.38 – 0.78	16.1	16.2	16.9	0.6	4.9
CARM <sub>VIS</sub>	0.52 – 0.96	20.9	21.0	22.0	0.3	5.2
Z	0.83 – 0.93	76.9	77.0	78.8	0.1	2.5
Y	1.00 – 1.10	78.3	78.5	83.8	0.2	7.0
J	1.17 – 1.33	149.3	149.4	156.4	0.1	4.7
H	1.50 – 1.75	119.4	119.5	122.3	0.1	2.5
K	2.07 – 2.35	153.4	153.7	157.7	0.2	2.8
CARM <sub>NIR</sub>	0.96 – 1.71	46.1	46.2	48.0	0.1	4.2
NIR	0.83 – 2.35	36.9	36.9	38.2	0.1	3.6

FFD, and the higher precision version incorporated in numpy’s gradient function. The top panels contain the spectrum in the small regions shown, indicating a large spectral line and three small lines near the continuum respectively. The derivative of the spectra is shown in the bottom panel with the FFD method shown with *blue squares* and the *numpy* gradient shown in *green stars*. The *orange circles* are the same as FFD but shifted horizontally to the midpoints between pixels. This is for illustrative purposes and to assess the effect of this offset when calculating the pixel weights.

There are three notable features observed between gradient methods. The first, which is expected from the FFD formulation is that the FFD gradient is offset to the left. The second is that when the horizontal offset is adjusted (orange circles) the gradients lie along the same curve. Both methods are trying to approximate the real gradient function of the spectrum and is again expected. The most important feature observed in this though is that there is a slight over-estimate of the gradient by the FFD method at the peaks. In the bottom panels of Figure 8.3, the points of highest gradient are always from the FFD method (blue/orange). This is the case for all spectral lines and as the optimal pixel weights are proportional to the gradient squared the FFD method will apply slightly higher pixel weights to these values, two points per line in the spectrum. The FFD will therefore produce a slightly smaller  $\delta V_{\text{RMS}}$  error compared to the more precise gradient function.

In Table 8.3 we calculate the  $\delta V_{\text{RMS}}$  using both gradient methods to determine their relative effect on the RV precision.

We took a PHOENIX-ACES spectrum with  $T_{\text{eff}}=3900\text{ K}$ , corresponding to M0 spectral type. The full theoretical precision is calculated (no telluric masking applied) with no rotational or instrumental broadening and the maximum of the continuum of each band scaled to 1. In this case the RV precisions are not comparable between bands and are only to assess the direct effect of the changing the numerical gradient. The bands name and the spanned wavelength are given. The columns A, B, C are the RV precision for the different gradient methods. The  $\delta V$  ratios are the relative difference in RV when changing from method A (the original FFD) to methods B and C. In this table column B is the FFD method but with the wavelength shifted to in between pixels, corresponding to the orange circles in Figure 8.3 while column C is the more precise gradient from *numpy*.

We find that changing to use the gradient from *numpy* increases the  $\delta V_{\text{RMS}}$  by 2.5–7%, (decreasing the RV precision), due to the over-estimated gradient from the FFD method. As the pixel weights Equation 8.8 are also proportional to  $\lambda^2$  column B was computed to assess the effect of the slight wavelength offset on the RV precision, visible in Figure 8.3. This small wavelength shift red-ward does change the RV precision by 0.1–0.6% which is an order of magnitude smaller than the relative change when using *numpy*’s gradient method.

Changing the method of numerical derivatives will change all the precision values given in the Figueira et al. (2016). This is a small impact on the precision compared to other components of the RV precision. For instance from Equation 8.18 a increase in  $\delta V_{\text{RMS}}$  of between 2.5–7% could equally be caused by a small decrease in the SNR from 100 (the value used in Figueira et al. (2016)) to between 95–98.

The current version of the software is now implemented with the gradient method provided by *numpy* package.

### 8.5.1 Masking Function

Another change made to the software is in the application of the masking function, and the treatment of telluric lines. As suggested in Connes (1985) and Bouchy et al. (2001) a custom masking function can be applied to the individual pixel weights in Equation 8.8, such as:

$$W'(i) = W(i)M(i),$$

where  $M(i)$  is the masking function and  $W'(i)$  are the modified pixel weights. This masking function can be used in particular for the removal of telluric lines, setting those weights to zero and is in essence what is done when wavelength selection is performed; assigning zero weight to all pixels outside the desired wavelength range.

This masking function can be used to easily apply the three conditions presented in Figueira et al. (2016). First the 3 masking functions will be defined, then followed by the quantification of how they differ from the previous implementation. The subscripts on the masking functions correspond to the three conditions.

$$M_1(i) = 1 \tag{8.28}$$

$$M_2(i) = \begin{cases} 0, & T(i) < \tau \\ 1, & T(i) \geq \tau \end{cases} \tag{8.29}$$

$$M_3(i) = T(i)^2 \tag{8.30}$$

Here,  $T(i)$  is the telluric transmission spectrum, while  $\tau$  is the transmission depth cut-off. For instance to mask out telluric lines deeper than 2%,  $\tau$  would be set at 0.98.

- Condition #1: The first mask,  $M_1$ , is the simplest case in which all pixel weights are treated equally. No telluric line masking is considered.
- Condition #2: In the second mask,  $M_2$ , the telluric line transmission,  $T(i)$  is used to create a boolean mask of 0's and 1's. When applying this mask to the pixel weights, the pixels effected by telluric lines have 0 weight, removing their contribution to the  $RV_{RMS}$ . Accounting for seasonal variation in Earth's barycentric motion can be easily incorporated into this mask, widening the regions masked out.
- Condition #3: The third mask,  $M_3$ , assumes the application of perfect telluric correction consistent with Condition #3. The pixel weights are modified by dividing the flux variance by the square of the transmission spectrum. As the flux variance is the denominator of Equation 8.8, this is equivalent to multiplication of the weights by a mask of the form  $M_3$ .

Having the three masks defined in this way makes the implementation of the RV precision simpler. In the original version there were three separate implementations, one for each condition. With this, as mentioned previously there was a issue with the implementation of Condition #2.

cite the equation when I refer to it

Check this if it is previous

### 8.5.1.1 Masking order

The order in which the masking is performed is also important. Masking should be applied only after calculation of the pixel weights. As the pixel weights depend on neighbouring points (through the calculation of the gradients), prematurely removing pixels will affect the precision results.

The original implementation of Condition #2 did just this, splitting the spectra into small sections in between the masked off telluric lines. The  $RV_{RMS}$  is calculated for each section and then the results are combined as the error on the weighted average in Equation 8.17. Analytically this identical to masking the pixel weights with  $M_2$  but not in practice when numerically implemented.

When the spectrum is split into small sections the number of edges increases and the number of pixels affected by any edge effects increases. Using the FFD method to compute the gradient the last pixel is removed/lost. A spectrum split in  $m$  sub-spectra will therefore lose  $m$  pixels due to edge effects (instead of only 1 pixel with the full spectrum). Even the *numpy* gradient is not immune to the edge effects in the sub-spectra when splitting the spectrum first. Even though there is no pixels lost, the first and last pixels of each sub-spectra are computed using forward or backward differences, rather than central differences (as they would be in the full spectrum). Hence the gradients and weights of some pixels are slightly changed due to the splitting occurring first.

Should I show the working of analytical working out of this in an appendix, or here?

We quantify the effect of splitting the spectrum before and after calculating the weights in Table 8.4. The columns label *Split* represents splitting the spectrum before calculating the pixel weights while the *Mask* columns calculate all the pixel weights first and then apply the  $M_2$  mask. The difference in RV precision between both situations and for both gradient methods are given. For the FFD gradient the ordering of masking changes decreases the  $RV_{RMS}$  by 0.2–0.7%, while for the *numpy* gradient it is increase but an order of magnitude smaller between 0.01–0.13%. The FFD gradient is causes a larger difference as points that were masked out are now included where as with the *numpy* gradient the end values are always included but their gradients are slightly changed. The last column is the difference ratio between the *Mask* column of both gradient method, this is consistent with Table 8.3 with the differences from two gradient methods between 2–7%. It shows that the difference from changing order of masking is 1–2 orders of magnitude smaller than changing the gradient method.

The code has been adjusted to consistently apply the masking after the pixel weights are calculated. This retains the most pixels, with the more accurate pixel weights. It has also been changed to just apply  $M_2$  rather than splitting and performing the weighted error calculation. This simplifies the implementation in calculating the RV precision.

did I check this was equivalent

The results from these spectra for conditions #1 and #3 are consistent with Figueira et al. (2016).

put this some where

For Condition #2 in which there was an error there is no meaningful relation between the new and old values.

put this line elsewhere.

### 8.5.2 Atmospheric masking bug

One thing that was revealed in testing was that there was an error in the application of Condition #2. When the telluric mask was shifted to account for barycentric motion of the earth, and the condition of 3 consecutive pixels in the telluric spectra being lower than the limit (due to the higher sampling) there was an software bug,

A check for this issue was discovered using this unit test.

**Table 8.4:** Relative RV precision difference for Condition #2 due to spectral splitting and order of applying the pixel mask. The ratio are the difference between *Split* and *Masked* implementations with the same gradient calculation. The last column is the ratio between the *Masked* versions using the FFD and numpy gradient methods and are consistent with Table 8.3. Results a for an M0 spectral type, with  $v \sin i = 1.0$  and  $R=100\,000$ .

Gradient Band	Split	Masked	$\Delta$ Ratio	Split	Masked	$\Delta$ Ratio	Masked
	$\text{m s}^{-1}$	$\text{m s}^{-1}$	%	$\text{m s}^{-1}$	$\text{m s}^{-1}$	%	$\Delta$ Ratio %
Z	7.42	7.38	-0.66	7.76	7.77	0.13	5.3
Y	4.75	4.74	-0.22	5.06	5.06	0.06	6.8
J	18.58	18.53	-0.29	19.57	19.57	0.01	5.6
H	6.08	6.05	-0.53	6.25	6.26	0.08	3.5
K	32.21	32.14	-0.22	33.48	33.49	0.05	4.2

**Listing 8.1:** Example unit test to catch masking bug. The assert statement checks that the mask continues to remove all absorption lines deeper than 2%.

```
def test_telluric_masking(wavelength, transmission):
    """Check mask still masks out all telluric lines > 0.98 after
    accounting for barycentre motion."""
    mask = telluric_mask(transmission, depth=0.98) # Create mask
    mask = barycentre_shift(wavelength, mask) # Extend mask
    assert numpy.all(transmission[mask] >= 0.98) # Check mask
```

The assert statements checks that when the mask is applied to the transmission spectrum again all of the values are outside of any deep telluric regions. A test like this would have caught this bug.

This bug means that all the RV precision values for Condition #2 published in Figueira et al. (2016) incorrect. As the applied masking was unevenly applied Figueira et al. (2016) the new values RV precision values do not all change in the same proportion or direction. Some specific wavelengths and resolutions are essentially unchanged while other results change by over  $20\,\text{m s}^{-1}$ . Even though there is an error with condition #2 they do not change the overall conclusions of the paper. These are

add conclusions not affected

### 8.5.3 SNR scaling

To analyse the relative precision of different spectra they need to normalized to a common reference point. In this section we detail how this was originally done and how this was changed to be adaptable to any library spectra and any reference band.

In the original code this was selected to be a SNR per pixel of 100 at the centre of the *J*-band at  $1.25\,\mu\text{m}$ . The normalization values for each band,  $vsini$  and resolution combination were hard-coded into the analysis. This made it impossible to easily adapt the code to other spectra or parameter combinations.

An automated SNR scaling procedure was created to remove the hard-coded values. This updated code finds the centre point of the band of reference for the given spectrum. Totals the photon count across one resolution element,  $\delta\lambda$ , and then takes the square root. This is using the definition of the SNR as  $\text{SNR} = \sqrt{N}$  for large N. This value is then used to scale the spectrum such that the SNR at the

reference point is the desired value.

$$SF = \frac{\sqrt{\sum_{\delta\lambda} A}}{\text{SNR}_{desired}} \quad (8.31)$$

$SF$  where  $SF$  is the scaling factor,  $\sum_{\delta\lambda} A$  is the sum of the point in one resolution element and  $\text{SNR}_{desired}$  is the desired SNR level requested.

This automated procedure enabled **4** different features.

- The ability to analysis other spectral models, not just corresponding to M0, M3, M6, M9 spectral types. - Scaling to a SNR per pixel level other than 100.
- A SNR per pixel other than 100 can be selected. - Allowing for other sampling levels (if desired)
- Not restricted to a model with 3 samples per resolution element.
- Different reference bands available. Results are not limited to being referenced from the *J*-band. For instance the RV precision can now be calculated for a given SNR at the centre of the *K*-band. This was one the features requested for the Exposure Time Calculators precision values. For NIRPS we provided precision values relative to each individual band, while for SPIRou they were relative to the J- and H-bands.

The default values for the SNR scaling a still 100 at the centre of the *J*-band, but there is now options to easily change these values.

The centre of each band was visually checked to ensure that there were no spectral lines at the reference locations> If a line was present at the reference point its depth variability across spectral types would affect the SNR scaling levels at a greater than the normal change in continuum amplitude/shape. 

As shown in Equation 8.15 the RV precision is inversely proportional to the SNR level. To access the RV precision of any of the values in Table at a different SNR level you can apply the following

$$\text{RV}_{\text{SNR}2} = \text{RV}_{\text{SNR}1} * \frac{\text{SNR}1}{\text{SNR}2}. \quad (8.32)$$

---

SNR plot/diagram

## 8.6 SPIRou and NIRPS ETC

Having this tool to calculate RV precisions efficiently lead to contributions to the Exposure Time Calculators (ETC) for both the SPIRou and NIRPS spectrographs.

In September 2017 we were requested to provide precision calculations for the SPIRou ETC<sup>10</sup>. These were the same table as Figueira et al. (2016) but with a each band referenced to 100 SNR in its own band. The modification to use the centre of any band was made to fulfil this request. Notes on the telluric correction issue affect on Condition 2.

In May 2018 we were requested to provide precision calculations for the NIRPS ETC. This extended the spectral range from M0, M3, M6, M9 at 3900, 3500, 2800, 2600 K respectively, but to all temperatures between 2500 and 4000 K inclusively. This provides a finer resolution coverage over the M spectral type, allowed by the PHOENIX-ACES library. Instrumental resolutions of 75 000 and 100 000 were requested to match the NIRPS instrument. The logg and metallicity, sampling rate remained at the Figueira et al. (2016) levels of 4.5, **0.0** and 3.0 respectively. Precisions were provided for SNR of 100 relative to the *J*, 

<sup>10</sup> [http://www.cfht.hawaii.edu/Instruments/SPIRou/SPIRou\\_etc.php](http://www.cfht.hawaii.edu/Instruments/SPIRou/SPIRou_etc.php)

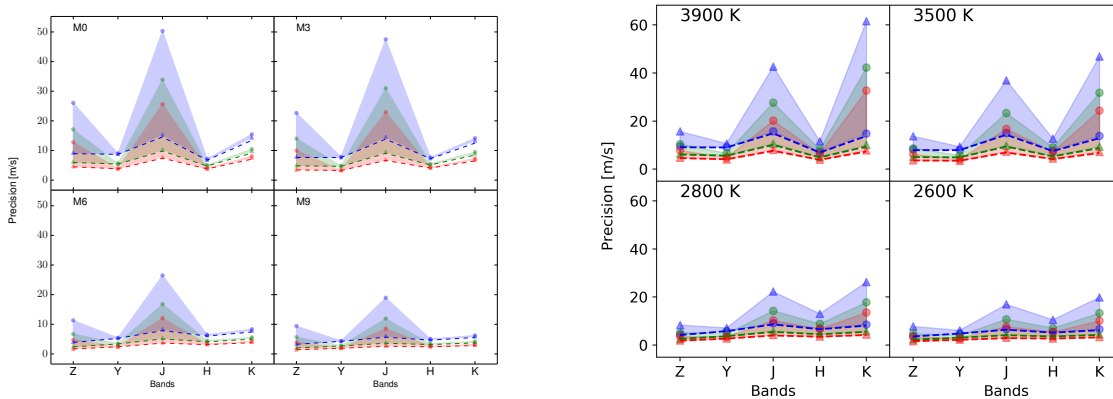


**Figure 8.4:** Left: Figure 1 from Figueira et al. (2016). Right: The same style figure with values updated from this work, computed with *eniric*. The main difference is the area of shaded region due to the problem with Condition #2 (which is the upper edge).

*H*-bands as well as to each band individually. Artigau 2018 (private communication 2018). suggested the truly relevant value is the SNR in *H*-band for NIRPS radial velocities.

The results can be manually generated using “eniric” with the following incantation (after installation and configuration of PHOENIX library spectra.) **A table of the precisions created for the NIRPS ETC are provided as an online table to our publication** Neal et al. 2018b (in prep.)<sup>11</sup>.

These values were both calculated and provided using the FFD gradient and with the incorrect masking order for Condition #2, splitting before calculating the pixel weights. As we demonstrated in Sections 8.5 and 8.5.1.1 these have a RV precision  $\sim 2\text{--}7\%$  better than what would be computed with the current implementation.

Check how to cite priv communication properly

Fix up when accepted

## 8.7 Updated Figueira 2016 results

figueira eta la plot 1, eniric plot

comparison of plots

## 8.8 metalicity / logg extension

Change to  $55 \text{ m s}^{-1}$  upper limit?

## 8.9 Application to CARMENES spectra

- target selection

- preparation of observed spectra
- Barnard’s star (Artigau 2018 comparison)

This work is work in progress. So far only 1 of 8 planned CARMENES spectra have been telluric corrected to calculate the RV precision.

I can calculate the RV precision from models though.

<sup>11</sup> Review at <https://github.com/openjournals/joss-reviews/issues/1053>

# Chapter 9

## Conclusions

### 9.1 Conclusions from Paper

This work explored two methods to try and detect the faint spectra of stellar companions, using high resolution near-infrared spectra. Two different methods were explored with many limitations uncovered.

The objective of the observations acquired in this program was to apply the differential technique. For the differential technique the observations need to be sufficiently separated, such that the RV of the companion is greater than the FWHM to avoid spectral cancellation of the companion. Unfortunately, due to operational reasons, this condition was not met. As such we employed an alternative method, that we termed the spectral recovery, which ended up revealing different difficulties.

For the spectral recovery the host-companion RV separation should also ideally be greater than the FWHM to avoid blended lines. The spectral mismatch between models and reality in the nIR negatively affects the performance of the synthetic recovery technique on the observed spectra. With all these effects we are unsuccessful in the detection of the nIRspectra of BD companions, with the mass upper-limits set at  $600 M_{Jup}$  from the synthetic recovery technique.

This work highlights many of the difficulties when dealing with the spectral recovery of nIRspectra. The obstacles to overcome are the data reduction of nIRCMOS detectors, that are not yet at the level of visible CCDs, along with a precise telluric correction and wavelength calibration (two interrelated aspects, as thoroughly discussed). Another important aspect is the mismatch between nIRhigh-resolution spectra and the observed spectra. In spite of the continuous effort of the modelling community, our work, along with several cited contemporary ones, shows that this mismatch is still one of the main factors preventing us from performing spectral recovery in the nIR. This work highlights that this is a compound problem for Brown Dwarfs, for which the spectral models are worse informed due to lack of observations at high-resolution.

Other than the improvement of the spectral models, the observing community can increase their odds of success by paying attention to the scheduling of observations and the wavelength domains to explore. Our work shows that observing in the areas of lower telluric absorption, as is frequently done, is not a guarantee of success due to the scarcity of deep lines in cold objects. Moreover, due to the mismatch between models and observations, the ability to obtain a first spectra before settling on a wavelength range, or changing settings on the fly, is extremely useful for the success of these campaigns.

We hope that this work can act as a guide for the planning of future observations of targets with faint BD and planetary companions with the upcoming generation of high resolution spectrographs in the near- and mid-infrared such as CRIRES+ and JWST observations.

Finish off this

NIR analysis  
work

## 9.2 Future Work

Future of RV precision

Machine learning techniques to the RV precision measured on the spectral library. For instance can it fit models of stellar parameters, or instrument/rotational broadening. Similar to theory?

A way to combine the information for the log $g$  and [Fe/H] observed in section 6.X.X...

Machine Learning RV precision of PHOENIX-ACES models.

---

Precision table  
needs fixed up

# Appendix A

## RV Precision Tables

The updated relative RV precision ( $\sigma_{RV}$  or  $dV_{RMS}$ ) results attainable from nIR spectra are presented in the following tables. Table A.1 shows the precision results for the same M-dwarfs analysed in Figueira et al. (2016). That is stellar temperatures 3900, 3500, 2800, 2600 K corresponding to spectral types M0, M3, M6, M9 respectively,  $\log g=4.5$  and  $[Fe/H]=0.0$ . The rotation applied are  $v\sin i=1, 5, 10 \text{ km s}^{-1}$  and instrumental profiles with  $R = 60k, 80k, 100k$ .

Columns 2–4 contain the RV precision calculated using PHOENIX-ACES spectra, as done in Figueira et al. (2016). These values differ from two effects. There is small difference in Conditions 1 and 3 from the change in numerical differentiation implemented (see Section 8.5). The values for Condition 2 however, are completely different due to the implementation error in the telluric masking discovered (see Section 8.5.2).

In columns 5–7 are the same RV precision calculation but using the BT-Settl spectral library instead (with same spectral parameters), a recent addition in *eniric*.

These can be created with *eniric* using the following shell incantation (after installation and configuration):

```
phoenix_precision.py -t 3900 3500 2800 2600 \
    -l 4.5 -m 0.5 \
    -r 60000 80000 100000 \
    -v 1.0 5.0 10.0 \
    -b Z Y J H K \
    --snr 100 \
    --ref_band J
```

# Temperature  
# Logg and Metalicity  
# Resolutions  
# Rotational velocities  
# Wavelength bands  
# Relative SNR  
# SNR reference band

*Eniric* was also used to calculate RV precision for the NIRPS and SPIRou. For SPIRou the requested precisions were provided with the SNR relative to the centre of each individual band. The values are provided in Table A.2 and can be generated with the following code; note the change in the *ref\_band* parameter.

Changing the reference band for the SNR scaling increases and decreases the precision in different bands due to the shape of the general black-body shape of the spectral profile. Comparing the precision values between Table A.1 and Table A.2, it has the effect of decreasing the  $\sigma_{RV}$  (increasing precision) in the *H*- and *K*-bands while increasing the  $\sigma_{RV}$  (decreasing precision) in the *Z*- and *Y*-bands. The RV

precision for the  $J$ -band remains unchanged, so is not included in Table A.2.

```
phoenix_precision.py -t 3900 3500 2800 2600 -l 4.5, -m 0.5 \
-r 60000 80000 100000 -v 1.0 5.0 10.0 -b Z Y J H K \
--snr 100 --ref_band self
```

For NIRPS RV precisions with an instrumental resolution of 75k was requested to match the NIRPS instrument, and provided relative to the  $J$ - and  $H$ -bands. The results for the NIRPS precision relative to the  $J$ -band are given in Table A.3, and can be reproduced with the following code.

```
phoenix_precision.py -t 3900 3500 2800 2600 -l 4.5, -m 0.5 \
-r 60000 75000 80000 100000 -v 1.0 5.0 10.0 \
-b Z Y J H K --snr 100 --ref_band H
```

**Table A.1:** RV precisions for the PHOENIX-ACES and BT-Settl synthetic spectral libraries. The PHOENIX-ACES values given here are the updated version of Table A.1 of Figueira et al. (2016).

Simulation (SpTp - Band - $v \cdot \sin i$ - R)	PHOENIX-ACES			BT-SETTL		
	$\sigma_{RV}$	$\sigma_{RV}$	$\sigma_{RV}$	$\sigma_{RV}$	$\sigma_{RV}$	$\sigma_{RV}$
	Cond. 1	Cond. 2	Cond. 3	Cond. 1	Cond. 2	Cond. 3
[m/s]	[m/s]	[m/s]	[m/s]	[m/s]	[m/s]	[m/s]
3900-Z-1.0-60k	9.7	15.5	10.0	9.4	15.3	9.7
3900-Z-1.0-80k	6.4	10.4	6.6	6.6	10.7	6.8
3900-Z-1.0-100k	4.7	7.8	4.9	5.2	8.5	5.3
3900-Z-5.0-60k	14.2	22.6	14.6	13.0	21.0	13.4
3900-Z-5.0-80k	10.9	17.6	11.3	10.1	16.4	10.5
3900-Z-5.0-100k	9.2	14.8	9.5	8.6	13.9	8.9
3900-Z-10.0-60k	24.5	38.6	25.3	21.8	35.1	22.4
3900-Z-10.0-80k	20.3	32.2	21.0	18.1	29.2	18.7
3900-Z-10.0-100k	17.8	28.2	18.3	15.9	25.6	16.3
3900-Y-1.0-60k	9.6	11.5	9.8	12.5	15.0	12.7
3900-Y-1.0-80k	6.0	7.1	6.0	8.3	10.0	8.4
3900-Y-1.0-100k	4.2	5.1	4.3	6.3	7.5	6.3
3900-Y-5.0-60k	15.5	18.4	15.7	18.6	22.3	18.9
3900-Y-5.0-80k	11.6	13.8	11.8	14.3	17.0	14.4
3900-Y-5.0-100k	9.7	11.5	9.8	11.9	14.3	12.1
3900-Y-10.0-60k	30.8	36.8	31.2	34.8	41.6	35.2
3900-Y-10.0-80k	25.2	30.1	25.5	28.6	34.3	29.0
3900-Y-10.0-100k	21.8	26.0	22.1	24.9	29.9	25.2
3900-J-1.0-60k	15.7	41.7	16.6	16.2	45.6	17.1
3900-J-1.0-80k	10.5	26.9	11.0	11.5	31.4	12.2
3900-J-1.0-100k	7.9	19.6	8.3	9.2	24.4	9.7
3900-J-5.0-60k	22.7	63.6	24.0	21.8	65.6	23.1

**Table A.1:** continued.

Simulation	PHOENIX-ACES			BT-SETTL		
	$\sigma_{RV}$	$\sigma_{RV}$	$\sigma_{RV}$	$\sigma_{RV}$	$\sigma_{RV}$	$\sigma_{RV}$
Cond. 1	Cond. 2	Cond. 3	Cond. 1	Cond. 2	Cond. 3	
3900-J-5.0-80k	17.5	48.1	18.5	17.1	50.2	18.2
3900-J-5.0-100k	14.8	40.3	15.6	14.6	42.1	15.4
3900-J-10.0-60k	38.6	122.9	41.0	35.4	122.3	37.7
3900-J-10.0-80k	32.0	100.7	34.0	29.5	100.5	31.4
3900-J-10.0-100k	28.0	87.6	29.8	25.9	87.5	27.6
3900-H-1.0-60k	7.2	11.4	7.4	7.6	11.9	7.8
3900-H-1.0-80k	5.0	8.0	5.1	5.4	8.4	5.5
3900-H-1.0-100k	4.0	6.3	4.0	4.2	6.6	4.3
3900-H-5.0-60k	10.1	15.9	10.3	10.8	16.8	11.0
3900-H-5.0-80k	7.9	12.4	8.0	8.3	13.1	8.5
3900-H-5.0-100k	6.6	10.5	6.8	7.0	11.0	7.2
3900-H-10.0-60k	17.5	27.3	17.9	18.8	29.4	19.2
3900-H-10.0-80k	14.5	22.7	14.9	15.6	24.4	16.0
3900-H-10.0-100k	12.7	19.9	13.0	13.6	21.3	14.0
3900-K-1.0-60k	14.5	63.7	15.5	13.7	63.2	14.6
3900-K-1.0-80k	9.7	43.6	10.4	9.6	45.2	10.3
3900-K-1.0-100k	7.4	33.6	8.0	7.6	36.1	8.1
3900-K-5.0-60k	21.7	90.3	23.2	19.4	85.4	20.8
3900-K-5.0-80k	16.6	70.0	17.7	15.0	67.0	16.1
3900-K-5.0-100k	13.9	59.2	14.8	12.6	56.9	13.5
3900-K-10.0-60k	39.4	155.8	42.1	34.2	142.8	36.6
3900-K-10.0-80k	32.6	128.9	34.9	28.4	118.5	30.4
3900-K-10.0-100k	28.5	112.5	30.5	24.8	104.0	26.6
3500-Z-1.0-60k	8.4	13.9	8.7	8.4	14.0	8.6
3500-Z-1.0-80k	5.2	8.8	5.4	5.6	9.4	5.7
3500-Z-1.0-100k	3.7	6.3	3.8	4.2	7.1	4.3
3500-Z-5.0-60k	13.2	21.3	13.6	12.3	20.1	12.7
3500-Z-5.0-80k	10.0	16.4	10.3	9.4	15.5	9.7
3500-Z-5.0-100k	8.3	13.6	8.6	7.9	13.0	8.2
3500-Z-10.0-60k	24.6	39.1	25.4	21.9	35.1	22.5
3500-Z-10.0-80k	20.3	32.4	20.9	18.1	29.1	18.6
3500-Z-10.0-100k	17.6	28.2	18.2	15.8	25.4	16.3
3500-Y-1.0-60k	8.5	10.1	8.6	11.3	13.3	11.4
3500-Y-1.0-80k	5.2	6.2	5.2	7.4	8.7	7.4
3500-Y-1.0-100k	3.6	4.3	3.7	5.5	6.5	5.5
3500-Y-5.0-60k	13.9	16.5	14.1	17.1	20.2	17.3
3500-Y-5.0-80k	10.4	12.3	10.5	13.0	15.3	13.1
3500-Y-5.0-100k	8.6	10.2	8.7	10.9	12.8	11.0

**Table A.1:** continued.

Simulation	PHOENIX-ACES			BT-SETTL		
	$\sigma_{RV}$	$\sigma_{RV}$	$\sigma_{RV}$	$\sigma_{RV}$	$\sigma_{RV}$	$\sigma_{RV}$
Cond. 1	Cond. 2	Cond. 3	Cond. 1	Cond. 2	Cond. 3	
3500-Y-10.0-60k	28.2	33.5	28.5	32.4	38.4	32.8
3500-Y-10.0-80k	23.0	27.3	23.3	26.7	31.5	27.0
3500-Y-10.0-100k	19.9	23.6	20.1	23.2	27.4	23.5
3500-J-1.0-60k	15.1	38.4	15.9	16.7	47.9	17.8
3500-J-1.0-80k	9.8	24.0	10.3	11.8	32.6	12.5
3500-J-1.0-100k	7.1	17.1	7.5	9.3	25.1	9.9
3500-J-5.0-60k	22.5	60.2	23.8	22.9	69.2	24.4
3500-J-5.0-80k	17.3	45.4	18.3	17.9	52.9	19.0
3500-J-5.0-100k	14.5	37.8	15.3	15.2	44.4	16.2
3500-J-10.0-60k	39.9	117.8	42.4	37.9	129.4	40.5
3500-J-10.0-80k	33.0	96.4	35.1	31.5	106.4	33.7
3500-J-10.0-100k	28.8	83.7	30.6	27.6	92.6	29.5
3500-H-1.0-60k	7.7	12.4	7.9	7.7	12.4	7.9
3500-H-1.0-80k	5.4	8.8	5.6	5.4	8.8	5.5
3500-H-1.0-100k	4.3	6.9	4.4	4.3	6.9	4.4
3500-H-5.0-60k	10.7	17.1	10.9	10.9	17.5	11.2
3500-H-5.0-80k	8.3	13.3	8.5	8.4	13.5	8.6
3500-H-5.0-100k	7.1	11.3	7.2	7.1	11.4	7.3
3500-H-10.0-60k	18.1	28.7	18.5	19.5	31.4	20.0
3500-H-10.0-80k	15.0	23.9	15.4	16.1	26.0	16.6
3500-H-10.0-100k	13.1	20.9	13.5	14.1	22.7	14.5
3500-K-1.0-60k	13.5	49.0	14.4	12.1	43.8	13.0
3500-K-1.0-80k	9.0	32.7	9.6	8.4	30.1	8.9
3500-K-1.0-100k	6.8	24.8	7.3	6.5	23.3	7.0
3500-K-5.0-60k	20.4	71.7	21.7	17.6	62.6	18.8
3500-K-5.0-80k	15.5	55.2	16.5	13.5	48.4	14.4
3500-K-5.0-100k	13.0	46.4	13.9	11.4	40.8	12.1
3500-K-10.0-60k	37.5	126.6	39.9	31.8	109.6	34.0
3500-K-10.0-80k	30.9	104.6	33.0	26.3	90.7	28.1
3500-K-10.0-100k	27.0	91.3	28.8	23.0	79.3	24.6
2800-Z-1.0-60k	4.4	8.4	4.5	4.0	7.6	4.2
2800-Z-1.0-80k	2.6	5.1	2.7	2.6	4.8	2.7
2800-Z-1.0-100k	1.8	3.6	1.9	1.9	3.5	1.9
2800-Z-5.0-60k	7.2	13.7	7.5	6.3	11.7	6.6
2800-Z-5.0-80k	5.4	10.3	5.6	4.8	8.8	4.9
2800-Z-5.0-100k	4.4	8.5	4.6	4.0	7.3	4.1
2800-Z-10.0-60k	14.6	27.3	15.2	12.6	22.8	13.0
2800-Z-10.0-80k	11.9	22.4	12.4	10.3	18.6	10.6

**Table A.1:** continued.

Simulation	PHOENIX-ACES			BT-SETTL		
	$\sigma_{RV}$	$\sigma_{RV}$	$\sigma_{RV}$	$\sigma_{RV}$	$\sigma_{RV}$	$\sigma_{RV}$
Cond. 1	Cond. 2	Cond. 3	Cond. 1	Cond. 2	Cond. 3	
2800-Z-10.0-100k	10.3	19.3	10.7	8.9	16.2	9.2
2800-Y-1.0-60k	5.8	7.4	5.9	11.7	14.0	11.9
2800-Y-1.0-80k	3.7	4.8	3.8	7.6	9.1	7.7
2800-Y-1.0-100k	2.7	3.5	2.7	5.6	6.7	5.7
2800-Y-5.0-60k	8.7	10.7	8.8	17.7	21.3	17.9
2800-Y-5.0-80k	6.7	8.3	6.8	13.5	16.2	13.7
2800-Y-5.0-100k	5.6	7.0	5.7	11.3	13.6	11.4
2800-Y-10.0-60k	14.7	17.5	14.9	32.5	39.0	32.9
2800-Y-10.0-80k	12.2	14.6	12.4	26.8	32.1	27.1
2800-Y-10.0-100k	10.7	12.8	10.8	23.3	28.0	23.6
2800-J-1.0-60k	8.8	23.2	9.3	11.0	31.7	11.8
2800-J-1.0-80k	5.5	14.4	5.8	7.6	21.5	8.1
2800-J-1.0-100k	4.0	10.2	4.2	5.8	16.3	6.2
2800-J-5.0-60k	13.5	35.9	14.3	15.6	45.3	16.7
2800-J-5.0-80k	10.3	27.3	10.9	12.1	35.1	13.0
2800-J-5.0-100k	8.6	22.8	9.1	10.2	29.6	10.9
2800-J-10.0-60k	24.3	63.8	25.7	26.7	78.5	28.5
2800-J-10.0-80k	20.1	52.9	21.2	22.2	65.1	23.7
2800-J-10.0-100k	17.5	46.1	18.5	19.4	57.0	20.7
2800-H-1.0-60k	6.6	12.8	6.9	5.7	11.1	5.9
2800-H-1.0-80k	4.4	8.5	4.6	3.9	7.5	4.0
2800-H-1.0-100k	3.3	6.4	3.5	3.0	5.8	3.1
2800-H-5.0-60k	9.8	18.8	10.2	8.4	16.4	8.7
2800-H-5.0-80k	7.5	14.4	7.8	6.5	12.6	6.7
2800-H-5.0-100k	6.3	12.1	6.5	5.4	10.5	5.6
2800-H-10.0-60k	17.8	34.7	18.4	15.6	31.0	16.2
2800-H-10.0-80k	14.7	28.7	15.2	12.9	25.5	13.3
2800-H-10.0-100k	12.8	25.0	13.3	11.2	22.2	11.6
2800-K-1.0-60k	8.2	27.0	8.7	7.1	22.9	7.5
2800-K-1.0-80k	5.4	17.9	5.7	4.8	15.6	5.1
2800-K-1.0-100k	4.0	13.5	4.3	3.7	12.0	4.0
2800-K-5.0-60k	12.4	39.7	13.2	10.3	33.3	11.0
2800-K-5.0-80k	9.4	30.5	10.0	7.9	25.6	8.4
2800-K-5.0-100k	7.9	25.6	8.4	6.6	21.5	7.1
2800-K-10.0-60k	23.0	70.7	24.6	19.1	59.6	20.4
2800-K-10.0-80k	19.0	58.5	20.3	15.8	49.3	16.8
2800-K-10.0-100k	16.6	51.1	17.7	13.8	43.0	14.7
2600-Z-1.0-60k	3.7	7.7	3.9	3.4	6.5	3.6

**Table A.1:** continued.

Simulation	PHOENIX-ACES			BT-SETTL		
	$\sigma_{RV}$	$\sigma_{RV}$	$\sigma_{RV}$	$\sigma_{RV}$	$\sigma_{RV}$	$\sigma_{RV}$
Cond. 1	Cond. 2	Cond. 3	Cond. 1	Cond. 2	Cond. 3	
2600-Z-1.0-80k	2.2	4.6	2.3	2.2	4.2	2.3
2600-Z-1.0-100k	1.5	3.2	1.6	1.6	3.0	1.7
2600-Z-5.0-60k	6.1	12.5	6.4	5.4	10.0	5.6
2600-Z-5.0-80k	4.6	9.4	4.8	4.0	7.6	4.2
2600-Z-5.0-100k	3.8	7.8	3.9	3.4	6.3	3.5
2600-Z-10.0-60k	12.3	24.9	12.9	10.6	19.6	11.0
2600-Z-10.0-80k	10.1	20.4	10.5	8.7	16.0	9.0
2600-Z-10.0-100k	8.7	17.6	9.1	7.5	13.9	7.8
2600-Y-1.0-60k	4.8	6.3	4.9	7.7	9.2	7.8
2600-Y-1.0-80k	3.0	4.0	3.1	5.0	5.9	5.0
2600-Y-1.0-100k	2.1	2.9	2.2	3.6	4.4	3.7
2600-Y-5.0-60k	7.2	9.1	7.3	11.7	14.2	11.9
2600-Y-5.0-80k	5.6	7.0	5.6	8.9	10.8	9.0
2600-Y-5.0-100k	4.7	5.9	4.7	7.4	9.0	7.5
2600-Y-10.0-60k	12.1	14.6	12.2	22.0	26.3	22.2
2600-Y-10.0-80k	10.1	12.2	10.2	18.0	21.6	18.3
2600-Y-10.0-100k	8.8	10.7	8.9	15.7	18.8	15.9
2600-J-1.0-60k	6.4	17.1	6.8	8.1	24.0	8.6
2600-J-1.0-80k	4.0	10.5	4.2	5.4	16.0	5.8
2600-J-1.0-100k	2.8	7.4	3.0	4.1	12.0	4.4
2600-J-5.0-60k	10.0	26.9	10.6	11.7	35.0	12.5
2600-J-5.0-80k	7.6	20.4	8.0	9.0	26.9	9.6
2600-J-5.0-100k	6.3	17.0	6.7	7.6	22.6	8.1
2600-J-10.0-60k	18.1	47.2	19.1	20.8	60.7	22.2
2600-J-10.0-80k	15.0	39.2	15.8	17.2	50.4	18.3
2600-J-10.0-100k	13.0	34.2	13.8	15.0	44.1	16.0
2600-H-1.0-60k	5.2	10.2	5.4	4.6	9.1	4.8
2600-H-1.0-80k	3.4	6.7	3.5	3.1	6.2	3.2
2600-H-1.0-100k	2.6	5.1	2.7	2.4	4.7	2.5
2600-H-5.0-60k	7.8	15.4	8.0	6.8	13.5	7.0
2600-H-5.0-80k	5.9	11.7	6.2	5.2	10.3	5.4
2600-H-5.0-100k	5.0	9.8	5.2	4.4	8.6	4.5
2600-H-10.0-60k	14.2	28.9	14.7	12.6	25.5	13.0
2600-H-10.0-80k	11.7	23.8	12.1	10.3	21.0	10.7
2600-H-10.0-100k	10.2	20.7	10.6	9.0	18.3	9.4
2600-K-1.0-60k	6.2	20.2	6.6	5.7	18.8	6.1
2600-K-1.0-80k	4.0	13.2	4.3	3.9	12.9	4.2
2600-K-1.0-100k	3.0	9.9	3.2	3.0	9.9	3.2

**Table A.1:** continued.

Simulation	PHOENIX-ACES			BT-SETTL		
	$\sigma_{RV}$	$\sigma_{RV}$	$\sigma_{RV}$	$\sigma_{RV}$	$\sigma_{RV}$	$\sigma_{RV}$
	Cond. 1	Cond. 2	Cond. 3	Cond. 1	Cond. 2	Cond. 3
2600-K-5.0-60k	9.4	30.1	10.0	8.3	27.2	8.9
2600-K-5.0-80k	7.1	23.0	7.6	6.4	20.9	6.8
2600-K-5.0-100k	6.0	19.3	6.4	5.3	17.6	5.7
2600-K-10.0-60k	17.4	54.0	18.6	15.2	48.5	16.2
2600-K-10.0-80k	14.4	44.7	15.3	12.5	40.1	13.4
2600-K-10.0-100k	12.5	39.1	13.4	10.9	35.0	11.7

**Table A.2:** RV precisions calculated for the SPIRou ETC. The same PHOENIX-ACES parameter combinations as Table A.1 but with the SNR=100 relative to the centre of each band individually.

Simulation (T <sub>eff</sub> -Band- $v \cdot \sin i$ -R)	$\sigma_{RV}$ (Cond. 1) [m/s]	$\sigma_{RV}$ (Cond. 2) [m/s]	$\sigma_{RV}$ (Cond. 3) [m/s]
3900-Z-1.0-60k	9.9	16.0	10.3
3900-Z-1.0-80k	6.6	10.7	6.8
3900-Z-1.0-100k	4.9	8.1	5.1
3900-Z-5.0-60k	14.5	23.2	15.0
3900-Z-5.0-80k	11.2	18.0	11.6
3900-Z-5.0-100k	9.4	15.2	9.7
3900-Z-10.0-60k	25.0	39.4	25.8
3900-Z-10.0-80k	20.7	32.9	21.4
3900-Z-10.0-100k	18.1	28.8	18.7
3900-Y-1.0-60k	10.0	11.9	10.1
3900-Y-1.0-80k	6.2	7.4	6.3
3900-Y-1.0-100k	4.4	5.3	4.5
3900-Y-5.0-60k	15.9	19.0	16.1
3900-Y-5.0-80k	12.0	14.3	12.1
3900-Y-5.0-100k	10.0	11.8	10.1
3900-Y-10.0-60k	31.6	37.8	32.0
3900-Y-10.0-80k	25.8	30.8	26.1
3900-Y-10.0-100k	22.4	26.7	22.6
3900-H-1.0-60k	7.3	11.5	7.4
3900-H-1.0-80k	5.1	8.1	5.2
3900-H-1.0-100k	4.0	6.4	4.1
3900-H-5.0-60k	10.2	16.0	10.4
3900-H-5.0-80k	7.9	12.5	8.1
3900-H-5.0-100k	6.7	10.5	6.8
3900-H-10.0-60k	17.5	27.3	17.9
3900-H-10.0-80k	14.5	22.7	14.8
3900-H-10.0-100k	12.7	19.8	13.0
3900-K-1.0-60k	10.5	46.3	11.3
3900-K-1.0-80k	7.1	31.8	7.6
3900-K-1.0-100k	5.4	24.5	5.8
3900-K-5.0-60k	15.7	65.4	16.8
3900-K-5.0-80k	12.0	50.8	12.8
3900-K-5.0-100k	10.1	42.9	10.8
3900-K-10.0-60k	28.5	112.6	30.4
3900-K-10.0-80k	23.6	93.1	25.2
3900-K-10.0-100k	20.6	81.2	22.0
3500-Z-1.0-60k	8.3	13.7	8.6
3500-Z-1.0-80k	5.2	8.7	5.4

**Table A.2:** continued.

Simulation	$\sigma_{RV}$ (Cond. 1)	$\sigma_{RV}$ (Cond. 2)	$\sigma_{RV}$ (Cond. 3)
3500-Z-1.0-100k	3.7	6.3	3.8
3500-Z-5.0-60k	12.9	20.9	13.3
3500-Z-5.0-80k	9.8	16.0	10.1
3500-Z-5.0-100k	8.2	13.4	8.5
3500-Z-10.0-60k	24.0	38.1	24.8
3500-Z-10.0-80k	19.7	31.5	20.4
3500-Z-10.0-100k	17.2	27.5	17.7
3500-Y-1.0-60k	8.7	10.3	8.8
3500-Y-1.0-80k	5.3	6.3	5.4
3500-Y-1.0-100k	3.7	4.5	3.8
3500-Y-5.0-60k	14.1	16.7	14.3
3500-Y-5.0-80k	10.6	12.5	10.7
3500-Y-5.0-100k	8.8	10.4	8.9
3500-Y-10.0-60k	28.5	33.9	28.8
3500-Y-10.0-80k	23.2	27.6	23.5
3500-Y-10.0-100k	20.1	23.9	20.3
3500-H-1.0-60k	7.6	12.2	7.8
3500-H-1.0-80k	5.4	8.7	5.5
3500-H-1.0-100k	4.2	6.9	4.3
3500-H-5.0-60k	10.5	16.7	10.7
3500-H-5.0-80k	8.2	13.1	8.4
3500-H-5.0-100k	6.9	11.1	7.1
3500-H-10.0-60k	17.6	28.0	18.1
3500-H-10.0-80k	14.6	23.3	15.0
3500-H-10.0-100k	12.8	20.4	13.1
3500-K-1.0-60k	9.9	35.8	10.6
3500-K-1.0-80k	6.6	24.0	7.0
3500-K-1.0-100k	5.0	18.2	5.3
3500-K-5.0-60k	14.8	52.3	15.8
3500-K-5.0-80k	11.3	40.2	12.1
3500-K-5.0-100k	9.5	33.8	10.1
3500-K-10.0-60k	27.2	92.1	29.1
3500-K-10.0-80k	22.5	76.0	24.0
3500-K-10.0-100k	19.6	66.3	20.9
2800-Z-1.0-60k	3.8	7.3	3.9
2800-Z-1.0-80k	2.3	4.5	2.4
2800-Z-1.0-100k	1.6	3.2	1.7
2800-Z-5.0-60k	6.1	11.6	6.4
2800-Z-5.0-80k	4.6	8.8	4.8
2800-Z-5.0-100k	3.8	7.3	4.0

**Table A.2:** continued.

Simulation	$\sigma_{RV}$ (Cond. 1)	$\sigma_{RV}$ (Cond. 2)	$\sigma_{RV}$ (Cond. 3)
2800-Z-10.0-60k	12.2	22.8	12.7
2800-Z-10.0-80k	9.9	18.7	10.4
2800-Z-10.0-100k	8.6	16.2	9.0
2800-Y-1.0-60k	5.6	7.1	5.7
2800-Y-1.0-80k	3.6	4.7	3.7
2800-Y-1.0-100k	2.6	3.4	2.7
2800-Y-5.0-60k	8.3	10.1	8.4
2800-Y-5.0-80k	6.4	7.9	6.5
2800-Y-5.0-100k	5.4	6.7	5.5
2800-Y-10.0-60k	13.8	16.4	13.9
2800-Y-10.0-80k	11.4	13.7	11.6
2800-Y-10.0-100k	10.0	12.0	10.1
2800-H-1.0-60k	6.5	12.6	6.8
2800-H-1.0-80k	4.4	8.5	4.6
2800-H-1.0-100k	3.3	6.4	3.5
2800-H-5.0-60k	9.6	18.3	9.9
2800-H-5.0-80k	7.3	14.1	7.6
2800-H-5.0-100k	6.2	11.8	6.4
2800-H-10.0-60k	17.2	33.5	17.8
2800-H-10.0-80k	14.2	27.6	14.7
2800-H-10.0-100k	12.4	24.1	12.8
2800-K-1.0-60k	6.3	20.8	6.7
2800-K-1.0-80k	4.2	13.9	4.5
2800-K-1.0-100k	3.1	10.5	3.4
2800-K-5.0-60k	9.5	30.4	10.1
2800-K-5.0-80k	7.2	23.3	7.7
2800-K-5.0-100k	6.0	19.6	6.4
2800-K-10.0-60k	17.5	53.7	18.7
2800-K-10.0-80k	14.4	44.4	15.4
2800-K-10.0-100k	12.6	38.8	13.4
2600-Z-1.0-60k	3.0	6.2	3.1
2600-Z-1.0-80k	1.8	3.8	1.9
2600-Z-1.0-100k	1.3	2.7	1.4
2600-Z-5.0-60k	4.8	9.8	5.0
2600-Z-5.0-80k	3.6	7.4	3.8
2600-Z-5.0-100k	3.0	6.2	3.2
2600-Z-10.0-60k	9.5	19.2	9.9
2600-Z-10.0-80k	7.7	15.7	8.1
2600-Z-10.0-100k	6.7	13.6	7.1
2600-Y-1.0-60k	4.4	5.8	4.5

**Table A.2:** continued.

Simulation	$\sigma_{RV}$ (Cond. 1)	$\sigma_{RV}$ (Cond. 2)	$\sigma_{RV}$ (Cond. 3)
2600-Y-1.0-80k	2.8	3.8	2.9
2600-Y-1.0-100k	2.0	2.7	2.1
2600-Y-5.0-60k	6.5	8.2	6.6
2600-Y-5.0-80k	5.1	6.4	5.1
2600-Y-5.0-100k	4.3	5.4	4.3
2600-Y-10.0-60k	10.7	12.9	10.8
2600-Y-10.0-80k	8.9	10.8	9.0
2600-Y-10.0-100k	7.8	9.5	7.9
2600-H-1.0-60k	5.2	10.3	5.4
2600-H-1.0-80k	3.5	6.9	3.6
2600-H-1.0-100k	2.7	5.2	2.8
2600-H-5.0-60k	7.7	15.3	8.0
2600-H-5.0-80k	5.9	11.7	6.1
2600-H-5.0-100k	5.0	9.8	5.2
2600-H-10.0-60k	13.9	28.4	14.5
2600-H-10.0-80k	11.5	23.3	11.9
2600-H-10.0-100k	10.0	20.4	10.4
2600-K-1.0-60k	5.0	16.2	5.3
2600-K-1.0-80k	3.3	10.7	3.5
2600-K-1.0-100k	2.5	8.0	2.6
2600-K-5.0-60k	7.4	23.9	7.9
2600-K-5.0-80k	5.7	18.3	6.1
2600-K-5.0-100k	4.8	15.4	5.1
2600-K-10.0-60k	13.7	42.5	14.6
2600-K-10.0-80k	11.3	35.1	12.1
2600-K-10.0-100k	9.9	30.7	10.5

**Table A.3:** RV precisions calculated for the NIRPS ETC. All temperatures spanning 2500–4000 K at a resolution of 75 000 and 100 000 only.

Simulation (T <sub>eff</sub> -Band- $v \cdot \sin i$ -R)	$\sigma_{RV}$ (Cond. 1) [m/s]	$\sigma_{RV}$ (Cond. 2) [m/s]	$\sigma_{RV}$ (Cond. 3) [m/s]
4000-Z-1.0-75k	6.9	11.2	7.1
4000-Z-1.0-100k	4.7	7.7	4.9
4000-Z-5.0-75k	11.2	18.2	11.6
4000-Z-5.0-100k	9.0	14.5	9.3
4000-Z-10.0-75k	20.5	32.6	21.1
4000-Z-10.0-100k	17.2	27.4	17.8
4000-Y-1.0-75k	6.8	8.1	6.8
4000-Y-1.0-100k	4.4	5.2	4.4

**Table A.3:** continued.

Simulation	$\sigma_{RV}$ (Cond. 1)	$\sigma_{RV}$ (Cond. 2)	$\sigma_{RV}$ (Cond. 3)
4000-Y-5.0-75k	12.5	14.9	12.6
4000-Y-5.0-100k	9.8	11.7	9.9
4000-Y-10.0-75k	26.4	31.6	26.8
4000-Y-10.0-100k	21.9	26.2	22.2
4000-J-1.0-75k	11.3	29.3	11.9
4000-J-1.0-100k	7.8	19.7	8.2
4000-J-5.0-75k	18.1	50.1	19.1
4000-J-5.0-100k	14.5	39.7	15.3
4000-J-10.0-75k	32.3	102.4	34.3
4000-J-10.0-100k	27.2	85.5	28.9
4000-H-1.0-75k	5.4	8.5	5.5
4000-H-1.0-100k	3.9	6.2	4.0
4000-H-5.0-75k	8.2	13.0	8.4
4000-H-5.0-100k	6.6	10.4	6.7
4000-H-10.0-75k	15.0	23.5	15.4
4000-H-10.0-100k	12.6	19.7	12.9
4000-K-1.0-75k	10.4	47.3	11.1
4000-K-1.0-100k	7.3	33.7	7.8
4000-K-5.0-75k	17.2	73.5	18.4
4000-K-5.0-100k	13.7	59.0	14.6
4000-K-10.0-75k	33.4	132.8	35.7
4000-K-10.0-100k	28.0	111.8	29.9
3900-Z-1.0-75k	7.0	11.4	7.2
3900-Z-1.0-100k	4.7	7.8	4.9
3900-Z-5.0-75k	11.5	18.6	11.9
3900-Z-5.0-100k	9.2	14.8	9.5
3900-Z-10.0-75k	21.2	33.6	21.8
3900-Z-10.0-100k	17.8	28.2	18.3
3900-Y-1.0-75k	6.6	7.9	6.7
3900-Y-1.0-100k	4.2	5.1	4.3
3900-Y-5.0-75k	12.3	14.7	12.5
3900-Y-5.0-100k	9.7	11.5	9.8
3900-Y-10.0-75k	26.3	31.4	26.6
3900-Y-10.0-100k	21.8	26.0	22.1
3900-J-1.0-75k	11.5	29.5	12.1
3900-J-1.0-100k	7.9	19.6	8.3
3900-J-5.0-75k	18.5	50.9	19.6
3900-J-5.0-100k	14.8	40.3	15.6
3900-J-10.0-75k	33.4	104.9	35.4
3900-J-10.0-100k	28.0	87.6	29.8

**Table A.3:** continued.

Simulation	$\sigma_{RV}$ (Cond. 1)	$\sigma_{RV}$ (Cond. 2)	$\sigma_{RV}$ (Cond. 3)
3900-H-1.0-75k	5.4	8.6	5.5
3900-H-1.0-100k	4.0	6.3	4.0
3900-H-5.0-75k	8.3	13.0	8.5
3900-H-5.0-100k	6.6	10.5	6.8
3900-H-10.0-75k	15.1	23.6	15.5
3900-H-10.0-100k	12.7	19.9	13.0
3900-K-1.0-75k	10.6	47.3	11.3
3900-K-1.0-100k	7.4	33.6	8.0
3900-K-5.0-75k	17.5	73.8	18.7
3900-K-5.0-100k	13.9	59.2	14.8
3900-K-10.0-75k	34.0	133.7	36.3
3900-K-10.0-100k	28.5	112.5	30.5
3800-Z-1.0-75k	6.9	11.3	7.2
3800-Z-1.0-100k	4.7	7.7	4.8
3800-Z-5.0-75k	11.7	18.7	12.0
3800-Z-5.0-100k	9.3	14.9	9.6
3800-Z-10.0-75k	21.7	34.2	22.4
3800-Z-10.0-100k	18.2	28.7	18.8
3800-Y-1.0-75k	6.5	7.7	6.5
3800-Y-1.0-100k	4.1	4.9	4.2
3800-Y-5.0-75k	12.1	14.4	12.3
3800-Y-5.0-100k	9.5	11.3	9.6
3800-Y-10.0-75k	26.0	31.0	26.3
3800-Y-10.0-100k	21.5	25.7	21.8
3800-J-1.0-75k	11.5	29.3	12.1
3800-J-1.0-100k	7.8	19.4	8.2
3800-J-5.0-75k	18.7	51.2	19.8
3800-J-5.0-100k	14.9	40.5	15.8
3800-J-10.0-75k	34.1	106.2	36.2
3800-J-10.0-100k	28.7	88.6	30.4
3800-H-1.0-75k	5.5	8.8	5.7
3800-H-1.0-100k	4.1	6.4	4.1
3800-H-5.0-75k	8.4	13.2	8.6
3800-H-5.0-100k	6.7	10.6	6.9
3800-H-10.0-75k	15.2	23.7	15.6
3800-H-10.0-100k	12.8	20.0	13.1
3800-K-1.0-75k	10.7	46.0	11.4
3800-K-1.0-100k	7.5	32.5	8.0
3800-K-5.0-75k	17.7	72.6	18.9
3800-K-5.0-100k	14.0	58.2	15.0

**Table A.3:** continued.

Simulation	$\sigma_{RV}$ (Cond. 1)	$\sigma_{RV}$ (Cond. 2)	$\sigma_{RV}$ (Cond. 3)
3800-K-10.0-75k	34.4	132.6	36.7
3800-K-10.0-100k	28.8	111.5	30.8
3700-Z-1.0-75k	6.8	11.1	7.0
3700-Z-1.0-100k	4.5	7.4	4.6
3700-Z-5.0-75k	11.6	18.7	12.0
3700-Z-5.0-100k	9.2	14.8	9.5
3700-Z-10.0-75k	22.0	34.6	22.7
3700-Z-10.0-100k	18.4	29.1	19.0
3700-Y-1.0-75k	6.3	7.5	6.3
3700-Y-1.0-100k	4.0	4.8	4.0
3700-Y-5.0-75k	11.9	14.1	12.0
3700-Y-5.0-100k	9.3	11.0	9.4
3700-Y-10.0-75k	25.6	30.4	25.9
3700-Y-10.0-100k	21.2	25.2	21.4
3700-J-1.0-75k	11.4	28.8	12.0
3700-J-1.0-100k	7.7	18.9	8.1
3700-J-5.0-75k	18.8	50.9	19.9
3700-J-5.0-100k	15.0	40.2	15.8
3700-J-10.0-75k	34.7	106.0	36.8
3700-J-10.0-100k	29.1	88.4	30.9
3700-H-1.0-75k	5.7	9.0	5.8
3700-H-1.0-100k	4.2	6.6	4.3
3700-H-5.0-75k	8.5	13.4	8.7
3700-H-5.0-100k	6.8	10.8	7.0
3700-H-10.0-75k	15.3	24.0	15.7
3700-H-10.0-100k	12.9	20.2	13.2
3700-K-1.0-75k	10.6	43.7	11.4
3700-K-1.0-100k	7.5	30.7	8.0
3700-K-5.0-75k	17.7	70.1	18.9
3700-K-5.0-100k	14.0	56.0	15.0
3700-K-10.0-75k	34.5	128.8	36.8
3700-K-10.0-100k	28.9	108.3	30.9
3600-Z-1.0-75k	6.3	10.5	6.6
3600-Z-1.0-100k	4.1	6.9	4.3
3600-Z-5.0-75k	11.2	18.2	11.6
3600-Z-5.0-100k	8.9	14.4	9.2
3600-Z-10.0-75k	21.8	34.5	22.5
3600-Z-10.0-100k	18.2	28.9	18.8
3600-Y-1.0-75k	6.0	7.2	6.1
3600-Y-1.0-100k	3.8	4.6	3.9

**Table A.3:** continued.

Simulation	$\sigma_{RV}$ (Cond. 1)	$\sigma_{RV}$ (Cond. 2)	$\sigma_{RV}$ (Cond. 3)
3600-Y-5.0-75k	11.5	13.6	11.6
3600-Y-5.0-100k	9.0	10.6	9.1
3600-Y-10.0-75k	24.9	29.6	25.2
3600-Y-10.0-100k	20.6	24.5	20.9
3600-J-1.0-75k	11.1	27.9	11.7
3600-J-1.0-100k	7.5	18.1	7.8
3600-J-5.0-75k	18.7	49.8	19.7
3600-J-5.0-100k	14.8	39.3	15.7
3600-J-10.0-75k	34.7	104.0	36.9
3600-J-10.0-100k	29.1	86.7	30.9
3600-H-1.0-75k	5.8	9.2	5.9
3600-H-1.0-100k	4.3	6.8	4.3
3600-H-5.0-75k	8.6	13.7	8.8
3600-H-5.0-100k	6.9	11.0	7.1
3600-H-10.0-75k	15.4	24.3	15.8
3600-H-10.0-100k	13.0	20.5	13.3
3600-K-1.0-75k	10.3	39.8	11.0
3600-K-1.0-100k	7.2	27.8	7.7
3600-K-5.0-75k	17.2	64.7	18.4
3600-K-5.0-100k	13.7	51.6	14.6
3600-K-10.0-75k	33.7	120.0	36.0
3600-K-10.0-100k	28.2	100.8	30.2
3500-Z-1.0-75k	5.8	9.7	6.0
3500-Z-1.0-100k	3.7	6.3	3.8
3500-Z-5.0-75k	10.6	17.3	10.9
3500-Z-5.0-100k	8.3	13.6	8.6
3500-Z-10.0-75k	21.1	33.8	21.8
3500-Z-10.0-100k	17.6	28.2	18.2
3500-Y-1.0-75k	5.8	6.9	5.8
3500-Y-1.0-100k	3.6	4.3	3.7
3500-Y-5.0-75k	11.0	13.1	11.2
3500-Y-5.0-100k	8.6	10.2	8.7
3500-Y-10.0-75k	24.0	28.5	24.3
3500-Y-10.0-100k	19.9	23.6	20.1
3500-J-1.0-75k	10.7	26.6	11.3
3500-J-1.0-100k	7.1	17.1	7.5
3500-J-5.0-75k	18.3	48.1	19.3
3500-J-5.0-100k	14.5	37.8	15.3
3500-J-10.0-75k	34.4	100.5	36.5
3500-J-10.0-100k	28.8	83.7	30.6

**Table A.3:** continued.

Simulation	$\sigma_{RV}$ (Cond. 1)	$\sigma_{RV}$ (Cond. 2)	$\sigma_{RV}$ (Cond. 3)
3500-H-1.0-75k	5.8	9.4	6.0
3500-H-1.0-100k	4.3	6.9	4.4
3500-H-5.0-75k	8.8	14.0	9.0
3500-H-5.0-100k	7.1	11.3	7.2
3500-H-10.0-75k	15.6	24.8	16.0
3500-H-10.0-100k	13.1	20.9	13.5
3500-K-1.0-75k	9.8	35.7	10.5
3500-K-1.0-100k	6.8	24.8	7.3
3500-K-5.0-75k	16.4	58.2	17.5
3500-K-5.0-100k	13.0	46.4	13.9
3500-K-10.0-75k	32.2	108.7	34.4
3500-K-10.0-100k	27.0	91.3	28.8
3400-Z-1.0-75k	5.3	8.9	5.5
3400-Z-1.0-100k	3.3	5.7	3.5
3400-Z-5.0-75k	9.8	16.3	10.2
3400-Z-5.0-100k	7.7	12.8	8.0
3400-Z-10.0-75k	20.2	32.7	20.8
3400-Z-10.0-100k	16.8	27.2	17.3
3400-Y-1.0-75k	5.5	6.6	5.6
3400-Y-1.0-100k	3.5	4.2	3.5
3400-Y-5.0-75k	10.5	12.4	10.6
3400-Y-5.0-100k	8.2	9.7	8.3
3400-Y-10.0-75k	22.3	26.4	22.5
3400-Y-10.0-100k	18.5	21.9	18.7
3400-J-1.0-75k	10.2	25.0	10.8
3400-J-1.0-100k	6.7	15.9	7.1
3400-J-5.0-75k	17.6	45.6	18.6
3400-J-5.0-100k	14.0	35.9	14.7
3400-J-10.0-75k	33.6	95.5	35.7
3400-J-10.0-100k	28.1	79.4	29.9
3400-H-1.0-75k	5.9	9.7	6.0
3400-H-1.0-100k	4.3	7.1	4.4
3400-H-5.0-75k	8.9	14.5	9.2
3400-H-5.0-100k	7.2	11.7	7.4
3400-H-10.0-75k	16.0	25.8	16.4
3400-H-10.0-100k	13.4	21.7	13.8
3400-K-1.0-75k	9.2	31.8	9.8
3400-K-1.0-100k	6.4	22.2	6.8
3400-K-5.0-75k	15.4	52.0	16.4
3400-K-5.0-100k	12.2	41.4	13.0

**Table A.3:** continued.

Simulation	$\sigma_{RV}$ (Cond. 1)	$\sigma_{RV}$ (Cond. 2)	$\sigma_{RV}$ (Cond. 3)
3400-K-10.0-75k	30.5	97.5	32.4
3400-K-10.0-100k	25.5	81.8	27.2
3300-Z-1.0-75k	4.8	8.2	5.0
3300-Z-1.0-100k	3.0	5.2	3.1
3300-Z-5.0-75k	9.1	15.3	9.4
3300-Z-5.0-100k	7.1	11.9	7.3
3300-Z-10.0-75k	19.0	31.3	19.7
3300-Z-10.0-100k	15.8	26.0	16.4
3300-Y-1.0-75k	5.8	7.1	5.9
3300-Y-1.0-100k	3.8	4.6	3.8
3300-Y-5.0-75k	10.3	12.2	10.4
3300-Y-5.0-100k	8.1	9.7	8.2
3300-Y-10.0-75k	19.9	23.5	20.1
3300-Y-10.0-100k	16.6	19.6	16.8
3300-J-1.0-75k	9.5	23.0	10.1
3300-J-1.0-100k	6.2	14.6	6.6
3300-J-5.0-75k	16.7	42.5	17.7
3300-J-5.0-100k	13.2	33.3	13.9
3300-J-10.0-75k	32.3	89.0	34.3
3300-J-10.0-100k	27.0	74.0	28.6
3300-H-1.0-75k	5.9	10.0	6.1
3300-H-1.0-100k	4.3	7.2	4.4
3300-H-5.0-75k	9.1	15.2	9.4
3300-H-5.0-100k	7.3	12.2	7.5
3300-H-10.0-75k	16.5	27.3	16.9
3300-H-10.0-100k	13.9	22.9	14.2
3300-K-1.0-75k	8.7	28.9	9.2
3300-K-1.0-100k	6.0	20.2	6.4
3300-K-5.0-75k	14.6	47.2	15.5
3300-K-5.0-100k	11.5	37.6	12.3
3300-K-10.0-75k	28.8	88.8	30.7
3300-K-10.0-100k	24.1	74.6	25.7
3200-Z-1.0-75k	4.3	7.5	4.5
3200-Z-1.0-100k	2.7	4.7	2.8
3200-Z-5.0-75k	8.3	14.2	8.6
3200-Z-5.0-100k	6.5	11.1	6.7
3200-Z-10.0-75k	17.8	29.8	18.4
3200-Z-10.0-100k	14.7	24.7	15.3
3200-Y-1.0-75k	5.5	6.7	5.6
3200-Y-1.0-100k	3.6	4.4	3.6

**Table A.3:** continued.

Simulation	$\sigma_{RV}$ (Cond. 1)	$\sigma_{RV}$ (Cond. 2)	$\sigma_{RV}$ (Cond. 3)
3200-Y-5.0-75k	9.7	11.6	9.8
3200-Y-5.0-100k	7.6	9.2	7.7
3200-Y-10.0-75k	18.4	21.7	18.6
3200-Y-10.0-100k	15.4	18.2	15.6
3200-J-1.0-75k	8.7	20.6	9.2
3200-J-1.0-100k	5.6	13.0	5.9
3200-J-5.0-75k	15.5	38.5	16.3
3200-J-5.0-100k	12.2	30.2	12.9
3200-J-10.0-75k	30.3	80.8	32.1
3200-J-10.0-100k	25.3	67.2	26.8
3200-H-1.0-75k	5.9	10.3	6.1
3200-H-1.0-100k	4.2	7.4	4.3
3200-H-5.0-75k	9.3	15.9	9.6
3200-H-5.0-100k	7.4	12.7	7.7
3200-H-10.0-75k	17.0	29.0	17.5
3200-H-10.0-100k	14.3	24.4	14.7
3200-K-1.0-75k	8.2	26.9	8.7
3200-K-1.0-100k	5.7	18.8	6.1
3200-K-5.0-75k	13.8	43.9	14.7
3200-K-5.0-100k	10.9	34.9	11.6
3200-K-10.0-75k	27.4	82.7	29.2
3200-K-10.0-100k	22.9	69.4	24.4
3100-Z-1.0-75k	4.0	7.3	4.2
3100-Z-1.0-100k	2.5	4.6	2.6
3100-Z-5.0-75k	7.8	13.8	8.1
3100-Z-5.0-100k	6.1	10.8	6.3
3100-Z-10.0-75k	16.7	29.0	17.3
3100-Z-10.0-100k	13.9	24.1	14.4
3100-Y-1.0-75k	5.5	6.8	5.6
3100-Y-1.0-100k	3.6	4.5	3.7
3100-Y-5.0-75k	9.4	11.3	9.5
3100-Y-5.0-100k	7.5	9.0	7.5
3100-Y-10.0-75k	17.3	20.5	17.5
3100-Y-10.0-100k	14.5	17.2	14.7
3100-J-1.0-75k	7.7	17.9	8.1
3100-J-1.0-100k	5.0	11.2	5.2
3100-J-5.0-75k	13.9	34.0	14.7
3100-J-5.0-100k	11.0	26.6	11.6
3100-J-10.0-75k	27.7	71.5	29.3
3100-J-10.0-100k	23.1	59.4	24.4

**Table A.3:** continued.

Simulation	$\sigma_{RV}$ (Cond. 1)	$\sigma_{RV}$ (Cond. 2)	$\sigma_{RV}$ (Cond. 3)
3100-H-1.0-75k	5.8	10.4	6.0
3100-H-1.0-100k	4.1	7.4	4.3
3100-H-5.0-75k	9.3	16.4	9.6
3100-H-5.0-100k	7.4	13.1	7.7
3100-H-10.0-75k	17.3	30.6	17.9
3100-H-10.0-100k	14.5	25.6	15.0
3100-K-1.0-75k	7.7	25.2	8.2
3100-K-1.0-100k	5.4	17.6	5.7
3100-K-5.0-75k	13.1	41.3	13.9
3100-K-5.0-100k	10.3	32.8	11.0
3100-K-10.0-75k	26.0	77.9	27.7
3100-K-10.0-100k	21.7	65.4	23.1
3000-Z-1.0-75k	3.6	6.8	3.8
3000-Z-1.0-100k	2.3	4.2	2.4
3000-Z-5.0-75k	7.1	12.9	7.4
3000-Z-5.0-100k	5.5	10.0	5.7
3000-Z-10.0-75k	15.3	27.1	15.9
3000-Z-10.0-100k	12.7	22.5	13.2
3000-Y-1.0-75k	5.0	6.3	5.1
3000-Y-1.0-100k	3.3	4.2	3.4
3000-Y-5.0-75k	8.6	10.4	8.7
3000-Y-5.0-100k	6.8	8.3	6.9
3000-Y-10.0-75k	15.7	18.6	15.9
3000-Y-10.0-100k	13.2	15.7	13.3
3000-J-1.0-75k	7.9	20.4	8.3
3000-J-1.0-100k	5.1	13.1	5.4
3000-J-5.0-75k	13.9	37.0	14.7
3000-J-5.0-100k	11.0	29.1	11.6
3000-J-10.0-75k	26.7	72.6	28.3
3000-J-10.0-100k	22.3	60.8	23.7
3000-H-1.0-75k	5.6	10.3	5.8
3000-H-1.0-100k	3.9	7.3	4.1
3000-H-5.0-75k	9.1	16.5	9.4
3000-H-5.0-100k	7.2	13.2	7.5
3000-H-10.0-75k	17.2	31.4	17.8
3000-H-10.0-100k	14.4	26.3	14.9
3000-K-1.0-75k	7.2	23.5	7.7
3000-K-1.0-100k	5.0	16.4	5.3
3000-K-5.0-75k	12.2	38.6	13.0
3000-K-5.0-100k	9.6	30.7	10.2

**Table A.3:** continued.

Simulation	$\sigma_{RV}$ (Cond. 1)	$\sigma_{RV}$ (Cond. 2)	$\sigma_{RV}$ (Cond. 3)
3000-K-10.0-75k	24.2	73.0	25.8
3000-K-10.0-100k	20.3	61.2	21.6
2900-Z-1.0-75k	3.3	6.2	3.4
2900-Z-1.0-100k	2.0	3.9	2.1
2900-Z-5.0-75k	6.4	11.8	6.6
2900-Z-5.0-100k	4.9	9.2	5.1
2900-Z-10.0-75k	13.8	25.1	14.4
2900-Z-10.0-100k	11.4	20.8	11.9
2900-Y-1.0-75k	4.6	5.8	4.6
2900-Y-1.0-100k	3.0	3.9	3.0
2900-Y-5.0-75k	7.8	9.6	7.9
2900-Y-5.0-100k	6.2	7.6	6.3
2900-Y-10.0-75k	14.2	16.8	14.3
2900-Y-10.0-100k	11.9	14.2	12.0
2900-J-1.0-75k	7.1	18.6	7.5
2900-J-1.0-100k	4.6	12.0	4.9
2900-J-5.0-75k	12.5	33.5	13.3
2900-J-5.0-100k	9.9	26.4	10.5
2900-J-10.0-75k	24.0	64.3	25.5
2900-J-10.0-100k	20.1	53.9	21.3
2900-H-1.0-75k	5.3	9.9	5.4
2900-H-1.0-100k	3.7	6.9	3.8
2900-H-5.0-75k	8.6	16.1	8.9
2900-H-5.0-100k	6.9	12.8	7.1
2900-H-10.0-75k	16.5	31.2	17.1
2900-H-10.0-100k	13.8	26.1	14.3
2900-K-1.0-75k	6.6	21.6	7.0
2900-K-1.0-100k	4.5	15.0	4.8
2900-K-5.0-75k	11.1	35.5	11.8
2900-K-5.0-100k	8.8	28.3	9.4
2900-K-10.0-75k	22.1	67.3	23.6
2900-K-10.0-100k	18.5	56.5	19.7
2800-Z-1.0-75k	2.9	5.7	3.0
2800-Z-1.0-100k	1.8	3.6	1.9
2800-Z-5.0-75k	5.7	10.9	5.9
2800-Z-5.0-100k	4.4	8.5	4.6
2800-Z-10.0-75k	12.4	23.3	13.0
2800-Z-10.0-100k	10.3	19.3	10.7
2800-Y-1.0-75k	4.1	5.3	4.2
2800-Y-1.0-100k	2.7	3.5	2.7

**Table A.3:** continued.

Simulation	$\sigma_{RV}$ (Cond. 1)	$\sigma_{RV}$ (Cond. 2)	$\sigma_{RV}$ (Cond. 3)
2800-Y-5.0-75k	7.1	8.7	7.2
2800-Y-5.0-100k	5.6	7.0	5.7
2800-Y-10.0-75k	12.7	15.2	12.9
2800-Y-10.0-100k	10.7	12.8	10.8
2800-J-1.0-75k	6.1	16.0	6.5
2800-J-1.0-100k	4.0	10.2	4.2
2800-J-5.0-75k	10.9	28.9	11.5
2800-J-5.0-100k	8.6	22.8	9.1
2800-J-10.0-75k	20.9	55.0	22.1
2800-J-10.0-100k	17.5	46.1	18.5
2800-H-1.0-75k	4.8	9.3	5.0
2800-H-1.0-100k	3.3	6.4	3.5
2800-H-5.0-75k	8.0	15.3	8.2
2800-H-5.0-100k	6.3	12.1	6.5
2800-H-10.0-75k	15.3	29.9	15.9
2800-H-10.0-100k	12.8	25.0	13.3
2800-K-1.0-75k	5.9	19.5	6.3
2800-K-1.0-100k	4.0	13.5	4.3
2800-K-5.0-75k	10.0	32.2	10.6
2800-K-5.0-100k	7.9	25.6	8.4
2800-K-10.0-75k	19.8	60.9	21.1
2800-K-10.0-100k	16.6	51.1	17.7
2700-Z-1.0-75k	2.6	5.3	2.7
2700-Z-1.0-100k	1.6	3.3	1.7
2700-Z-5.0-75k	5.2	10.2	5.4
2700-Z-5.0-100k	4.0	7.9	4.2
2700-Z-10.0-75k	11.3	21.9	11.8
2700-Z-10.0-100k	9.3	18.1	9.7
2700-Y-1.0-75k	3.7	4.8	3.7
2700-Y-1.0-100k	2.4	3.2	2.4
2700-Y-5.0-75k	6.4	8.0	6.5
2700-Y-5.0-100k	5.1	6.4	5.2
2700-Y-10.0-75k	11.5	13.8	11.6
2700-Y-10.0-100k	9.7	11.6	9.8
2700-J-1.0-75k	5.2	13.6	5.5
2700-J-1.0-100k	3.4	8.7	3.5
2700-J-5.0-75k	9.3	24.9	9.9
2700-J-5.0-100k	7.4	19.6	7.8
2700-J-10.0-75k	18.0	47.1	19.1
2700-J-10.0-100k	15.1	39.5	16.0

**Table A.3:** continued.

Simulation	$\sigma_{RV}$ (Cond. 1)	$\sigma_{RV}$ (Cond. 2)	$\sigma_{RV}$ (Cond. 3)
2700-H-1.0-75k	4.3	8.3	4.4
2700-H-1.0-100k	3.0	5.8	3.1
2700-H-5.0-75k	7.1	13.9	7.4
2700-H-5.0-100k	5.7	11.0	5.9
2700-H-10.0-75k	13.8	27.6	14.3
2700-H-10.0-100k	11.5	23.1	12.0
2700-K-1.0-75k	5.2	17.2	5.5
2700-K-1.0-100k	3.5	11.9	3.8
2700-K-5.0-75k	8.8	28.5	9.4
2700-K-5.0-100k	6.9	22.7	7.4
2700-K-10.0-75k	17.4	54.0	18.6
2700-K-10.0-100k	14.6	45.3	15.5
2600-Z-1.0-75k	2.5	5.2	2.6
2600-Z-1.0-100k	1.5	3.2	1.6
2600-Z-5.0-75k	4.8	9.9	5.1
2600-Z-5.0-100k	3.8	7.8	3.9
2600-Z-10.0-75k	10.5	21.3	11.0
2600-Z-10.0-100k	8.7	17.6	9.1
2600-Y-1.0-75k	3.3	4.4	3.4
2600-Y-1.0-100k	2.1	2.9	2.2
2600-Y-5.0-75k	5.9	7.4	6.0
2600-Y-5.0-100k	4.7	5.9	4.7
2600-Y-10.0-75k	10.5	12.7	10.6
2600-Y-10.0-100k	8.8	10.7	8.9
2600-J-1.0-75k	4.4	11.7	4.7
2600-J-1.0-100k	2.8	7.4	3.0
2600-J-5.0-75k	8.0	21.6	8.5
2600-J-5.0-100k	6.3	17.0	6.7
2600-J-10.0-75k	15.6	40.8	16.5
2600-J-10.0-100k	13.0	34.2	13.8
2600-H-1.0-75k	3.7	7.4	3.9
2600-H-1.0-100k	2.6	5.1	2.7
2600-H-5.0-75k	6.3	12.4	6.5
2600-H-5.0-100k	5.0	9.8	5.2
2600-H-10.0-75k	12.2	24.8	12.7
2600-H-10.0-100k	10.2	20.7	10.6
2600-K-1.0-75k	4.4	14.4	4.7
2600-K-1.0-100k	3.0	9.9	3.2
2600-K-5.0-75k	7.6	24.3	8.1
2600-K-5.0-100k	6.0	19.3	6.4

**Table A.3:** continued.

Simulation	$\sigma_{RV}$ (Cond. 1)	$\sigma_{RV}$ (Cond. 2)	$\sigma_{RV}$ (Cond. 3)
2600-K-10.0-75k	15.0	46.5	16.0
2600-K-10.0-100k	12.5	39.1	13.4
2500-Z-1.0-75k	2.5	5.5	2.6
2500-Z-1.0-100k	1.6	3.5	1.6
2500-Z-5.0-75k	4.8	10.4	5.0
2500-Z-5.0-100k	3.7	8.2	3.9
2500-Z-10.0-75k	10.3	22.0	10.9
2500-Z-10.0-100k	8.6	18.3	9.0
2500-Y-1.0-75k	3.1	4.2	3.1
2500-Y-1.0-100k	2.0	2.7	2.0
2500-Y-5.0-75k	5.5	7.1	5.6
2500-Y-5.0-100k	4.4	5.7	4.4
2500-Y-10.0-75k	9.9	12.2	10.0
2500-Y-10.0-100k	8.4	10.3	8.5
2500-J-1.0-75k	3.7	10.0	3.9
2500-J-1.0-100k	2.4	6.3	2.5
2500-J-5.0-75k	6.8	18.7	7.3
2500-J-5.0-100k	5.4	14.7	5.7
2500-J-10.0-75k	13.5	35.7	14.3
2500-J-10.0-100k	11.3	29.9	11.9
2500-H-1.0-75k	3.3	6.5	3.4
2500-H-1.0-100k	2.3	4.4	2.4
2500-H-5.0-75k	5.5	11.0	5.7
2500-H-5.0-100k	4.4	8.7	4.5
2500-H-10.0-75k	10.7	21.9	11.1
2500-H-10.0-100k	9.0	18.3	9.3
2500-K-1.0-75k	3.8	11.8	4.0
2500-K-1.0-100k	2.6	8.0	2.7
2500-K-5.0-75k	6.5	20.5	6.9
2500-K-5.0-100k	5.1	16.2	5.5
2500-K-10.0-75k	12.8	39.8	13.7
2500-K-10.0-100k	10.8	33.4	11.5

## Appendix B

# Artefacts in Optimal Extraction

As mentioned in Section 5.1.3.1 there were several artefacts observed in the *optimal* reduction of the DRACS pipeline, coinciding with spikes in the *rectangular* reduction. A list of all specific nods of each observation and detector that were observed to contain artefacts and were replaced with the method developed are provided in Table B.1.

With 8 nods per observation, and 4 CRIRES detectors for the 17 observations there are 544 individual nod spectra. Table B.1 identifies the 79 individual nods (14.5%) that were found to contain artefacts while Table B.2 provides a tally of the frequency of artefacts occurring within each nod position of the nod cycle. Only 16/68 (23.5%) detector-observations have all nods without any artefacts while no observation is completely free of artefacts across all 4 detectors.

Tallying the number of artefacts that occur per detector and nod position reveals three main features. The first is that there are around  $1.3\text{--}1.5\times$  more artefacts that occur on the second detector compared to the other three detectors individually. This may be due to a physical defect with this detector, such as the large scratch seen in Figure 5.2, or it is possibly due to the relatively featureless spectrum on the second detector. Either will make it easier to visually detect artefacts in the spectra, or easier for artefacts to be created by the pipeline. The second is that there are more artefacts in the seventh and eighth nods with  $\sim 40\%$  of the artefacts in the last 2/8 of observations (see Table B.2). As the artefacts occur later in the nod cycle this suggests that they may be related to the operation of the instrumentation, for which the probability is built up over the repeated nod cycle observations, however this is just speculation.

There does not seem to be a connection between the nod position as both position A and B have half of the artefacts. There is a higher number of artefacts occurring in the last two nods, suggesting that there may be some correlation to the length of the observation. The growth in artefacts over time is not linear with a rapid increase starting around the sixth nod.

The third thing that is noticed is the difference in the number of artefacts seen in the first observation of HD 30501 compared to the other three. This was observed four months before the others, which were observed within the same week. The later three observations all have larger number of artefacts  $2\text{--}3\times$  compared to the first observation.

The ideas presented here are only observations and speculation on the causes. Tests for statistical significance of the differences observed have not been performed and is beyond the scope of this work.

Figures B.1 to B.6 show more examples of observed spectra in which spikes and artefacts are observed. One example is given for each target, selected to show a variety of the artefacts observed.

**Table B.1:** Identification of all the optimally reduced nod spectra which had artefacts and were replaced by the rectangular extractions, after correction for bad pixel spikes. The numbers represent the position (1–8) in the nod cycle ABBAABBA. The number of the observation for each target is given in the second column (#).

Target	#	Detector					Total
		1	2	3	4		
HD 4747	1	8	5, 8	8	1, 5, 8		7
HD 162020	1	-	7, 8	-	-		2
HD 162020	2	-	2	-	8		2
HD 167665	1	2, 4	8	1, 6	4, 5		7
HD 167665	2	2	3	1	8		4
HD 167665	3	6	3, 7	-	8		4
HD 168443	1	-	-	-	7, 8		2
HD 168443	2	-	2, 4	6	8		4
HD 202206	1	-	6, 7	1	-		3
HD 202206	2	5	-	7, 8	-		3
HD 202206	3	8	3	6	6		4
HD 211847	1	-	5, 7	2	4		4
HD 211847	2	2	1, 7	7	8		5
HD 30501	1	7	7	-	8		3
HD 30501	2	7, 8	3, 5, 7, 8	2, 7	2, 3		10
HD 30501	3	4, 8	2, 6, 7	4, 8	7		8
HD 30501	4	1, 2, 4	3	5, 6	6		7
		16	27	17	19	79/544	

**Table B.2:** Tally of nod cycle positions in which their optimally reduced spectra were affected by these artefacts and replaced.

Nod Number	1	2	3	4	5	6	7	8	Total
Nod Position	A	B	B	A	A	B	B	A	
Tally	6	10	6	7	7	9	15	19	79

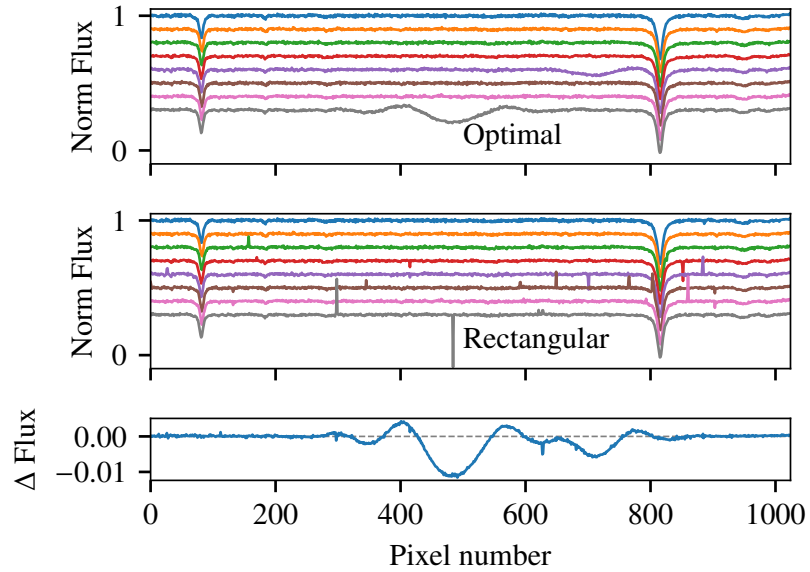


**Figure B.1:** Artefact example for the second detector of HD 4747. The top panel contains the eight normalized nod spectra obtained using optimal extraction. The middle panel shows nod spectra using only rectangular extraction. The bottom panel shows the difference between a combined spectrum using optimal nods only and a combined spectrum in which the identified nods are replaced with their rectangular counterparts as per Section 5.1.3.1. A vertical offset is included between each spectra for clarity. The nod spectra are in observation order from top to bottom. In this example there are artefacts in the 5th (purple) and eighth (grey) nod spectra around 700 and 500 pixels respectively.

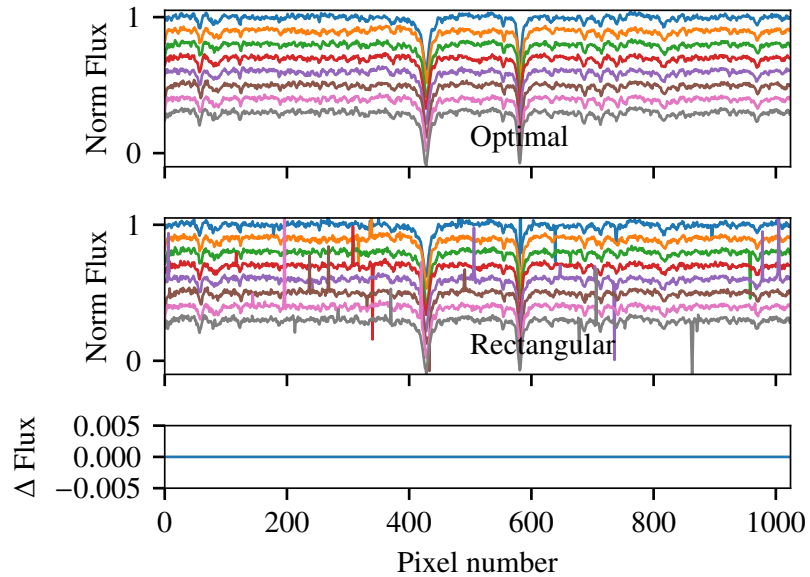


**Figure B.2:** Same as Figure B.1 but for the first detector of the second observation of HD 162020. In this example there are several large spikes observed in the rectangular extraction but they do not appear to effect the optimally extracted nods (there are no artefacts).

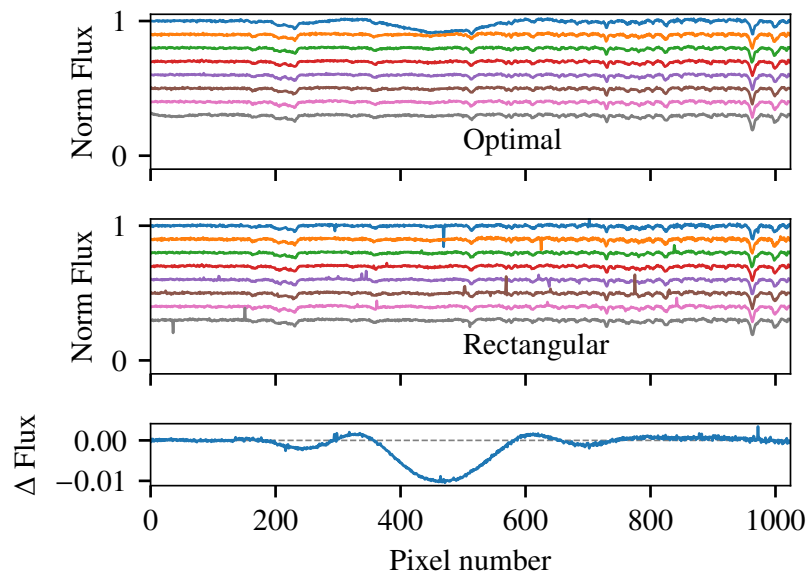


**Figure B.3:** Same as Figure B.1 but for the third detector of the second observation of HD 167665. In this example a small spike in the first spectrum (blue) around pixel 450 causes an extended dip in the optimally extracted nod.

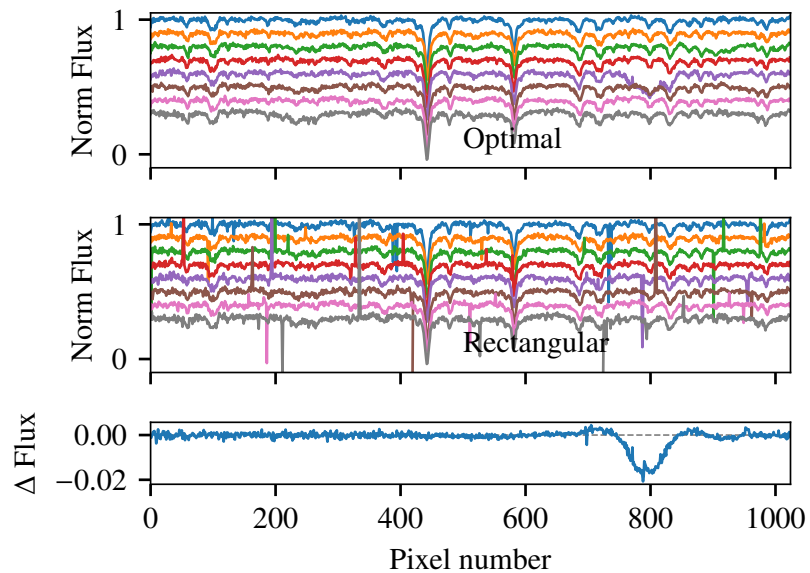


**Figure B.4:** Same as Figure B.1 but for the 1st detector of the second observation of HD 202206. In this example there are several large spikes but only one produces an artefact. This is on the 5th nod (purple) around pixel 800.

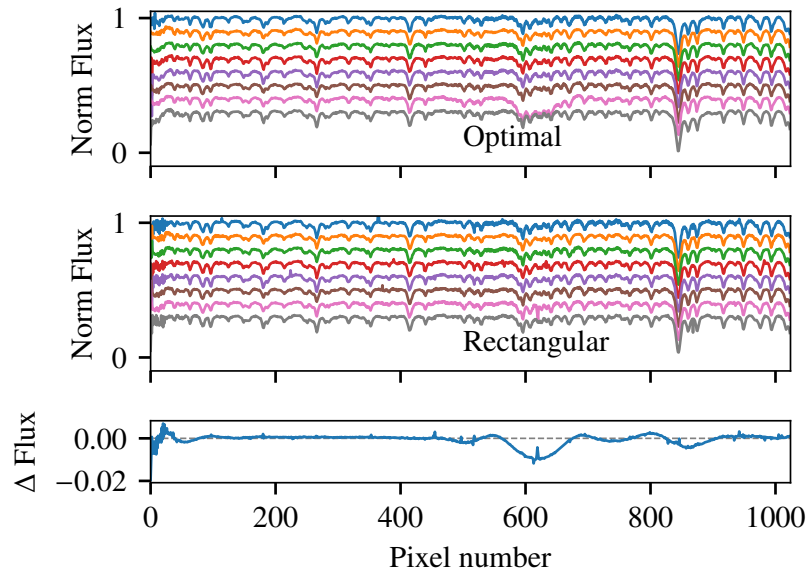


**Figure B.5:** Same as Figure B.1 but for the fourth detector of the first observation of HD 168443. In this example a barely visible spike on the 7th nod (pink) causes a deviation in the optimal nod around pixel 610. There is also a second small spike on the eighth nod (grey) around pixel 850, between two spectral lines.

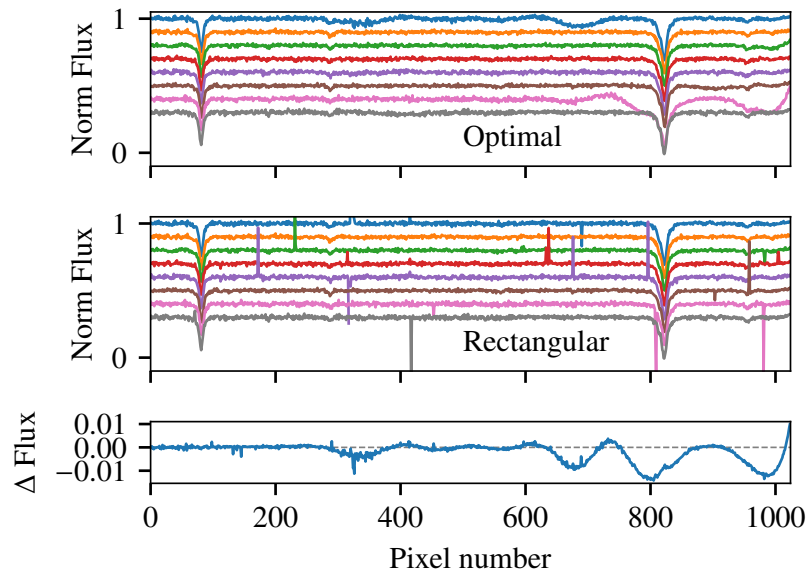


**Figure B.6:** Same as Figure B.1 but for the second detector of the second observation of HD 211847. In this example two large spikes around 800 and 1000 in the 7th nod (pink) create large deviations in the optimally reduced spectra. A spike in the first nod (blue) around pixel 700 also causes a bump. There is also some extra noise in the first nod around pixel 350.

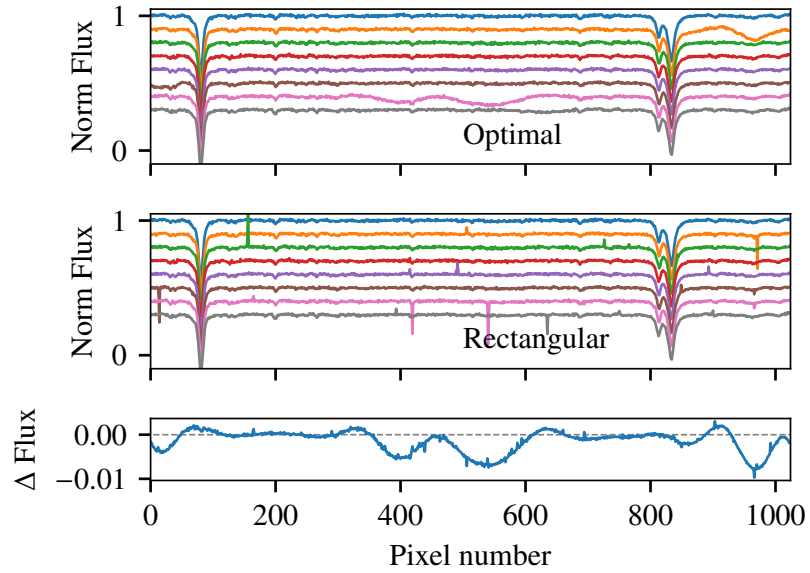


**Figure B.7:** Same as Figure B.1 but for the second detector of the second observation of HD 30501. In this example there are artefact causing spikes in four places. The second nod (orange) around pixel 950, the 6th nod (brown) around pixel 20 and two spikes in the 7th nod (pink) around pixels 400 and 550.

In each image the top panel contains the 8 nod spectra extracted using the optimal method, which includes variance weighting. The middle panel contains the rectangular extraction only (no variance weighting). The bottom panel shows the difference between the average combined spectra from the top and middle panels.

It is clear that the large extracted artefacts occur due to single spikes observed in the rectangular extraction. What is unclear is the other factors that affect their cause. For example in Figure B.2 several spikes are seen but no artefacts are created.

## Multi-detector wavelength calibration

In this Appendix we provide an example of multi-detector wavelength calibration. This is to try and improve the wavelength calibration on the detectors in which a limited number of telluric lines fall.

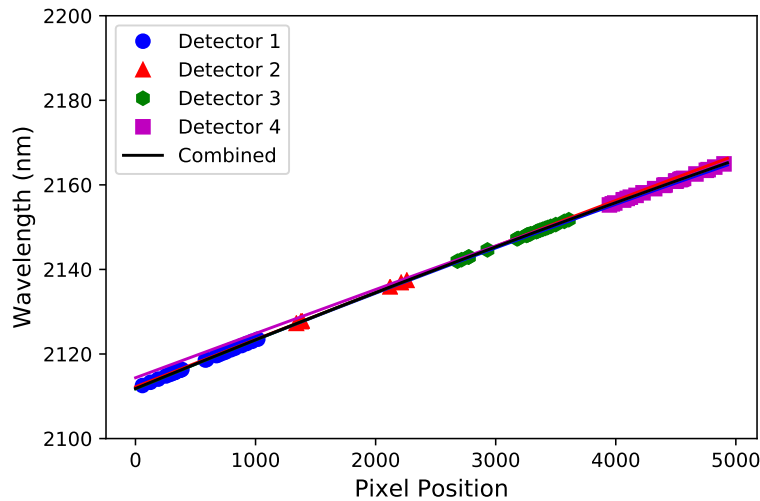
The spectrum recorded across the four detectors is created from a single dispersion and should, in theory, be able to be modelled by a single polynomial. Figure C.1 shows the pixel-wavelength calibrating points for the 4 detectors, along with the individual fits, extended over the four detectors. At this scale all four lines are basically similar except for the fourth detector near the wavelength region of detector 1 where it is slightly higher. On top is also a line indicating a polynomial fit made using the points from all four detectors and including the fixed gaps between detectors.

Figure C.2 shows the difference between the individual detectors and the combined fit. Within the individual detectors the absolute wavelength difference is less than 0.5 nm at the edges of detector one, however the differences exceed 0.3 nm outside of the original detector. They are quadratic in shape as they are the difference between two quadratics.

The combined fit is made by first assigning each horizontal pixel of each detector the position between 0 and 4095 in pixel coordinates of the CRIRES detectors. A transformation is made into a pseudo-physical pixel coordinates from the left edge of the first detector by including the gaps between the detectors (in pixels). The parameters  $gap_1$ ,  $gap_2$ ,  $gap_3$  are the 3 gaps between neighbouring detectors gaps and are defined in pixel space as follows:

$$gap = \begin{cases} 0, & 0 = < psl < 1024 \\ gap_1, & 1024 = < psl < 2048 \\ gap_1 + gap_2, & 2048 = < psl < 3072 \\ gap_1 + gap_2 + gap_3, & 3072 = < psl < 4096 \end{cases}$$

The pixel widths of these gaps can be fixed to known values (e.g. 282, 278, and 275 pixels (Brogi et al., 2016)) or allowed to vary and included in the fitting process.



**Figure C.1:** Pixel-wavelength calibration points for each detector are given by the different markers. The quadratic fit of each individual detector is given with the same corresponding colour. A combined quadratic fit, using fixed detector gaps is shown in black.

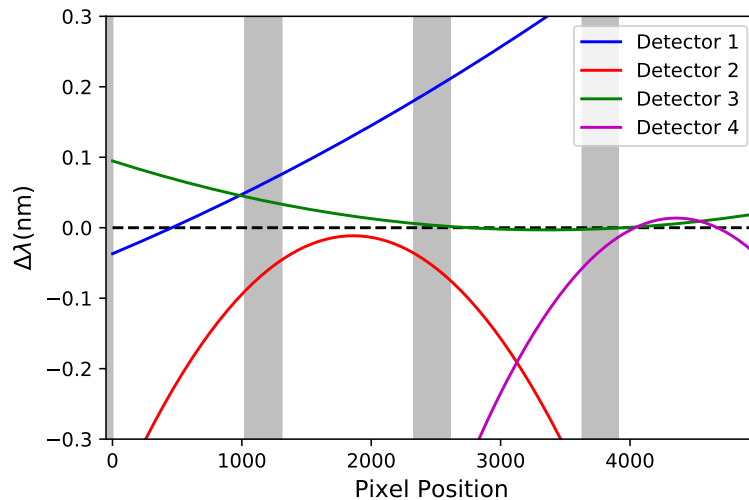


**Figure C.2:** Wavelength difference of individual quadratic fits to the quadratic fit combined all four detectors and fixed gaps.

**Table C.1:** Example of multi-detector fitting parameters obtained for HD 30501 observation 2 under different scenarios.

	Combined		Variable Gaps
	Fixed Gaps		
a3 (u)	-	$(-2 \pm 3) \times 10^{-12}$	$(-2 \pm 1) \times 10^{-12}$
a2 (q)	$(-1.77 \pm 0.03) \times 10^{-7}$	$(-1.6 \pm 0.2) \times 10^{-7}$	$(-1.47 \pm 0.07) \times 10^{-7}$
a1 (m)	$0.01170 \pm 0.00002$	$0.01167 \pm 0.00005$	$0.01162149 \pm 0.00004$
a0 (b)	$2111.83 \pm 0.01$	$2111.84 \pm 0.02$	$2111.86 \pm 0.02$
gap <sub>1</sub>	283	283	$291.7 \pm 3.5$
gap <sub>2</sub>	561	561	$570.5 \pm 5.4$
gap <sub>3</sub>	836	836	$844.2 \pm 7.1$
$\chi^2$	11.2	10.7	4.6
$\chi^2_{red}$	0.156	0.151	0.066
BIC	-129.3	-128.6	-184.1
			-186.7

## C.1 Comparing variable gaps

This example does not include the height on the detectors the spectrum falls or any skewness of the spectrum to pixel rows or any miss-alignment between the detectors. All which could have some affect on a global wavelength calibration.

Table C.1 shows the fit parameters obtained as well as some fit statistics for quadratic and cubic fitting, comparing the full combined fit with fixed or variable gaps.

Figure C.3 also show the distribution of the fit parameters for the quadratic fit with fixed (left) and variable gaps (right) obtained using the *emcee* python package<sup>1</sup>, which performs a Markov chain Monte Carlo simulation. The cloud of points reveal the correlations between different parameters. For instance the narrow diagonals indicate a strong correlation between the parameters given on the axis. There are strong correlations between the quadratic parameters, q, m, b with m being negatively correlated to all other parameters. It also shows strong positive correlations between the variable detector gaps.

They plot on the left with fix detector gaps, is almost identical to the top 3 rows of the figure on the right.

This is just a simple representation of the idea, it has not been used in this thesis for wavelength calibration

reread and fix  
up still

---

<sup>1</sup> <http://dfm.io/emcee/current/>

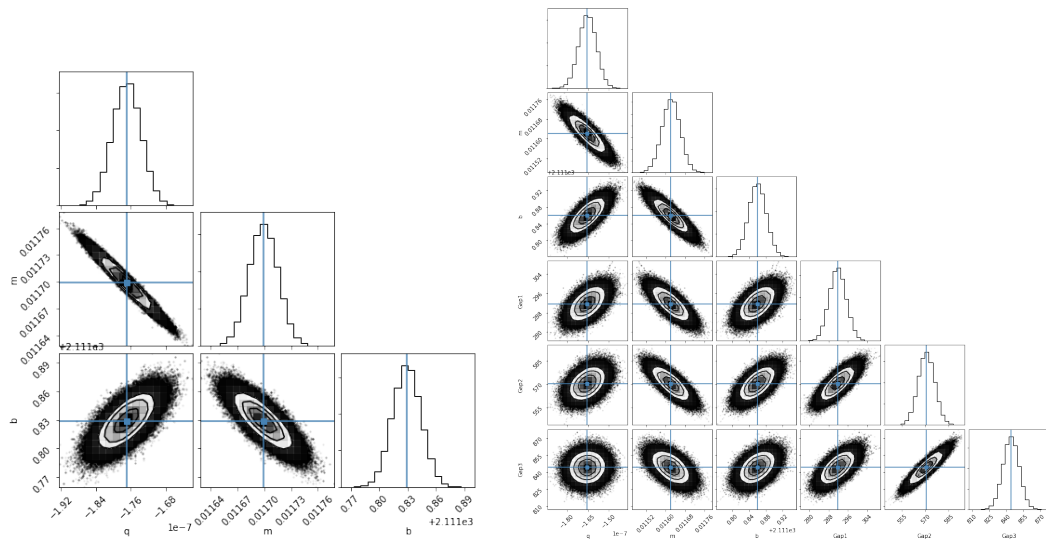


**Figure C.3:** Corner plots of combined fitting of four detectors. The elliptical point clouds indicate there are correlations between parameters. (left) Combined fit with fixed detector gaps. (right) Combined fit with variable detector gaps.

# Appendix D

## Vacuum wavelengths

Astronomical light is refracted as it enters Earth's atmosphere, as the medium changes from the vacuum of space and to air. The index of refraction,  $n$ , is the factor at which the velocity,  $v$ , and wavelength  $\lambda$  of electromagnetic radiation changes from their values in a vacuum.

$$n = \frac{\lambda_{vac}}{\lambda_{air}}, \frac{v_{vac}}{v_{air}} \quad (\text{D.1})$$

The index of refraction of air is very close to 1, but has a complex wavelength dependence which also depends on atmospheric composition (e.g. CO<sub>2</sub>, H<sub>2</sub>O), temperature and pressure. There are several empirical formula for the index of refraction of air (e.g. Edlén, 1953; Peck et al., 1972; Ciddor, 1996). As an example the refractive index given by Ciddor (1996), based on optical and infrared measurements and valid up to 1.7 μm, is:

$$n - 1 = \frac{0.05792105}{238.0185 - \lambda^{-2}} + \frac{0.00167917}{57.362 - \lambda^{-2}}. \quad (\text{D.2})$$

This is measured at standard, dry air at 15°C, 101.325 kPa and with 450 ppm CO<sub>2</sub>. Beyond 1.7 μm there are only theoretical models of the refractive index of air, due to lack of experimental data. For example Mathar (2007) provides theoretical values between 1.3–24 μm for common air pressure and temperature of ground-based observatories.

In this work we extensively use spectral wavelengths specified in a vacuum. The first is because the empirical relations are not valid beyond 1.7 μm, while the CRIRES spectra investigated are observed around 2.1 μm and the CRIRES instrument manual provides all measurements in vacuum wavelengths.

The TAPAS synthetic transmission models Bertaux et al. (2014) used for telluric correction are available for download in vacuum wavelengths or air wavelengths<sup>1</sup>. The PHOENIX-ACES library of synthetic spectra used also provide spectra in vacuum wavelengths. Remaining exclusively in vacuum wavelengths means that no errors are introduced from the conversion between air and vacuum wavelengths in the nIR. As such, the vacuum TAPAS models are obtained and the observations calibrated using vacuum wavelengths.

---

<sup>1</sup> The wavenumber,  $1/\lambda$ , is also available.

# Appendix E

## PhD output

This section lists the activities in which I have been involved over the duration of my doctoral training.

In summary, over the duration of my doctoral training:

- I have two first author publications under review, one with the Monthly Notices of the Royal Astronomical Society (MNRAS) and one with Journal of Open Source Software (JOSS). A third paper is in preparation.
- I was also involved as a co-author in five more articles (Figueira et al., 2016; Barros et al., 2017; Santerne et al., 2018; Lillo-Box et al., 2018; Ulmer-Moll et al., 2018),
- I also had the opportunity to attend one international conferences, two international schools and one national conference, in which I presented an oral contribution and a poster.
- I tutored at the 11<sup>th</sup>, 12<sup>th</sup>, and 13<sup>th</sup> edition of the Physics Summer School for the Faculty of Science of the University of Porto.
- I was invited to be a proofreader for an outreach book Figueira et al. (2015).
- I also gained experience as an astronomical observer, with two observing runs, using HARPS-N and ESPRESSO.

Fix up at end

I now proceed to list all the above in detail.

## E.1 Publications

A&A 586, A101 (2016)  
 DOI: 10.1051/0004-6361/201526900  
 © ESO 2016

**Astronomy  
 &  
 Astrophysics**

### Radial velocity information content of M dwarf spectra in the near-infrared

P. Figueira<sup>1</sup>, V. Zh. Adibekyan<sup>1</sup>, M. Oshagh<sup>1</sup>, J. J. Neal<sup>1,2</sup>, B. Rojas-Ayala<sup>1</sup>, C. Lovis<sup>3</sup>, C. Melo<sup>4</sup>, F. Pepe<sup>3</sup>, N. C. Santos<sup>1,2</sup>, and M. Tsantaki<sup>1</sup>

<sup>1</sup> Instituto de Astrofísica e Ciências do Espaço, Universidade do Porto, CAUP, Rua das Estrelas, 4150-762 Porto, Portugal  
 e-mail: pedro.figueira@astro.up.pt

<sup>2</sup> Departamento de Física e Astronomia, Faculdade de Ciências, Universidade do Porto, Portugal

<sup>3</sup> Observatoire Astronomique de l'Université de Genève, 51 Ch. des Maillettes, – Sauverny – 1290 Versoix, Suisse

<sup>4</sup> European Southern Observatory, Alonso de Córdova 3107, Vitacura, Casilla 19001, Santiago 19, Chile

Received 6 July 2015 / Accepted 16 October 2015

#### ABSTRACT

**Aims.** We evaluate the radial velocity (RV) information content and achievable precision on M0–M9 spectra covering the ZYJHK bands. We do so while considering both a perfect atmospheric transmission correction and discarding areas polluted by deep telluric features, as done in previous works.

**Methods.** To simulate the M-dwarf spectra, PHOENIX-ACES model spectra were employed; they were convolved with rotational kernels and instrumental profiles to reproduce stars with a  $v \sin i$  of 1.0, 5.0, and 10.0 km s<sup>-1</sup> when observed at resolutions of 60 000, 80 000, and 100 000. We considered the RV precision as calculated on the whole spectra, after discarding strongly polluted areas, and after applying a perfect telluric correction. In the latter option, we took into account the reduction in the number of recorded photons due to a transmittance lower than unity and considered its effect on the noise of the recorded spectra. In our simulations we paid particular attention to the details of the convolution and sampling of the spectra, and we discuss their impact on the final spectra.

**Results.** Our simulations show that the most important parameter ruling the difference in attainable precision between the considered bands is the spectral type. For M0–M3 stars, the bands that deliver the most precise RV measurements are the Z, Y, and H band, with relative merits depending on the parameters of the simulation. For M6–M9 stars, the bands show a difference in precision that is within a factor of ∼2 and does not clearly depend on the band; this difference is reduced to a factor smaller than ∼1.5 if we consider a non-rotating star seen at high resolution. We also show that an M6–M9 spectrum will deliver a precision about two times better as an M0–M3 spectra with the same signal-to-noise ratio. Finally, we note that the details of modeling the Earth atmosphere and interpreting the results have a significant impact on which wavelength regions are discarded when setting a limit threshold at 2–3%. The resolution element sampling on the observed spectra plays an important role in the atmospheric transmission characterization. As a result of the multiparameter nature of the problem, it is very difficult to precisely quantify the impact of absorption by the telluric lines on the RV precision, but it is an important limiting factor to the achievable RV precision.

**Key words.** techniques: radial velocities – instrumentation: spectrographs – methods: data analysis – stars: low-mass

#### 1. Introduction

The technique of spectroscopy is central to the study of stars and has allowed astronomy to gather a significant body of knowledge from the few photons a star provides us. During the past 20 years, spectroscopy was extensively applied in an emerging field in astronomy: the study of exoplanets. Following the discovery of 51 Peg b in 1995 (Mayor & Queloz 1995), more than 1900 planets were discovered, with masses and radii down to those of Earth (e.g., Dumusque et al. 2012; Barclay et al. 2013; Pepe et al. 2013). The radial velocity (RV) technique, with which the very first planet around a solar-type star was found, is still one of the most widely used detection methods; it is the main contributor to our knowledge of the mass of known exoplanets. The hunt for the exoplanet with the lowest mass pushed the RV precision down to the subm/s domain and motivated the construction of instruments such as ESPRESSO, which aims at a precision of 10 cm/s (Mégevand et al. 2012; Pepe et al. 2014b).

The RV signature of a planet scales with the mass of the star with  $M_*^{-2/3}$  and with the planetary orbital period with  $P_{\text{orb}}^{-1/3}$ . For an Earth-mass planet orbiting inside the habitable zone around a solar-type star, the RV amplitude is 10 cm/s, while for a planet with the same characteristics but orbiting an M7 dwarf, the RV amplitude is larger than 1 m/s. This is due to both a lower host mass and a closer habitable zone (a consequence of the lower luminosity output of these hosts). This relatively high amplitude contributed to an increased interest in the search for exoplanets around the low-mass M-dwarf (0.5–0.08  $M_\odot$ ) and led to the first estimates of the fraction of M dwarfs hosting Earth-mass planets inside the habitable zone (Bonfils et al. 2013). The intrinsic faintness of the stars in the visible domain limited these surveys to the brightest one hundred stars of our neighborhood and, along with activity, photon noise contribution to the noise budget proved to be the limiting factor. Spurred by the abundance of exoplanets, the exoplanet hunters did not rest in their efforts, and in the last several years, a new research direction

## Precise masses for the transiting planetary system HD 106315 with HARPS $\star$

S. C. C. Barros<sup>1,2\*</sup>, H. Gosselin<sup>2,23</sup>, J. Lillo-Box<sup>3</sup>, D. Bayliss<sup>4</sup>, E. Delgado Mena<sup>1</sup>, B. Brugger<sup>2</sup>, A. Santerne<sup>2</sup>, D. J. Armstrong<sup>5</sup>, V. Adibekyan<sup>1</sup>, J. D. Armstrong<sup>6</sup>, D. Barrado<sup>7</sup>, J. Bento<sup>8</sup>, I. Boisse<sup>2</sup>, A. S. Bonomo<sup>9</sup>, F. Bouchy<sup>4</sup>, D. J. A. Brown<sup>5</sup>, W. D. Cochran<sup>10</sup>, A. Collier Cameron<sup>11</sup>, M. Deleuil<sup>2</sup>, O. Demangeon<sup>1</sup>, R. F. Diaz<sup>4,12,13</sup>, A. Doyle<sup>5</sup>, X. Dumusque<sup>4</sup>, D. Ehrenreich<sup>4</sup>, N. Espinoza<sup>14,15</sup>, F. Faedi<sup>5</sup>, J. P. Faria<sup>1,16</sup>, P. Figueira<sup>1</sup>, E. Foxell<sup>5</sup>, G. Hébrard<sup>17,18</sup>, S. Hojjatpanah<sup>1,16</sup>, J. Jackman<sup>5</sup>, M. Lendl<sup>19</sup>, R. Ligi<sup>2</sup>, C. Lovis<sup>4</sup>, C. Melo<sup>3</sup>, O. Mousis<sup>2</sup>, J. J. Neal<sup>1,16</sup>, H. P. Osborn<sup>5</sup>, D. Pollacco<sup>5</sup>, N. C. Santos<sup>1,16</sup>, R. Sefako<sup>20</sup>, A. Shporer<sup>21</sup>, S. G. Sousa<sup>1</sup>, A. H. M. J. Triaud<sup>22</sup>, S. Udry<sup>4</sup>, A. Vigan<sup>2</sup>, and A. Wyttenbach<sup>4</sup>

<sup>1</sup> Instituto de Astrofísica e Ciências do Espaço, Universidade do Porto, CAUP, Rua das Estrelas, PT4150-762 Porto, Portugal e-mail: susana.barros@astro.up.pt

<sup>2</sup> Aix Marseille Univ, CNRS, LAM, Laboratoire d'Astrophysique de Marseille, Marseille, France

<sup>3</sup> European Southern Observatory (ESO), Alonso de Cordova 3107, Vitacura, Casilla 19001, Santiago de Chile, Chile

<sup>4</sup> Observatoire Astronomique de l'Université de Genève, 51 Chemin des Maillettes, 1290 Versoix, Switzerland

<sup>5</sup> Department of Physics, University of Warwick, Gibbet Hill Road, Coventry, CV4 7AL, UK

<sup>6</sup> Institute for Astronomy, University of Hawaii, 34 Ohia Ku Street, Pukalani, Maui, Hawaii 96790

<sup>7</sup> Depto. de Astrofísica, Centro de Astrobiología (CSIC-INTA), ESAC campus 28692 Villanueva de la Cañada (Madrid), Spain

<sup>8</sup> Research School of Astronomy and Astrophysics, Australian National University, Mount Stromlo Observatory, Cotter Road, Weston Creek, ACT 2611, Australia

<sup>9</sup> INAF – Osservatorio Astrofisico di Torino, Strada Osservatorio 20, I-10025, Pino Torinese (TO), Italy

<sup>10</sup> McDonald Observatory and Department of Astronomy, The University of Texas at Austin, Austin Texas USA

<sup>11</sup> Centre for Exoplanet Science, SUPA School of Physics & Astronomy, University of St Andrews, North Haugh ST ANDREWS, Fife, KY16 9SS

<sup>12</sup> Universidad de Buenos Aires, Facultad de Ciencias Exactas y Naturales. Buenos Aires, Argentina

<sup>13</sup> CONICET - Universidad de Buenos Aires. Instituto de Astronomía y Física del Espacio (IAFE). Buenos Aires, Argentina.

<sup>14</sup> Instituto de Astrofísica, Facultad de Física, Pontificia Universidad Católica de Chile, Av. Vicuña Mackenna 4860, 782-0436 Macul, Santiago, Chile

<sup>15</sup> Millennium Institute of Astrophysics, Av. Vicuña Mackenna 4860, 782-0436 Macul, Santiago, Chile

<sup>16</sup> Departamento de Física e Astronomia, Faculdade de Ciencias, Universidade do Porto, Rua Campo Alegre, 4169-007 Porto, Portugal

<sup>17</sup> Institut d'Astrophysique de Paris, UMR7095 CNRS, Université Pierre & Marie Curie, 98bis boulevard Arago, 75014 Paris, France

<sup>18</sup> Aix Marseille Univ, CNRS, OHP, Observatoire de Haute Provence, Saint Michel l'Observatoire, France

<sup>19</sup> Space Research Institute, Austrian Academy of Sciences, Schmiedlstr. 6, 8042, Graz, Austria

<sup>20</sup> South African Astronomical Observatory, PO Box 9, Observatory, 7935

<sup>21</sup> Division of Geological and Planetary Sciences, California Institute of Technology, Pasadena, CA 91125, USA

<sup>22</sup> Institute of Astronomy, University of Cambridge, Madingley Road, CB3 0HA, Cambridge, United Kingdom

<sup>23</sup> Université de Toulouse, UPS-OMP, IRAP, Toulouse, France

Received ??, ??; accepted ??

### ABSTRACT

**Context.** The multi-planetary system HD 106315 was recently found in K2 data. The planets have periods of  $P_b \sim 9.55$  and  $P_c \sim 21.06$  days, and radii of  $r_b = 2.44 \pm 0.17 R_\oplus$  and  $r_c = 4.35 \pm 0.23 R_\oplus$ . The brightness of the host star ( $V=9.0$  mag) makes it an excellent target for transmission spectroscopy. However, to interpret transmission spectra it is crucial to measure the planetary masses.

**Aims.** We obtained high successional radial velocities for HD 106315 to determine the mass of the two transiting planets discovered with Kepler K2. Our successful observation strategy was carefully tailored to mitigate the effect of stellar variability.

**Methods.** We modelled the new radial velocity data together with the K2 transit photometry and a new ground-based partial transit of HD 106315c to derive system parameters.

**Results.** We estimate the mass of HD 106315b to be  $12.6 \pm 3.2 M_\oplus$  and the density to be  $4.7 \pm 1.7 g cm^{-3}$ , while for HD 106315c we estimate a mass of  $15.2 \pm 3.7 M_\oplus$  and a density of  $1.01 \pm 0.29 g cm^{-3}$ . Hence, despite planet c having a radius almost twice as large as planet b, their masses are consistent with one another.

**Conclusions.** We conclude that HD 106315c has a thick hydrogen-helium gaseous envelope. A detailed investigation of HD 106315b using a planetary interior model constrains the core mass fraction to be 5–29%, and the water mass fraction to be 10–50%. An alternative, not considered by our model, is that HD 106315b is composed of a large rocky core with a thick H-He envelope. Transmission spectroscopy of these planets will give insight into their atmospheric compositions and also help constrain their core compositions.

**Key words.** planetary systems: detection – planetary systems: fundamental parameters – planetary systems: composition— stars: individual HD 106315, EPIC 201437844 – techniques: photometric – techniques: radial velocities

## An Earth-sized exoplanet with a Mercury-like composition

A. Santerne<sup>1</sup>, B. Brugger<sup>1</sup>, D. J. Armstrong<sup>2</sup>, V. Adibekyan<sup>3</sup>, J. Lillo-Box<sup>4</sup>, H. Gosselin<sup>1,5</sup>, A. Aguichine<sup>1,6</sup>, J.-M. Almenara<sup>7</sup>, D. Barrado<sup>8</sup>, S. C. C. Barros<sup>3</sup>, D. Bayliss<sup>7</sup>, I. Boisse<sup>1</sup>, A. S. Bonomo<sup>9</sup>, F. Bouchy<sup>7</sup>, D. J. A. Brown<sup>2</sup>, M. Deleuil<sup>1</sup>, E. Delgado Mena<sup>3</sup>, O. Demangeon<sup>3</sup>, R. F. Díaz<sup>10,11,7</sup>, A. Doyle<sup>2</sup>, X. Dumusque<sup>7</sup>, F. Faedi<sup>2,12</sup>, J. P. Faria<sup>3,13</sup>, P. Figueira<sup>4,3</sup>, E. Foxell<sup>2</sup>, H. Giles<sup>7</sup>, G. Hébrard<sup>14,15</sup>, S. Hojjatpanah<sup>3,13</sup>, M. Hobson<sup>1</sup>, J. Jackman<sup>2</sup>, G. King<sup>2</sup>, J. Kirk<sup>2</sup>, K. W. F. Lam<sup>2</sup>, R. Ligi<sup>1</sup>, C. Lovis<sup>7</sup>, T. Louden<sup>2</sup>, J. McCormac<sup>2</sup>, O. Mousis<sup>1</sup>, J. J. Neal<sup>3,13</sup>, H. P. Osborn<sup>2,1</sup>, F. Pepe<sup>7</sup>, D. Pollacco<sup>2</sup>, N. C. Santos<sup>3,13</sup>, S. G. Sousa<sup>3</sup>, S. Udry<sup>7</sup> & A. Vigan<sup>1</sup>

<sup>1</sup>Aix Marseille Univ, CNRS, CNES, LAM, Marseille, France

<sup>2</sup>Department of Physics, University of Warwick, Gibbet Hill Road, Coventry, CV4 7AL, UK

<sup>3</sup>Instituto de Astrofísica e Ciências do Espaço, Universidade do Porto, CAUP, Rua das Estrelas, 4150-762 Porto, Portugal

<sup>4</sup>European Southern Observatory (ESO), Alonso de Cordova 3107, Vitacura, Casilla 19001, Santiago de Chile, Chile

<sup>5</sup>Université de Toulouse, UPS-OMP, IRAP, Toulouse, France

<sup>6</sup>Paris-Saclay Université, ENS Cachan, 61 av. du Président Wilson, 94230 Cachan, France

<sup>7</sup>Observatoire Astronomique de l'Université de Genève, 51 Chemin des Maillettes, 1290 Versoix, Switzerland

<sup>8</sup>Dept. de Astrofísica, Centro de Astrobiología (CSIC-INTA), ESAC campus 28692 Villanueva de la Cañada (Madrid), Spain

<sup>9</sup>INAF – Osservatorio Astrofisico di Torino, Strada Osservatorio 20, I-10025, Pino Torinese (TO), Italy

<sup>10</sup>Universidad de Buenos Aires, Facultad de Ciencias Exactas y Naturales. Buenos Aires, Argentina

<sup>11</sup>CONICET - Universidad de Buenos Aires. Instituto de Astronomía y Física del Espacio (IAFE). Buenos Aires, Argentina

<sup>12</sup>INAF – Osservatorio Atrofisico di Catania, via S. Sofia 78, 95123, Catania, Italy

<sup>13</sup>Departamento de Física e Astronomia, Faculdade de Ciencias, Universidade do Porto, Rua Campo Alegre, 4169-007 Porto, Portugal

<sup>14</sup>Institut d'Astrophysique de Paris, UMR7095 CNRS, Universite Pierre & Marie Curie, 98bis boulevard Arago, 75014 Paris, France

<sup>15</sup>Aix Marseille Univ, CNRS, OHP, Observatoire de Haute Provence, Saint Michel l'Observatoire, France

The Earth, Venus, Mars, and some extrasolar terrestrial planets<sup>1</sup> have a mass and radius that is consistent with a mass fraction of about 30% metallic core and 70% silicate mantle<sup>2</sup>. At the inner frontier of the solar system, Mercury has a completely different composition, with a mass fraction of about 70% metallic core and 30% silicate mantle<sup>3</sup>. Several formation or evolution scenarios are proposed to explain this metal-rich composition, such as a

## The *TROY* project: II. Multi-technique constraints on exotrojans in nine planetary systems ★,★★,★★★

J. Lillo-Box<sup>1</sup>, A. Leleu<sup>2</sup>, H. Parviainen<sup>3,4,5</sup>, P. Figueira<sup>1,6</sup>, M. Mallonn<sup>7</sup>, A.C.M. Correia<sup>8,9,10</sup>, N.C. Santos<sup>6,11</sup>, P. Robutel<sup>8</sup>, M. Lendl<sup>12</sup>, H.M.J. Boffin<sup>13</sup>, J.P. Faria<sup>6,11</sup>, D. Barrado<sup>14</sup>, J. Neal<sup>6,11</sup>

<sup>1</sup> European Southern Observatory (ESO), Alonso de Cordova 3107, Vitacura Casilla 19001, Santiago 19, Chile  
 e-mail: jllollobox@eso.org

<sup>2</sup> Physics Institute, Space Research and Planetary Sciences, Center for Space and Habitability - NCCR PlanetS, University of Bern, Bern, Switzerland

<sup>3</sup> Instituto de Astrofísica de Canarias (IAC), E-38200 La Laguna, Tenerife, Spain

<sup>4</sup> Dept. Astrofísica, Universidad de La Laguna (ULL), E-38206 La Laguna, Tenerife, Spain

<sup>5</sup> Sub-department of Astrophysics, Department of Physics, University of Oxford, Oxford, OX1 3RH, UK

<sup>6</sup> Instituto de Astrofísica e Ciências do Espaço, Universidade do Porto, CAUP, Rua das Estrelas, PT4150-762 Porto, Portugal

<sup>7</sup> Leibniz-Institut für Astrophysik Potsdam, An der Sternwarte 16, D-14482 Potsdam, Germany

<sup>8</sup> IMCCE, Observatoire de Paris - PSL Research University, UPMC Univ. Paris 06, Univ. Lille 1, CNRS, 77 Avenue Denfert-Rochereau, 75014 Paris, France

<sup>9</sup> Department of Physics, University of Coimbra, 3004-516 Coimbra, Portugal

<sup>10</sup> CIDMA, Departamento de Física, Universidade de Aveiro, Campus de Santiago, 3810-193 Aveiro, Portugal

<sup>11</sup> Departamento de Física e Astronomia, Faculdade de Ciências, Universidade do Porto, Portugal

<sup>12</sup> Space Research Institute, Austrian Academy of Sciences, Schmiedlstr. 6, 8042 Graz, Austria

<sup>13</sup> ESO, Karl Schwarzschild Strasse 2, 85748 Garching, Germany

<sup>14</sup> Depto. de Astrofísica, Centro de Astrobiología (CSIC-INTA), ESAC campus 28692 Villanueva de la Cañada (Madrid), Spain

In preparation

### ABSTRACT

**Context.** Co-orbital bodies are the byproduct of planet formation and evolution, as we know from the Solar System. Although planet-size co-orbitals do not exist in our planetary system, dynamical studies show that they can remain stable for long periods of time in the gravitational well of massive planets. Should they exist, their detection is feasible with the current instrumentation.

**Aims.** In this paper, we present new ground-based observations searching for these bodies co-orbiting with nine close-in ( $P < 5$  days) planets, using different observing techniques. The combination of all of them allows us to restrict the parameter space of any possible trojan in the system.

**Methods.** We use multi-technique observations (radial velocity, precision photometry and transit timing variations), both newly acquired in the context of the *TROY* project and publicly available, to constrain the presence of planet-size trojans in the Lagrangian points of nine known exoplanets.

**Results.** We find no clear evidence of trojans in these nine systems through any of the techniques used down to the precision of the observations. However, this allows us to constrain the presence of any potential trojan in the system, specially in the trojan mass/radius versus libration amplitude plane. In particular, we can set upper mass limits in the super-Earth mass regime for six of the studied systems.

**Key words.** Planets and satellites: gaseous planets, fundamental parameters; Techniques: radial velocity, transits; Minor planets, asteroids: general

### 1. Introduction

The development of state-of-the-art instrumentation and space-based facilities in the past decades boosted the discovery of extrasolar planets up to several thousands of detections<sup>1</sup>. This

plethora has shown the wide diversity of intrinsic and orbital properties that planets can have. Exoplanet research is currently focused on the deep understanding of the planet composition, structure and atmosphere, in parallel to the search for Earth analogues. From our own system, we know that extrasolar systems should also host other components that also played an important role in moulding the architecture and properties of the planets. In the Solar System, moons and more recently trojans (e.g., Lucy mission, Levison et al. 2017) are targets for *in situ* exploration since they contain clues on the formation and early evolution of our planetary system (e.g., Morbidelli et al. 2005; Borisov et al. 2017).

Trojan bodies co-rotate with planets in a wide variety of orbital configurations, mainly in tadpole (orbiting the gravity

\* Based on observations collected at the Centro Astronómico Hispano Alemán (CAHA) at Calar Alto, operated jointly by the Max-Planck Institut für Astronomie and the Instituto de Astrofísica de Andalucía (CSIC).

\*\* Partly based on data obtained with the STELLA robotic telescopes in Tenerife, an AIP facility jointly operated by AIP and IAC.

\*\*\* Based on observations collected at the European Organisation for Astronomical Research in the Southern Hemisphere under ESO programmes 297.C-5051, 098.C-0440(A), and 298.C-5009

<sup>1</sup> <http://exoplanet.eu>

# Telluric correction in the near-infrared: standard star or synthetic transmission?

S. Ulmer-Moll<sup>1,2</sup>, P. Figueira<sup>3,1</sup>, J. J. Neal<sup>1,2</sup>, N. C. Santos<sup>1,2</sup> and M. Bonnefoy<sup>4</sup>

<sup>1</sup> Instituto de Astrofísica e Ciências do Espaço, Universidade do Porto, CAUP, Rua das Estrelas, 4150-762 Porto, Portugal

<sup>2</sup> Departamento de Física e Astronomia, Faculdade de Ciências, Universidade do Porto, Portugal

<sup>3</sup> European Southern Observatory, Alonso de Cordova 3107, Vitacura, Santiago, Chile

<sup>4</sup> Univ. Grenoble Alpes, CNRS, IPAG, F-38000 Grenoble, France

Received ...; accepted ...

## ABSTRACT

**Context.** The Earth's atmospheric absorption is an important limiting factor for ground-based spectroscopic observations, with the near-infrared and infrared regions being the most affected. Several software packages, that produce a synthetic atmospheric transmission spectrum, have been developed to correct for the telluric absorption, namely *Molecfit*, *TellFit*, and *TAPAS*.

**Aims.** Our goal is to compare the correction achieved using these three telluric correction packages and the division by a telluric standard star. We want to evaluate the best method to correct near-infrared high-resolution spectra as well as the limitations of each software package and methodology.

**Methods.** We apply the telluric correction methods to CRIRES archival data taken in the J and K bands. We explore how the achieved correction level varies depending on the atmospheric T-P profile used in the modeling, the depth of the atmospheric lines, and the molecules creating the absorption.

**Results.** We found that the *Molecfit* and *TellFit* corrections lead to smaller residuals for the water lines. The standard star method corrects best the oxygen lines. *Molecfit* and the standard star method corrections result in global offsets always below 0.5% for all lines; the offset is similar with *TellFit* and *TAPAS* for the  $H_2O$  lines and around 1% for the  $O_2$  lines. All methods and software packages result in a scatter between 3% and 7% inside the telluric lines. The use of a tailored atmospheric profile for the observatory leads to a scatter two times smaller, and the correction level improves with lower values of precipitable water vapor.

**Conclusions.** The synthetic transmission methods lead to an improved correction compared to the standard star method for the water lines in the J band, with no loss of telescope time but the oxygen lines were better corrected by the standard star method.

**Key words.** atmospheric effects – radiative transfer – instrumentation: spectrographs – methods: data analysis – techniques: spectroscopic

## 1. Introduction

In ground-based observations, the light coming from a celestial object is partly or totally absorbed by the Earth's atmosphere, a phenomenon that is strongly wavelength-dependent. Even if the position of an observatory is carefully chosen to minimize the impact of the atmosphere, there is still a need to correct for telluric absorption. In spectroscopic studies, the species present in the atmosphere imprint absorption or emission lines on top of the spectra of the target. In absorption, the telluric lines create what is called the transmission spectrum of the Earth's atmosphere. The volume mixing ratio of the different molecules as function of height (that can be understood in terms of density profile) present in the atmosphere and the atmospheric conditions (pressure, temperature) affect the telluric lines in their shape, depth, and position in wavelengths. **High winds can shift the telluric features, and Figueira et al. (2012) showed that an horizontal wind model can account for some of these shifts and is in agreement with radiosonde measurements.** Thus, the transmission spectrum depends strongly in the time and location of the observations. Every molecule contributes differently to the final transmission. For example,  $H_2O$  leads to an absorption over a very wide wavelength range, spanning the optical, the near infrared, and the infrared. This absorption defines the near infrared bands over which photometry and spectroscopy was done

for many years. The water vapor shows hourly to seasonal variations which are challenging to correct (Adelman et al. 2003; Wood 2003).  $O_2$  absorption might be easier to correct, because it provides sharp, deep and well-defined features and the  $O_2$  volume mixing ratio is more stable in the atmosphere.  $O_2$  bands and individual lines in the optical have been studied for a long time (Wark & Mercer 1965; Caccin et al. 1985). When observations are done through cirrus clouds, the atmospheric transmission is not impacted. Cirrus clouds are thin clouds made of ice crystals and usually found at altitudes higher than 6 km (Wyllie et al. 1994). The ice crystals transmit most of the incoming stellar light and do not introduce water features in the transmission spectrum.

A correction of telluric absorption is required when the studies aim at high spectral fidelity; for example it is an essential step to characterize planetary and exoplanetary atmospheres (e.g. Bailey et al. (2007); Cotton et al. (2014); Brogi et al. (2014)). Telluric correction has also been studied in the context of exoplanet search through radial velocity (RV) measurements.

Earlier on, the telluric lines started to be used as a wavelength calibration to measure precise radial velocities (Griffin & Griffin 1973). The atmosphere can be considered as a gas cell which imposes its absorption features on the target spectrum. Smith (1982) and Balthasar et al. (1982) used  $O_2$  lines as wave-

## E.2 Talks and Seminars

TALK

### Towards exoplanetary atmospheres: new data reduction techniques for the nIR.

**Location:** XXVI Encontro Nacional de Astronomia e Astrofísica (ENAA), Aveiro, Portugal    **Date:** 2016, Sept. 09  
**File:** <http://gravitation.web.ua.pt/enaa2016/index2a62.html?q=node/3>

**Abstract:**

Exoplanetary atmospheres are one of the forefronts of exoplanet science. The measurement of exoplanet atmospheres can help break degeneracies in the mass-radius relationship for solid exoplanets allowing proper derivation of the planets properties, and may provide important clues to the origin and evolution of planets. The technological breakthrough of high-resolution spectrographs ( $\Delta\lambda/\lambda = 100,000$ ) allow for the separation and wavelength tracking of individual molecular spectral features. This allows for the separation of the stationary telluric absorption lines from the moving planet-star spectral lines. We focus our initial investigation on extracting the atmospheric signal of brown dwarfs, which are interesting objects between giant planets and small stars. Brown dwarf targets are good candidates to begin our investigation as their larger mass induces larger radial velocity shifts to the atmospheric lines and their larger radius (and surface area) produce a stronger signal compared to smaller planets. In this talk I will discuss the ongoing work of my PhD towards extracting the signal of brown dwarf atmospheres from high-resolution nIRspectra. I will discuss the methodology and techniques developed towards extracting the spectral lines of the atmospheres and show some of our current results.

### E.3 Posters

POSTER

#### Towards Exoplanet Atmospheres: new data reduction for the nIR

**Location:** *IVth Azores International Advanced School in Space Sciences*, Horta, Faial, Azores Islands, Portugal

**Date:** 2016, July 17–27

**File:** <http://www.iastro.pt/research/conferences/faial2016/>

**Abstract:**

In this poster I outline the goal of the direct subtraction technique, detailing the data preparation and correct steps needed. It shows the first results of applying the direct subtraction on our observations. The poster is provided on the next page.

POSTER

#### Towards Exoplanet Atmospheres: new data reduction for the nIR

**Location:** *XXVI Encontro Nacional de Astronomia e Astrofísica (ENAA)*, Aveiro, Portugal

**Date:** 2016, Sept. 09

**File:** <http://gravitation.web.ua.pt/enaa2016/index2a62.html?q=node/3>

**Abstract:**

I presented the same poster at ENAA as I did at the IVth Azores International Advanced School in Space Sciences.



# Towards Exoplanet Atmospheres: new data reduction for the nIR

Jason J. Neal, P. Figueira, N. C. Santos, C. H. F. Melo

## 1) Objective

- Reduce near-Infrared CRIRES spectra with high fidelity
- Extract spectra of exoplanetary atmospheres

## 2) Methods

- CRIRES reduction with in-house IRAF pipeline: Data Reduction Algorithm for CRIRES Spectra (DRACS).
- Obtain models of atmospheric absorption spectra from TAPAS web-service [Bertaux *et al.* 2014, A&A, 564, A96].

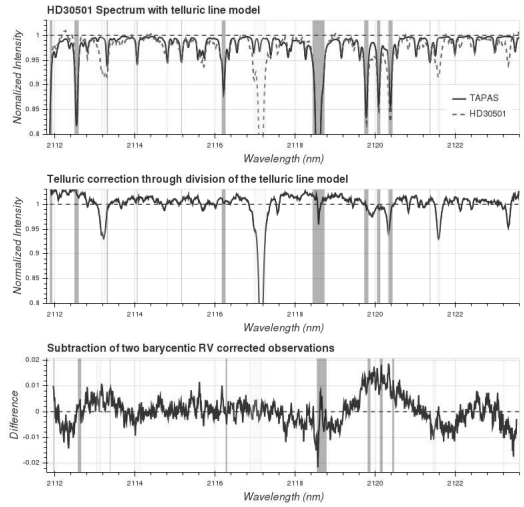
$$I_{tell}(\lambda) = 1 - \sum_{j=1}^m \text{Telluric lines} \quad (1)$$

- Wavelength calibrate the observations using the telluric absorption spectrum imprinted by the atmosphere.

$$I_{obs}(pix) = 1 - \left( \sum_{j=1}^m \text{Telluric} \times \sum_{k=1}^n \text{Stellar} \right) \quad (2)$$

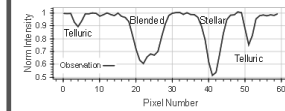
- Correct observations for telluric absorption by dividing by the same TAPAS telluric absorption models.
- Correct for Earth's barycentric motion then subtract two observations to cancel out the stellar absorption lines.

## 4) Results

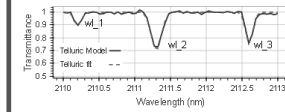


## 3) Calibration

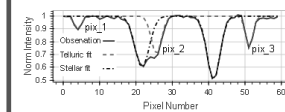
Simulated observation of 2 stellar and 3 telluric lines



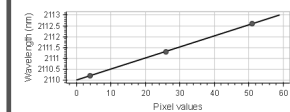
Fit Eq. 1 to telluric model to obtain the line centers in wavelength space ( $wl_i$ ).



Fit Eq. 2 to the observation to obtain the telluric line centers in pixel space ( $pix_i$ ).



A second order polynomial is applied to the fitted gaussian line centers  $wl_i$  and  $pix_i$ .



## 5) Future Work

- Model and extract the exoplanetary lines in the subtracted spectra.
- Apply these tools to 7 stars that host brown dwarf companions.



## E.4 Attended Conferences and Schools

### CONFERENCE

#### Towards Other Earths II:The star-planet connection

**Location:** Porto, Portugal

**Date:** 2014, Sept. 15–19

**Website** <http://www.astro.up.pt/investigacao/conferencias/toe2014/>

##### Description:

The study of extrasolar planets is one of the most active areas of research of modern astronomy. The number of discoveries attests for the importance of a topic that reaches out and captivates the imagination of scientists and public alike. This conference aims at reviewing the state of the art of star-planet connection, with some focus on the detection and characterization of Earth like planets orbiting other stars. We propose to debate how the field of extrasolar planets will evolve in respect to this and how it will face the challenges of the upcoming years.

### CONFERENCE

#### I Vietri Advanced School on Exoplanetary Science

**Location:** 2015, May 25–29

**Date:** Vietri sul Mare  
(Salerno), Italy

**Website** <http://www.iiassvietri.it/en/asex2015.html>

##### Description:

The School was aimed to provide a comprehensive, state-of-the-art picture of a variety of relevant aspects of the fast-developing, highly interdisciplinary field of extrasolar planets research. The Lecture topics of the School were focused on exoplanet detection with the Radial Velocity, Photometric Transits, Gravitational Microlensing, and Direct Imaging techniques. The Lectures were delivered by four senior researchers to an audience of graduate students, Ph.D students and young post-docs.

## IVth Azores International Advanced School in Space Sciences

**Location:** 2016, July 17–27

**Date:** Horta, Faial, Azores Islands, Portugal

**Website** <http://www.iastro.pt/research/conferences/faial2016/>

### Description:

This International Advanced School addresses the topics at the forefront of scientific research being conducted in the fields of stellar physics and exoplanetary science. It is mainly aimed at PhD and MSc students (although postdocs are also encouraged to apply) in any field of Astrophysics.

Students will be given the opportunity to present their own research work by bringing a poster to the School. The School provides an opportunity for the young researchers to network with fellow students and lecturers, thereby promoting awareness of areas outside the main specialization of the student, and potential cross-fertilization of techniques and concepts.

The School covers two scientific topics that share many synergies and resources: Asteroseismology and Exoplanets. Therefore, the program aims at building opportunities for cooperation and sharing of methods that will benefit both communities. This cooperation has experienced great success in the context of past space missions such as CoRoT and Kepler. Upcoming photometry and astrometry from space, as well as complementary data from ground-based networks, will continue to foster this cooperation. Observations of bright stars and clusters in the ecliptic plane are being made by the repurposed K2 mission, and NASA's TESS and ESA's CHEOPS missions will soon start obtaining similar data over the entire sky. ESA's PLATO mission will then build upon these successes by providing photometric light curves on a wealth of stars. Ground-based spectroscopy from the Stellar Observations Network Group (SONG) will complement the satellite data for the brightest stars in the sky, as will also be the case with the new generation of high-precision spectrographs being developed for the ESO, like the Echelle SPectrograph for Rocky Exoplanets and Stable Spectroscopic Observations (ESPRESSO).

## XXVI Encontro Nacional de Astronomia e Astrofísica

**Location:** Aveiro, Portugal

**Date:** 2016, Sept. 08–09

**File:** <http://gravitation.web.ua.pt/enaa2016/index2a62.html?q=node/3>

### Abstract:

The main goal of this national meeting is to present a general overview of the international state of the art research done in Astronomy and Astrophysics. ENAA also allows for researchers to get together and discuss scientific ideas and policies, strengthen the collaboration between national researchers and integrate young researchers in the community through the presentation of their work.

## E.5 Outreach

### ROOF READING

#### Astro Homus

**Location:** 2015 May

**Date:** Porto, Portugal

**Website** <http://astrohomus.astro.up.pt/livro>

##### Description:

Was involved in proofreading the outreach book *Astro Homus* (Figueira et al., 2015) which highlights the people working in Astronomy.

## E.6 Other

TEACHING

### Monitor at the 11<sup>th</sup>, 12<sup>th</sup>, 13<sup>th</sup> Physics Summer School

**Location:** Faculty of Science, University of Porto, Portugal    **Date:** 2015–2017

**Website** <http://e-fisica.fc.up.pt/edicoes/>

**Description:**

Instructing and monitoring 4–5 secondary school students through activities related to planet detection and characterization. One week per year.

*Na sua Edição a Escola desafia os participantes com o programa mais radical de sempre com projectos envolvendo lasers, supercondutores, nanotecnologias, física espacial, fibras ópticas, biosensores e astrofísica. Projectos que abrangem as três grandes áreas de investigação do DFA, Física, Astronomia e Engenharia Física. Assim, se tens apetência pelo conhecimento e pelo processo de investigação que permite inquirir a Natureza e testar hipóteses acerca das causas das coisas, então deixa-te arrastar pelo encantamento da experimentação e do entendimento das ideias mais profundas e abrangentes. O DFA garante uma viagem através do Universo, do microcosmo ao macrocosmo, inserindo-te num projecto que te dilatará a imaginação. Tens coragem? Aparece!*

OBSERVING

### HARPS-N@Telescopio Nazionale Galileo observing run

**Location:** La Palma, Spain

**Date:** 2017 Feb. 6–8

**Website** <http://www.tng.iac.es/instruments/harps/>

**Description:**

Observing runs are an essential part of the training of any astronomer. During my PhD I had the opportunity to observe for 3 nights on HARPS-N. These were for the *TROY* project, with which some IA-Porto researchers were collaborating. These observations were to fill in the phase curve of previously detected low-mass exoplanets to further constrain their masses. These observations were used in Lillo-Box et al. (2018).

OBSERVING

### ESPRESSO@VLT

**Location:** Paranal, Chile

**Date:** 2019 Jan. 4–10

**Website** <https://www.eso.org/sci/facilities/paranal/instruments/espresso.html>

**Description:**

An observing run with ESPRESSO at Paranal was completed between 4–10 January 2019. This observed the transit of WASP-121 as part of the ESPRESSO GTO program in P102 as well as observing several transit follow up targets and targets for Radial Velocity blind searches.

# Bibliography

- Adams, E. R., S. Seager, and L. Elkins-Tanton (2008). “Ocean Planet or Thick Atmosphere: On the Mass-Radius Relationship for Solid Exoplanets with Massive Atmospheres”. In: *The Astrophysical Journal* 673, pp. 1160–1164.
- Adibekyan, V. Z., S. G. Sousa, N. C. Santos, E. D. Mena, et al. (2012). “Chemical Abundances of 1111 FGK Stars from the HARPS GTO Planet Search Program - Galactic Stellar Populations and Planets”. In: *Astronomy and Astrophysics* 545, A32.
- Allard, F. (2013). “The BT-Settl Model Atmospheres for Stars, Brown Dwarfs and Planets”. In: *Proceedings of the International Astronomical Union* 8.S299. 00007, pp. 271–272.
- Allard, F., D. Homeier, and B. Freytag (2012a). “Models of Very-Low-Mass Stars, Brown Dwarfs and Exoplanets”. In: *Philosophical Transactions of the Royal Society of London Series A* 370. 00280, pp. 2765–2777.
- Allard, F., D. Homeier, B. Freytag, and C. M. Sharp (2012b). “Atmospheres From Very Low-Mass Stars to Extrasolar Planets”. In: EAS Publications Series. Vol. 57. eprint: arXiv:1206.1021, pp. 3–43.
- Allard, F. and P. H. Hauschildt (1995). “Model Atmospheres for M (Sub)Dwarf Stars. 1: The Base Model Grid”. In: *The Astrophysical Journal* 445, pp. 433–450.
- Allard, F., P. H. Hauschildt, D. R. Alexander, A. Tamanai, and A. Schweitzer (2001). “The Limiting Effects of Dust in Brown Dwarf Model Atmospheres”. In: *The Astrophysical Journal* 556, pp. 357–372.
- Alonso, R., T. M. Brown, G. Torres, D. W. Latham, et al. (2004). “TrES-1: The Transiting Planet of a Bright K0 V Star”. In: *The Astrophysical Journal Letters* 613, pp. L153–L156.
- Andreasen, D. T., S. G. Sousa, E. Delgado Mena, N. C. Santos, M. Tsantaki, B. Rojas-Ayala, and V. Neves (2016). “Near-Infrared Spectroscopy of the Sun and HD 20010. Compiling a New Line List in the near-Infrared”. In: *Astronomy and Astrophysics* 585, A143.
- Artigau, É., D. Kouach, J.-F. Donati, R. Doyon, et al. (2014). “SPIRou: The near-Infrared Spectropolarimeter/High-Precision Velocimeter for the Canada-France-Hawaii Telescope”. In: *Proc. SPIE*. Ground-Based and Airborne Instrumentation for Astronomy V. Vol. 9147. 00047. International Society for Optics and Photonics, p. 914715.
- Artigau, É., L. Malo, R. Doyon, P. Figueira, X. Delfosse, and N. Astudillo-Defru (2018). “Optical and Near-Infrared Radial Velocity Content of M Dwarfs: Testing Models with Barnard’s Star”. In: *The Astronomical Journal* 155, p. 198.
- Asplund, M., N. Grevesse, A. J. Sauval, and P. Scott (2009). “The Chemical Composition of the Sun”. In: *Annual Review of Astronomy and Astrophysics* 47, pp. 481–522.

- Astudillo-Defru, N., X. Bonfils, X. Delfosse, D. Ségransan, et al. (2015). “The HARPS Search for Southern Extra-Solar Planets. XXXVI. Planetary Systems and Stellar Activity of the M Dwarfs GJ 3293, GJ 3341, and GJ 3543”. In: *Astronomy and Astrophysics* 575, A119.
- Bailey, J., A. Simpson, and D. Crisp (2007). “Correcting Infrared Spectra for Atmospheric Transmission”. In: *Publications of the Astronomical Society of the Pacific* 119, pp. 228–236.
- Baraffe, I., G. Chabrier, T. Barman, F. Allard, and P. H. Hauschildt (2003). “Evolutionary Models for Cool Brown Dwarfs and Extrasolar Giant Planets. The Case of HD 20945”. In: *Astronomy and Astrophysics* 402.2. 00000, pp. 701–712. arXiv: astro-ph/0302293.
- Baraffe, I., D. Homeier, F. Allard, and G. Chabrier (2015). “New Evolutionary Models for Pre-Main Sequence and Main Sequence Low-Mass Stars down to the Hydrogen-Burning Limit”. In: *Astronomy and Astrophysics* 577. 00280, A42. arXiv: 1503.04107.
- Baranne, A., D. Queloz, M. Mayor, G. Adrianzyk, et al. (1996). “ELodie: A Spectrograph for Accurate Radial Velocity Measurements.” In: *Astronomy and Astrophysics Supplement Series* 119, pp. 373–390.
- Barber, R. J., J. Tennyson, G. J. Harris, and R. N. Tolchenov (2006). “A High-Accuracy Computed Water Line List”. In: *Monthly Notices of the Royal Astronomical Society* 368.3, pp. 1087–1094.
- Barclay, T., J. Pepper, and E. V. Quintana (2018). “A Revised Exoplanet Yield from the Transiting Exoplanet Survey Satellite (TESS)”. In: *ArXiv e-prints* 1804, arXiv:1804.05050.
- Barge, P., A. Baglin, M. Auvergne, H. Rauer, et al. (2008). “Transiting Exoplanets from the CoRoT Space Mission. I. CoRoT-Exo-1b: A Low-Density Short-Period Planet around a G0V Star”. In: *Astronomy and Astrophysics* 482, pp. L17–L20.
- Barman, T. S., B. Macintosh, Q. M. Konopacky, and C. Marois (2011). “Clouds and Chemistry in the Atmosphere of Extrasolar Planet HR8799b”. In: *The Astrophysical Journal* 733, p. 65.
- Barnes, J. R., T. S. Barman, H. R. A. Jones, C. J. Leigh, A. C. Cameron, R. J. Barber, and D. J. Pinfield (2008). “HD 179949b: A Close Orbiting Extrasolar Giant Planet with a Stratosphere?” In: *Monthly Notices of the Royal Astronomical Society* 390.3, pp. 1258–1266.
- Barnes, J. W. (2007). “Effects of Orbital Eccentricity on Extrasolar Planet Transit Detectability and Light Curves”. In: *Publications of the Astronomical Society of the Pacific* 119.859, p. 986.
- Barros, S. C. C., H. Gosselin, J. Lillo-Box, D. Bayliss, et al. (2017). “Precise Masses for the Transiting Planetary System HD 106315 with HARPS”. In: *Astronomy & Astrophysics* 608, A25.
- Batista, V., J.-P. Beaulieu, D. P. Bennett, A. Gould, J.-B. Marquette, A. Fukui, and A. Bhattacharya (2015). “Confirmation of the OGLE-2005-BLG-169 Planet Signature and Its Characteristics with Lens-Source Proper Motion Detection”. In: *The Astrophysical Journal* 808, p. 170.
- Bean, J. L., E. Miller-Ricci Kempton, and D. Homeier (2010). “A Ground-Based Transmission Spectrum of the Super-Earth Exoplanet GJ 1214b”. In: *Nature* 468. 00283, pp. 669–672.
- Beaulieu, J.-P., D. P. Bennett, P. Fouqué, A. Williams, et al. (2006). “Discovery of a Cool Planet of 5.5 Earth Masses through Gravitational Microlensing”. In: *Nature* 439, pp. 437–440.
- Benedict, G. F. and T. E. Harrison (2017). “HD 202206: A Circumbinary Brown Dwarf System”. In: *The Astronomical Journal* 153, p. 258.
- Bertaux, J. L., R. Lallement, S. Ferron, C. Boonne, and R. Bodichon (2014). “TAPAS, a Web-Based Service of Atmospheric Transmission Computation for Astronomy”. In: *Astronomy and Astrophysics* 564. 00041, A46.
- Beuzit, J.-L., M. Feldt, K. Dohlen, D. Mouillet, et al. (2008). “SPHERE: A Planet Finder Instrument for the VLT”. In: *Ground-Based and Airborne Instrumentation for Astronomy II. Ground-Based and*

- Airborne Instrumentation for Astronomy II. Vol. 7014. International Society for Optics and Photonics, p. 701418.
- Bevington, P. R. and D. K. Robinson (2003). *Data Reduction and Error Analysis for the Physical Sciences*. p.g. 208-212. McGraw-Hill. 320 pp.
- Binney, J. and M. Merrifield (1998). *Galactic Astronomy*.
- Bonfanti, A., S. Ortolani, and V. Nascimbeni (2016). “Age Consistency between Exoplanet Hosts and Field Stars”. In: *Astronomy and Astrophysics* 585, A5.
- Borucki, W., D. G. Koch, G. Basri, N. Batalha, et al. (2011). “Characteristics of Kepler Planetary Candidates Based on the First Data Set”. In: *The Astrophysical Journal* 728, p. 117.
- Borucki, W., D. Koch, G. Basri, N. Batalha, et al. (2008). “Finding Earth-Size Planets in the Habitable Zone: The Kepler Mission”. In: Exoplanets: Detection, Formation and Dynamics. Vol. 249, pp. 17–24.
- Boss, A. P. (1997). “Giant Planet Formation by Gravitational Instability.” In: *Science* 276, pp. 1836–1839.
- Bouchy, F., F. Pepe, and D. Queloz (2001). “Fundamental Photon Noise Limit to Radial Velocity Measurements”. In: *Astronomy and Astrophysics* 374.2. 00258, pp. 733–739.
- Bozza, V., L. Mancini, and A. Sozzetti, eds. (2016). *Methods of Detecting Exoplanets: 1st Advanced School on Exoplanetary Science*. Astrophysics and Space Science Library. Springer International Publishing.
- Broeg, C., A. Fortier, D. Ehrenreich, Y. Alibert, et al. (2013). “CHEOPS: A Transit Photometry Mission for ESA’s Small Mission Programme”. In: *European Physical Journal Web of Conferences* 47, p. 03005.
- Brogi, M., R. J. de Kok, S. Albrecht, I. A. G. Snellen, J. L. Birkby, and H. Schwarz (2016). “Rotation and Winds of Exoplanet HD 189733 b Measured with High-Dispersion Transmission Spectroscopy”. In: *The Astrophysical Journal* 817.2. 00000, p. 106. arXiv: 1512.05175.
- Brogi, M., R. J. de Kok, J. L. Birkby, H. Schwarz, and I. A. G. Snellen (2014). “Carbon Monoxide and Water Vapor in the Atmosphere of the Non-Transiting Exoplanet HD 179949 B”. In: *Astronomy and Astrophysics* 565. 00000, A124.
- Brogi, M., I. A. G. Snellen, R. J. de Kok, S. Albrecht, J. Birkby, and E. J. W. de Mooij (2012). “The Signature of Orbital Motion from the Dayside of the Planet  $\tau$  Boötis B”. In: *Nature* 486. 00000, pp. 502–504.
- Brugger, B., O. Mousis, M. Deleuil, and F. Deschamps (2017). “Constraints on Super-Earth Interiors from Stellar Abundances”. In: *The Astrophysical Journal* 850, p. 93.
- Burke, C. J., F. Mullally, S. E. Thompson, J. L. Coughlin, and J. F. Rowe (2019). “Re-Evaluating Small Long-Period Confirmed Planets From Kepler”. In: *arXiv e-prints* 1901, arXiv:1901.00506.
- Burrows, A., T. Guillot, W. B. Hubbard, M. S. Marley, D. Saumon, J. I. Lunine, and D. Sudarsky (2000). “On the Radii of Close-in Giant Planets”. In: *The Astrophysical Journal Letters* 534.1, p. L97.
- Burrows, A., M. Marley, W. B. Hubbard, J. I. Lunine, et al. (1997). “A Nongray Theory of Extrasolar Giant Planets and Brown Dwarfs”. In: *The Astrophysical Journal* 491, pp. 856–875.
- Butler, R. P. and G. W. Marcy (1996). “A Planet Orbiting 47 Ursae Majoris”. In: *The Astrophysical Journal Letters* 464, p. L153.
- Butler, R. P., G. W. Marcy, E. Williams, H. Hauser, and P. Shirts (1997). “Three New “51 Pegasi-Type” Planets”. In: *The Astrophysical Journal Letters* 474, pp. L115–L118.
- Caffau, E., H.-G. Ludwig, M. Steffen, B. Freytag, and P. Bonifacio (2011). “Solar Chemical Abundances Determined with a CO5BOLD 3D Model Atmosphere”. In: *Solar Physics* 268.2, p. 255.
- Cameron, A. C. (2012). “Extrasolar Planets: Astrophysical False Positives”. In: *Nature* 492.7427, pp. 48–50.

- Chabrier, G. and I. Baraffe (2000). "Theory of Low-Mass Stars and Substellar Objects". In: *Annual Review of Astronomy and Astrophysics* 38.1. 00483, pp. 337–377. arXiv: astro-ph/0006383.
- Charbonneau, D., T. M. Brown, D. W. Latham, and M. Mayor (2000). "Detection of Planetary Transits Across a Sun-like Star". In: *The Astrophysical Journal Letters* 529, pp. L45–L48.
- Charbonneau, D., T. M. Brown, R. W. Noyes, and R. L. Gilliland (2002). "Detection of an Extrasolar Planet Atmosphere\*". In: *The Astrophysical Journal* 568.1, p. 377.
- Chauvin, G., A.-M. Lagrange, C. Dumas, B. Zuckerman, et al. (2004). "A Giant Planet Candidate near a Young Brown Dwarf. Direct VLT/NACO Observations Using IR Wavefront Sensing". In: *Astronomy and Astrophysics* 425, pp. L29–L32.
- Chen, J. and D. M. Kipping (2016). "Probabilistic Forecasting of the Masses and Radii of Other Worlds". In: *The Astrophysical Journal* 834.1, p. 17. arXiv: 1603.08614.
- Chenciner, A. (2007). "Three Body Problem". In: *Scholarpedia* 2.10, p. 2111.
- Ciddor, P. E. (1996). "Refractive Index of Air: New Equations for the Visible and near Infrared". In: *Applied Optics* 35.9, pp. 1566–1573.
- Clough, S. A. and M. J. Iacono (1995). "Line-by-Line Calculation of Atmospheric Fluxes and Cooling Rates: 2. Application to Carbon Dioxide, Ozone, Methane, Nitrous Oxide and the Halocarbons". In: *Journal of Geophysical Research: Atmospheres* 100.D8. 00002, pp. 16519–16535.
- Collaboration, G., A. G. A. Brown, A. Vallenari, T. Prusti, et al. (2018). "Gaia Data Release 2. Summary of the Contents and Survey Properties". In: *ArXiv e-prints*, arXiv:1804.09365.
- Collaboration, G., T. Prusti, J. H. J. de Bruijne, A. G. A. Brown, et al. (2016). "The Gaia Mission". In: *Astronomy and Astrophysics* 595, A1.
- Connes, P., M. Martic, and J. Schmitt (1996). "Demonstration of Photon-Noise Limit in Stellar Radial Velocities". In: *Astrophysics and Space Science* 241.1, p. 61.
- Connes, P. (1985). "Absolute Astronomical Accelerometry". In: *Astrophysics and Space Science* 110.2, pp. 211–255.
- Correia, A. C. M., S. Udry, M. Mayor, J. Laskar, et al. (2005). "The CORALIE Survey for Southern Extra-Solar Planets. XIII. A Pair of Planets around HD 202206 or a Circumbinary Planet?" In: *aap* 440. 00000, pp. 751–758.
- Cotton, D. V., J. Bailey, and L. Kedziora-Chudczer (2014). "Atmospheric Modelling for the Removal of Telluric Features from Infrared Planetary Spectra". In: *Monthly Notices of the Royal Astronomical Society* 439. 00007, pp. 387–399.
- Crepp, J. R., E. J. Gonzales, E. B. Bechter, B. T. Montet, et al. (2016). "The TRENDS High-Contrast Imaging Survey. VI. Discovery of a Mass, Age, and Metallicity Benchmark Brown Dwarf". In: *The Astrophysical Journal* 831. 00004.
- Cumming, A., G. W. Marcy, and R. P. Butler (1999). "The Lick Planet Search: Detectability and Mass Thresholds". In: *The Astrophysical Journal* 526, pp. 890–915.
- Czekala, I., S. M. Andrews, K. S. Mandel, D. W. Hogg, and G. M. Green (2015). "Constructing A Flexible Likelihood Function For Spectroscopic Inference". In: *The Astrophysical Journal* 812.2. 00022, p. 128. arXiv: 1412.5177.
- Czesla, S., T. Molle, and J. H. M. M. Schmitt (2018). "A Posteriori Noise Estimation in Variable Data Sets. With Applications to Spectra and Light Curves". In: *Astronomy and Astrophysics* 609, A39.

- De Kok, R. J., M. Brogi, I. A. G. Snellen, J. Birkby, S. Albrecht, and E. J. de Mooij (2013). "Detection of Carbon Monoxide in the High-Resolution Day-Side Spectrum of the Exoplanet HD 189733b". In: *Astronomy and Astrophysics* 554. 00086, A82.
- Deeg, H. (1998). "Photometric Detection of Extrasolar Planets by the Transit-Method". In: *Brown Dwarfs and Extrasolar Planets*. Brown Dwarfs and Extrasolar Planets. Vol. 134. ASP Conference Series #134, p. 216.
- Díaz, R. F., J. M. Almenara, A. Santerne, C. Moutou, A. Lethuillier, and M. Deleuil (2014). "PASTIS: Bayesian Extrasolar Planet Validation - I. General Framework, Models, and Performance". In: *Monthly Notices of the Royal Astronomical Society* 441, pp. 983–1004.
- Dieterich, S. B., T. J. Henry, W.-C. Jao, J. G. Winters, A. D. Hosey, A. R. Riedel, and J. P. Subasavage (2014). "The Solar Neighborhood. XXXII. The Hydrogen Burning Limit". In: *The Astronomical Journal* 147, p. 94.
- Dorn, R. J., G. Anglada-Escude, D. Baade, P. Bristow, et al. (2014). "CRIRES+: Exploring the Cold Universe at High Spectral Resolution". In: *The Messenger* 156, pp. 7–11.
- Edlén, B. (1953). "The Dispersion of Standard Air\*". In: *JOSA* 43.5, pp. 339–344.
- ESA (1997). "The HIPPARCOS and TYCHO Catalogues. Astrometric and Photometric Star Catalogues Derived from the ESA HIPPARCOS Space Astrometry Mission". In: ESA Special Publication. Vol. 1200.
- ESO (2017). *ESO Call for Proposals - P101*.
- Esteves, L. J., E. J. W. De Mooij, and R. Jayawardhana (2013). "Optical Phase Curves of Kepler Exoplanets". In: *The Astrophysical Journal* 772.1, p. 51.
- Ferluga, S., L. Floreano, U. Bravar, and C. Bédalo (1997). "Separating the Spectra of Binary Stars-I. A Simple Method: Secondary Reconstruction". In: *Astronomy and Astrophysics Supplement Series* 121.1. 00012, pp. 201–209.
- Figueira, P., V. Z. Adibekyan, M. Oshagh, J. J. Neal, et al. (2016). "Radial Velocity Information Content of M Dwarf Spectra in the Near-Infrared". In: *Astronomy and Astrophysics* 586. 00002, A101.
- Figueira, P., F. Pepe, C. H. F. Melo, N. C. Santos, et al. (2010). "Radial Velocities with CRIRES: Pushing Precision down to 5-10 m/S". In: *Astronomy and Astrophysics* 511. 00057, A55.
- Figueira, P. and S. Neves (2015). *Astro Homus*. CAUP.
- Fischer, D. A. and J. Valenti (2005). "The Planet-Metallicity Correlation". In: *The Astrophysical Journal* 622, pp. 1102–1117.
- Fitzpatrick, R. (2012). *An Introduction to Celestial Mechanics*.
- Fortney, J. J. and N. Nettelmann (2010). "The Interior Structure, Composition, and Evolution of Giant Planets". In: *Space Science Reviews* 152.1-4, pp. 423–447.
- Fowler, A. M. and I. Gatley (1990). "Demonstration of an Algorithm for Read-Noise Reduction in Infrared Arrays". In: *The Astrophysical Journal Letters* 353, p. L33.
- Fressin, F., G. Torres, D. Charbonneau, S. T. Bryson, et al. (2013). "The False Positive Rate of Kepler and the Occurrence of Planets". In: *The Astrophysical Journal* 766, p. 81.
- Freudling, W., M. Romaniello, D. M. Bramich, P. Ballester, et al. (2013). "Automated Data Reduction Workflows for Astronomy. The ESO Reflex Environment". In: *Astronomy and Astrophysics* 559, A96.
- Freytag, B., F. Allard, H.-G. Ludwig, D. Homeier, and M. Steffen (2010). "The Role of Convection, Overshoot, and Gravity Waves for the Transport of Dust in M Dwarf and Brown Dwarf Atmospheres". In: *Astronomy and Astrophysics* 513, A19.

- Gagné, J., J. K. Faherty, A. J. Burgasser, É. Artigau, et al. (2017). “SIMP J013656.5+093347 Is Likely a Planetary-Mass Object in the Carina-Near Moving Group”. In: *The Astrophysical Journal Letters* 841, p. L1.
- Gandolfi, D., O. Barragan, J. Livingston, M. Fridlund, et al. (2018). “TESS’s First Planet: A Super-Earth Transiting the Naked-Eye Star \$\pi\$ Mensae”. In: *ArXiv e-prints* 1809, arXiv:1809.07573.
- Gontcharov, G. A., A. A. Andronova, and O. A. Titov (2000). “New Astrometric Binaries among HIPPARCOS Stars”. In: *Astronomy and Astrophysics* 355, pp. 1164–1167.
- Goodman, J. (2009). “Thermodynamics of Atmospheric Circulation on Hot Jupiters”. In: *The Astrophysical Journal* 693, pp. 1645–1649.
- Gray, D. F. (2005). *The Observation and Analysis of Stellar Photospheres*. 3rd ed. Cambridge University Press.
- Gregory, P. C. (2011). “Bayesian Re-Analysis of the Gliese 581 Exoplanet System”. In: *Monthly Notices of the Royal Astronomical Society* 415, pp. 2523–2545.
- Gullikson, K., S. Dodson-Robinson, and A. Kraus (2014). “Correcting for Telluric Absorption: Methods, Case Studies, and Release of the TelFit Code”. In: *The Astronomical Journal* 148.3. 00015, p. 53.
- Hadrava, P. (2009). “Disentangling of Spectra - Theory and Practice”. In: 00013. arXiv: 0909.0172 [astro-ph].
- Halbwachs, J.-L., F. Arenou, M. Mayor, S. Udry, and D. Queloz (2000). “Exploring the Brown Dwarf Desert with Hipparcos”. In: *Astronomy and Astrophysics* 355. 00198, pp. 581–594.
- Hatzes, A. P. and W. D. Cochran (1992). “Spectrograph Requirements for Precise Radial Velocity Measurements”. In: European Southern Observatory Conference and Workshop Proceedings. Vol. 40, p. 275.
- Hatzes, A. P. and H. Rauer (2015). “A Definition for Giant Planets Based on the Mass-Density Relationship”. In: *The Astrophysical Journal Letters* 810, p. L25.
- Hauschildt, P. H., F. Allard, and E. Baron (1999). “The NextGen Model Atmosphere Grid for  $3000 \leq \text{Teff} \leq 10,000$  K”. In: *The Astrophysical Journal* 512. 01086, pp. 377–385.
- Hauschildt, P. H., E. Baron, and F. Allard (1997). “Parallel Implementation of the PHOENIX Generalized Stellar Atmosphere Program”. In: *The Astrophysical Journal* 483, pp. 390–398.
- Heng, K. and A. P. Showman (2015). “Atmospheric Dynamics of Hot Exoplanets”. In: *Annual Review of Earth and Planetary Sciences* 43.1, pp. 509–540.
- Hoeijmakers, H. J., R. J. de Kok, I. A. G. Snellen, M. Brogi, J. L. Birkby, and H. Schwarz (2015). “A Search for TiO in the Optical High-Resolution Transmission Spectrum of HD 209458b: Hindrance Due to Inaccuracies in the Line Database”. In: *Astronomy and Astrophysics* 575, A20.
- Hoeijmakers, H. J., D. Ehrenreich, K. Heng, D. Kitzmann, et al. (2018). “Atomic Iron and Titanium in the Atmosphere of the Exoplanet KELT-9b”. In: *Nature* 560.7719, p. 453.
- Holczer, T., T. Mazeh, G. Nachmani, D. Jontof-Hutter, et al. (2016). “Transit Timing Observations from Kepler. IX. Catalog of the Full Long-Cadence Data Set”. In: *The Astrophysical Journal Supplement Series* 225, p. 9.
- Holman, M. J., D. C. Fabrycky, D. Ragozzine, E. B. Ford, et al. (2010). “Kepler-9: A System of Multiple Planets Transiting a Sun-Like Star, Confirmed by Timing Variations”. In: *Science* 330, p. 51.
- Holman, M. J. and N. W. Murray (2005). “The Use of Transit Timing to Detect Terrestrial-Mass Extrasolar Planets”. In: *Science* 307, pp. 1288–1291.

- Horne, K. (1986). "An Optimal Extraction Algorithm for CCD Spectroscopy". In: *Publications of the Astronomical Society of the Pacific* 98. 01548, pp. 609–617.
- Howell, S. B. (2000). *Handbook of CCD Astronomy*.
- Huang, C. X., J. Burt, A. Vanderburg, M. N. Günther, et al. (2018a). "TESS Discovery of a Transiting Super-Earth in the \$\Pi\$ Mensae System". In: *ArXiv e-prints* 1809, arXiv:1809.05967.
- Huang, C. X., A. Shporer, D. Dragomir, M. Fausnaugh, et al. (2018b). "Expected Yields of Planet Discoveries from the TESS Primary and Extended Missions". In: *ArXiv e-prints* 1807, arXiv:1807.11129.
- Husser, T.-O., S. W.-. von Berg, S. Dreizler, D. Homeier, A. Reiners, T. Barman, and P. H. Hauschildt (2013). "A New Extensive Library of PHOENIX Stellar Atmospheres and Synthetic Spectra". In: *Astronomy and Astrophysics* 553. 00243, A6. arXiv: 1303.5632.
- Jha, S., D. Charbonneau, P. M. Garnavich, D. J. Sullivan, T. Sullivan, T. M. Brown, and J. L. Tonry (2000). "Multicolor Observations of a Planetary Transit of HD 209458". In: *The Astrophysical Journal* 540.1, p. L45.
- Kaeufl, H.-U., P. Ballester, P. Biereichel, B. Delabre, et al. (2004). "CRIRES: A High-Resolution Infrared Spectrograph for ESO's VLT". In: *Ground-based Instrumentation for Astronomy* 5492. 00000, p. 1218.
- Kalas, P., J. R. Graham, E. Chiang, M. P. Fitzgerald, et al. (2008). "Optical Images of an Exosolar Planet 25 Light-Years from Earth". In: *Science* 322, p. 1345.
- Kerber, F., G. Nave, C. J. Sansonetti, and P. Bristow (2009). "From Laboratory to the Sky: Th–Ar Wavelength Standards for the Cryogenic Infrared Echelle Spectrograph (CRIRES)". In: *Physica Scripta* 2009.T134. 00009, p. 014007.
- Klüter, J., U. Bastian, M. Demleitner, and J. Wambsganss (2018). "Prediction of Astrometric Microlensing Events from Gaia DR2 Proper Motions". In: arXiv: 1807.11077 [astro-ph].
- Knutson, H. A. (2009). "Characterizing the Atmospheres of Hot Jupiters: From Spectra to Multi-Color Maps". In: *Transiting Planets* 253, p. 255.
- Knutson, H. A., D. Charbonneau, L. E. Allen, J. J. Fortney, et al. (2007a). "A Map of the Day–Night Contrast of the Extrasolar Planet HD 189733b". In: *Nature* 447.7141, pp. 183–186.
- Knutson, H. A., D. Charbonneau, R. W. Noyes, T. M. Brown, and R. L. Gilliland (2007b). "Using Stellar Limb-Darkening to Refine the Properties of HD 209458b". In: *The Astrophysical Journal* 655.1, p. 564.
- Kolbl, R., G. W. Marcy, H. Isaacson, and A. W. Howard (2015). "Detection of Stars Within \$\sim\$0.8 in of Kepler Objects of Interest". In: *The Astronomical Journal* 149, p. 18.
- Koll, D. D. B. and D. S. Abbot (2016). "Temperature Structure and Atmospheric Circulation of Dry Tidally Locked Rocky Exoplanets". In: *The Astrophysical Journal* 825, p. 99.
- Kostogryz, N., M. Kürster, T. Yakobchuk, Y. Lyubchik, and M. Kuznetsov (2013). "A Spectral Differential Approach to Characterizing Low-Mass Companions to Late-Type Stars". In: *Astronomische Nachrichten* 334.7. 00000, pp. 648–660.
- Kreidberg, L., J. L. Bean, J.-M. Désert, B. Benneke, et al. (2014). "Clouds in the Atmosphere of the Super-Earth Exoplanet GJ 1214b". In: *Nature* 505.7481, pp. 69–72.
- Ku, H. H. (1966). *Notes on the Use of Propagation of Error Formulas*. National Bureau of Standards.
- Kubas, D., J. P. Beaulieu, D. P. Bennett, A. Cassan, et al. (2012). "A Frozen Super-Earth Orbiting a Star at the Bottom of the Main Sequence". In: *Astronomy and Astrophysics* 540, A78.
- Kurucz, R. L. (1979). "Model Atmospheres for G, F, A, B, and O Stars". In: *The Astrophysical Journal Supplement Series* 40, pp. 1–340.

- Kuzuhara, M., M. Tamura, T. Kudo, M. Janson, et al. (2013). “Direct Imaging of a Cold Jovian Exoplanet in Orbit around the Sun-like Star GJ 504”. In: *The Astrophysical Journal* 774, p. 11.
- Lebzelter, T., A. Seifahrt, S. Uttenthaler, S. Ramsay, et al. (2012). “CRIRES-POP. A Library of High Resolution Spectra in the near-Infrared”. In: *Astronomy and Astrophysics* 539, A109.
- Lillo-Box, J., A. Leleu, H. Parviainen, P. Figueira, et al. (2018). “The TROY Project. II. Multi-Technique Constraints on Exotrojans in Nine Planetary Systems”. In: *Astronomy and Astrophysics* 618, A42.
- Lindegren, L. and D. Dravins (2003). “The Fundamental Definition of “radial Velocity””. In: *Astronomy and Astrophysics* 401, pp. 1185–1201.
- Lissauer, J. J., G. W. Marcy, J. F. Rowe, S. T. Bryson, et al. (2012). “Almost All of Kepler’s Multiple-Planet Candidates Are Planets”. In: *The Astrophysical Journal* 750.2, p. 112.
- Lockwood, A. C., J. A. Johnson, C. F. Bender, J. S. Carr, T. Barman, A. J. W. Richert, and G. A. Blake (2014). “Near-IR Direct Detection of Water Vapor in Tau Boötis B”. In: *The Astrophysical Journal Letters* 783.2. 00038, p. L29.
- López-Morales, M., R. D. Haywood, J. L. Coughlin, L. Zeng, et al. (2016). “Kepler-21b: A Rocky Planet Around a V = 8.25 Magnitude Star”. In: *The Astronomical Journal* 152, p. 204.
- Lopez, E. D. and J. J. Fortney (2014). “Understanding the Mass-Radius Relation for Sub-Neptunes: Radius as a Proxy for Composition”. In: *The Astrophysical Journal* 792, p. 1.
- Lovis, C. and F. Pepe (2007). “A New List of Thorium and Argon Spectral Lines in the Visible”. In: *Astronomy & Astrophysics* 468.3, pp. 1115–1121.
- Ma, B. and J. Ge (2014). “Statistical Properties of Brown Dwarf Companions: Implications for Different Formation Mechanisms”. In: *Monthly Notices of the Royal Astronomical Society* 439.3, p. 2781.
- Macintosh, B. A., J. R. Graham, D. W. Palmer, R. Doyon, et al. (2008). “The Gemini Planet Imager: From Science to Design to Construction”. In: *Adaptive Optics Systems*. Adaptive Optics Systems. Vol. 7015. International Society for Optics and Photonics, p. 701518.
- Madhusudhan, N. and A. Burrows (2012). “Analytic Models for Albedos, Phase Curves, and Polarization of Reflected Light from Exoplanets”. In: *The Astrophysical Journal* 747.1, p. 25.
- Maldonado, J. and E. Villaver (2017). “Searching for Chemical Signatures of Brown Dwarf Formation”. In: *Astronomy and Astrophysics* 602, A38.
- Marcy, G. W. and R. P. Butler (1996). “A Planetary Companion to 70 Virginis”. In: *The Astrophysical Journal Letters* 464, p. L147.
- Marois, C., R. Doyon, R. Racine, D. Nadeau, et al. (2005). “Direct Exoplanet Imaging around Sun-like Stars: Beating the Speckle Noise with Innovative Imaging Techniques”. In: *Journal of the Royal Astronomical Society of Canada* 99, p. 130.
- Marois, C., B. Macintosh, T. Barman, B. Zuckerman, et al. (2008). “Direct Imaging of Multiple Planets Orbiting the Star HR 8799”. In: *Science* 322.5906, pp. 1348–1352. pmid: 19008415.
- Marois, C., B. Zuckerman, Q. M. Konopacky, B. Macintosh, and T. Barman (2010). “Images of a Fourth Planet Orbiting HR 8799”. In: *Nature* 468, pp. 1080–1083.
- Martins, J. H. C., N. C. Santos, P. Figueira, J. P. Faria, et al. (2015). “Evidence for a Spectroscopic Direct Detection of Reflected Light from 51 Pegasi B”. In: *Astronomy and Astrophysics* 576, A134.
- Mathar, R. J. (2007). “Refractive Index of Humid Air in the Infrared: Model Fits”. In: *Journal of Optics A: Pure and Applied Optics* 9.5, p. 470.
- Mawet, D., P. Riaud, O. Absil, and J. Surdej (2005). “Annular Groove Phase Mask Coronagraph”. In: *The Astrophysical Journal* 633, pp. 1191–1200.

- Mayor, M., F. Pepe, D. Queloz, F. Bouchy, et al. (2003). "Setting New Standards with HARPS". In: *The Messenger* 114, pp. 20–24.
- Mayor, M. and D. Queloz (1995). "A Jupiter-Mass Companion to a Solar-Type Star". In: *Nature* 378.6555, pp. 355–359.
- Mazeh, T., E. L. Martin, D. Goldberg, and H. A. Smith (1997). "Detecting Faint Secondaries of Spectroscopic Binaries: HD 101177B and 149414A". In: *Monthly Notices of the Royal Astronomical Society* 284.2, 00014, pp. 341–347.
- Mégevand, D., F. M. Zerbi, P. Di Marcantonio, A. Cabral, et al. (2014). "ESPRESSO: The Radial Velocity Machine for the VLT". In: *Proc. SPIE*. Ground-Based and Airborne Instrumentation for Astronomy V. Vol. 9147, 91471H.
- Meier, R. J. (2005). "On Art and Science in Curve-Fitting Vibrational Spectra". In: *Vibrational Spectroscopy* 39.2, pp. 266–269.
- Melo, C., N. C. Santos, W. Gieren, G. Pietrzynski, et al. (2007). "A New Neptune-Mass Planet Orbiting HD 219828". In: *Astronomy and Astrophysics* 467, pp. 721–727.
- Ment, K., J. A. Dittmann, N. Astudillo-Defru, D. Charbonneau, et al. (2018). "A Second Planet with an Earth-like Composition Orbiting the Nearby M Dwarf LHS 1140". In: *ArXiv e-prints* 1808, arXiv:1808.00485.
- Mordasini, C., Y. Alibert, W. Benz, and D. Naef (2009). "Extrasolar Planet Population Synthesis. II. Statistical Comparison with Observations". In: *Astronomy and Astrophysics* 501.3, p. 1161.
- Mordasini, C., Y. Alibert, H. Klahr, and T. Henning (2012). "Characterization of Exoplanets from Their Formation. I. Models of Combined Planet Formation and Evolution". In: *Astronomy and Astrophysics* 547, A111.
- Moulton, F. R. (1914). *An Introduction to Celestial Mechanics*.
- Moutou, C., A. Vigan, D. Mesa, S. Desidera, P. Thébault, A. Zurlo, and G. Salter (2017). "Eccentricity in Planetary Systems and the Role of Binarity - Sample Definition, Initial Results, and the System of HD 211847". In: *Astronomy and Astrophysics* 602, 00001, A87.
- Mullally, F., S. E. Thompson, J. L. Coughlin, C. J. Burke, and J. F. Rowe (2018). "Kepler's Earth-like Planets Should Not Be Confirmed without Independent Detection: The Case of Kepler-452b". In: *The Astronomical Journal* 155.5, p. 210.
- Murray, C. D. and A. C. M. Correia (2010). "Keplerian Orbits and Dynamics of Exoplanets". In: *Exoplanets*. Ed. by S. Seager. 00000. University of Arizona Press, pp. 15–23.
- Muterspaugh, M. W., B. F. Lane, S. R. Kulkarni, M. Konacki, et al. (2010). "The Phases Differential Astrometry Data Archive. V. Candidate Substellar Companions to Binary Systems". In: *The Astronomical Journal* 140, pp. 1657–1671.
- Nemravová, J. A., P. Harmanec, M. Brož, D. Vokrouhlický, et al. (2016). "ξ Tauri: A Unique Laboratory to Study the Dynamic Interaction in a Compact Hierarchical Quadruple System". In: *Astronomy and Astrophysics* 594, A55.
- Nicholls, C. P., T. Lebzelter, A. Smette, B. Wolff, et al. (2017). "CRIRES-POP: A Library of High Resolution Spectra in the near-Infrared-II. Data Reduction and the Spectrum of the K Giant 10 Leonis". In: *Astronomy and Astrophysics* 598, 00000, A79.
- Nikolov, N., D. K. Sing, N. P. Gibson, J. J. Fortney, et al. (2016). "VLT FORS2 Comparative Transmission Spectroscopy: Detection of Na in the Atmosphere of WASP-39b from the Ground". In: *The Astrophysical Journal* 832.2, p. 191.

- Oreshenko, M., K. Heng, and B.-O. Demory (2016). "Optical Phase Curves as Diagnostics for Aerosol Composition in Exoplanetary Atmospheres". In: *Monthly Notices of the Royal Astronomical Society* 457.4, p. 3420.
- Passegger, V. M., S. W.-v. Berg, and A. Reiners (2016). "Fundamental M-Dwarf Parameters from High-Resolution Spectra Using PHOENIX ACES Models: I. Parameter Accuracy and Benchmark Stars". In: *Astronomy and Astrophysics* 587. 00006, A19. arXiv: 1601.01877.
- Peck, E. R. and K. Reeder (1972). "Dispersion of Air\*". In: *JOSA* 62.8, pp. 958–962.
- Pepe, F., M. Mayor, F. Galland, D. Naef, et al. (2002). "The CORALIE Survey for Southern Extra-Solar Planets VII. Two Short-Period Saturnian Companions to HD 108147 and HD 168746". In: *Astronomy and Astrophysics* 388, pp. 632–638.
- Pepe, F., P. Molero, S. Cristiani, R. Rebolo, et al. (2014a). "ESPRESSO: The next European Exoplanet Hunter". In: *Astronomische Nachrichten* 335.1, p. 8.
- Pepe, F., A. C. Cameron, D. W. Latham, E. Molinari, et al. (2013). "An Earth-Sized Planet with an Earth-like Density". In: *Nature* 503, pp. 377–380.
- Pepe, F., D. Ehrenreich, and M. R. Meyer (2014b). "Instrumentation for the Detection and Characterization of Exoplanets". In: *Nature* 513, pp. 358–366.
- Perryman, M. A. C. (2000). "Extra-Solar Planets". In: *Reports on Progress in Physics* 63.8, p. 1209.
- Perryman, M. (2011). *The Exoplanet Handbook*. Cambridge University Press.
- Perryman, M., J. Hartman, G. Á. Bakos, and L. Lindegren (2014). "Astrometric Exoplanet Detection with Gaia". In: *The Astrophysical Journal* 797.1, p. 14.
- Pilyavsky, G., S. Mahadevan, S. R. Kane, A. W. Howard, et al. (2011). "A Search for the Transit of HD 168443b: Improved Orbital Parameters and Photometry". In: *apj* 743, 162. 00014, p. 162.
- Piskorz, D., B. Benneke, N. R. Crockett, A. C. Lockwood, et al. (2016). "Evidence for the Direct Detection of the Thermal Spectrum of the Non-Transiting Hot Gas Giant HD 88133 B". In: *The Astrophysical Journal* 832.2, p. 131.
- Piskunov, N. E. and J. A. Valenti (2002). "New Algorithms for Reducing Cross-Dispersed Echelle Spectra". In: *Astronomy and Astrophysics* 385.3. 00257, pp. 1095–1106.
- Pollacco, D. L., I. Skillen, A. Collier Cameron, D. J. Christian, et al. (2006). "The WASP Project and the SuperWASP Cameras". In: *Publications of the Astronomical Society of the Pacific* 118, pp. 1407–1418.
- Pollack, J. B., O. Hubickyj, P. Bodenheimer, J. J. Lissauer, M. Podolak, and Y. Greenzweig (1996). "Formation of the Giant Planets by Concurrent Accretion of Solids and Gas". In: *Icarus* 124, pp. 62–85.
- Quarteroni, A., R. Sacco, and F. Saleri (2000). *Numerical Mathematics*. Texts in applied mathematics 37. New York: Springer. 654 pp.
- Queloz, D., F. Bouchy, C. Moutou, A. Hatzes, et al. (2009). "The CoRoT-7 Planetary System: Two Orbiting Super-Earths". In: *Astronomy & Astrophysics* 506.1, pp. 303–319.
- Quirrenbach, A., P. J. Amado, I. Ribas, A. Reiners, et al. (2018). "CARMENES: High-Resolution Spectra and Precise Radial Velocities in the Red and Infrared". In: Ground-Based and Airborne Instrumentation for Astronomy VII. Vol. 0702, 107020W.
- Rajpurohit, A. S., C. Reylé, F. Allard, D. Homeier, M. Schultheis, M. S. Bessell, and A. C. Robin (2013). "The Effective Temperature Scale of M Dwarfs". In: *Astronomy and Astrophysics* 556, A15.
- Ranc, C., A. Cassan, M. D. Albrow, D. Kubas, et al. (2015). "MOA-2007-BLG-197: Exploring the Brown Dwarf Desert". In: *Astronomy and Astrophysics* 580, A125.

- Rauer, H., C. Catala, C. Aerts, T. Appourchaux, et al. (2014). “The PLATO 2.0 Mission”. In: *Experimental Astronomy* 38.1-2, p. 249.
- Redfield, S. (2010). “Extrasolar Planets: Fluorescent Methane Spotted”. In: *Nature* 463, pp. 617–618.
- Redfield, S., M. Endl, W. D. Cochran, and L. Koesterke (2008). “Sodium Absorption from the Exoplanetary Atmosphere of HD 189733b Detected in the Optical Transmission Spectrum”. In: *The Astrophysical Journal Letters* 673, p. L87.
- Reiners, A., M. Zechmeister, J. A. Caballero, I. Ribas, et al. (2018). “The CARMENES Search for Exoplanets around M Dwarfs. High-Resolution Optical and near-Infrared Spectroscopy of 324 Survey Stars”. In: *Astronomy and Astrophysics* 612, A49.
- Ricker, G. R., J. N. Winn, R. Vanderspek, D. W. Latham, et al. (2015). “Transiting Exoplanet Survey Satellite (TESS)”. In: *Journal of Astronomical Telescopes, Instruments, and Systems* 1, p. 014003.
- Rickman, H. (2001). “Transactions of the International Astronomical Union Proceedings of the Twenty-Fourth General Assembly.” In: *Transactions of the International Astronomical Union, Series B* 24.
- Robertson, P., S. Mahadevan, M. Endl, and A. Roy (2014). “Stellar Activity Masquerading as Planets in the Habitable Zone of the M Dwarf Gliese 581”. In: *Science* 345, pp. 440–444.
- Rodler, F., M. Lopez-Morales, and I. Ribas (2012). “Weighing the Non-Transiting Hot Jupiter  $\tau$  Boo B”. In: *The Astrophysical Journal Letters* 753.1. 00077, p. L25.
- Rogers, L. A. (2015). “Most 1.6 Earth-Radius Planets Are Not Rocky”. In: *The Astrophysical Journal* 801, p. 41.
- Rothman, L., I. Gordon, Y. Babikov, A. Barbe, et al. (2013). “The HITRAN2012 Molecular Spectroscopic Database”. In: *Journal of Quantitative Spectroscopy and Radiative Transfer* 130. 01706, pp. 4–50.
- Rothman, L., I. Gordon, A. Barbe, D. Benner, et al. (2009). “The HITRAN 2008 Molecular Spectroscopic Database”. In: *Journal of Quantitative Spectroscopy and Radiative Transfer* 110.9-10. 00000, pp. 533–572.
- Sahlmann, J., D. Segransan, D. Queloz, S. Udry, et al. (2011). “Search for Brown-Dwarf Companions of Stars”. In: *Astronomy and Astrophysics* 525. 00115, A95. arXiv: 1009.5991.
- Sallum, S., K. B. Follette, J. A. Eisner, L. M. Close, et al. (2015). “Accreting Protoplanets in the LkCa 15 Transition Disk”. In: *Nature* 527.7578, pp. 342–344.
- Sanchis-Ojeda, R., J. N. Winn, and D. C. Fabrycky (2013). “Starspots and Spin-Orbit Alignment for Kepler Cool Host Stars”. In: *Astronomische Nachrichten* 334.1-2, pp. 180–183. arXiv: 1211.2002.
- Santerne, A., J.-P. Beaulieu, B. Rojas Ayala, I. Boisse, et al. (2016a). “Spectroscopic Characterisation of Microlensing Events. Towards a New Interpretation of OGLE-2011-BLG-0417”. In: *Astronomy and Astrophysics* 595, p. L11.
- Santerne, A., B. Brugger, D. J. Armstrong, V. Adibekyan, et al. (2018). “An Earth-Sized Exoplanet with a Mercury-like Composition”. In: *Nature Astronomy* 2.5, pp. 393–400.
- Santerne, A., R. F. Díaz, C. Moutou, F. Bouchy, et al. (2012). “SOPHIE Velocimetry of Kepler Transit Candidates. VII. A False-Positive Rate of 35% for Kepler Close-in Giant Candidates”. In: *Astronomy and Astrophysics* 545, A76.
- Santerne, A., M. Endl, A. Hatzes, F. Bouchy, C. Moutou, and M. Deleuil (2011). “Radial Velocity Follow-up of CoRoT Transiting Exoplanets”. In: European Physical Journal Web of Conferences. Vol. 11. eprint: arXiv:1101.0463, p. 02001.

- Santerne, A., F. Fressin, R. F. Díaz, P. Figueira, J.-M. Almenara, and N. C. Santos (2013). “The Contribution of Secondary Eclipses as Astrophysical False Positives to Exoplanet Transit Surveys”. In: *Astronomy & Astrophysics* 557, A139.
- Santerne, A., C. Moutou, M. Tsantaki, F. Bouchy, et al. (2016b). “SOPHIE Velocimetry of Kepler Transit Candidates. XVII. The Physical Properties of Giant Exoplanets within 400 Days of Period”. In: *Astronomy and Astrophysics* 587, A64.
- Santos, N. C., V. Adibekyan, P. Figueira, D. T. Andreasen, et al. (2017). “Observational Evidence for Two Distinct Giant Planet Populations”. In: *Astronomy and Astrophysics* 603. 00001, A30.
- Santos, N. C., G. Israelian, and M. Mayor (2004). “Spectroscopic [Fe/H] for 98 Extra-Solar Planet-Host Stars. Exploring the Probability of Planet Formation”. In: *Astronomy and Astrophysics* 415, pp. 1153–1166.
- Santos, N. C., G. Israelian, M. Mayor, J. P. Bento, P. C. Almeida, S. G. Sousa, and A. Ecuvillon (2005). “Spectroscopic Metallicities for Planet-Host Stars: Extending the Samples”. In: *aap* 437. 00000, pp. 1127–1133.
- Santos, N. C., A. Santerne, J. P. Faria, J. Rey, et al. (2016). “An Extreme Planetary System around HD 219828. One Long-Period Super Jupiter to a Hot-Neptune Host Star”. In: *Astronomy and Astrophysics* 592, A13.
- Schlaufman, K. C. (2018). “Evidence of an Upper Bound on the Masses of Planets and Its Implications for Giant Planet Formation”. In: *The Astrophysical Journal* 853, p. 37.
- Schmid, H. M., D. Gisler, F. Joos, H. P. Povel, et al. (2005). “ZIMPOL/CHEOPS: A Polarimetric Imager for the Direct Detection of Extra-Solar Planets”. In: Astronomical Polarimetry: Current Status and Future Directions. Vol. 343, p. 89.
- Schwarz, G. (1978). “Estimating the Dimension of a Model”. In: *The Annals of Statistics* 6.2, pp. 461–464.
- Schwarz, H., M. Brogi, R. de Kok, J. Birkby, and I. A. G. Snellen (2015). “Evidence against a Strong Thermal Inversion in HD 209458b from High-Dispersion Spectroscopy”. In: *Astronomy and Astrophysics* 576, A111.
- Seager, S., M. Kuchner, C. A. Hier-Majumder, and B. Militzer (2007). “Mass-Radius Relationships for Solid Exoplanets”. In: *The Astrophysical Journal* 669, pp. 1279–1297.
- Seager, S. and D. D. Sasselov (2000). “Theoretical Transmission Spectra during Extrasolar Giant Planet Transits”. In: *The Astrophysical Journal* 537.2, p. 916.
- Seelmann, A. M., P. H. Hauschildt, and E. Baron (2010). “A 3D Radiative Transfer Framework . VII. Arbitrary Velocity Fields in the Eulerian Frame”. In: *Astronomy and Astrophysics* 522, A102.
- Seifahrt, A., H. U. Käufl, G. Zängl, J. L. Bean, M. J. Richter, and R. Siebenmorgen (2010). “Synthesising, Using, and Correcting for Telluric Features in High-Resolution Astronomical Spectra . A near-Infrared Case Study Using CRIRES”. In: *Astronomy and Astrophysics* 524, A11.
- Shan, Y. and G. Li (2018). “Obliquity Variations of Habitable Zone Planets Kepler-62f and Kepler-186f”. In: *The Astronomical Journal* 155.6, p. 237.
- Simon, K. P. and E. Sturm (1994). “Disentangling of Composite Spectra”. In: *Astronomy and Astrophysics* 281. 00000, pp. 286–291.
- Sing, D. K., J. J. Fortney, N. Nikolov, H. R. Wakeford, et al. (2016). “A Continuum from Clear to Cloudy Hot-Jupiter Exoplanets without Primordial Water Depletion”. In: *Nature* 529.7584, p. 59.
- Sirbu, D., S. Thomas, R. Belikov, and E. Bendek (2017a). “Techniques for High-Contrast Imaging in Multi-Star Systems. II. Multi-Star Wavefront Control”. In: *The Astrophysical Journal* 849, p. 142.

- Sirbu, D., R. Belikov, E. Bendek, E. Holte, A. J. Riggs, and S. Shaklan (2017b). “Prospects for Exoplanet Imaging in Multi-Star Systems with Starshades”. In: Society of Photo-Optical Instrumentation Engineers (SPIE) Conference Series. Vol. 0400. eprint: arXiv:1709.00041, p. 104001D.
- Skrutskie, M. F., R. M. Cutri, R. Stiening, M. D. Weinberg, et al. (2006). “The Two Micron All Sky Survey (2MASS)”. In: *The Astronomical Journal* 131, pp. 1163–1183.
- Smette, A., H. Sana, S. Noll, H. Horst, et al. (2015). “Molecfit: A General Tool for Telluric Absorption Correction - I. Method and Application to ESO Instruments”. In: *Astronomy and Astrophysics* 576. 00067, A77.
- Snellen, I. A. G., B. R. Brandl, R. J. De Kok, M. Brogi, J. Birkby, and H. Schwarz (2014). “Fast Spin of the Young Extrasolar Planet  $\beta$  Pictoris B”. In: *Nature* 509. 00000, p. 63.
- Snellen, I. A. G. and A. G. A. Brown (2018). “The Mass of the Young Planet Beta Pictoris b through the Astrometric Motion of Its Host Star”. In: *Nature Astronomy*.
- Snellen, I. A. G., R. J. de Kok, and E. J. W. De Mooij (2010). “The Orbital Motion, Absolute Mass and High-Altitude Winds of Exoplanet HD209458b”. In: *Nature* 465.7301, p. 1049.
- Snellen, I. A. G., R. de Kok, J. Birkby, B. Brandl, et al. (2015). “Combining High-Dispersion Spectroscopy (HDS) with High Contrast Imaging (HCI): Probing Rocky Planets around Our Nearest Neighbors”. In: *Astronomy & Astrophysics* 576, A59. arXiv: 1503.01136.
- Soderblom, D. R. (2010). “The Ages of Stars”. In: *Annual Review of Astronomy and Astrophysics* 48. 00241, pp. 581–629.
- Sorahana, S., I. Yamamura, and H. Murakami (2013). “On the Radii of Brown Dwarfs Measured with AKARI Near-Infrared Spectroscopy”. In: *The Astrophysical Journal* 767.1, p. 77. arXiv: 1304.1259.
- Sousa, S. G., N. C. Santos, M. Mayor, S. Udry, et al. (2008). “Spectroscopic Parameters for 451 Stars in the HARPS GTO Planet Search Program. Stellar [Fe/H] and the Frequency of Exo-Neptunes”. In: *aap* 487. 00390, pp. 373–381.
- Spiegel, D. S., A. Burrows, and J. A. Milsom (2011). “The Deuterium-Burning Mass Limit for Brown Dwarfs and Giant Planets”. In: *The Astrophysical Journal* 727, p. 57.
- Starovoit, E. D. and A. E. Rodin (2017). “On the Existence of Planets around the Pulsar PSR B0329+54”. In: *Astronomy Reports* 61, pp. 948–953.
- Sterken, C. and J. Manfroid (1992). *Astronomical Photometry: A Guide*. Astrophysics and Space Science Library. Springer Netherlands.
- Stevenson, K. B., J.-M. Désert, M. R. Line, J. L. Bean, et al. (2014). “Thermal Structure of an Exoplanet Atmosphere from Phase-Resolved Emission Spectroscopy”. In: *Science* 346, pp. 838–841.
- Suzuki, D., D. P. Bennett, T. Sumi, I. A. Bond, et al. (2016). “The Exoplanet Mass-Ratio Function from the MOA-II Survey: Discovery of a Break and Likely Peak at a Neptune Mass”. In: *The Astrophysical Journal* 833, p. 145.
- Tinetti, G., A. Vidal-Madjar, M.-C. Liang, J.-P. Beaulieu, et al. (2007). “Water Vapour in the Atmosphere of a Transiting Extrasolar Planet”. In: *Nature* 448.7150, pp. 169–171.
- Tody, D. (1993). “IRAF in the Nineties”. In: *Astronomical Data Analysis Software and Systems II*. Ed. by R. J. Hanisch, R. J. V. Brissenden, and J. Barnes. Vol. 52. Astronomical Society of the Pacific Conference Series. 00000, p. 173.
- Triaud, A. (2016). “Exoplanets: Migration of Giants”. In: *Nature* 537.7621, pp. 496–497.

- Tsantaki, M., S. G. Sousa, V. Z. Adibekyan, N. C. Santos, A. Mortier, and G. Israelian (2013). “Deriving Precise Parameters for Cool Solar-Type Stars. Optimizing the Iron Line List”. In: *aap* 555, A150. 00077, A150.
- Udalski, A., B. Paczynski, K. Zebrun, M. Szymanski, et al. (2002). “The Optical Gravitational Lensing Experiment. Search for Planetary and Low-Luminosity Object Transits in the Galactic Disk. Results of 2001 Campaign”. In: *Acta Astronomica* 52, pp. 1–37.
- Udry, S., M. Mayor, D. Naef, F. Pepe, D. Queloz, N. C. Santos, and M. Burnet (2002). “The CORALIE Survey for Southern Extra-Solar Planets: VIII. The Very Low-Mass Companions of HD 141937, HD 162020, HD 168443 and HD 202206: Brown Dwarfs or “Superplanets”?”. In: *Astronomy and Astrophysics* 390.1. 00158, pp. 267–279.
- Ulmer-Moll, S., P. Figueira, J. J. Neal, N. C. Santos, and M. Bonnefoy (2018). “Telluric Correction in the Near-Infrared: Standard Star or Synthetic Transmission?”. In: *arXiv e-prints*, arXiv:1811.08915.
- Vacca, W. D., M. C. Cushing, and J. T. Rayner (2003). “A Method of Correcting Near-Infrared Spectra for Telluric Absorption”. In: *Publications of the Astronomical Society of the Pacific* 115.805. 00000, p. 389.
- Vanderspek, R., C. X. Huang, A. Vanderburg, G. R. Ricker, et al. (2018). “TESS Discovery of an Ultra-Short-Period Planet around the Nearby M Dwarf LHS 3844”. In: *ArXiv e-prints* 1809, arXiv:1809.07242.
- Vogt, S. S., R. P. Butler, E. J. Rivera, N. Haghjipour, G. W. Henry, and M. H. Williamson (2010). “The Lick-Carnegie Exoplanet Survey: A  $3.1\text{ M} \oplus$  Planet in the Habitable Zone of the Nearby M3V Star Gliese 581”. In: *The Astrophysical Journal* 723, pp. 954–965.
- Wang, J., D. Mawet, G. Ruane, R. Hu, and B. Benneke (2017). “Observing Exoplanets with High Dispersion Coronagraphy. I. The Scientific Potential of Current and Next-Generation Large Ground and Space Telescopes”. In: *The Astronomical Journal* 153, p. 183.
- Weiss, L. M., G. W. Marcy, J. F. Rowe, A. W. Howard, et al. (2013). “The Mass of KOI-94d and a Relation for Planet Radius, Mass, and Incident Flux”. In: *The Astrophysical Journal* 768, p. 14.
- Wenger, M., F. Ochsenbein, D. Egret, P. Dubois, et al. (2000). “The SIMBAD Astronomical Database. The CDS Reference Database for Astronomical Objects”. In: *Astronomy and Astrophysics Supplement Series* 143, pp. 9–22.
- Whitworth, A., M. R. Bate, Å. Nordlund, B. Reipurth, and H. Zinnecker (2007). “The Formation of Brown Dwarfs: Theory”. In: *Protostars and Planets V*. 00087, pp. 459–476.
- Winn, J. N. (2010). “Transits and Occultations”. In: arXiv: 1001.2010 [astro-ph].
- Wolszczan, A. and D. A. Frail (1992). “A Planetary System around the Millisecond Pulsar PSR1257 + 12”. In: *Nature* 355.6356, pp. 145–147.
- Wyttenbach, A., D. Ehrenreich, C. Lovis, S. Udry, and F. Pepe (2015). “Spectrally Resolved Detection of Sodium in the Atmosphere of HD 189733b with the HARPS Spectrograph”. In: *Astronomy and Astrophysics* 577, A62.
- Zechmeister, M., A. Reiners, P. J. Amado, M. Azzaro, et al. (2018). “Spectrum Radial Velocity Analyser (SERVAL). High-Precision Radial Velocities and Two Alternative Spectral Indicators”. In: *Astronomy and Astrophysics* 609, A12.
- Zucker, S. and T. Mazeh (1994). “Study of Spectroscopic Binaries with TODCOR. 1: A New Two-Dimensional Correlation Algorithm to Derive the Radial Velocities of the Two Components”. In: *The Astrophysical Journal* 420. 00376, pp. 806–810.

- Zucker, S. and T. Mazeh (2001). “Analysis of the Hipparcos Observations of the Extrasolar Planets and the Brown Dwarf Candidates”. In: *The Astrophysical Journal* 562.1. 00060, p. 549.
- Zurlo, A. and M. Bonnefoy (2015). “New SPHERE Results on the Planetary System around HR8799”. In: AAS/Division for Extreme Solar Systems Abstracts. Vol. 3, p. 202.05.